CONTROL OF A PERMANENT MAGNET SYNCHRONOUS GENERATOR-BASED WIND ENERGY CONVERSION SYSTEM

By

Ester Hamatwi

A thesis submitted in fulfillment of the requirements for the degree of

MASTER OF SCIENCE IN ELECTRICAL ENGINEERING

DEPARTMENT OF ELECTRICAL, ELECTRONIC AND COMPUTER ENGINEERING

COLLEGE OF AGRICULTURE, ENGINEERING AND SCIENCE

UNIVERSITY OF KWAZULU-NATAL

September 2016

Supervisor: Prof. I. E. Davidson

Co-Supervisor: Prof. M. N. Gitau

DECLARATION 1-PLAGIARISM

I, Ester Hamatwi, declare that

1. The research reported in this dissertation, except where otherwise indicated, is my original research.
2. This dissertation has not been submitted for any degree or examination at any other university.
3. This dissertation does not contain other person's data, pictures, graphs or other information unless specifically acknowledged as being sourced from other persons.
4. This dissertation does not contain other person's writing unless specifically acknowledged as being sourced from other researchers. Where other written sources have been quoted, then:
    a. Their words have been re-written but the general information attributed to them has been referenced.
    b. Where their exact words have been used, then their writing has been placed in italics and inside quotation marks and referenced.
5. This dissertation does not contain text, graphics or tables copied and pasted from the internet, unless specifically acknowledged, and the source being detailed in the thesis and in the Reference sections.

Signed:

…….

Ms. Ester Hamatwi

As the candidate's Supervisor, I agree/do not agree to the submission of this thesis. Signed:

……

Prof. I. E. Davidson/ Prof. M.N. Gitau

Date:

Dedicated, in thankful appreciation for the support, encouragement, and understanding to my beloved father, mother, and siblings.

ACKNOWLEDGEMENTS

I would like to express my sincere gratitude to the almighty God for consistently being my pillar of strength, for guiding me, giving me courage; persistence and faith that I needed to carry out this project.

Secondly, I would like to express my gratitude to the few people that have contributed to the successful completion of this project and without whom this thesis would not have been possible:

- My main supervisor, Prof I. E. Davidson for his invaluable professional and career-building advice, guidance and his enormous patience throughout the development of my research.
- My co-supervisor, Prof. M. N. Gitau for his guidance throughout the duration of my studies, for making time to assist me in refining my research focus area, and for critically reviewing my thesis and giving mind-sharpening ideas and knowledgeable experience.
- My loving family, friends and fellow postgraduates who have helped and gave me encouragement throughout the duration of my studies.
- Eskom, for granting me financial support to pursue my studies under the Eskom Power Plant Engineering Institute (EPPEI) Program. Thank you for believing in me and awarding me the financial grant.

ABSTRACT

Wind energy has proven to be a competitive and an environmentally friendly renewable energy resource for generating electricity. Wind farms are usually located far from the load centers; hence the generated power has to be transmitted over long distances to load centers. High voltage direct current (HVDC) transmission system is the preferred means for transmitting bulk power over long distances when compared to high voltage alternating current (HVAC) transmission system. An HVDC transmission system increases the transmission capacity, improves the system stability, and possesses lower transmission losses. In this research investigation, a 690V, 2MW wind turbine-driven permanent magnet synchronous generator is modelled to be integrated into a local 33kV AC grid via a three- level neutral-point-clamped voltage source converter (VSC)-based HVDC transmission system. Three control schemes were implemented, namely: pitch-angle controller, generator-side converter controller, and a grid-side converter controller to optimize the system performance. The stability analysis and controller modeling was carried out in MATLAB using bode plots and step response curves. The proposed subsystems and the control schemes were implemented in PSIM software package to evaluate the overall system's performance. The simulations were carried out on the model and it was concluded that the grid-side converter controller ensured maximum power point tracking when the wind speed was lower than the wind turbine(WT)'s rated wind speed. Conversely, as the wind speed exceeded the WT's rated wind speed, the pitch-angle controller was activated. This increased the angle of attack thereby reducing the power coefficient in order to shed off the aerodynamic power. Furthermore, the DC-link voltage was stabilized within the allowable limits to ensure a continuous flow of active power from the WT to the grid and the reactive power transfer between the grid-side converter and the AC utility grid was maintained to a minimum to ensure a unity power factor. The comparison analysis of the new control approach to the traditional control approach illustrated that for the new control approach, the ability of the DC-link voltage controller to keep the DC-link voltage within the allowable limits does not get impaired during fault conditions. Therefore, the power continues flowing from the WT generator to the grid. Conversely, it was observed that for the traditional control approach, the ability of the DC-link voltage controller to stabilize the DC-link voltage gets impaired and therefore it can no longer effectively transfer as much active power from the WT generator to the grid. Therefore, the new control approach proved to be effective in terms of stabilizing the DC-link voltage during fault conditions thereby enhancing the WT’s fault-ride-through capability.

DECLARATION 2- PUBLICATIONS

The following publications emanated from this research investigation:

[1] E. Hamatwi, I.E. Davidson and M.N. Gitau, "Modeling and Control of Voltage Source Converters for Grid Integration of a Wind Turbine System". *Proceedings of the IEEE PES Power Africa Conference*, Livingstone, Zambia, 28 June - 2 July 2016, pages 98-106.

[2] E. Hamatwi, I.E. Davidson, M.N. Gitau, R. Vajeth and K. Pickster, "Power Control Techniques in Voltage Source Converters for Grid Integration of Wind Energy". *Proceedings of the 3rd Eskom Power Plant Engineering Institute Student Workshop*, Eskom Academy of Learning, Midrand, South Africa, 11-12 July 2016.

[3] E. Hamatwi, I. E. Davidson and M.N. Gitau, "Control of multi-Level Voltage Source Converters Integrating a Wind Turbine System into the Grid", *Proceedings of the 5th International Conference on Renewable Energy Research and Applications*, Birmingham, United Kingdom, 20-23 November 2016.

[4] E. Hamatwi, I. E. Davidson and M.N. Gitau "Pitch-Angle Control of a Wind Turbine Equipped with a Permanent Magnet Synchronous Generator," *Proceedings of the 25th South African Universities Power Engineering Conference*, Cape Town, South Africa, January 2017.

[5] E. Hamatwi, I. E. Davidson and M.N. Gitau " Control of a Wind Turbine Equipped with a Permanent Magnet Synchronous Generator for Maximum Power Point Tracking," *Proceedings of the 25th South African Universities Power Engineering Conference*, Cape Town, South Africa, January 2017.

Signed:

…….

Ester Hamatwi

TABLE OF CONTENTS

Page

TABLE OF FIGURES

Page

LIST OF TABLES

Page

LIST OF ABBREVIATIONS

AC: Alternating Current

APOD: Alternative Phase Opposition Disposition

CHB: Cascaded H-Bridge

CkT: Clarke Transformation

DC: Direct Current

DFIG: Doubly-Fed Induction Generator

DQ: Direct-Quadrature

FC: Flying-Capacitor

FRT: Fault Ride Through

FSWT: Fixed Speed Wind Turbine

GM: Gain Margin

HCS: Hill Climb Search

HVAC: High Voltage Alternating Current Transmission System

HVDC: High Voltage Direct Current Transmission System

IGBT: Insulated Gate Bipolar Transistor

IPP: Independent Power Producers

IRP: Integrated Resource Plan

LCC: Line Commutated Converter

MPPT: Maximum Power Point Tracking

NPC: Neutral-Point Clamped

ORB: Optimal Relationship Based MPPT

OTC: Optimal Torque Control MPPT

PCC: Point of Common Coupling

PD: Phase Disposition

PLL: Phase Locked Loop

PMSG: Permanent Magnet Synchronous Generator

PM: Phase Margin

POD: Phase Opposition Disposition

P&O: Perturb & Observe

PWM: Pulse-Width Modulation

PT: Park Transformation

RE: Renewable Energy

VSC: Voltage Source Converter

SFO-PWM: Switching Frequency Optimal Pulse Width Modulation

SHE-PWM: Selective Harmonic Elimination Pulse Width Modulation

SPWM: Sinusoidal Pulse Width Modulation

SVM: Space Vector Modulation

THI-PWM: Third Harmonic Injection Pulse Width Modulation

TSR: Tip Speed Ratio

WECS: Wind Energy Conversion System

WF: Wind Farm

WT: Wind Turbine

WTG: Wind Turbine Generator

VOC: Vector Oriented Control

VSWT: Variable Speed Wind Turbine

CHAPTER 1: INTRODUCTION

1.1 Background Study

Until recently, Eskom, South Africa's dominant electric utility has been experiencing power challenges such as periodic-load shedding due to the power demand that is outstripping the available supply. South Africa's power generation is mainly coal-based due to large coal reserves as shown in Table 1.1. However, due to the lack of capital for investing in coal-based generating plants, the government plans that by 2030, renewable energy (RE) sources should represent 20% of the total installed capacity [1]. This is mainly due to the fact that RE sources represent a sustainable, non-depreciable and environmentally friendly alternative power generation method over the conventional methods.

Table 1.1 shows South Africa's existing power generation capacity and the 20-year generation capacity projections under the Integrated Resource Plan (IRP).

Table 1. 1: South Africa's Planned Generation Capacity [2]

	Existing Generation		**Total Capacity (MW)**
Energy Source	**Capacity (MW)**	**Energy (GWh)**	**2011 IRP (MW)**
Coal fired	37 715	218 212	6 250
Hydro-electric	661	1 904	2 609
Pump storage	1 400	2 962	3 000
Gas turbines	2 426	709	6 280
Nuclear	1 910	23 502	9 600
Renewable Energy	3	2	17800
Total Capacity	44 115	247 291	42 539

Wind energy has recently proven to be a fast-growing, competitive and an environmentally friendly renewable energy resource for generating electricity. This is mainly due to the growth in the size of commercial wind turbine designs and an increase in their power ratings from a kilowatts power capacity to megawatts power capacity [3, 4].

Figure 1.1 shows the advancement in the size and power ratings of commercial wind turbines.

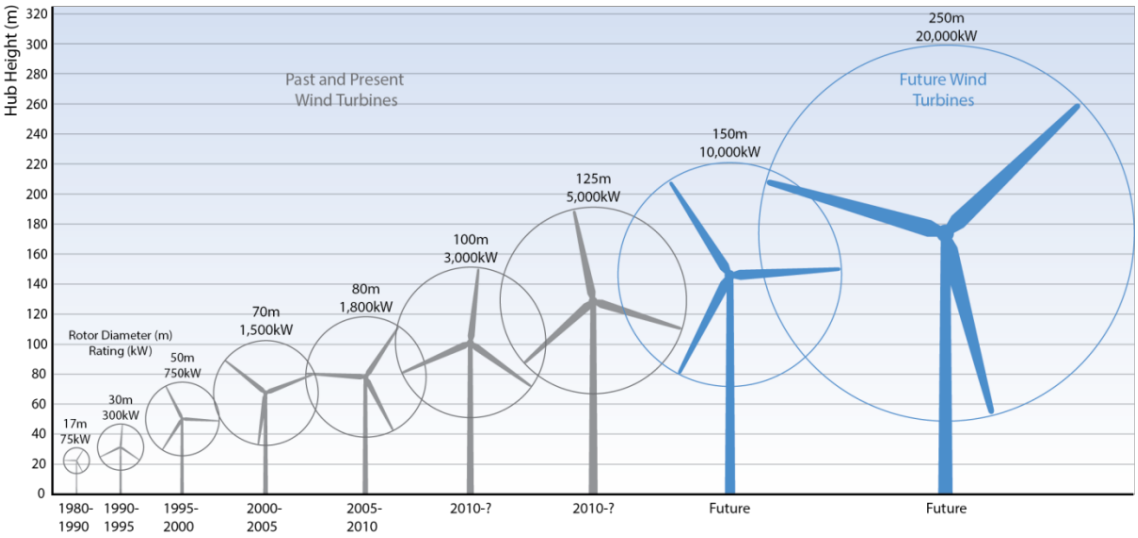

Figure 1. 1: Advancement in the size of commercial wind turbines [5]

According to Szewczuk[6], South Africa's potential of wind energy/power is generally good along the coastal areas of Western and Eastern Cape. The same applies to the neighboring country, Namibia [7]. A number of wind farms have been installed in the coastal areas of South Africa. Wind farms are usually located far from the load centers for minimal disturbances and for optimal power generation[8]. Thus, the generated power from wind farms has to be transmitted over long distances. Therefore, there is a need to use most efficient and reliable bulk power transmission system. High Voltage Direct Current (HVDC) transmission is preferred to High Voltage Alternating Current (HVAC) transmission system over long distances. HVDC increases the transmission capacity and system stability, it is associated with lower transmission losses, and it is often easier to obtain the right-of-way for HVDC lines due to the reduced environmental impacts [9-11].

The Line Commutated Converter (LCC)-based HVDC transmission system with thyristors as their main switching devices has a long and successful history, with high reliability and low conversion losses[9]. However, the technical restrictions of LCC such as the inability to achieve full controllability of the system, high harmonic contents and the dependence of switch commutation on the stiffness of the grid voltage limits the use of LCC in some transmission and distribution applications. This includes: supplying power to isolated loads and dead/weak networks, integrating small-scale generation systems such as renewable energy sources into the utility grid and interconnecting multi-terminal networks [9, 12].

The rapid development in the field of the self-commutated power electronic switch, the insulated gate bipolar transistor (IGBT) led to the implementation of Voltage Source Converter (VSC)- based HVDC transmission systems [10, 13, 14]. VSCs operate at high switching frequencies utilizing the pulse-width modulation technique. The VSC-based HVDC technology is of increasing interest as it offers several benefits over LCC, namely: independent control of active and reactive power, fast response in case of disturbances due to increased switching frequency, ability to connect to weak networks, ability to interconnect asynchronous and multi-terminal networks, no risk of commutation failures and minimal environmental impacts[15].

A wind speed generator (WTG) can be classified either as a fixed speed or as a variable speed WTG[16]. The variable-speed wind turbine (VSWT) can extract optimal power at different wind speeds while the fixed-speed wind turbine (FSWT) can only extract optimal power at the rated wind speed. Therefore, a VSWT yields more power than an FSWT thereby maximizing the aerodynamic efficiency of the WT[16]. Due to the intermittent nature of wind, power electronic converters are normally employed to integrate WTs into the power utility grid. This is usually implemented to ensure optimal extraction of power from the wind source and to ensure that the characteristics of the WT under consideration matches with the requirements of grid connections, namely: voltage level, frequency, active power and reactive power [17].

A VSC can be classified either as a two-level or a multi-level converter topology depending on the arrangement of the semiconductor switches of the converter [18]. Two-level VSC topologies are robust, have a simple configuration and a reliable performance. However, they are associated with high switching losses and they output a waveform with poor quality and hence, they require extra filtering elements [16]. On the other hand, multi-level VSCs synthesizes voltages with better waveform quality, and hence they cut down on the size and number of filtering elements [16, 19]. Furthermore, multilevel converters are associated with lower switching losses and higher overall efficiency. Multilevel converter topologies are becoming very attractive in large wind turbine applications.

The direct control and vector control are the well-developed control techniques used to carry out the control of active and reactive power in grid-connected WECS [20-22]. Several literature studies carried out a comparative analysis of these control techniques and it was concluded that, although the direct control technique has a fast dynamic response and it is easy to implement, the vector control technique has a better performance due to lower current distortions, higher grid power factor, and higher overall efficiency. Fault ride-through capability can be defined as the ability of a wind turbine to remain connected to the power utility grid during fault conditions to offer grid support [16].

Considering the vector control technique, there are two generic control approaches used to control the grid-side converter and the generator-side converter, namely: traditional/ conventional and new control approach. In the traditional control approach, the controller applied to the generator-side converter is commonly used for controlling the rotor speed to achieve maximum power extraction from the wind resource and to control the stator voltage. On the other hand, the controller applied to the grid-side converter is used to stabilize the DC-link voltage and to carry out the control of reactive power exchanged between the converter and the power utility grid [16, 19, 23-25]. The new control approach reverses the functions of the traditional converter station's control approach. According to the literature [26, 27], the traditional control approach, although not beneficial from a fault-ride-through point of view, it is well developed and it is commonly employed in existing VSC projects. Although the new control approach is still undergoing development, several studies have proven that it is beneficial from a fault-ride-through capability point of view.

1.1 Problem Statement

With the energy demand growing at a high rate, the main supply grid is being pressurized leading to grid instability and reduced power quality. Renewable energy is a preferred solution to meeting load demands over fossil fuels. However due to the placement of renewable energy (RE) sources far away from the load sinks, the power generated is required to be transmitted over long distances to be integrated into the main supply grid.

The solution to overcoming this problem is the use of the HVDC transmission which is the preferred bulk power transmission system over HVAC transmission system. This is mainly because, HVDC transmission systems are associated with minimal transmission losses over long distances, and low costs, and reduced environmental impacts. Although the LCC-based HVDC is a mature technology, it is not suitable for grid-integration of RE sources. Therefore, the VSC- based HVDC must be implemented in future HVDC projects.

Furthermore, although the two-level VSC topologies are commonly used and well developed, they are associated with high switching losses and they require extra electromagnetic interference (EMI) filters. Therefore, more focus needs to be put on implementing multi-level converter topologies because they are associated with lower switching losses, higher overall efficiency, and cuts down on the size and number of filtering elements. Moreover, the traditional converter control approach becomes impaired during grid faults and as a consequence, the wind turbine's fault ride-through capability gets impaired as well. Therefore, the new control approach needs to be adopted in wind energy conversion systems to improve the fault ride-through capability of wind turbines.

1.2 Objectives of the Study

This research investigation aims at developing a 3-level Neutral-Point-Clamped (NPC) multi-level VSC-based HVDC transmission system and evaluating its potential use in integrating a 2MW, 690V variable speed wind turbine into a 33kV power utility grid.

More specific objectives defining the scope of this thesis are:

- Carry out a thorough review of the concept of VSC-based HVDC transmission system.
- Develop a wind energy conversion system using PSIM software package comprising of:
  - A wind turbine coupled to a permanent magnet synchronous generator (PMSG)
  - The generator-side (rectifier) and grid-side converter (inverter) stations made up of a 3-level neutral-point-clamped VSC topology.
  - A power stage made up of a phase reactor, a power transformer and an AC source representing the 33kV power utility grid.
- Design the proposed controllers in the frequency domain using bode plots and step response curves in MATLAB software package.

The proposed controllers are:

  - Pitch-angle control: for limiting the amount of power extracted from the wind resource when the wind speed exceeds the WT's rated wind speed.
  - Generator-side converter (rectifier) control: to stabilise the DC-link voltage to ensure continuous active power flow from the wind turbine generator to the utility grid, and to control the stator voltage to avoid the risk of over-voltages.
  - Grid-side converter (Inverter) control: to control the rotor speed for maximum power point tracking (MPPT) and to control the reactive power control to ensure unity power factor.

- Apply these controllers to the wind energy conversion system in order to evaluate their effectiveness in improving the performance of the overall system. This is evaluated by carrying out the following analyses:
  - MPPT control analysis over a wide range of wind speeds using the Optimal Relation-Based (ORB) MPPT control strategy.
  - Pitch-angle control analysis using the rotor-speed-based technique during high wind speeds.
  - Stator Voltage control analysis over a wide range of wind speeds.
  - Reactive power control analysis to ensure unity power factor.
  - DC-link voltage control analysis.

1.3 Research Questions

The research investigation is characterized by the following questions:

- How can a wind turbine coupled to a PMSG be controlled to ensure optimal power extraction from the wind resource at a particular instant and thereby optimizing its aerodynamic efficiency?
- How can a wind turbine be controlled to ensure that it is protected from sudden wind gusts?
- How can the WT's fault ride-through capability be improved?

1.4 Significance of the Study

This project will provide a detailed design of a VSC-based HVDC transmission system and its controllers derived from fundamental principles that will be of significant use to Eskom in terms of planning and integration of wind farms into the existing AC grid/network through HVDC transmission links. This will complement existing power generation capacity in South Africa and improve the energy mix.

1.5 Project Contribution

Several studies have been carried out in the area of grid integration of wind energy system employing two-level converters in the intermediate converter stations and applying the conventional control approach. However, so far fewer studies have been carried out in the areas of implementing multilevel converters in place of two-level converters in these applications. Furthermore, the new control approach that is to be implemented in this study has only been applied to two-level VSCs. This research investigation ought to divert into the research of currently increasing interest, which is the implementation of multilevel VSCs that overcome most of the challenges experienced when two-level VSC topologies are implemented. Furthermore, this study also focuses on a new converter control approach which ought to improve the WT's fault ride-through capability.

1.6 Limitations and Delimitations

At this point, the research investigation will be limited to software simulations only. Furthermore, the study will only focus on control and analysis of one wind turbine that is rated at 2MW to be integrated into a 33kV grid. The converter stations will be connected in a back-to-back HVDC configuration.

1.7 Dissertation Outline

This dissertation is made up of nine chapters. **Chapter 1** dealt with a brief background study of the research investigation, the problem statement of the study, objectives of the study, the research questions that this study intends to answer, justification/significance of the study as well the limitations and delimitations of the study. **Chapter 2** focuses on a brief overview of the HVDC technology with special emphasis on the comparison of HVDC and HVAC transmission systems, HVDC configurations, and HVDC technologies: LCC and VSC, and their advantages and shortcomings. The chapter goes on to briefly cover the operating principles of a VSC-based HVDC transmission system, its system components, and the different VSC topologies. The chapter carries on with an overview of the wind energy conversion system emphasizing on the wind turbine components and the control techniques used for power limitation during high wind gusts and for maximum power point tracking during low wind speeds. Furthermore, the chapter discusses the traditional/conventional and new converter control approaches. Moreover, the chapter covers the pulse width modulation techniques used for the control of voltage source converters. Moreover, the chapter discusses the compensators used for improving the entire system's performance.

Chapter 3 covers the detailed mathematical modelling and sizing of the proposed wind energy conversion system's components. **Chapter 4** focuses on the mathematical modelling of a 3-level neutral-point-clamped VSC emphasizing on the dynamics on the AC-side and on the DC-side. Moreover, the chapter covers the derivation of the transfer functions for the outer and inner control loops for the controllers applied to the grid-side and generator-side converters. **Chapter 5** discusses the design specifications that are to be achieved or met in this study. Moreover, the chapter covers the design and frequency-domain stability analysis of the controller applied to the generator-side converter using Bode plots and step response curves in MATLAB software package. Furthermore, the chapter deals with the design and frequency-domain stability analysis of a pitch angle controller.

Chapter 6 covers the design and frequency-domain stability analysis of the controller applied to the grid-side converter using Bode plots and step response curves in MATLAB software package. **Chapter 7** focuses on the modeling and implementation of the system components and controllers in PSIM software package to further analyze the entire system's performance. **Chapter 8** focuses on discussing the simulation results and validating whether the proposed model and the control schemes meet the objectives and whether the research questions have been answered. **Chapter 9** concludes the thesis and brings about recommendations and future work.

The appendix section covers the current VSC-based HVDC projects in operation worldwide, Clarke and Park transformations, and a brief review the South African grid code requirements for integrating wind energy systems into the main power utility grid. Furthermore, the M-files with the MATLAB codes of the proposed controllers are also included in the appendix section.

CHAPTER 2: LITERATURE REVIEW

This chapter focuses on a brief overview of the HVDC technology with special emphasis on the comparison of HVDC and HVAC transmission systems, HVDC configurations, HVDC technologies: LCC and VSC, and their advantages and shortcomings. The chapter goes on to briefly cover the operating principles of a VSC-based HVDC transmission system, its system components, and the different VSC topologies. The chapter carries on with an overview of the wind energy conversion system emphasizing on the wind turbine components and the control techniques used for power limitation during high wind gusts and for maximum power point tracking during low wind speeds. Furthermore, the chapter discusses the traditional/conventional and new converter control approaches. Moreover, the chapter covers the pulse width modulation techniques used for the control of voltage source converters. The compensators used for improving the entire system's performance are also briefly discussed in this chapter.

2.1 Overview of HVDC Transmission Systems

2.1.1 HVDC Technology

An HVDC Transmission system is a technology that uses direct current to transmit bulk electrical power over long distances efficiently, in contrast with the HVAC transmission system [28]. The transmission path can either be overhead lines or underground/submarine cables. The HVDC technology was developed during the 1930s by ASEA, the Swedish electrical conglomerate [12]. In the 1950s, the research into mercury-arc technology begun, this led to the implementation of the world's first commercial HVDC power link interconnecting the island of Gotland (Sweden) and Sweden via a submarine cable [29, 30]. After a few years, HVDC transmission systems based LCCs employing thyristor switches commercially known as HVDC Classic were implemented [9]. However, the technical restrictions of LCC limited its use in some transmission and distribution applications. The rapid development in the field of self-commutated power electronic switches such as the insulated gate bipolar transistor (IGBT) led to the implementation of HVDC transmission systems based on VSC [10, 14]The VSC technology overcomes the shortcomings of LCC and it is increasingly used more often in transmission and distribution systems. The VSC technology is commercially available as HVDC light developed by ABB and HVDC plus developed by Siemens [9, 12].

2.1.2 Comparison of HVDC and HVAC Transmission Systems

The choice between an HVAC and HVDC system is mainly based on economic and technical factors such as transmission distance and medium; overhead lines or underground/ submarine cable. HVDC transmission is the preferred bulk power transmission system over long distances compared to HVAC transmission system [9, 10]. It should be noted that this is only true for distances above a certain distance called the breakeven distance as shown in Figure 2.1 [28]. The breakeven distance for HVDC overhead lines and underground /submarine cables is in the region of 400-700km and 25-50km, respectively [11].

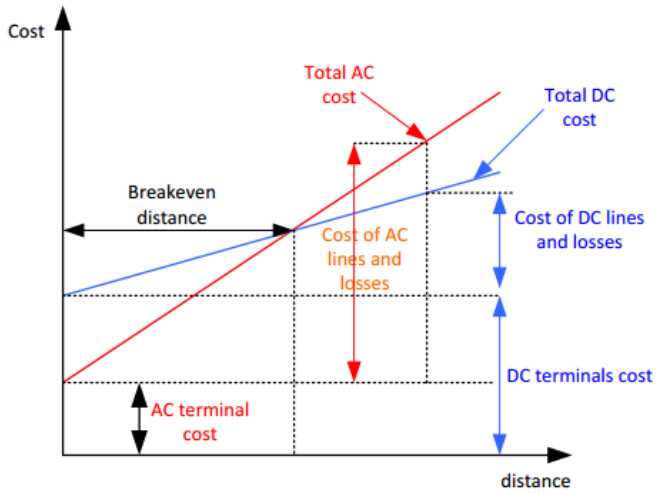

Figure 2. 1: HVDC and HVAC breakeven distance [28]

Advantages of HVDC transmission systems over HVAC transmission systems

- **Investment costs**: The HVAC technology requires three conductors, one for each phase while the HVDC technology only requires two conductors; this significantly cuts down on the investment cost [28].
- **Supporting towers**: HVAC transmission systems are associated with massive towers while the HVDC transmission system requires smaller supporting towers. Therefore, it is often easier to obtain the right-of-way for DC cables due to the reduced environmental impacts [31].
- **Electromagnetic interferences**: the interference with nearby communication lines is minimal in HVDC transmission systems than in HVAC transmission systems.
- **Transmission losses**: Considering the fact that there is no skin and proximity effect associated with HVDC technology, the overall system losses are lower in HVDC than in HVAC transmission systems.
- **Interconnection of asynchronous networks**: the HVDC technology makes it possible to interconnect asynchronous networks; power grids operating at

difference frequencies [32]. Moreover, the HVDC system fully decouples the interconnected AC systems and hence prevents the propagation of fault from one AC network to another [19].

Drawbacks of HVDC transmission systems

- Inability to use power transformers: Although the HVDC technology can be said to be more attractive and advantageous for transmitting power over long distances, it is impossible to use transformers to alter the voltage level along the transmission path unlike in HVAC technology [32]
- Cost of converter stations: the HVDC system converter stations are more expensive compared to HVAC system converter stations. This is due to the additional AC/DC converter in each substation [31].

2.1.3 HVDC Transmission System Configurations

The HVDC Transmission links can be classified into different configurations depending on the arrangement of the converter stations, namely: mono-polar, bipolar, multi-terminal and back-to-back HVDC system configurations [19].

2.1.3.1 Mono-polar HVDC System Configuration

This configuration is made up of two converters connected together using a single pole as shown in Figure 2.2. A ground or metallic path can be used as a return path depending on the application.

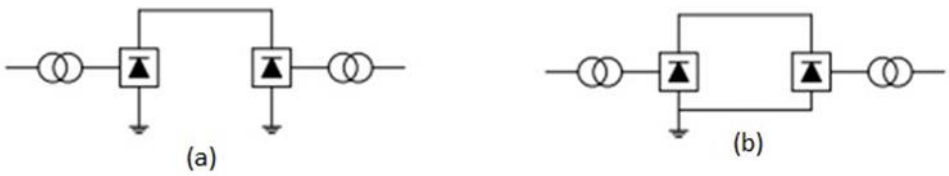

Figure 2. 2: Mono-polar HVDC system configurations; (a) with ground return, (b) with metallic return [32]

Although the use of ground return causes environmental concerns due to the use of electrodes and continuous flow of ground current, the use of one high-voltage conductor reduces the cost and transmission losses [19]. Conversely, the use of metallic return means that there is no ground current and the return cable is usually not fully insulated; hence reducing the expenditure on the dc cables. This configuration is applied in most submarine HVDC transmission systems.

2.1.3.2 Bipolar HVDC System Configuration

In this configuration, two conductors; negative and positive polarity, are used to connect the converter stations. Figure 2.3 shows the bipolar HVDC system configuration

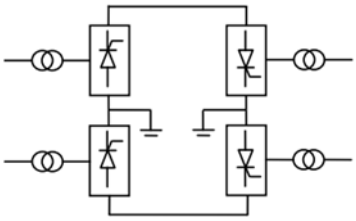

Figure 2. 3: Bipolar HVDC system configuration [33]

Basically, a bipolar system is made up of two monopolar systems. If the neutral point is grounded on both sides, it is possible to use one pole independently making it possible to transmit power even if one pole is out of service [32].

2.1.3.3 Back-to-Back HVDC System Configuration

The converter stations in this configuration are located at the same site as shown in Figure 2.4. Therefore, the power is not transmitted over long distances.

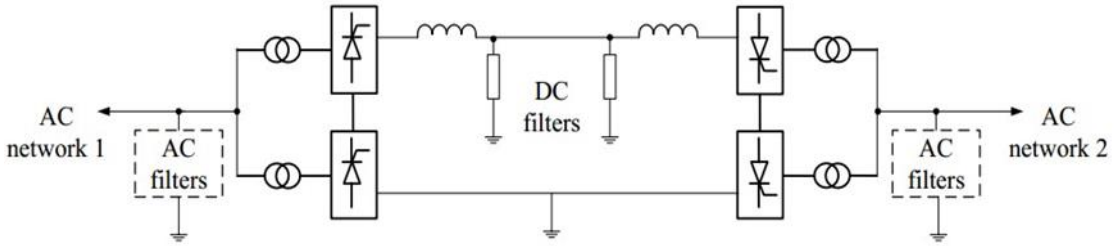

Figure 2. 4: Back-to-back HVDC system configuration [33]

This configuration can be monopolar or bipolar and it is mainly used to interconnect asynchronous systems [33].

2.1.3.4 Multi-terminal HVDC Systems

Multi-terminal HVDC (MTDC) configurations are made up of three or more converter stations; some converters operating as rectifiers and others operating as inverters [33]. An MTDC network can be of a series type or a parallel type [32]. A parallel MTDC network can be further classified to be either of a radial type or a mesh type. Figure 2.5 (a), (b) and (c) shows the series, parallel: radial type and parallel: mesh type multi-terminal DC configurations, respectively.

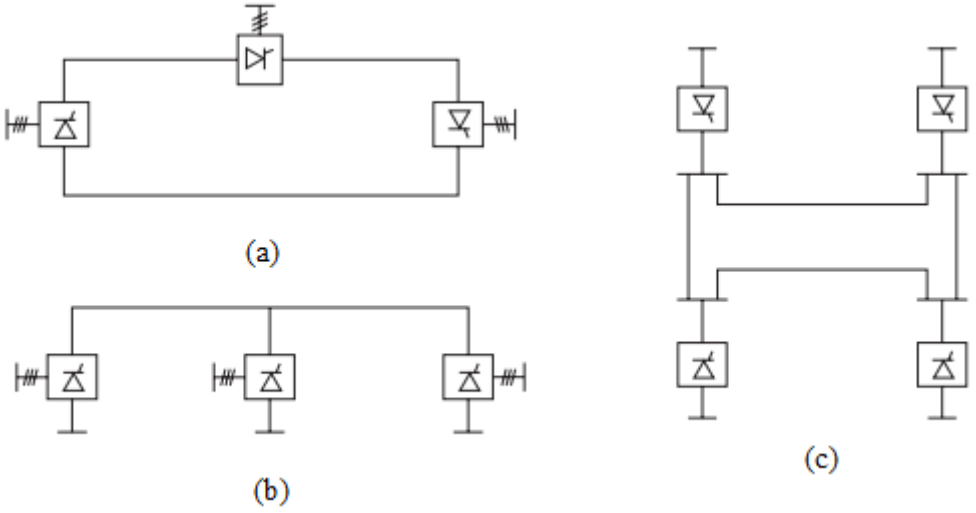

Figure 2. 5: Multi-terminal HVDC system configurations: (a) series; (b) parallel: radial; (c) parallel: mesh [32]

When the series and parallel MTDC configurations are combined, they form a hybrid MTDC system. The series and parallel MTDC systems are considered to be cost effective, reliable and are associated with less conversion losses compared to the point-to-point connections[34]. However, the hybrid configuration is not justified from an economic point of view due to the higher number of converter stations.

2.1.4 Comparison of LCC- and VSC-based HVDC Transmission Systems

Until recently, HVDC transmission systems have been based on Line Commutated Converters (LCC). The following technical restrictions limited their use in some transmission and distribution applications [15, 19, 35]:

- The dependence of converter switches' commutation on the stiffness of the grid voltage, hence it requires an AC network with a live AC voltage to operate. This makes LCC not suitable for interconnecting weak or dead networks.
- The requirement to change the DC voltage polarity to achieve power reversal.
- High total harmonic distortion, hence large filtering components are required. Large filtering components are associated with high reactive power consumption which is in order of 50% to 60% of the converter rating.
- The need for a telecommunication link between the converter stations.
- LCC-based HVDC transmission systems are more sensitive to AC network disturbances and hence there is a high risk of commutation failure.

Despite the fact that the VSC-based HVDC transmission systems are associated with high investment costs as well as high switching losses mainly due to the high switching frequency, they have gained more interest in transmission and distribution systems. This is due to the advantages they offer such as [15, 19, 35, 36]:

- VSCs use Pulse Width Modulation (PWM) to generate a sinusoidal signal that is used to commutate the converter switches, thus, it operates independently of the AC network short circuit ratio. This makes the VSC-HVDC links more attractive for interconnecting weak and dead networks such as off-shore wind farms and isolated loads.
- VSC-HVDC links are less sensitive to AC network disturbances and thus there is minimal risk of commutation failures.
- The real and reactive power can be controlled independent of one another.
- The rectifier and inverter stations operate independent of each other, thus there is no need for a communication link and hence, there is no delay in the control process.
- Fast response in case of disturbances due to increased switching frequency; better fault-ride-through capability
- VSCs can generate lagging and leading reactive power. The reactive power required for filtering varies from 0% to 33% depending on the converter topology, modulation technique, and switching frequency.
- Low total harmonic distortion thereby reducing the size of filtering components.
- Power reversal is achieved by changing DC current polarity instead of changing the DC voltage polarity.

2.1.5 Application of VSC-based HVDC Transmission Systems

HVDC transmission systems based on VSCs are becoming more attractive and desirable in industrial applications due to their improved performance, efficiency and modularity. Some areas where the VSC-based HVDC technologies are applied are [9, 11, 12]:

- Supplying power to environmentally sensitive areas such as city centers.
- Supplying power to remote and isolated load centers such as islands with dead networks and offshore wind farms by employing submarine cables.
- Allowing in-feed of power from small scale generation sources such as renewable energy sources.
- Interconnecting asynchronous networks.

Ever since the first commercial installation of the HVDC technology; the commercial link between Sweden mainland and the island of Gotland in 1954, a number of HVDC transmission systems have been installed worldwide. Table B.1 in appendix B summarizes the worldwide VSC-based HVDC projects in operation [9, 12, 15, 28].

2.1.6 Overview of VSC-based HVDC Transmission System

2.1.6.1 Components of a VSC-based HVDC Transmission System

Figure 2.6 shows the configuration of a typical VSC-based HVDC transmission system [15, 35].

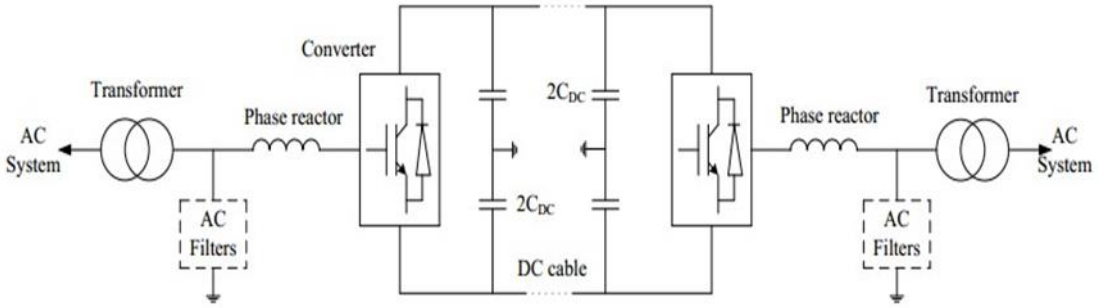

Figure 2. 6: VSC-HVDC system configuration [35]

The functions of the VSC-HVDC system components are explained briefly as follow:

2.1.6.1 (a) Voltage Source Converters

The two converter stations have the same configuration. One converter station operates as a rectifier and another as an inverter [37]. The two converter stations can be connected either back-to-back or via a DC cable depending on the application. They are built using self-commutated switches with turn-off capability, namely: the gate turn-off thyristors (GTOs) or insulated gate bipolar transistors (IGBTs) [37]. Currently, the voltage and current rating of IGBTs are limited to 6.5kV and 2.4kA, respectively [19]. For many transmission applications, these converter switches are connected in series to enable operation at different transmission voltage levels. The converter uses sinusoidal Pulse Width Modulation (SPWM) with high frequency to synthesize a sinusoidal waveform that turns converter switches on and off several times per fundamental period [19].

2.1.6.1(b) Converter Transformers

The converter transformers interconnect the VSCs to the AC systems. They are mainly used to step up/down the grid voltage to a voltage level that is well suited for the VSCs.

Usually, these transformers are of single-phase three-winding type, but can be arranged in any other forms depending on the transportation requirements and rated power[33].

2.1.6.1(c) Phase Reactors

The current flowing through the phase reactors is regulated to enable the control of the active and reactive power. Moreover, the phase reactors are used as AC filters to reduce the harmonics of the AC currents caused by the commutation of the converter switches in order to provide the desired fundamental frequency converter voltage [33].

2.1.6.1(d) AC Filters

To prevent the injection of AC voltage harmonics which arises from the switching of the converter switches from being injected into the AC systems. The harmonics generated are directly related to PWM switching frequency of the converter. Therefore, the AC filters are normally employed to get rid of these harmonic contents [33, 37].

2.1.6.1(e) DC Capacitors

The DC-link comprises of two equally sized capacitors which are normally used for energy storage for power flow control purposes and to reduce the ripple content in the DC voltage [37]. Therefore, the size of each DC-link capacitor is a tradeoff between the desired DC-link voltage, acceptable DC-link voltage ripples, and the speed of stabilizing the DC-link voltage [37]. To have small ripple content in the DC output voltage, a large capacitor is required; however, it slows down the control of the active and reactive power. Alternatively, a small capacitor results in fast control of the active and reactive power at a risk of high ripple content in the DC voltage.

2.1.6.1(f) DC Cables

The fluid-filled cables, such as oil-filled and gas-pressurized, the solid cables, and the polymer cables are the three main types of DC cables well suited for high voltage DC transmission systems [28, 35].

2.1.6.2 Operating Principle of a Voltage Source Converter

Figure 2.7 shows the simplified VSC-HVDC link circuit.

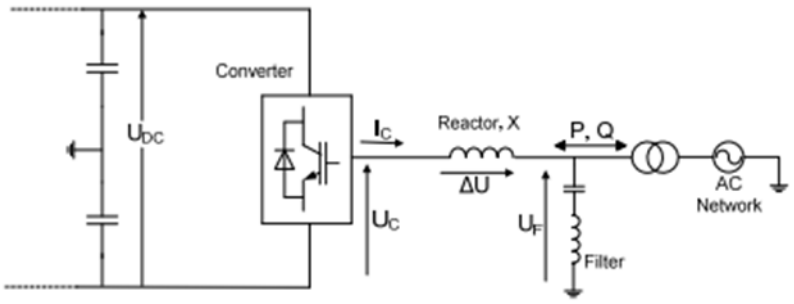

Figure 2. 7: Simplified VSC-HVDC circuit [38]

A VSC can be considered as a controllable synchronous machine with no mass whose fundamental frequency output voltage U_C is given by Eq. (2.1) [19]

$$U_C = \frac{1}{2} m \times U_{dc} \times \sin(wt + \phi) \tag{2.1}$$

Where m represents the modulation index, ω is the fundamental frequency and φ is the phase shift of the converter output voltage U_C. If the filter voltage U_f is taken as a reference, the active and reactive power exchanged between the converter and the AC system are represented by Eq. (2.2) and Eq. (2.3), respectively [19]

$$P = \frac{U_f U_C \sin\phi}{X} \tag{2.2}$$

$$Q = \frac{U_f (U_f - U_C \cos\phi)}{X} \tag{2.3}$$

Equation (2.2) indicates that the control of active power is achieved by varying the phase shift ϕ between the converter's terminal voltage and the filter bus voltage, while Eq. (2.3) indicates that the control of reactive power is achieved by varying the magnitude of the converter's terminal voltage with respect to the filter bus voltage [38].

2.1.6.3 Four-quadrant Operation of a Voltage Source Converter

The P-Q circle diagram given in Figure 2.8 illustrates the direction of the active power flow, as well as the direction of inductive and capacitive reactive power, exchanged between a converter and the AC system. The figure explains the 4-quadrant operation of a VSC.

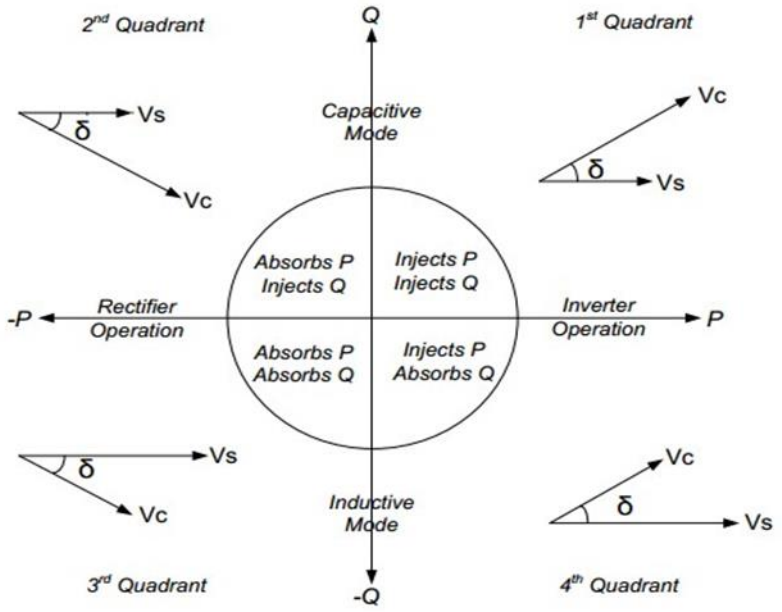

Figure 2. 8: Four-quadrant operation of VSC [37]

2.1.6.3(a) Inverter Operating Mode

The first and fourth quadrants fall under the inverter operation mode. The first quadrant shows that the AC system voltage is less than the converter voltage and lags it by angle δ, and hence, the converter injects active and capacitive reactive power into the AC network [37]. In the fourth quadrant, the converter voltage is less than the AC system voltage and leads it by angle δ [37]. Hence, the converter injects active power into the AC network while absorbing inductive reactive power.

2.1.6.3(b) Rectifier Operating Mode

The second and the third quadrants fall under the rectifier operation mode. In the second quadrant, the AC system voltage is less than the converter voltage and leads it by angle δ. Hence, the converter absorbs the active power and injects capacitive reactive power into the AC network. In the third quadrant, the AC system voltage is greater than the converter voltage and leads it by angle δ. Hence, the converter absorbs the active and inductive reactive power.

When the power, current and voltage limits are enforced on the P-Q diagram, amount of the active and reactive power exchanged between the converter(s) and the AC system can be determined. Figure 2.9 shows the typical P-Q limits of a VSC-HVDC link. It should be noted that these limits can be changed to suit different requirements and applications.

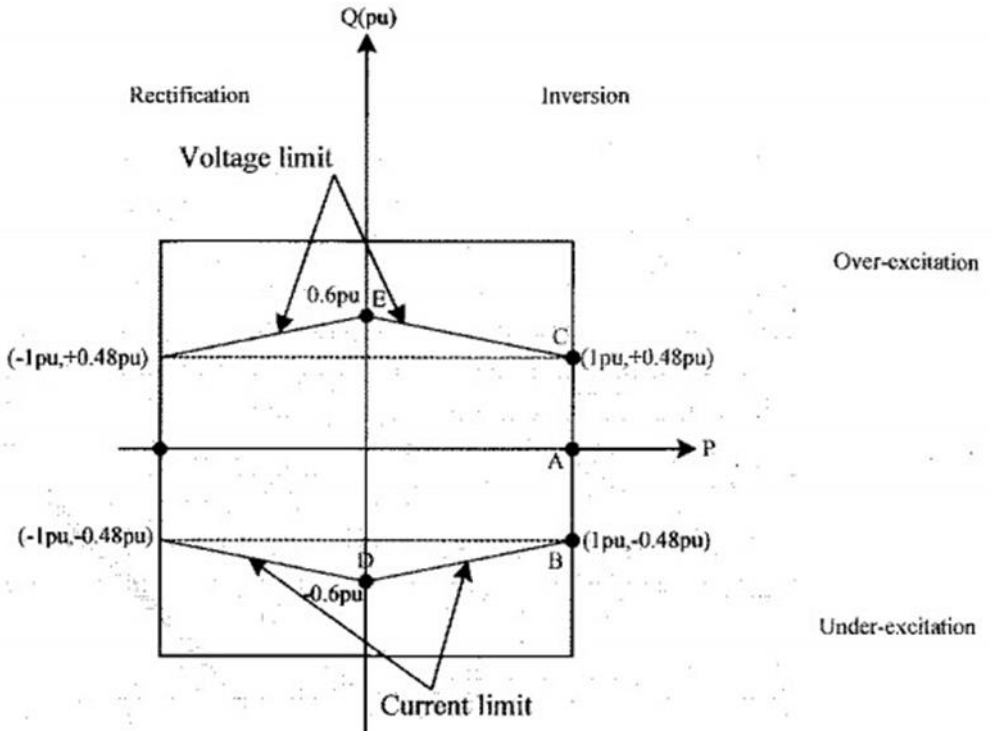

Figure 2. 9: VSC-HVDC link capability curve (P-Q) envelope [19]

It is shown that when the converter station operates at its maximum active power capability, its ability to generate reactive power is limited to ±0.48pu. Whereas, when the converter station is operating at zero active power, its reactive power is limited to ±0.6pu as indicated by points *D* and *E* [19]. Point *D* represents the region where the converter delivers maximum inductive reactive power at reduced converter voltage; limited by the IGBTs' current handling capability. While point *E* represents the region where the converter increases its output voltage relative to the grid voltage to deliver capacitive reactive power; limited by the maximum available DC voltage [19].

2.1.6.4 Voltage Source Converter Topologies

A converter can be classified to be either of a two-level or a multi-level topology depending on the arrangement of the semiconductor switches of the converter [17, 18, 39].

2.1.6.4(a) Two-level VSC Topology

A 3-phase two-level VSC topology consists of 3 legs, one for each phase. Each leg has two switches as shown in Figure 2.10.

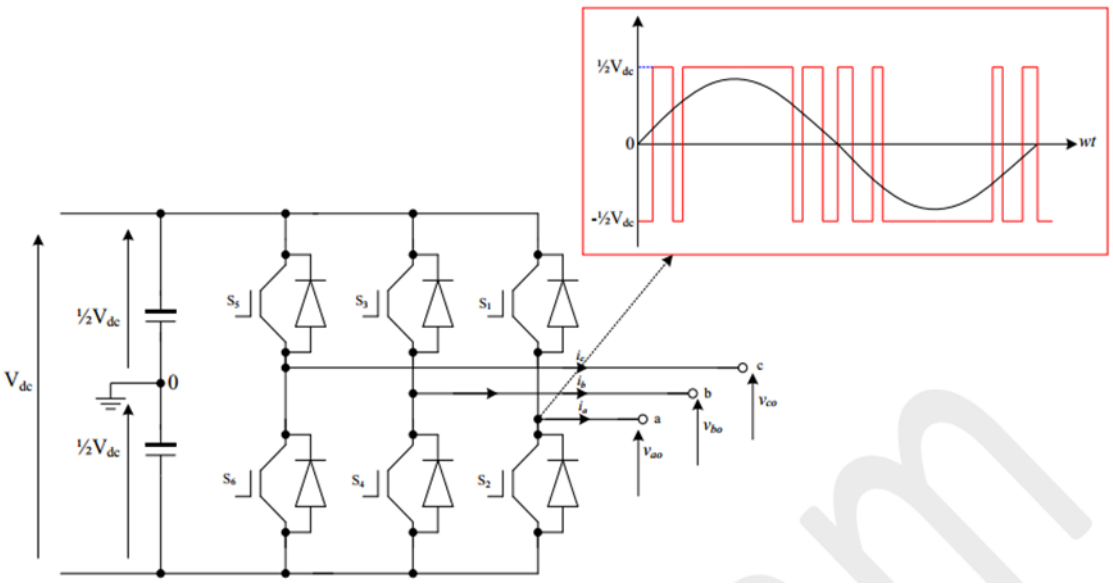

Figure 2. 10: Two-level VSC topology [19]

In a 2-level VCS converter, the two switches of each leg operate as compliments of one another. This means that, if the first switch of phase *a* (S_{a1}) is turned on, that is S_{a1}=1, then the second switch of phase *a* (S_{a2}) must be off, that is S_{a2}=0, and the same is applied to the remaining phases *b* and *c*[19]. This converter topology outputs 2 voltage levels: $1/2V_{DC}$ and $-1/2V_{DC}$[19].

- **Advantages and drawbacks**

Although 2-level VSC topologies are robust, have a simple configuration and a reliable performance, they are associated with high switching losses and they require extra electromagnetic interference (EMI) filters [16].

2.1.6.4(b) Multilevel VSC Topology

Multilevel converter topologies output more than two voltage levels. A multi-level converter synthesizes a sinusoidal voltage of an improved waveform quality from several voltage levels obtained from the DC-link [40, 41].

The traditional multilevel VSC topologies are the neutral-point-clamped (NPC), the flying capacitor (FC), the cascaded H-bridge (CHB), and the modular multilevel converter (MMC) [16, 42]. Figure 2.11 shows the four multilevel converter topologies.

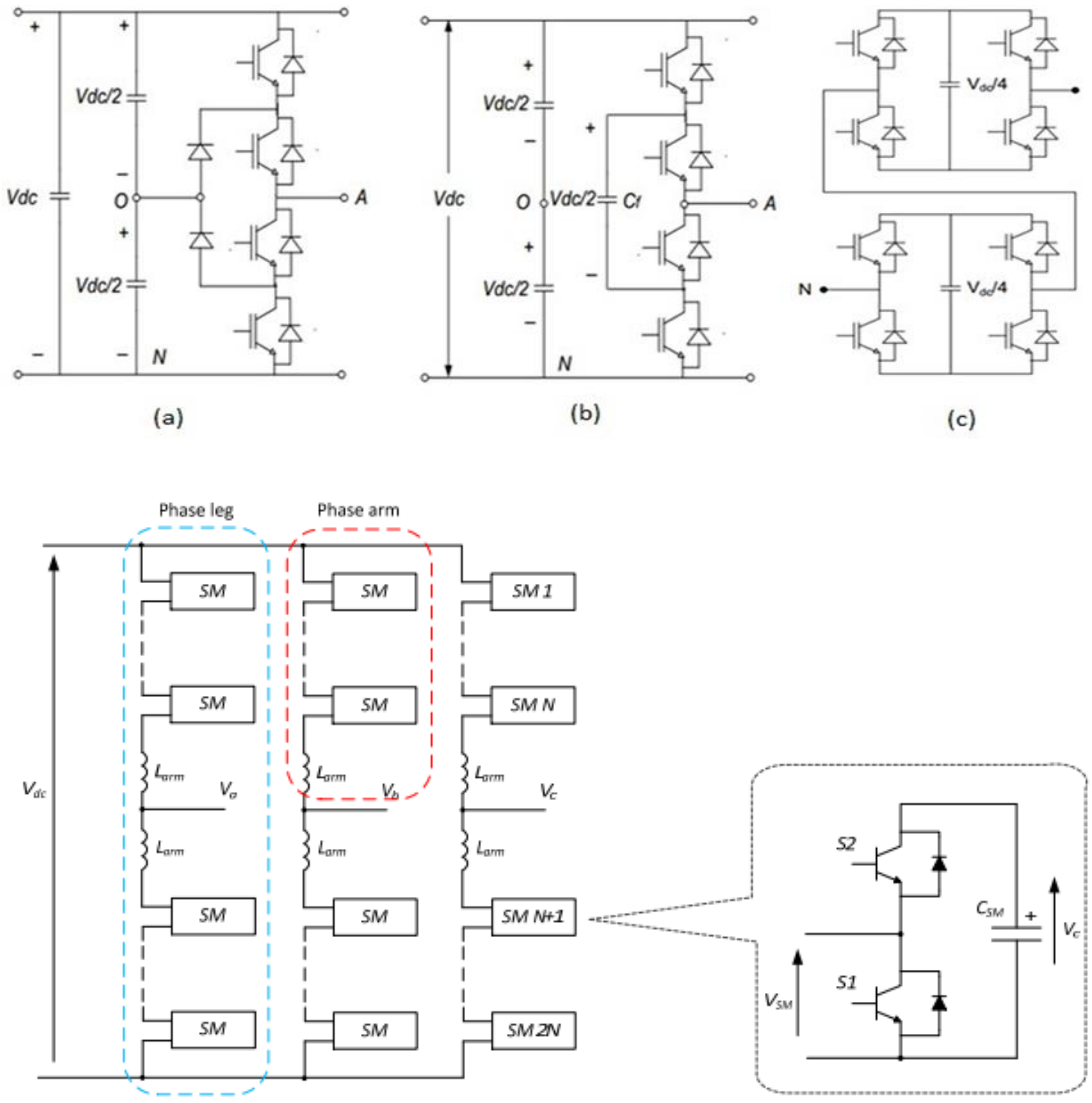

Figure 2. 11: Multilevel converter topologies (a) NPC; (b) FC; (c) CHB; (d) MMC [19, 37]

The NPC uses clamping diodes joined to the centre point of the DC-link to split the DC-link voltage into a number of voltage levels [16, 42]. The FC converter topology employs the same operating technique as the NPC. However, the FC uses floating capacitors instead of diodes used in the NPC. The Cascaded H-bridge (CHB) consists of series-connected full bridge converter modules whereby each module is fed by a separate DC capacitor. A modular multilevel converter (MMC) is made up of a number of submodules (SM) which comprises of half-bridge made up of 2 bidirectional switches connected in parallel with a capacitor[19, 43, 44]. A converter arm is formed by connecting a number of these SMs in series with an inductor as shown in Fig. 2.1 (d).

Comparative studies of the NPC, FC, CHB and MMC multilevel converter topologies have been carried out in literature highlighting their strengths and weaknesses [16, 18, 19, 42, 45]. The advantages and disadvantages of these multilevel converter topologies are briefly discussed as follow:

(a) Neutral Point Clamped Multilevel VSC

- **Strengths**

- Small sized DC capacitors
- Good quality AC output waveform
- Small footprint
- Reactive power flow can be controlled

- **Weaknesses**

- Challenges associated with balancing the voltage across the DC-link capacitors
- Uneven loss distribution between devices
- Excessive clamping diodes are required in higher level applications

(b) Flying Capacitor Multilevel VSC

- **Strengths**

- Improved output AC voltage waveform quality compared to the NPC topology
- Better fault ride-through capability during power outages and severe disturbances due to a large number of storage capacitors.
- Both real and reactive power can be controlled.

- **Weaknesses**

- In higher level applications, this topology becomes very expensive due to the requirement of a large number of storage capacitors with different voltage ratings.
- Complex converter's control system
- Increased complexity of the DC-link capacitor voltage balancing which limits its extension beyond a five-level converter topology.
- Higher switching frequency and switching losses compared to the NPC topology.
- Lack of modularity prevents its adoption in high-voltage applications.

(c) Cascaded H-bridge Multilevel VSC

- **Strengths**

- Requires the least number of components than the NPC and FC multilevel converter topologies for the same number of voltage levels.

- It is possible to package the modular circuit layout because all levels have the same structure.
- The charge balance of the separate DC voltage sources can be readily achieved.

- **Weaknesses**

- The application of the topology is limited due to the fact that each DC-link is required to be isolated.
- The cell capacitors are replaced with isolated active DC sources in case the real power is needed. This requires complex transformers to provide the isolated active DC sources.

(d) Modular multilevel converter (MMC)

- **Strengths**[46, 47]

- There is no need for AC-side and DC-side filters due to the harmonic cancellation between the submodules (SMs).
- MMCs are operated at a very low PWM carrier frequency; hence the conduction and switching losses are low. This means that the topology is more efficient.
- The MMC has a modular structure and hence it is easy to implement and its power and voltage ratings can easily be scaled by increasing the number of SMs.
- The possibility of the converter to keep operating for a certain period even if some SMs have failed makes the MMC more reliable.
- The DC-link capacitors can be omitted because the currents in the MMC and DC-link are continuous.
- The elimination of harmonic filters and DC-link capacitors reduces the footprint of the MMC topology.

- **Weaknesses**

- To ensure that the MMC operates effectively, the MMC is associated with additional control requirements such as balancing the SM capacitor voltages and eliminating the circulating current. This makes the design of the MMC controller sophisticated[44].

To sum up, multi-level converters can handle higher voltages and synthesize voltages with better waveform quality compared to the 2-level converter topologies [16]. Moreover, multilevel converters are associated with lower harmonic distortion; lower switching losses, higher overall efficiency, and cuts down on the size and number of filtering elements. However, they also have shortcomings such as higher conduction losses due to the high number of semiconductor devices in the conduction path, control circuit complexity, voltage imbalance across the upper and lower DC-link capacitors, and unequal current stress on the semiconductor switches [16, 18].

Multilevel converter topologies are becoming very attractive in large WT applications [48]. According to [12, 19], the NPC converter is the only topology widely used in HVDC systems with several practical systems presently in operation. Furthermore, it has been concluded that NPC multilevel converters with more than three levels are not suitable for high-voltage applications. This is due to the lack of converter's modularity and the DC-link capacitor voltage balancing becomes unachievable as the number of levels increases.

2.1.6.5 Control Strategies of Voltage Source Converters

The direct control and vector control are the well-developed control techniques used to carry out the control of the power, voltage and current in grid-connected WECS and they are discussed further in the literature [20-22]. Freire *et. al* [20] carried out a comparative study on the direct and vector control strategies. It was concluded that, although the direct control technique has a fast dynamic response and it is easy to implement, vector control techniques have a better performance due to lower current distortions, higher grid power factor, and higher overall efficiency. The presence of low-frequency resonance when the VSC is connected to a weak network is one of the major drawbacks of vector control technique.

2.1.6.5(a) Direct/power Angle Control Strategy

In the direct control technique, the control of the active power is achieved by changing the power angle between the converter's fundamental output voltage and the AC system voltage. Whereas, the control of the reactive power is achieved by changing the magnitude of the VSC voltage relative to the magnitude of the AC system voltage[20] .

2.1.6.5(b) Vector Control Strategy

The vector control technique controls the instantaneous active and reactive power independently in the *dq* synchronous reference frame. It has a dual control loop structure made up of an inner current control loop and an outer control loop. The outer control loops can be used to control the DC-link voltage, the AC voltage, and the active and reactive power [20]. The output signals from the outer control loops serve as reference currents for the inner current control loops.

2.2 Overview of the Wind Energy Conversion System

2.2.1 Wind Turbine Structure and Operating Principles

Figure 2.12 shows the components of a typical wind turbine.

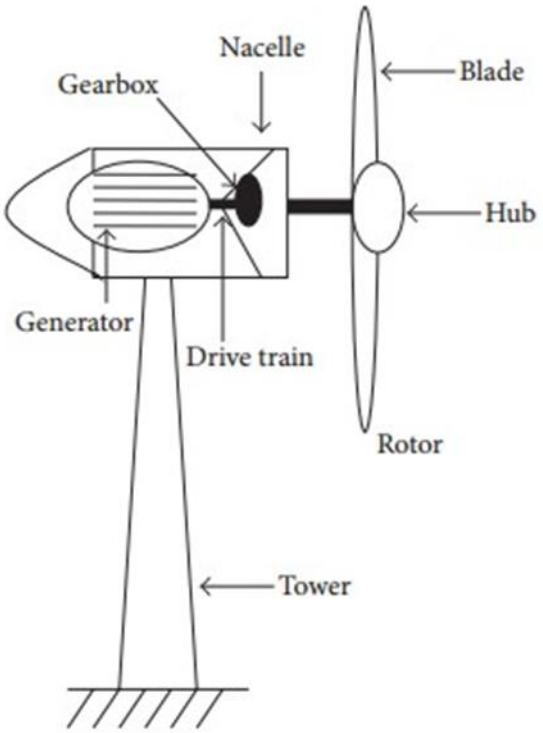

Figure 2. 12: Wind Turbine Components [49]

2.2.1.1 Energy Conversion Process

The striking wind turns the blades around a rotor to convert kinetic energy into mechanical energy. The mechanical energy is converted to electrical energy as the rotor turns the shaft that is connected to the generator.

2.2.1.2 WT Components and their functions

- **Rotor**: performs the conversion of kinetic energy into mechanical energy
- **Generator**: performs the conversion of mechanical energy into electrical energy
- **Gearbox/ drive-train**: Couples the low-speed shaft to the high-speed shaft.
- **Nacelle**: Provides a shelter for the gearbox, generator, and other micro-components.
- **Tower**: Acts as a support for the turbine blades to expose them to wind in order to capture more power from the wind.

2.2.1.3 Classification of Wind Turbines

Depending on the orientation and the WT's axis of rotation, a WT can be classified as a horizontal axis wind turbine (HAWT) or a vertical axis wind turbine (VAWT) [49]. Figure 2.13shows the HAWT and VAWT.

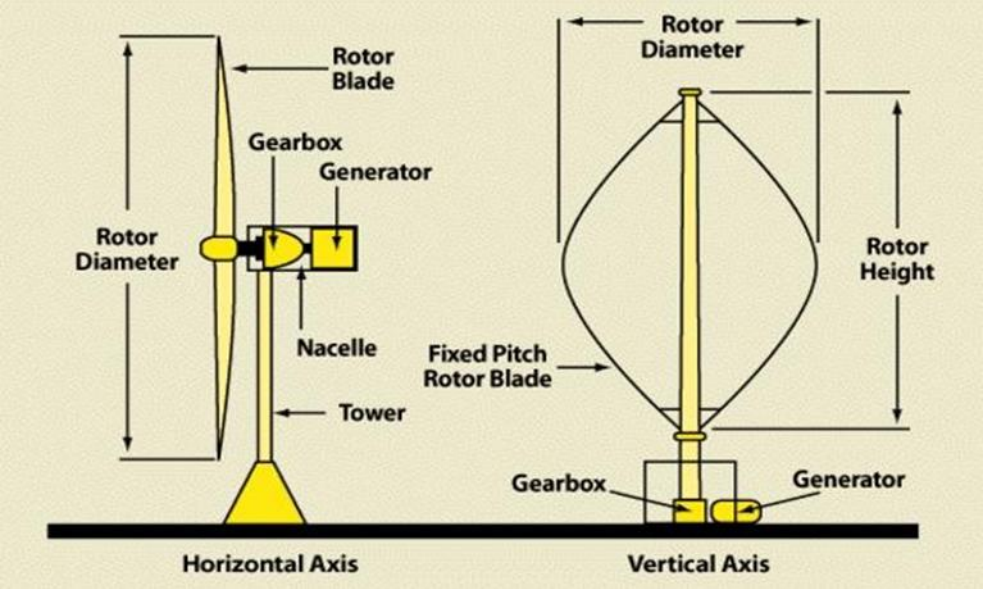

Figure 2. 13: Horizontal axis and Vertical axis wind turbines [49]

Despite the fact that the HAWTs need a stronger and higher tower to support the nacelle which in turn increases the installation costs, they are highly efficient because the WT blades are exposed to stronger winds. On the other hand, the VAWTs are associated with lower installation costs. However, their efficiency is very low and they are prone to high torque fluctuations and mechanical vibrations [49, 50].

2.2.1.4 Operating Regions of a Wind Turbine

Figure 2.14 illustrates the operating regions of a WT. The WT generator starts to extract aerodynamic power from the wind resource when the wind speed is at/exceeds the cut-in wind speed and stops when the wind speed is at/ is approaching the cut-out wind speed [51].

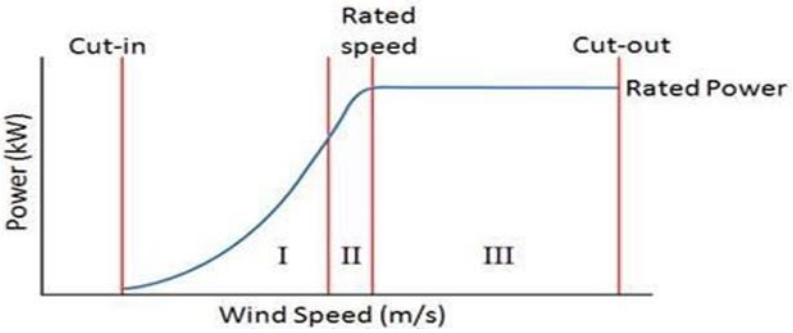

Figure 2. 14: Wind Turbine Operation regions [51]

The wind turbine operating regions are summarized as follows [51]:

- Region I: the wind turbine operates below the rated rotor speed and the rated power.

- Region II: the wind turbine is operating around the rated rotor speed and rated power.
- Region III: the turbine is operating at full power and rated speed.

2.2.1.5 Overview of the Wind Turbine Generators

In the early stages of wind power development, the wind farms where made up of fixed speed wind turbines (FSWT) and induction generator-based WTs. These WT generators were integrated into the utility grid without converters included [17, 52]. However, the shortcomings of these generators such as low efficiency, limited fault-ride-through ability and large power fluctuations limited their applications [16]. With the advancement in power electronic converters and the increasing interest in grid integration of wind energy, VSWT generators are emerging as the preferred technology [52, 53]. Several studies in the areas of VSWT systems equipped with permanent magnet synchronous generators are given in literature [54-58].

Due to the intermittent nature of wind, converters are normally employed to integrate WTs into the power utility grid to ensure that the characteristics of the WT under consideration match the grid standards [17]. The interface between the WT and the grid comprises of a generator- side converter, an intermediate DC-link capacitor, and a grid-side converter. Whereby, the generator-side converter changes the variable-magnitude-variable-frequency AC power from the WT generator to DC, the DC-link capacitor then stabilizes the DC voltage which is further converted by the grid-side converter to fixed AC power on the grid side at desired frequency and voltage level.

Modern variable speed wind turbines (VSWT) systems are based on doubly fed induction generators (DFIGs) with partially-rated power electronic interfaces or permanent magnet synchronous generators (PMSGs) with fully-rated electronic interfaces as shown in Fig. 2.15 [16, 39].

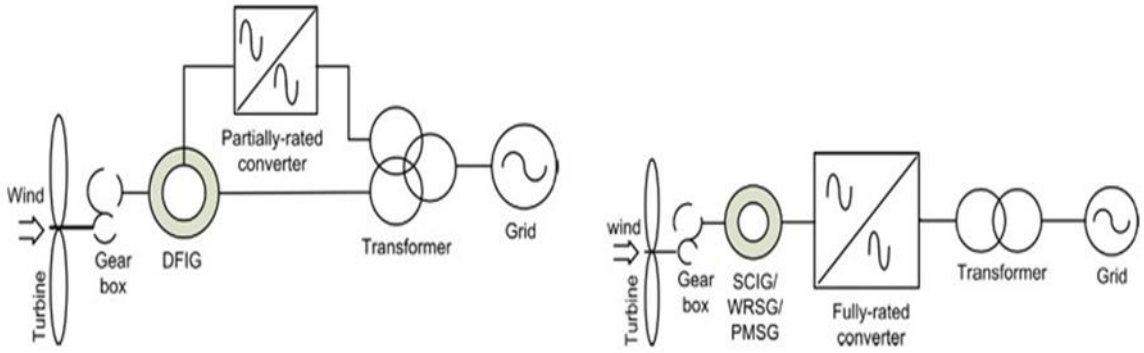

Figure 2. 15: Variable speed wind energy conversion system with partially-rated and fully-rated power converters [59]

- **Doubly-fed Induction Generator-based WECS**

The DFIG-based WECS is coupled to the grid via a partially-rated converter connected to the rotor circuit while the stator is directly connected to the grid. The power converter controls the rotor speed, the active and reactive power and performs reactive power compensation [16].

The use of slip-rings and the protection issues in the event of grid faults are the major drawbacks of DFIG based WECS.

- **Permanent Magnet Synchronous Generator-based WECS**

The PMSG-based WECS is connected to the grid via a fully-rated power electronic converter. The fully-rated power converter fully decouples the WT from the grid disturbances thereby allowing full controllability of the system and improved fault-ride-through capability. The PMSG-based WECSs are becoming more popular and more preferred over DFIG-based WECS due to a number of advantages, namely: high energy density, ease of controllability, low maintenance cost and the self-excitation system [16, 59, 60]. The direct-driven multi-pole PMSG concept is currently gaining interest because of the elimination of the gearbox thereby improving the efficiency of the VSWT. Figure 2. 16 shows a direct-driven PMSG-based WECS

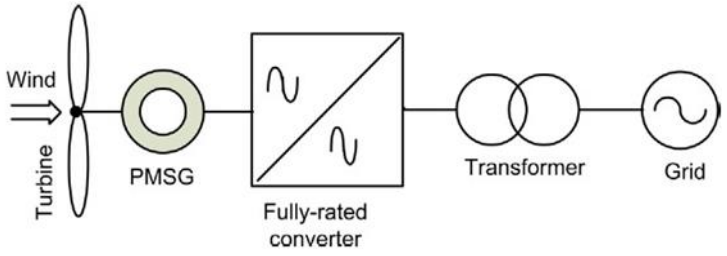

Figure 2. 16: Variable speed direct drive (gearbox-less) wind power generation system with fully-rated power converter [59]

A direct-drive PMSG is employed in this research investigation to operate the wind turbine system. Therefore, the PMSG modelling and design will be discussed further.

2.2.2 Mathematical Modelling and Analysis of the WECS's Components

2.2.2.1 Wind Turbine Mathematical Model

The power P_w that is available for extraction from the wind resource is defined by Eq. (2.4) [61]

$$P_W = \frac{1}{2}\rho A v_w^{\,2} \tag{2.4}$$

Where: ρ is the air density which equals to 1.225kg/m3 at sea level, A is the area swept by the rotor blades [m2] ($A = \pi r^2$, r being the radius of the rotor blade in m) and v_w is the wind speed upstream of the rotor [m/s].

The fraction of the aerodynamic power P_m extracted from the wind resource by a WT is related to the wind power P_m *by* the power coefficient C_p using Eq. (2.5) [61]

$$P_m = P_w C_p \tag{2.5}$$

Therefore, the algebraic relationship between the wind speed and mechanical power extracted is described by Eq. (2.6) [16, 49]

$$P_m = \frac{1}{2}\rho A C_p(\lambda, \beta) v_w^{\,3} \tag{2.6}$$

The C_p is dependent on the pitch-angle β [degrees] and the tip speed ratio λ given by Eq. (2.7)

$$\lambda = \frac{r\omega_r}{v_w} \tag{2.7}$$

Where: ω_{rot} *is* the rotor angular speed [rad/s] and r is the rotor blade radius[m].

Figure 2.17 shows the pitch-angle β which is defined as the angle between the plane of rotation and the blade's cross-section chord.

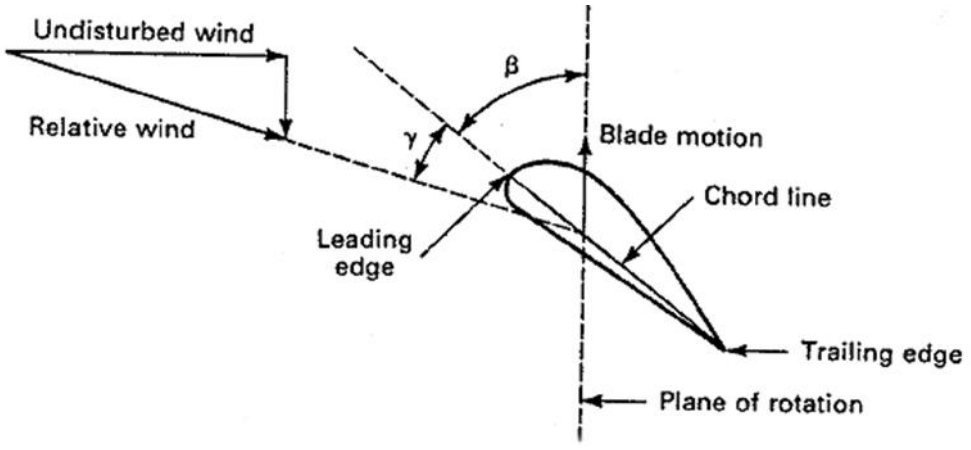

Figure 2. 17: Pitch Angle [62]

According to [63], C_p has a theoretical maximum value of 0.593. This is known as the Benz limit. This means that the amount of power extracted from the wind resource is always less than 59.3%. [62, 64]. Equation (2.8) is used to calculate C_p for different values of λ and β [65].

$$C_p(\lambda,\beta) = C_1(C_2\frac{1}{\lambda_i} - C_3\beta - C_4\beta^x - C_5)e^{-C_6(1/\lambda_i)} \tag{2.8}$$

The coefficients C_1-C_6 and x varies for various wind turbine generators (WTG). In this study, the coefficients of the WTG used are; C_1=0.5, C_2=116, C_3=0.4, C_4=0, C_5=5, and C_6=21. The parameter λ_i is defined by Eq. (2.9)

$$\lambda_i = \frac{1}{\frac{1}{\lambda + 0.08\beta} - \frac{0.035}{1+\beta^3}} \tag{2.9}$$

The aerodynamic torque T_m [N.m] given by Eq. (2.10) is defined as the ratio of the aerodynamic power P_m *to* the turbine rotor speed ω_r [62]

$$T_m = \frac{P_m}{\omega_r} \tag{2.10}$$

2.2.2.2 Drive Train Mathematical Model

A drive train is a portion of the wind turbine that transmits torque from the low-speed shaft to the high-speed shaft. The drive train consists of a rotor, low-speed shaft, gearbox, high-speed shaft and a generator [52, 62]. The drive-train system is modelled as a number of discrete masses connected together by springs and defined by damping and stiffness coefficients [62]. The following four types of drive-train models are usually used:

- Six-mass drive train model
- Three-mass drive train model
- Two-mass drive train model
- One-mass or lumped drive train model

Figure 2.18 illustrates the schematic diagram of a drive train model.

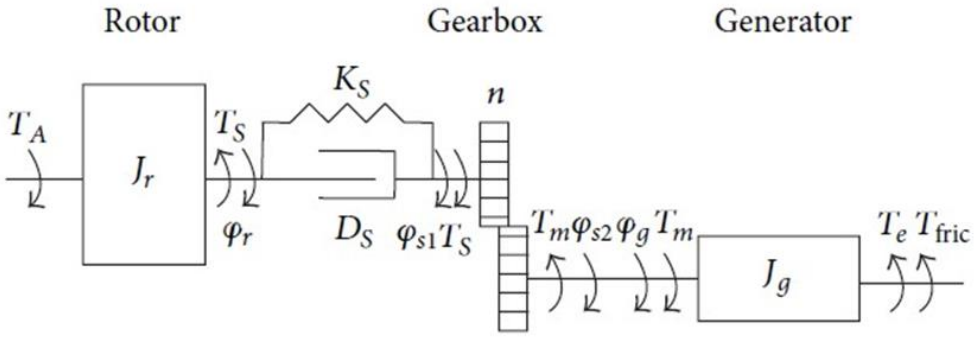

Figure 2. 18: Schematic diagram of a drive train model [49]

The complexity of the drive train varies with the interest of the study and application. For instance, if the study is focusing on problems such as torsional fatigue, dynamic stability or application of fixed speed wind turbines, the dynamics from the low-speed and high-speed shafts have to be considered. Therefore, two-mass or more sophisticated models are required [16, 52, 62, 65]. However, if the study is focusing on the integration of a WT into the power utility grids, the drive train can be treated as a one-lumped mass model for the sake of time efficiency and acceptable precision[52, 62]. However, it should be noted that this is only applicable when the study is focusing on the decoupling of the VSWT from the grid using fully-rated power electronic converters [65]. Therefore, a lumped-mass drive train is considered in this research investigation, and hence it will be briefly discussed further. Figure 2.19 shows the lumped-mass drive train.

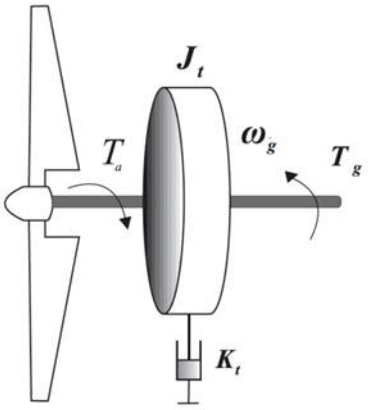

Figure 2. 19: Lumped-mass drive train [62]

Equation (2.11) gives the mathematical representation of the lumped-mass drive train model with the parameters referred to the generator side [52, 62].

$$\frac{d\omega_r}{dt} = \frac{T_m - T_e - B_{eq}\omega_r}{J_{eq}} \tag{2.11}$$

Where ω_r is the mechanical angular speed [rad/s], T_m is the aerodynamic/mechanical torque [N.m], T_e is the electromagnetic torque that is transferred to the generator side [N.m], B_{eq} is the equivalent damping coefficient [N.m/s] and J_{eq} is the equivalent inertia of the generator [kg.m^2], which is calculated using Eq. (2.12)

$$J_{eq} = J_g + \frac{J_w}{n_g^2} \tag{2.12}$$

Where J_g and J_w are the generator and rotor inertias, respectively, and n_g is the gear ratio. For a lumped-mass drive train, the gearbox ratio is equal to one.

2.2.2.3 Permanent Magnet Synchronous Generator Mathematical Model

The equations describing a PMSG have been discussed in more details in Kundur [66]. The dynamic modelling of a PMSG is normally carried out in the direct-quadrature (*dq*) synchronous reference frame with the q-axis 90˚ ahead of the d-axis with respect to the direction of rotation[52, 55, 62].

Figure 2.20 shows the *dq* reference frame used, where θ is the angle between the rotor's d-axis and the stator axis. The transformation from *abc* reference frame to *αβ* stationary reference frame and then to *dq* synchronous rotating reference frame is carried out using Clarke and Park's transformation given in Appendix B.

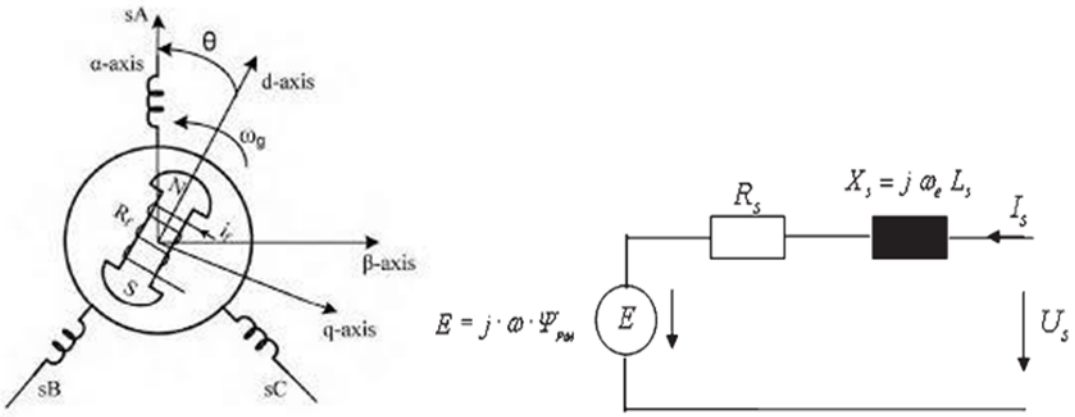

Figure 2. 20: d-q and α-β axis of a typical PMSG, and the equivalent circuit of a PMSG [38]

The mathematical model of the PMSG is normally carried out with an assumption that the windings are distributed in a sinusoidal manner and the saturation, eddy currents, and hysteresis losses are neglected [64]. Equation (2.13) represents the PMSG's stator currents in *dq*-synchronous reference frame [16, 25, 52, 55, 56]

$$\begin{aligned}\frac{di_{sd}}{dt} &= -\frac{R_s}{L_{sd}} i_{sd} + \omega_{se} \frac{L_{sq}}{L_{sd}} i_{sq} + \frac{1}{L_{sd}} U_{sd} \\ \frac{di_{sq}}{dt} &= -\frac{R_s}{L_{sq}} i_{sq} - \omega_{se} \left(\frac{L_{sd}}{L_{sq}} i_{sq} + \frac{1}{L_{sq}} \psi_f\right) + \frac{1}{L_{sq}} U_{sq}\end{aligned} \tag{2.13}$$

Where i_{sd} and i_{sq} are the d-axis and q-axis generator currents, respectively; L_{sd} and L_{sq} are the d-axis and q-axis inductances [H], respectively; R_s is the stator winding resistance [Ω]; ψ_f is the permanent magnetic flux [Wb]; U_{sd} and U_{sq} are the d-axis and q-axis generator voltages, respectively and ω_{se} is the electrical rotating speed [rad/s] of the generator, defined by Eq. (2.14)

$$\omega_{se} = n_p \omega_{sg} \tag{2.14}$$

Where n_p represents the number of pole pairs in the rotor and ω_{sg} is the rotor's mechanical rotational speed.

Figure 2.21 shows the equivalent circuits of the PMSG in the *dq* synchronous rotating reference frame.

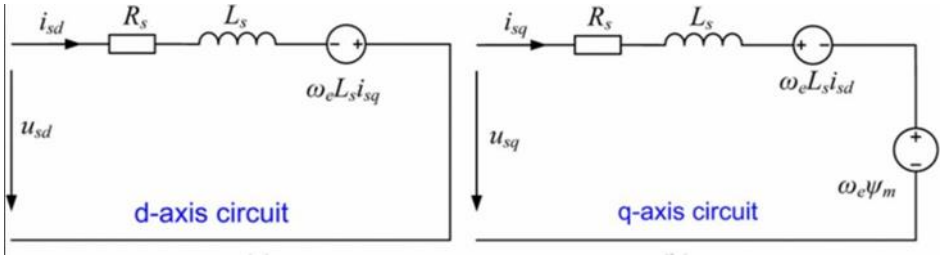

Figure 2. 21: d-axis and q-axis equivalent circuits of the PMSG [52]

The electromagnetic torque of the PMSG is given by Eq. (2.15)

$$T_e = 1.5 n_p [\psi_f i_{qs} + (L_{ds} - L_{qs}) i_{ds} i_{qs}] \tag{2.15}$$

For non-salient pole and low speed, surface mounted PMSGs, $L_{sd} \approx L_{sq}$ *[16, 67]*. As a result, the electromagnetic torque is given by Eq. (2.16)

$$T_e = 1.5 n_p \psi_f i_{qs} \tag{2.16}$$

2.2.3 Control of Wind Turbine System

2.2.3.1 Maximum Power Point Tracking

Certain control techniques are employed to enable the optimal extraction of aerodynamic power from the wind resource when the wind speed is lower than the WT's rated wind speed. This can be achieved when the WT operates at optimal aerodynamic power coefficient C_{p_opt} and optimal tip speed ratio λ_{opt} [68]. A number of maximum power point tracking (MPPT) methods have been developed and have been discussed in the literature [16, 69-72].

2.2.3.1(a) Optimal relationship-based (ORB) control

The ORB is a well-developed MPPT strategy which ensures optimal extraction of power from the wind resource by using a pre-calculated look-up table. Therefore, the knowledge of the WT's MPPT curve is a prerequisite [16, 73]. The measured rotor speed is used to track the optimal power from the wind turbine's maximum power curve relative to the change in the wind speed. Figure 2.22 illustrates the ORB MPPT technique.

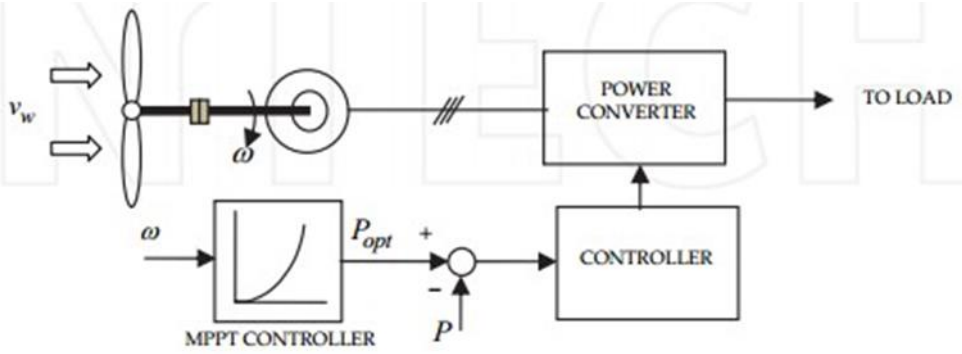

Figure 2. 22: Optimal Relationship-Based MPPT technique[74]

The optimal output power from the wind turbine is described by Eq. (2.17) [16]:

$$P_{opt} = \frac{1}{2}\rho A C_{P_{opy}} \left(\frac{\omega_{r_{opy}} \times r}{\lambda_{opt}}\right)^3$$
$$P_{opt} = K_{opt}\omega_{r_{opt}}{}^3 \tag{2.17}$$

Where, K_{opt} is the optimal power constant showing the optimal power associated with the corresponding optimal rotor speed ωr_opt. K_{opt} is obtained from wind turbine characteristics using Eq. (2.18)

$$K_{opt} = \frac{1}{2}\rho A C_{P_{opt}} \left(\frac{r}{\lambda_{opt}}\right)^3 \tag{2.18}$$

Figure 2.23 shows a typical wind turbine's power curve indicating the generated power as a function of rotor speeds for different wind speeds. The optimal power extraction can be achieved if the MPPT controller allows the generated power to properly track the optimal power curve with variations in wind speed.

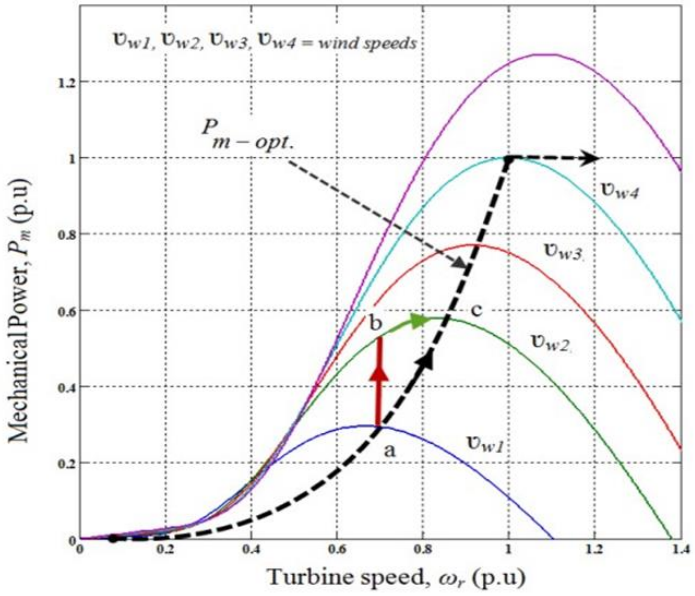

Figure 2. 23: Generated power as a function of the rotor speed for various wind speeds [55]

Advantages of ORB MPPT strategy

- Ease of implementation
- Good dynamic response
- No requirement for a wind speed sensor/anemometer
- Produces a smoother output power compared to other MPPT strategies

Disadvantages of ORB MPPT strategy

- The wind turbine's optimal power curve is a pre-requisite and it varies from one system to another.
- The efficiency of the power curve will decrease as the system ages.
- Requires a lot of memory space to store the look-up table.

2.2.3.1(b) Tip Speed Ratio (TSR) Control

To extract maximum power using TSR technique, the rotor speed is regulated with respect to the change in wind speed to maintain the tip speed ratio at an optimal value [75]. Therefore, the optimal TSR value of the wind turbine is a pre-requisite. The measured wind speed is then used to compute the desired optimal rotor speed using Eq. (2.19)

$$\omega_r = \frac{\lambda_{opt} v_w}{r} \tag{2.19}$$

Figure 2.24 illustrates the tip speed ratio MPPT control strategy.

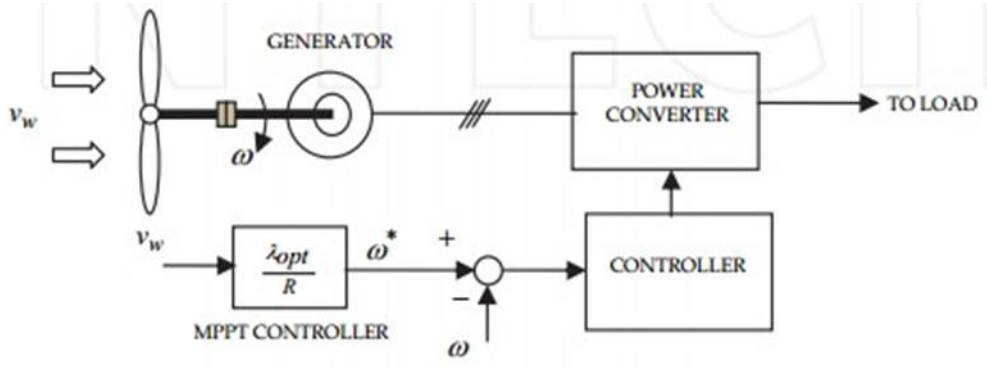

Figure 2. 24: Tip Speed Ratio MPPT strategy[74]

Advantages of TSR MPPT strategy

- Simple to implement

- Fast responses to wind speed

Disadvantages of TSR MPPT strategy

- The presence of the wind speed sensor adds to the system cost.
- The strategy operates accurately if the wind speed is measured accurately.
- It is associated with high fluctuations in output power due to its non-minimum phase characteristics [74].

2.2.3.1(c) Optimal Torque Control (OTC)

The MPPT is ensured by generating an optimal torque reference from the measured rotor speed and the wind turbine characteristics as shown in Fig. 2.25

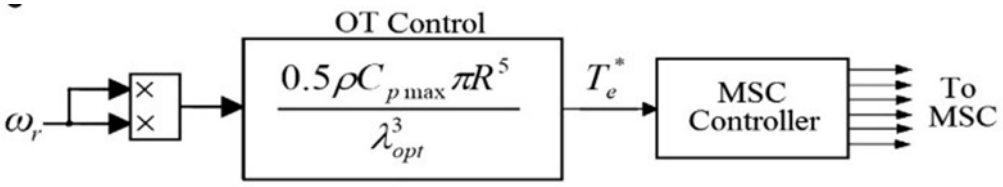

Figure 2. 25: Optimal Torque Control MPPT strategy[16]

The optimal torque reference is derived from the optimal power given in Eq. (2.17) as follow,

$$T_{opt} = \frac{P_{opt}}{\omega_{r_{opt}}}$$

$$T_{opt} = \frac{\frac{1}{2}\rho A C_{p_{opt}} \left(\frac{\omega_{r_{opt}} \times r}{\lambda_{opt}}\right)^3}{\omega_{r_{opt}}} \tag{2.20}$$

$$T_{opt} = K_{opt}\omega_{r_{opt}}{}^2$$

The OTC adjusts the electromagnetic torque of the generator according to an optimal reference torque curve to indirectly regulate the generated active power through a closed-loop control of the generator torque [16].

Advantages of OTC MPPT strategy

- Simple to implement
- Quick response and efficient

Disadvantages of OTC MPPT strategy

- The non-linear relationship between the extracted wind power and the generator torque makes it difficult to extend the strategy to situations with different power requirements.
- The wind turbine's optimal reference torque curve is required and it varies from one system to another.
- The efficiency of the reference torque curve will decrease as the system ages.

2.2.3.1(d) Perturb and Observe (PO)/ Hill Climb Search Control (HSC)

The PO/HSC MPPT control algorithm is carried out by changing a control variable in small step sizes and keeping track the variations in the target variable until the point of maximum power extraction is reached[16]. This strategy eliminates the need for speed sensors, and the knowledge of the wind turbine parameters is not a pre-requisite. The tracking algorithm monitors the variations in the generator's output power and then adjusts the generator speed to achieve maximum power generation [74]. Figure 2.26 demonstrates the concept of PO/HSC.

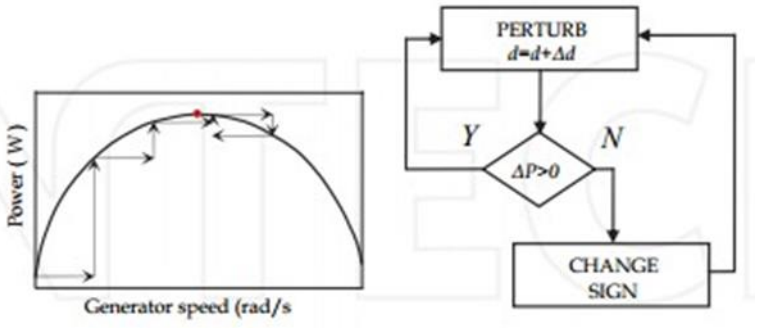

Figure 2. 26: PO/ HCS MPPT strategy[74]

Advantages of PO/HSC MPPT strategy

- The elimination of speed sensors and pre-knowledge of the wind turbine parameters makes this strategy less complex, less costly, more reliable and flexible.
- When pitch angle control is incorporated, the algorithm does not need to be reprogrammed for each variation in pitch angle.

Disadvantages of PO/HSC MPPT Strategy

- The algorithm searches for MPPT in the wrong direct during high wind gusts. This reduces the strategy's efficiency under rapid changes in wind speed.
- Large step sizes are associated with high power oscillations around the MPPT and small step sizes reduce the response speed of the strategy.

The selection of the best MPPT strategy is a trade-off between the response speed, efficiency, cost, lifespan, and reliability. Among these control strategies, the ORB and OTC MPPT techniques are extensively employed in WECS because of their simplicity, quick response and they are highly efficient in power smoothing enhancement [16, 74, 75]. However, the OTC optimizes the captured mechanical power instead of the output electrical power. Moreover, the variation in the wind speed is not reflected directly on the reference torque, and hence this reduces the efficiency of this MPPT control strategy[76]. Therefore, the ORB MPPT control strategy has been implemented in this study because it is more efficient, reliable and cheaper to implement.

2.2.3.2 Power Limitation Control

The power limitation control technique is responsible for protecting the VSWT from sudden wind gusts. This is ensured by increasing the pitch-angle when the wind speed exceeds the WT's rated wind speed. As a result, the aerodynamic power coefficient *Cp* is reduced to shed off the aerodynamic power extracted from the wind resource [16, 22, 51]. The pitch-angle controller remains inactive during low wind speeds and only gets activated during high wind speeds.

According to literature, a pitch-angle control strategy can either be a wind speed based; rotor speed based or generator power based depending on the input signals used to generate the desired pitch angle [77, 78] [79-81]. The rotor speed based power limitation control is said to be more accurate and it is highly used in many applications. This strategy is implemented in this study, and hence it is discussed further. In this strategy, the measured rotor speed is compared to the reference rotor speed. The error signal is then sent to the controller to generate a reference pitch-angle as shown in Figure 2.27. The reference pitch-angle is then sent to the pitch actuator.

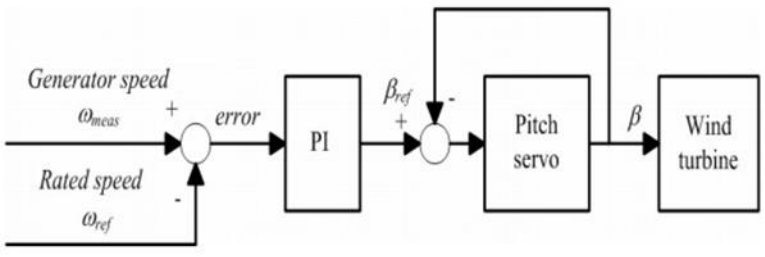

Figure 2. 27: Generator rotor speed pitch angle control strategy[78]

In the pitch actuator, the reference pitch angle β_{ref} generated from the controller is then compared to the desired pitch angle β. The pitch actuator is a hydraulic or mechanical system which is used to turn the wind turbine blades along their longitudinal axis away from the striking wind [79].

Figure 2.29 shows a typical pitch actuator model.

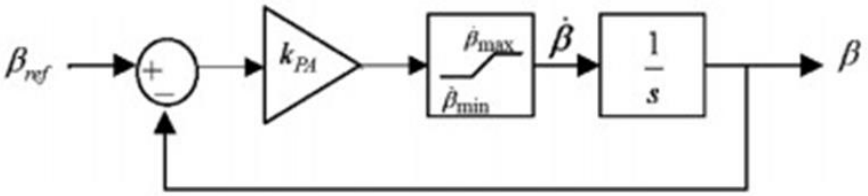

Figure 2. 28: Block diagram of the Pitch Actuator model [79]

2.3 Converter control approaches for wind energy conversion systems

The control of the VSCs interconnecting a wind turbine to the electrical grid is of significant importance in the behavior of the entire system during normal and fault conditions. Considering the vector control approach, there are two generic control approaches used to control the converter stations, namely: traditional/ conventional and new control approach. Although the traditional control approach is somewhat not beneficial from a fault ride-through point of view, it is well developed and it is commonly employed in existing VSC-based projects. According to Hansen et al. [26, 27], the new control approach is said to be beneficial from a fault ride-through capability point of view.

2.3.1 Traditional/conventional control approach

Figure 2.29 shows a sketch of the traditional converter control approach

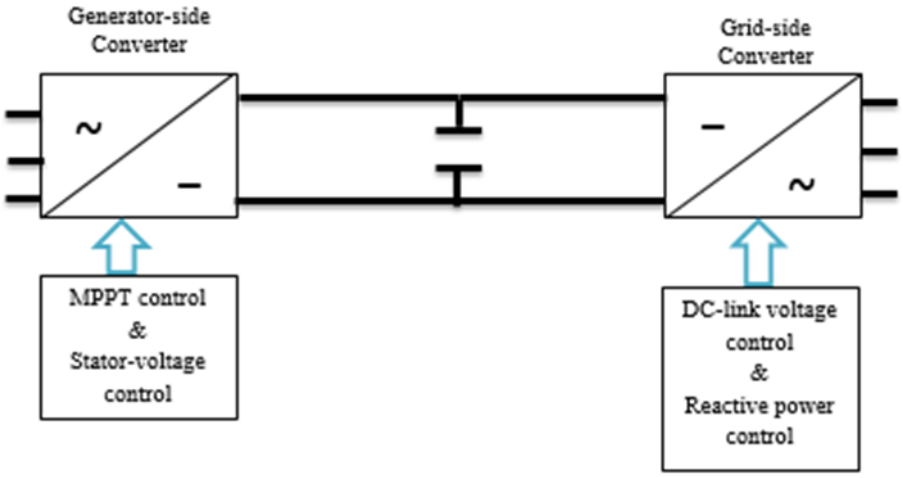

Figure 2. 29: Traditional Converter Control Approach

The controller applied to the generator-side converter carries out the MPPT and stator voltage control while the controller applied to the grid-side converter controls the DC-link voltage and the reactive power flowing into the power utility grid[16, 23].

2.3.2 New Converter control approach

The new control approach reverses the functions of the converter controllers. Figure 2.30 shows a sketch of the new converter control approach.

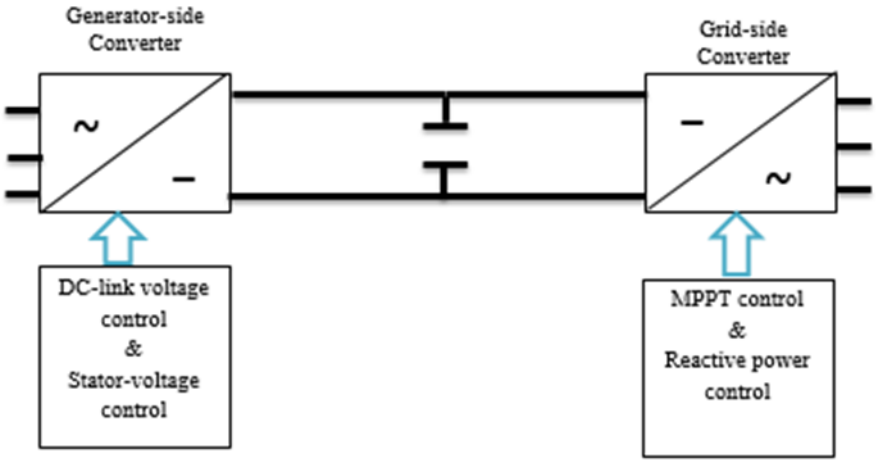

Figure 2. 30: New Converter Control Approach

The controller applied to the generator-side converter is used to stabilize the DC-link voltage and the stator voltage and keep them constant at their rated values, while the controller applied to the grid-side converter controls the rotor speed for MPPT and the reactive power flowing into the grid to ensure unity power factor [26, 27].

From a fault ride-through capability point of view, the traditional converter control approach is said to be unable to ensure the wind turbines' fault-ride-through capability. This is because, during grid fault conditions, the grid-side converter controller's ability to stabilize the DC-link voltage gets impaired and therefore it can no longer transfer the active power from the wind turbine generator to the grid. The surplus power leads to the charging of the DC-link capacitor(s) causing over-voltages in the DC-link. Furthermore, the surplus power leads to the acceleration of the turbine's rotor. Consequently, this may lead to a significant damage to the converter stations and the DC-link capacitor(s) [26, 27]. In this case, a chopper is commonly used as an additional measure to burn the surplus power during grid faults to reduce the power imbalance in the entire system. However, this tends to increase the cost of the entire system.

The new control approach is considered to be beneficial from a fault ride-through and economic point of view over the traditional control approach because of the following reasons:

- The generator-side converter is de-coupled from the grid and hence its DC-link voltage controller's performance does not get impaired during grid fault conditions.

- During a grid fault, the generator-side converter reduces the power generated by the wind turbine's generator which then reduces the amount of active power flowing to the DC-link and thus keeping the DC-link voltage constant.
- Since the issue of surplus power gets resolved by the generator-side converter, there is no need for additional measures such as choppers, and hence this cuts down on the cost of the entire system.

2.4 Pulse Width Modulation Strategies for Voltage Source Converters

In VSCs, the commutation of converter switches is realized by synthesizing a sinusoidal signal that turns them on and off several times per fundamental period. This is done to control the magnitude and phase angle of the converter terminal output voltage relative to the AC system voltage. The VSCs can be controlled using one of the following pulse width modulation (PWM) techniques [19, 82, 83]:

- Selective harmonic elimination PWM
- Sinusoidal PWM
- Space vector modulation

The PWM strategies that are briefly discussed are for a basic two-level VSC that comprises of two converter switches per leg.

2.4.1 Selective Harmonic Elimination PWM (SHE-PWM)

SHE-PWM strategy identifies the switching angles of the output phase voltage by setting the magnitude of the phase voltage and specifying the voltage harmonics to be eliminated [73, 84]. As a result, the fundamental phase voltage is chopped into a number of small pulses with notches located at the specified firing angles and the pre-determined harmonics are eliminated from the converter's output voltage.

Figure 2.31 shows how SHE-PWM defines three switching angles (a_1, a_2 and a_3) on the phase voltage and form gating signals for the switches of one phase of a three-phase 2-level VSC. The first angle is used to set the fundamental magnitude and the remaining angles are used to eliminate the specified low-order harmonics.

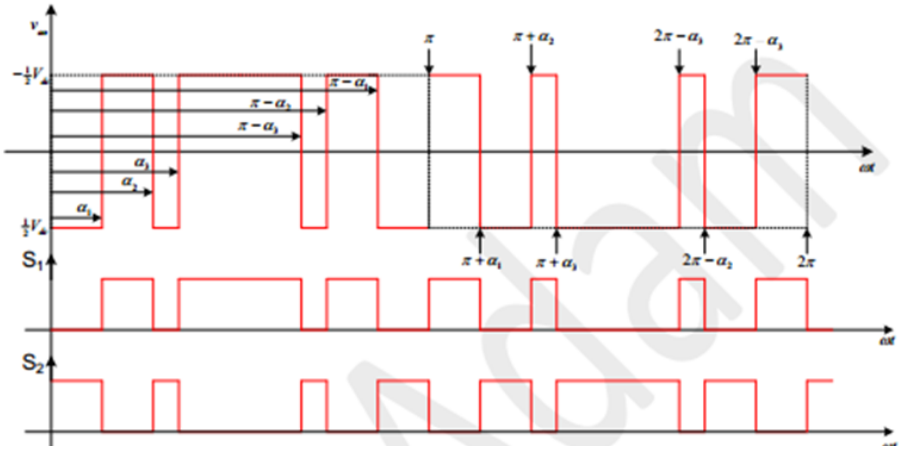

Figure 2. 31: Output phase voltage and the corresponding gate signals[19]

Advantages of SHE-PWM

- Low switching losses due to its ability to target pre-determined harmonics and control the fundamental voltage without creating unnecessary switching instances.
- Improves the DC link voltage utilization depending on the number of harmonics to be eliminated.

Disadvantages of SHE-PWM

- Requires offline calculations and a look-up table to store the switching angles.
- Difficulty to be realized practically and low and high modulation indices due to the switching angles that tends to be very close to each other.

2.4.2 Sinusoidal PWM (SPWM)

SPWM is a simple and widely used modulation technique used to control both one-phase and three-phase VSCs. The gating pulses used to turn the converter switches on and off are generated by comparing a low-frequency reference signal to a high-frequency carrier signal as shown in Figure 2.32 [19].

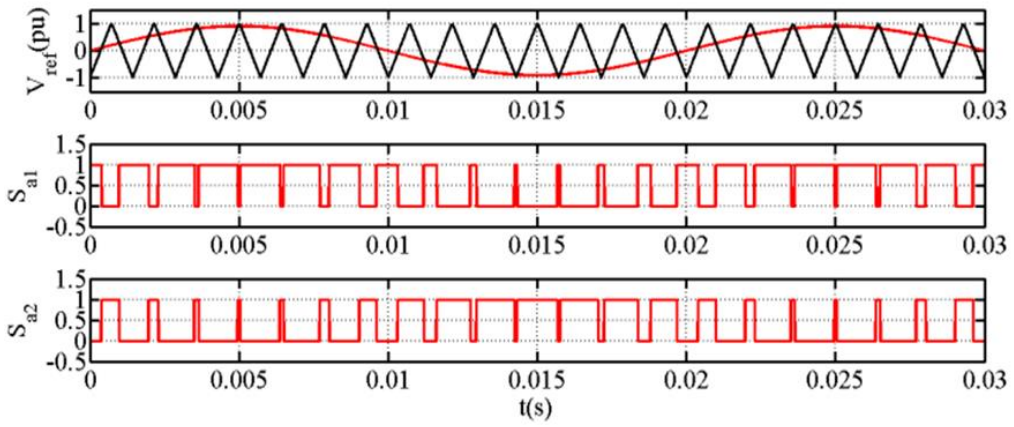

Figure 2. 32: Generation of gating signals using SPWM[19]

When the low-frequency reference signal exceeds the high-frequency carrier signal, the gating signal rises to *one*, otherwise the gating signal falls to *zero*. The frequency of the reference signal is normally selected equal to the frequency of the fundamental output voltage, while the frequency of the carrier signal is selected higher than the reference signal's frequency. The frequency ratio m_f is defined by Eq. (2.21) [19]

$$m_f = \frac{f_c}{f} \tag{2.21}$$

Higher values of m_f produce higher quality output voltage and current.

Advantages of SPWM

- It is highly attractive in many applications due to its simplicity and effectiveness in harmonic suppression.

Disadvantages of SPWM

- The quality of the converter output AC voltage decreases with a decrease in modulation index.
- Requires a high carrier frequency to generate a fundamental converter output voltage and current of high quality.
- Poor DC link voltage utilization

2.4.3 Space Vector Modulation (SVM)

SVM uses the concept of mapping the possible switch combinations of the VSC into the *α-β* plane as shown in Figure 2.33[85].

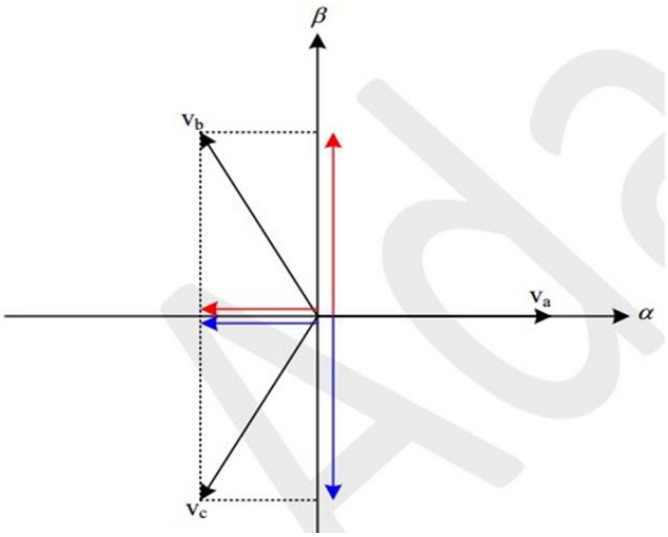

Figure 2. 33: Transformation of three-phase variables into α-β plane[19]

The VSC output voltages (v_{a0}, v_{b0}, v_{c0}) corresponding to each switch combination are transformed into their equivalent v_α and v_β using Clark's given by Eq. (2.22) [82]

$$\begin{bmatrix} v_\alpha \\ v_\beta \end{bmatrix} = \frac{2}{3}\begin{bmatrix} 1 & -\frac{1}{2} & -\frac{1}{2} \\ 0 & \frac{\sqrt{3}}{2} & -\frac{\sqrt{3}}{2} \end{bmatrix}\begin{bmatrix} v_{a0} \\ v_{b0} \\ v_{c0} \end{bmatrix} \tag{2.22}$$

Figure 2.34 (a) and (b) shows the SVM diagram for a two-level VSC consisting of six sectors and the generation of the reference voltage in the first sector of the SVM diagram, respectively.

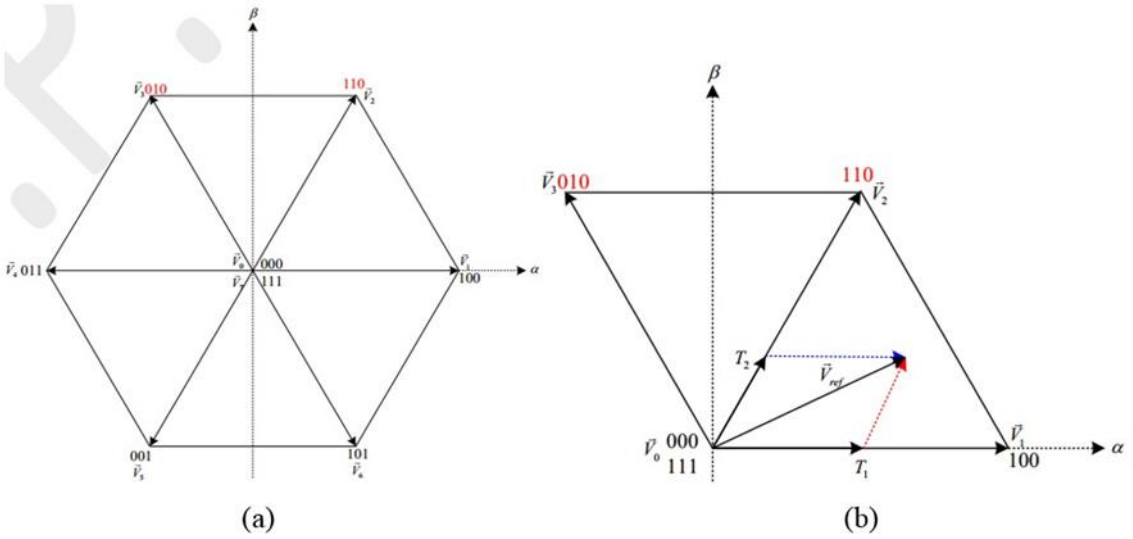

Figure 2. 34: SVM diagram for 2-level VSC; (b) Voltage generation in the first sector [19]

SVM exploits the six active switch states;100, 110, 010, 011, 010, 101, and two passive switch states; 000, 111 to approximate the target reference voltage vector V_{ref}, assuming the inverter switched output voltage has the same fundamental volt-second average as that of the target reference waveform over one switching cycle[19].

The reference vector V_{ref} in each sector is calculated by averaging the nearest three vectors. For instance, the reference vector for the first sector shown in Figure 2.36 (b) is given by Eq. (2.23)[19]

$$T_s\overline{V}_{ref} = t_0\overline{V}_0 + t_1\overline{V}_1 + t_2\overline{V}_2 \tag{2.23}$$

Where V_0, V_1, V_2 are the nearest voltage vectors and t_0, t_1, t_3 represents the dwell times of the voltage vectors. The sum of the dwell times of all vectors within one switching period is equal to the switching period T_s, given by Eq. (2.24)

$$T_s = T_0 + T_1 + T_2 \tag{2.24}$$

Advantages of SVM

- Offers increased flexibility in term of pulse placement within the switching period and sequence selection.
- Improves the utilization of the DC link voltage.
- Suitable for digital implementation in Digital Signal Processing (DSP) and microcontrollers.

Disadvantages of SVM

- Limited to motor drive applications because it is developed for balanced three-phase balanced AC systems.
- Requires a high switching frequency to generate an out voltage and current of good quality.

In this study, SPWM is used to synthesize the voltage signals used for the commutation of the VSC switches. This is mainly due to its effectiveness in harmonic suppression and also due to its simplicity. Since the converter under investigation in this study is a three-level NPC converter, the SPWM for that topology is discussed further as follow.

2.4.4 Sinusoidal PWM (SPWM) for Three-Level NPC VSC

The SPWM for the 3-Level NPC VSC is derived from the carrier disposition strategy presented by Carrara et al. [8]. It is stated that, for an N-level NPC multilevel converter, N-1 high-frequency triangular carriers with the same frequency and magnitude are arranged in such a way that they occupy the band between $V_{dc}/2$ to $-V_{dc}/2$ [19, 86]. The low-frequency reference signal for each phase is then compared to these carrier signals to generate the gating pulses used to turn the converter switches *on* and *off*. When the reference signal is greater than the carrier signal, the converter switch corresponding to that carrier signal is switched *on*, otherwise it is switched *off*. The modulation index for multilevel converters is given by Eq. (2.25) [19]

$$m = \frac{A_{m1}}{\frac{1}{2}(N-1)A_c} \tag{2.25}$$

Where: N is the number of levels, and Am and Ac are the amplitudes of the reference signal and the carrier signal, respectively.

There are three main carrier arrangements used to synthesize the gating pulses for NPC VSCs[19, 86, 87]:

2.4.4.1 Alternative Phase Opposition Disposition (APOD)

The carrier signals are arranged in such a way that each signal is shifted by 180 degrees from the subsequent signal as shown in Figure 2.35

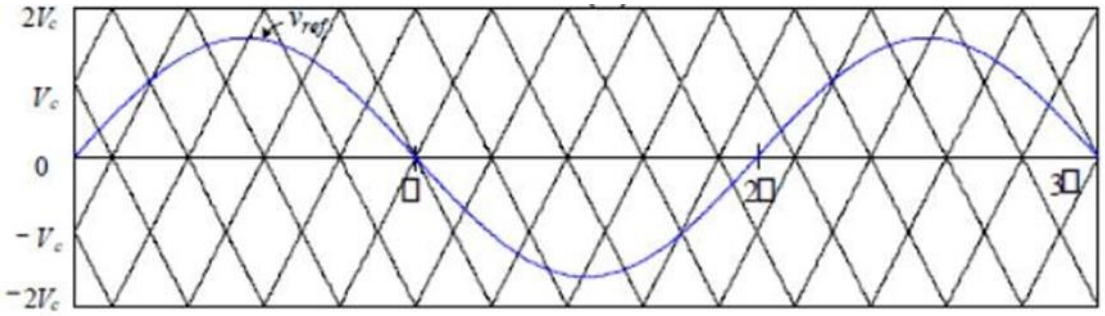

Figure 2. 35: Alternative Phase Opposition Disposition Carrier Arrangement (APOD)[19]

2.4.4.2 Phase Opposition Disposition (POD)

The carrier signals are arranged in such a way that, the signals above the zero reference are in phase but they are shifted by 180 degrees from the signals below the zero reference as shown in Figure 2.36

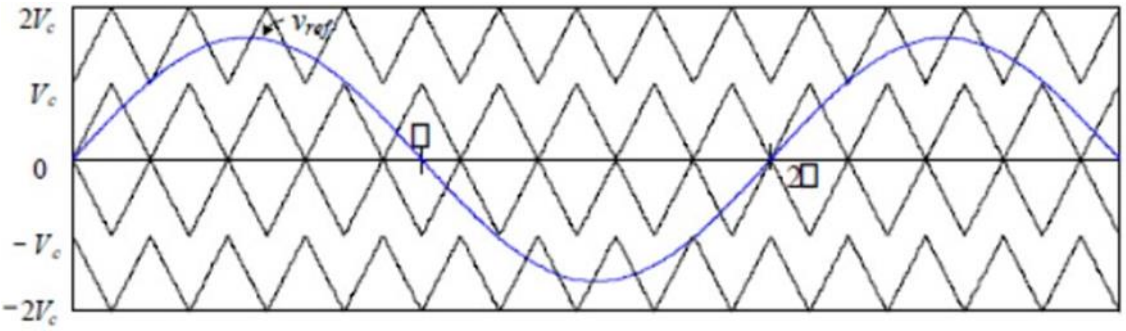

Figure 2. 36: Phase Opposition Disposition Carrier Arrangement[19]

2.4.4.3 Phase Disposition (PD)

In PD, all carrier signals above and below the zero reference are arranged in phase with one another as shown in Figure 2.37

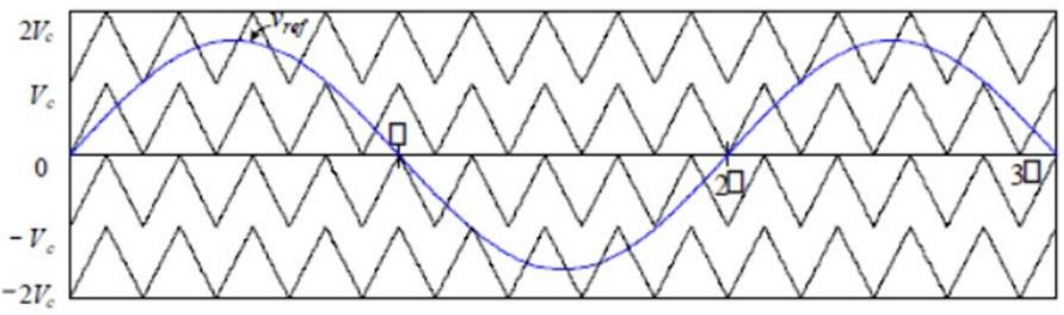

Figure 2. 37: Phase Disposition Carrier Arrangement[19]

The effect of different carrier arrangements on NPC converter output voltage's harmonic distribution and switching losses are discussed in [19]. When PD carriers are used, the first and second carrier frequency harmonics are removed from the line-to-line voltage. Furthermore, the main contributors to the generation of harmonic currents are the sidebands of the first and second carrier frequency harmonics in the line voltage. Since the magnitudes of the side band harmonics are smaller than the carrier frequency components, the inverter output current waveforms will improve significantly, hence reducing the size of the required AC filters. On the other hand, when POD or APOD carrier arrangements are used, most of the harmonics in the side bands do not cancel out in the line-to-line voltage. Therefore, these arrangements have poor harmonic performance compared to the PD carrier arrangement. Therefore, in this study, the PD carrier arrangement is employed to synthesize the gating signals for the 3-level NPC converter switches.

2.5 Fundamentals of Control Systems

2.5.1 Phase Margin and Gain Margin

In frequency response techniques, the gain and phase margins are the important indicators of system robustness, performance and stability and hence, they are widely used for controller designs. Phase and gain margins are determined by using Bode plots of the system's open-loop transfer function.

Gain margin: the amount of additional open-loop gain, expressed in decibels (dB) that is needed to make the closed-loop system unstable. The gain margin lies between the magnitude curve and the 0dB line corresponding to the phase crossover frequency; the frequency where the phase curve cuts the -180° axis on the phase plot[88, 89].

Phase margin: the additional open-loop phase shift that is needed at unity gain to make the closed-loop system unstable. The phase margin lies between the phase curve and the -180° axis corresponding to the gain crossover frequency; the frequency at which the magnitude curve cuts the 0dB axis on the bode plot[88, 89].

Figure 2.38 shows the graphical representation of the gain and phase margin and their corresponding cross-over frequencies.

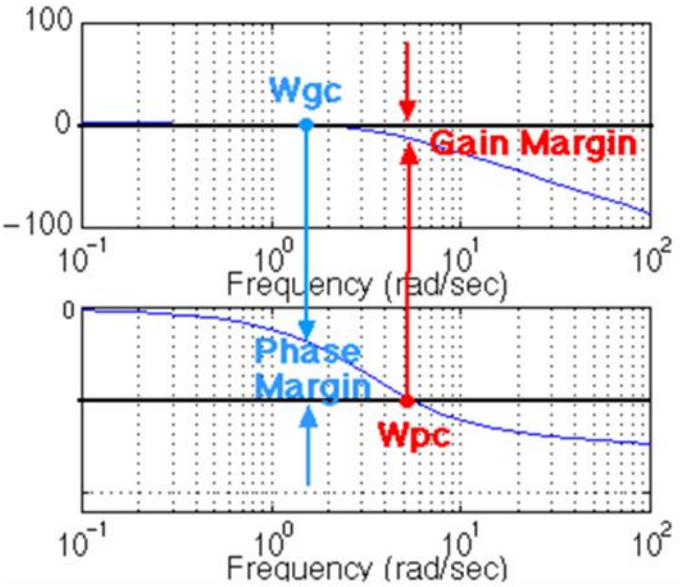

Figure 2. 38: Graphical representation of gain and phase margin and their corresponding cross-over frequencies

In frequency domain, controllers are mainly and incorporated into the entire systems to carry out the following tasks [90-94]:

- Improving the steady state errors by increasing the Bode's gain.
- Improving system stability by increasing/decreasing the phase and gain margins to their desired values.
- Reducing the percentage overshoot by increasing/decreasing the phase margin to the desired value.
- Achieving the desired rise time by increasing/decreasing the system's bandwidth frequency to the desired value.

However, it is not possible to satisfy all of these requirements at the same time, and hence some requirements are normally compromised depending on the main function of that particular controller.

Analysis of the magnitude and phase plots at frequencies near the bandwidth frequency provides valuable information about the performance of the system. According to [93], a gain margin ≥8dB and a phase margin ≥45° are usually required for many systems. There are a number of types of controllers that are used for the purpose of improving the open-loop system's stability in order to obtain or meet certain design specifications. The widely used controllers can be classified into two categories:

- **Controllers**: proportional-derivative (PD), proportional-integral (PI) and proportional- integral-derivative (PID)[93].
- **Compensators**: phase-lag compensator, phase-lead compensator and lag-lead compensator [93].

Currently, PI, PD, and PID controllers are widely used in academia and in industrial control systems because they have a simple structure, simple design procedure and they are cost-effective [94-97]. However, the design procedure of PD, PI and PID controllers involves determining the P, I and D gains which are usually tuned using a trial-and-error procedure[98]. Therefore, poorly tuned controller gains reduce the accuracy and the dynamic performance of the entire control system. Moreover, these controllers are linear, have a constricted operating range, prone to changes in machine parameters, and their design procedure does not take into consideration the initial performance of the uncompensated system [3]. Therefore, control systems comprising of PI, PD and PID controllers are ineffective when applied to nonlinear and uncertain systems [95]. On the other hand, phase-lead, phase-lag, and lag-lead compensators are associated with a design procedure that is well defined from fundamental principles as opposed to the trial-and-error design procedure. Moreover, the initial performance of the uncompensated system is taken into consideration prior to the controllers' modelling and design. The compensators are designed in the frequency domain to achieve the desired design specifications using bode plots and step-response curves. This makes the latter design procedure more accurate. For this reason, the compensators are employed in this study and hence, they are discussed in more details as follow.

2.5.2 Phase-Lead, Phase-Lag and Lag-Lead Compensators

Phase-lead and phase-lag compensators are mainly used for classical loop shaping of a particular system. This is done by improving the gain and phase stability margins to obtain the desired system performance and achieve the pre-defined design objectives.

2.5.2.1 Phase-Lead Compensator

A phase-lead compensator, also known as the PD type compensator improves the performance of the open-loop system by adjusting the systems' phase curve in the bode plot[92]. This is done by adding a positive phase shift to the phase curve to obtain the desired phase margin at the desired gain crossover frequency while minimizing disturbances on the system's magnitude curve at that frequency.

A basic phase-lead compensator is represented by a single zero on the negative real axis close to the origin and a single pole to the left of the zero[88]. The compensator is modeled using Eq. (2.26)[92]

$$G_{c,lead}(s) = K_c\left[\frac{1}{\alpha}\frac{(s+z_c)}{(s+p_c)}\right] = K_c\left[\frac{(s/z_c+1)}{(s/p_c+1)}\right] = K_c\left[\frac{(\tau s+1)}{(\alpha\tau s+1)}\right] \quad (2.26)$$

Where; $p_c>z_c$; $\alpha=z_c/p_c<1$; $\tau=1/z_c=1/\alpha p_c$; $z_c>0$ and $p_c>0$

Figure 2.39 shows the bode plot indicating the magnitude and phase curves of a typical phase-lead compensator.

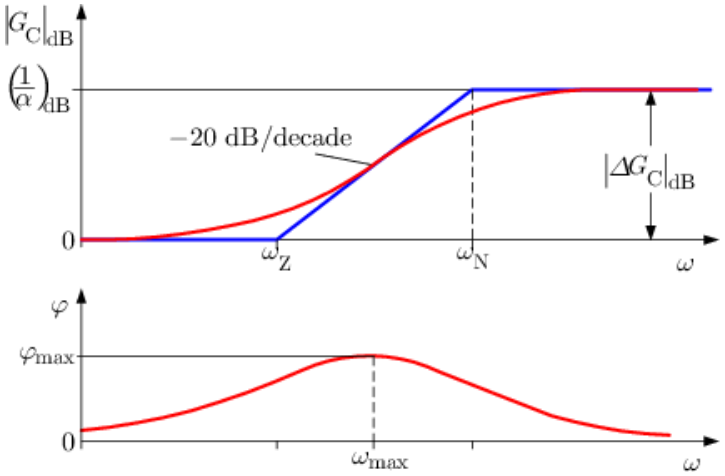

Figure 2. 39: Magnitude and phase plots of a typical phase-lead compensator

The phase-lead compensator amplifies the phase and magnitude curve at the intermediate and high frequencies. This correlates to increasing the phase margin and bandwidth of the system leading to an enhanced system stability and transient response. This is mainly due to the reduced response time, rise time and settling time.

The procedures used to design a typical phase-lead compensator are as follow [88, 92, 99]:

a) Computing the uncompensated phase margin

This step includes determining the amount of phase shift at the gain cross-over frequency of the uncompensated system and calculating the uncompensated phase margin using Eq. (2.27)[92].

$$PM_{uncompensated} = 180^o + \angle G(j\omega_{crossover}) \quad (2.27)$$

b) Determination of the positive phase shift φ_{max} and attenuation α

In this step, the phase-boost φ_{max} that the phase-lead compensator needs to provide in order to yield the desired phase-margin is determined. The required phase-boost is calculated using Eq. (2.28)[92]

$$\phi_{\max} = PM_{desired} - PM_{uncompensated} \tag{2.28}$$

The calculated phase-boost φ_{max} can then be used to determine the attenuation α using Eq. (2.29)[92]

$$\alpha = \frac{1-\sin(\phi_{\max})}{1+\sin(\phi_{\max})} \tag{2.29}$$

A phase-lead compensator is restricted to provide a phase shift not more than 90° since it only has a single zero. Hence, if more phase shift is needed, multiple stages of identical lead compensators connected in series can be implemented. Furthermore, it is recommended that $\alpha \geq 0.1$ should be used when designing a phase-lead compensator to limit the amount of shift in the magnitude curve and to avoid the use of system components with large values.

c) Locating the zero z_c and pole p_c

The location of the zero z_c and the pole p_c of the compensator is determined using the attenuation α and the desired crossover frequency $\omega_{crossover}$ [92].

$$\begin{aligned} z_c &= \omega_{compensated}\sqrt{\alpha} \\ p_c &= \frac{z_c}{\alpha} \end{aligned} \tag{2.30}$$

The zero and pole must be placed appropriately to ensure that the phase shift is obtained at the cross-over frequency.

2.5.2.2 Phase-Lag Compensator

A phase-lag compensator, also known as the PI type compensator improves the performance of the open-loop system by adjusting the magnitude curve to obtain the desired gain crossover frequency while minimizing disturbances on the phase curve at that frequency[90]. This is done by dropping the magnitude curve to 0db at the desired cross-over frequency.

This alternatively adds a negative phase shift to reduce the current phase margin to the desired value at the specified crossover frequency. A basic phase-lag compensator is described by a single pole on the negative real axis close to the origin and a zero to the left of the pole[88]. The compensator is modeled using Eq. (2.31)[90]

$$G_{c,lag}(s) = K_c\left[\frac{1}{\alpha}\frac{(s+z_c)}{(s+p_c)}\right] = K_c\left[\frac{(s/z_c+1)}{(s/p_c+1)}\right] = K_c\left[\frac{(\tau s+1)}{(\alpha\tau s+1)}\right] \tag{2.31}$$

Where; $p_c > z_c$; $\alpha = z_c/p_c > 1$; $\tau = 1/z_c = 1/\alpha p_c$; $z_c > 0$ and $p_c > 0$

Figure 2.40 shows the bode plot indicating the magnitude and phase curves of a typical phase-lag compensator.

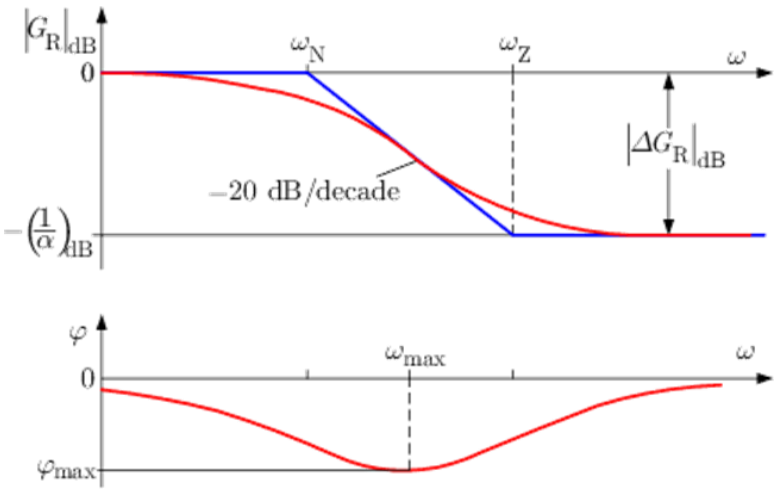

Figure 2. 40: Magnitude and phase curves of typical phase-lag compensator

The phase-lag compensator attenuates the phase and magnitude curve at the intermediate and high frequencies. This correlates to reducing the phase margin and bandwidth of the system thereby enhancing the system stability and reduced steady-state error. However, the system response becomes much slower due to the reduced rise and settling time.

The following steps outline the procedures used to design a typical phase-lag compensator [90]:

a) Determination of the gain crossover frequency

This step focuses on determining the gain crossover frequency that will correspond to the phase margin of the compensated system by computing the phase margin located at the desired gain crossover frequency using Eq. (2.32)[90]

$$PM_{\omega_{compensated}} = -180^{o} + PM_{desired} \tag{2.32}$$

b) Determination of α

In this step, the amount of attenuation in decibels (dB) that the phase-lag compensator must provide to drop the magnitude curve to 0dB at the compensated gain crossover frequency is computed using Eq. (2.33)[90]

$$\alpha = 10^{\left(\frac{|G(j\omega_{compensated})|_{db}}{10}\right)} \tag{2.33}$$

c) Locating the zero z_c and pole p_c

The compensated system's crossover frequency $\omega_{compensated}$ and the phase attenuation α are then used to determine the location of the zero z_c and pole p_c using Eq. (2.34)[90]

$$\begin{aligned} z_c &= \omega_{compensated}\sqrt{\alpha} \\ p_c &= \frac{z_c}{\alpha} \end{aligned} \tag{2.34}$$

Alternatively, the phase-lag compensator may be designed as follow:

The first step is to compute the phase-attenuation needed to obtain the desired phase margin by subtracting the phase margin of the current system from the desired phase margin as follow,

Phase-attenuation=$PM_{desired}$ -$PM_{current}$

The phase-attenuation needed is then used to locate the pole p_c and zero z_c of the phase-lag compensator by calculating the frequency [Hz] where the pole and zero will be located using Eq. (2.35) [90]

$$\begin{aligned} f_z &= f_{BW}\sqrt{\frac{1-\sin(phase-attenuation)}{1+\sin(phase-attenuation)}} \\ f_p &= f_{BW}\sqrt{\frac{1+\sin(phase-attenuation)}{1-\sin(phase-attenuation)}} \end{aligned} \tag{2.35}$$

Where; f_{BW} is the desired bandwidth. The angular frequencies where the pole and zero of the phase-lag compensator are located are calculated as using Eq. (2.36)

$$\begin{aligned} \omega_p &= 2\pi f_p \\ \omega_z &= 2\pi f_z \end{aligned} \tag{2.36}$$

Therefore, the transfer function of the phase-lag compensator is given by Eq. (2.37) [90]

$$\begin{aligned} &\mathrm{G}_{\mathrm{lag}}(\mathrm{s}) = \mathrm{G}_{\mathrm{co}}\left(\frac{\tau_{lag}\mathrm{s}+1}{\alpha\tau_{lag}\mathrm{s}+1}\right) \\ &where; \\ &\alpha = \omega_z / \omega_p \\ &\mathrm{G}_{\mathrm{co}} = \sqrt{\alpha} \\ &\tau_{lag} = 1/\omega_z \end{aligned} \tag{2.37}$$

2.5.2.3 Lag-Lead Compensator

The lag-lead compensator combines the features and functions of the phase-lead and phase-lag compensators. Therefore, it is just a series connection of the two compensators. A basic lag-lead compensator consists of two zeros and two poles. The lag-lead compensator is designed using Eq. (2.38)[91]

$$
\begin{aligned}
G_{c,lag\_lead}(s) &= K_c\left[\left[\frac{1}{\alpha_{lag}}\frac{(s+z_{c_{lag}})}{(s+p_{c_{lag}})}\right]\times\left[\frac{1}{\alpha_{lead}}\frac{(s+z_{c_{lead}})}{(s+p_{c_{lead}})}\right]\right] \\
&= K_c\left[\left[\frac{(s/z_{c_{lag}}+1)}{(s/p_{c_{lag}}+1)}\right]\times\left[\frac{(s/z_{c_{lead}}+1)}{(s/p_{c_{lead}}+1)}\right]\right] \\
&= K_c\left[\left[\frac{(\tau_{lag}s+1)}{(\alpha_{lag}\tau_{lag}s+1)}\right]\times\left[\frac{(\tau_{lead}s+1)}{(\alpha_{lead}\tau_{lead}s+1)}\right]\right]
\end{aligned}
\tag{2.38}
$$

2.6 Chapter Summary

This chapter mainly dealt with a thorough review of the HVDC technology, the wind energy conversion system (WECS), the different control techniques for grid-connected WECSs, the different PWM techniques and the fundamentals of control systems. The detailed comparisons and trade-off evaluations led to the selection of the fundamental components given in Table 2.1 which are explored further and implemented to carry out the proposed research investigation.

Table 2. 1: Selection of the Fundamental Components of the proposed WECS

Component Type	All components	Selected Component	Reason
VSC Converter Topology	- 2-level converter topology - Multilevel converter topology o Neutral-point clamped o Flying-capacitor o Cascaded H-bridge	Multilevel converter topology: 3-level Neutral Point Clamped VSC	- It can handle higher voltages and synthesize voltages with better waveform quality compared to the 2-level converter topologies [16]. - It is associated with lower harmonic distortion; lower switching losses, higher overall efficiency, and cuts down on the size and number of filtering elements.

	○ Modular multilevel		- Currently, the NPC converter is the only topology widely used in HVDC systems with several practical systems presently in operation [12].
VSC control strategy	- Direct/ power angle control - Vector-oriented control	Vector-oriented control (VOC)	- The VOC has a better performance due to lower current distortions. - The VOC is associated with a higher grid power factor, and higher overall efficiency.
Orientation of the WT's axis of rotation	- Horizontal axis - Vertical axis	Horizontal axis wind turbine	- It is highly efficient compared to the vertical-axis WT because the WT blades are exposed to stronger winds[49, 50].
Type of Wind Turbine (WT)	- Variable speed wind turbine - Fixed speed wind turbine	Variable Speed WT (VSWT)	- The VSWT can extract optimal power at different wind speeds. Therefore, it yields more power than a fixed-speed WT thereby maximizing the aerodynamic efficiency of the WT[16].
Type of WT generator	- Modern WT generators: ○ Doubly-fed induction generator ○ Permanent magnet synchronous generator	Permanent magnet synchronous generator (PMSG)	- A PMSG is associated with high energy density, ease of controllability, low maintenance cost and the self-excitation system as opposed to the doubly-fed induction generator [16, 59, 60]. - The increasing interest in multi-pole PMSG concept means that the gearbox will be eliminated thereby reducing the weight of the nacelle and the cost of the WT while also

			improving the efficiency of the VSWT[27].
Type of MPPT control strategy	- Optimal relationship-based - Tip-Speed Ratio - Optimal Torque Control - Hill-climb/ perturb and observe	Optimal relationship-based (ORB)	- The ORB technique is reliable, has a quick response, simple and cheaper to implement, and it is highly efficient in power smoothing enhancement [16, 74, 75].
Type of PWM strategy	- Selective Harmonic Elimination - Sinusoidal PWM - Space Vector modulation	Sinusoidal PWM (SPWM)	- The SPWM is effective in harmonic suppression and it is simple to implement[19].
Type of carrier signal arrangement for 3-level NPC	- Alternative Phase Opposition Disposition (APOD) - Phase Opposition Disposition (POD) - Phase Disposition (PD)	Phase Disposition (PD)	- When PD carriers are used, the first and second carrier frequency harmonics are removed from the line-to-line voltage. - The main contributors to the generation of harmonic currents are the sidebands of the 1st and 2nd carrier frequency harmonics in the line voltage. - The magnitudes of the side band harmonics are smaller than the carrier frequency components. Therefore, the inverter output current waveforms will improve significantly thereby reducing the size of the required AC filters.

Type of Controllers	- PI, PD, and PID controllers - Phase-lead, Phase-lag and Lead-lag compensators	Phase-lag, phase-lead and lead-lag compensators	- Phase-lead, phase-lag, and lag-lead compensators are associated with a design procedure that is well defined from fundamental principles as opposed to the trial-and-error design procedure associated with PI, PD, and PID controllers. - The initial performance of the uncompensated system is taken into consideration prior to the controllers' modelling and design.

CHAPTER 3: MATHEMATICAL MODELLING AND COMPONENT'S SIZING

This chapter covers the mathematical modelling and sizing of the proposed permanent magnet synchronous generator (PMSG)-based wind turbine, the 3-level NPC voltage source converter, the DC-link capacitor bank, the phase reactor and the power transformer.

3.1 Wind Energy Conversion System

The wind turbine (WT) under consideration is a variable speed horizontal axis wind turbine equipped with a 690V, 2MW PMSG. The drive train implemented is of a lumped-mass type. This means that the wind turbine is connected to the generator via a gearless drive train[27]. Table 3.1 and Table 3.2 shows the parameters of a typical wind turbine and a PMSG, respectively.

Table 3. 1: Wind Turbine Specifications [64]

Parameters	Value
Rated Mechanical Power (MW)	2
Cut-in wind speed(m/s)	4
Rated wind speed (m/s)	13
Cut-out wind speed (m/s)	25
Number of rotor blades	3
Length of blades (m)	37.5
Rotor diameter (m)	76.42
Rotor area (m^2)	4587
Speed range (rpm)	13-21.9
Rated speed (rpm)	19
Rotor mass(kg)	40

Table 3. 2: Permanent Magnet Synchronous Generator Specifications [50]

Parameter	Value
Generator Type	PMSG, 2.0MW, 690V, 9.75Hz
Rated Mechanical Power (MW)	2
Rated Apparent Power (MVA)	2.2419
Rated line-to-line voltage (V, rms)	690

Rated Phase Voltage (V, rms)	398.4
Rated Stator Current (A, rms)	1867.76
Rated Stator Frequency (Hz)	9.75
Rated Power Factor	0.8921
Rated Rotor Speed (rpm)	22.5
Number of Pole Pairs	26
Rated Mechanical Torque (kNm)	848.826
Rated Rotor Flux Linkage (Wb, rms)	5.8264
Stator Winding Resistance, R_s (mΩ)	0.821
d-axis Synchronous Inductance (mH)	1.5731
q-axis Synchronous Inductance (mH)	1.5731

The inertia of a particular WT depends on the mass of the rotor, rotor blade length, and the number of rotor blades. The wind turbine inertia J_{WT} is defined by Eq. (3.1) [50]

$$J_{WT} = m(\frac{L_{blade}}{n_{blades}})^2 \tag{3.1}$$

Where; m is the rotor mass [kg], L_{blade} is the length of the rotor blades [m] and n_{blade} is the number of rotor blades.

Using the parameters in Table 3.1, the WT's inertia is calculated as follow

$$J_{WT} = 40kg(\frac{37.5m}{3})^2 = 6250kg/m^2$$

The calculated inertia value is in the same order of magnitude with the other 2MW wind turbines that are available in the industry, for instance, the wind turbines with the same rated power manufactured by Vestas and Gamesa.

The energy stored in the rotor mass is related to the wind turbine inertia J_{WT} and rated rotor speed ω_r by Eq. (3.2)[50]

$$E_{WT} = \frac{1}{2} J_{WT}(\omega_r)^2 \tag{3.2}$$

Where; $\omega_r = \frac{2\pi f}{polepairs}$

Therefore, the energy stored in the rotor mass is calculated as follows

$$E_{WT} = \frac{1}{2} \times 6.25 \times 10^6 \times (\frac{2\pi \times 9.75}{26}) = 1.73 \times 10^7 J$$

The inertia constant is defined as the ratio of the energy stored in the rotor mass to the wind turbine generator's rated apparent power S_{WT}. The inertia constant is given by Eq. (3.3) [50]

$$H_{WT} = \frac{E_{WT}}{S_{WT}} \tag{3.3}$$

$$H_{WT} = \frac{1.73\times10^{7}}{2.2419MVA} = 7.73$$

The wind turbine's rated optimal power coefficient C_p and tip speed ratio λ can be calculated using the parameters given in Table 3.1 and Table 3.2 and recalling Eq. (2.6) and Eq. (2.7). Therefore, the tip speed ratio for a wind turbine with a rotor radius of 38.21m, a rated rotor speed of 2.356rad/s, and a rated wind speed of 13m/s, is equal to,

$$\lambda = \frac{r\omega_r}{v_w} = \frac{(2.356)(38.21)}{13} = 6.92$$

The power coefficient of a WT with a rated active power of 2MW, a rotor area of 4587m/s^2, a rated wind speed of 13m/s and the air density of 1.225kg.m/s, is calculated as follow,

$$P_m = \frac{1}{2}\rho A C_p(\lambda,\beta) v_w{}^3$$

$$C_p = \frac{2P_m}{\rho A v_w{}^3} = \frac{2(2\times10^6)}{1.225\times4587\times13^3} = 0.324$$

3.2 Three-level NPC Voltage Source Converter modeling

The converter topology employed in this study is a three-level Neutral Point Clamped VSC topology. The size of the converter depends on the steady state performance requirements, the amount of active power to be transferred and the voltage support requirement at the point of common coupling (PCC). VSCs operate within specified limits and hence it is required that the converter terminal voltages be kept within those limits. Typical voltage limits are 95% to 105% and 90% to 110%[38]. The operating limits mainly depend on the maximum current allowed to flow through the IGBT switches, the maximum DC-link voltage, and the maximum DC current through the DC cable, whereby, the DC-link voltage limit is the dominant factor[38].

The minimum DC-link voltage required to avoid converter saturation when using SPWM is given by Eq. (3.4) [19, 26, 38]

$$V_{dc} = 2\sqrt{\frac{2}{3}}\times V_{LL} \tag{3.4}$$

Where V_{LL} is the line-to-line voltage.

Therefore, using the wind turbine's rated line-to-line voltage given in Table 3.1, the DC-link voltage is calculated as follow,

$$V_{dc} = 2\sqrt{\frac{2}{3}} \times 690V = 1126.77V$$

Considering the voltage limits of 95% to 105%, the DC-link voltage must remain within the acceptable range of ±5% of the fundamental value, that is, 1070.43V to 1183.11V.

The peak of the fundamental component of the converter's output line-to-line voltage is related to the steady-state modulation index m and DC-link voltage V_{dc} by Eq.(3.5)[19, 38]

$$V_{C_{LL}} = \frac{1}{2}\sqrt{\frac{3}{2}} \times V_{DC} \times m \tag{3.5}$$

To avoid saturation effects and to operate within the linear modulation index range, the PWM modulation index is limited to 1, that is $0<m\leq1$[19]. Therefore, in this study, the modulation index is taken to be 0.9 which is employed in most commercial applications[38].

Therefore, the converter's output terminal voltage is calculated as follow

$$V_{C_{LL}} = \frac{1}{2}\sqrt{\frac{3}{2}} \times 1126.77 \times 0.9 = 620.62V$$

Considering the voltage limits of 95% to 105%, the converter's output terminal voltage must remain within the acceptable range of ±5% of the fundamental value, that is, 589.89V to 651.66V. These limits are monitored by limiting the amount of current following through the converter switches.

3.3 DC-Link capacitor Sizing

The DC-link comprises of two equally sized capacitors. The DC-link capacitor size is characterized by a time constant τ given by Eq. (3.6) [38].

$$\tau = \frac{0.5 C_{DC} {V_{DC}}^2}{S_C} \tag{3.6}$$

Where: V_{DC} is the DC-link voltage and S_N is the apparent power rating of the converter.

The time constant τ is defined as the time needed to charge the capacitor from zero to the rated DC voltage V_{DC} if the converter is supplied with a constant active power equal to the

converter's apparent power S_N [38]. The time constant is usually chosen to be relatively small (less than 10ms) to satisfy small ripple and small transient over-voltages on the DC voltage and for fast control of active and reactive power[38]. In this study, the power rating of the converter is taken be 3MVA to accommodate the active power rating of the wind turbine generator of 2MW and any additional reactive power. Therefore, the equivalent DC-link capacitance is determined by rearranging Eq. (3.6) as follow,

$$C_{DC} = \frac{\tau S_N}{0.5 V_{DC}^{\ 2}} \tag{3.7}$$

Using a time constant of 5ms, the DC-link voltage calculated using Eq. (3.4) and the converter rating of 3MVA, the DC-link capacitor size is equal to,

$$C_{DC\_eq} = \frac{5\times10^{-3}\times3\times10^{6}}{0.5\times1126.77^{2}} = 23.63mF$$

The individual capacitor sizes are determined as follow

$$\frac{1}{C_{DC\_eq}} = \frac{1}{C_{DC\_1}} + \frac{1}{C_{DC\_2}}$$

$$C_{DC\_1} = C_{DC\_2} = 47.26mF$$

3.4 Phase Reactor sizing

The size of the interfacing phase reactor is a trade-off between the switching frequency, converter saturation, and the control algorithm, whereby the converter saturation plays a major role. According to [100], the phase reactor is to be sized such that the minimum reference current's tracking time Δt is less that the time constant of the converter's current controller. Eq. (3.8) describes the tracking time.

$$\Delta t = \frac{0.9L}{\omega_e (V_{LL} - V_{LL\max})} \times 0.612 V_{dc} \tag{3.8}$$

Where V_{LL} is the AC-side's line-to-line voltage, V_{LLmax} is converter's output terminal voltage calculated using Eq. (3.5), L is the interfacing reactor's inductance, and ω_e is the electrical angular frequency.

In this study, the switching frequency of the current controller is chosen to be one-fifth of the PWM converter's switching frequency in order to supply a sufficient bandwidth and increase the current controller's response. The PWM converter's switching frequency is chosen to be 2 kHz which is sufficient enough for voltage source converters.

Therefore, the switching frequency of the current controller is 400Hz, giving a switching time of 2.5ms which also represents the time constant of the converter's current controller. Since the reference current's tracking time is required to be much smaller than the current controller's time constant, it is therefore taken to be one tenth of the current controller's switching time.

That is, $\frac{1}{10} \times 2.5 \times 10^{-3} = 0.25ms$

Therefore, considering the system's electrical angular frequency of 314.16rad/s (50Hz), and the AC-side line-to-line voltage of 690, and the converter's output terminal voltage of 620.62V, the smoothing inductor L is calculated as follow,

$$L = \frac{\Delta t \omega_e (V_{LL} - V_{LL\max})}{0.9 \times 0.612 V_{dc}}$$
$$= \frac{0.25 \times 10^{-3} \times 314.16 \times (0.612(1126.77) - 0.612(1126.77)(0.9))}{0.9 \times 0.612(1126.77)} = 66.5mH$$

3.5 Power Transformer

The 690V wind turbine is to be integrated into a 33kV utility grid. The transformer is required to step up the converter's output terminal voltage level to the local grid's voltage level. That is, from 620.62V to 33kV. Therefore the ratio of the primary winding to the secondary winding is determined using Eq. (3.9)

$$\frac{N_p}{N_s} = \frac{V_p}{V_s}$$
$$\Rightarrow \frac{\frac{1}{2}\sqrt{\frac{3}{2}} V_{dc} m}{33kV} = \frac{N_p}{N_s} \quad (3.9)$$
$$N_p = \frac{\frac{1}{2}\sqrt{\frac{3}{2}}(1126.77) \times 0.9}{33000} N_s$$
$$N_p = 0.0188 N_s$$

3.6 Chapter Summary

This chapter dealt with the sizing of the components making up a wind energy conversion system. The computed values are summarized in Table 3.3

Table 3. 3: Sizes of the wind energy conversion system components

Component	Value
WT generator's power and voltage rating	2MW, 690V
The wind turbine inertia	6250kg/m^2
DC-link voltage	1126.77V - Ranging from 95% to 105% of the rated value. That is, 1070.43V to 1183.11V
The peak of the fundamental component of the converter's output line-to-line voltage	620.62 V - In the range of ±5% of the fundamental value, that is, 589.89V to 651.66V
DC-link capacitor size	- Equivalent capacitance is 23.63mF - Individual capacitor size is 47.26mF
Phase reactor size	66.5mH

CHAPTER 4: DERIVATION OF THE CONTROL SYSTEM'S TRANSFER FUNCTIONS

This chapter focuses on the mathematical modelling of a three-level neutral-point-clamped (NPC) VSC topology emphasizing on its AC-side and DC-side dynamics. Moreover, the chapter covers the derivation of the open-loop and closed-loop transfer functions of the pitch-angle controller as well as the grid-side and generator-side converter controllers.

4.1 Operating Principles of a 3-level Neutral-Point Clamped Converter

Figure 4.1 shows one phase of a three-level neutral point clamped (NPC) converter

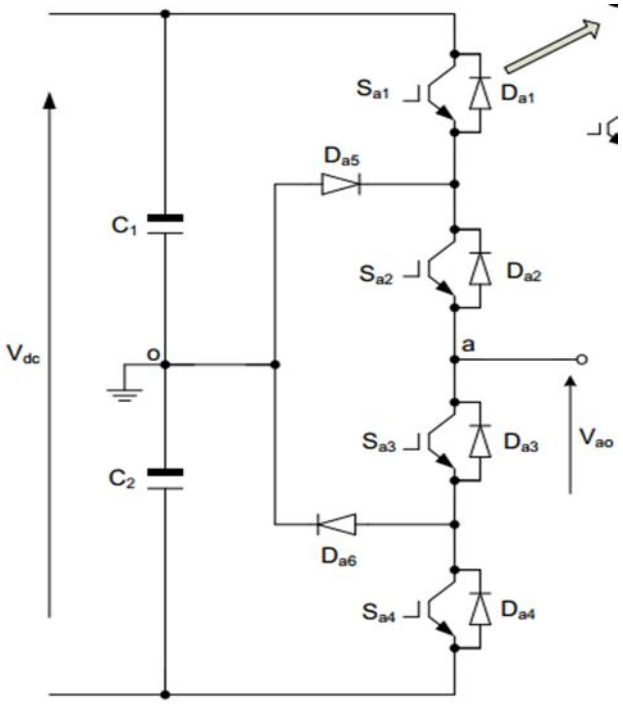

Figure 4. 1: One phase of a 3-level neutral point clamped converter[19]

A three-level NPC converter has four switches per phase and it generates three voltage levels: $V_{dc}/2$, 0 and $-V_{dc}/2$. In a 3-level NPC VSC topology, switches S_{a1}, S_{a2}, S_{a3} and S_{a4} of phase *a* operate as compliments of one another. Therefore, turning S_{a1} on excludes S_{a3} from switching on, and switching S_{a2} on excludes S_{a4} from switching on, and the same applies to the remaining phases *b* and *c* with a phase shift of -120˚ for phase *b* and a phase shift of -240˚ for phase *c*[19, 86]. On this basis, the converter terminal voltages at *a, b* and *c* relative to the midpoint *o* can be synthesized from the DC-link voltage V_{dc} as shown by Eq. (4.1)[19]:

$$
\begin{aligned}
V_{a0} &= \frac{1}{2}V_{dc}[S_{a1}S_{a2} - (1-S_{a1})(1-S_{a2})] \\
V_{b0} &= \frac{1}{2}V_{dc}[S_{b1}S_{b2} - (1-S_{b1})(1-S_{b2})] \\
V_{c0} &= \frac{1}{2}V_{dc}[S_{c1}S_{c2} - (1-S_{c1})(1-S_{c2})]
\end{aligned} \tag{4.1}
$$

Equation (4.1) shows that switching S_{a1} and S_{a2} *on* connects the converter's output phase *a* to $V_{DC}/2$; turning off S_{a1} and keeping S_{a2} *on* connects the output to 0V; and turning both switches *off* connects the output phase *a* to $-V_{DC}/2$.

The current in the NPC converter switches and neutral point can be related to the output phase currents i_a, i_b, and i_c by using the switching function given by Eq. (4.2)

$$
\begin{aligned}
i_{sa1} &= S_{a1}i_a, i_{sa2} = S_{a2}i_a; i_n = (1-S_{a1})S_{a2}i_a \\
i_{sb1} &= S_{b1}i_b, i_{sb2} = S_{b2}i_b; i_n = (1-S_{b1})S_{b2}i_b \\
i_{sc1} &= S_{c1}i_c, i_{sc2} = S_{c2}i_c; i_n = (1-S_{c1})S_{c2}i_c
\end{aligned} \tag{4.2}
$$

The currents in the clamping diodes are defined as $i_{Da5} = i_n$ and $i_{Da6} = 0$ when ia≥0; and $i_{Da5} = 0$ and $i_{Da6} = i_n$ when ia<0.

4.1.1 AC-side dynamics for a 3-L NPC Converter

The equation describing the AC-side dynamics of the NPC converter is described by Eq. (4.3)[19]:

$$
\frac{d}{dt}\begin{bmatrix} i_a \\ i_b \\ i_c \end{bmatrix} = \begin{bmatrix} \frac{V_{a0}-V_{ag}}{L_t} \\ \frac{V_{b0}-V_{bg}}{L_t} \\ \frac{V_{c0}-V_{cg}}{L_t} \end{bmatrix} - \begin{bmatrix} \frac{R_t}{L_t} & 0 & 0 \\ 0 & \frac{R_t}{L_t} & 0 \\ 0 & 0 & \frac{R_t}{L_t} \end{bmatrix} \begin{bmatrix} i_a \\ i_b \\ i_c \end{bmatrix} \tag{4.3}
$$

Where V_{a0}, V_{b0}, and V_{c0} are the converter's output voltages for each phase given by Eq. (4.1), V_{ag}, V_{bg}, and V_{cg} are the grid voltages, and R_t and L_t are the resistance and inductance of the interfacing reactor.

The equation describing the AC-side dynamics of the NPC is in the form of three sinusoidal waveforms representing the 3 AC phases. Calculations in *abc*-frame are complex due to the sinusoidal components and its variability in the time-frame. Therefore, to facilitate the control design of 3-phase converters, the 3-phase variables need to be transformed into two-phase variables [38, 86]. Clarke and Park's transforms are used for carrying out this transformation.

Whereby, Clarke transformation is responsible for transforming *abc* to *αβ* reference frame, while the Park transformation is responsible for transforming *abc* to *dq* reference frame. The three-phase variables are recovered with the inverse transforms.

The *dq* version of Eq. (4.3) is obtained by applying Park transformation to it. Firstly, the equation is rewritten in compact matrix form as shown in Eq. (4.4)[19, 86]

$$L_t I_{ident} \frac{di_{abc}}{dt} = V_{abc0} - V_{abcg} - R_r I_{ident} i_{abc} \tag{4.4}$$

Where I_{ident} *is* the identity matrix given by,

$$I_{ident} = \begin{bmatrix} 1 & 0 & 0 \\ 0 & 1 & 0 \\ 0 & 0 & 1 \end{bmatrix}$$

Using Park Transformation and omitting the zero sequence, Eq. (4.4) becomes Eq. (4.5) [19, 86],

$$\begin{bmatrix} L_t & 0 \\ 0 & L_t \end{bmatrix} \begin{bmatrix} \frac{di_d}{dt} \\ \frac{di_q}{dt} \end{bmatrix} = \begin{bmatrix} V_{d0} - V_{dg} \\ V_{d0} - V_{dg} \end{bmatrix} - \begin{bmatrix} R_t & 0 \\ 0 & R_t \end{bmatrix} \begin{bmatrix} i_d \\ i_q \end{bmatrix} - \begin{bmatrix} 0 & -\omega L_t \\ \omega L_t & 0 \end{bmatrix} \begin{bmatrix} i_q \\ i_d \end{bmatrix} \tag{4.5}$$

The final equation describing the AC-side dynamics of the NPC in *dq* reference frame is given by Eq. (4.6)[19, 86]

$$\begin{aligned} \frac{di_d}{dt} &= \frac{V_{d0} - V_{dg} - R_t i_d + \omega L_t i_q}{L_t} \\ \frac{di_q}{dt} &= \frac{V_{q0} - V_{qg} - R_t i_q - \omega L_t i_d}{L_t} \end{aligned} \tag{4.6}$$

Using the d-q axis theory, the instantaneous real and reactive power exchanged between the grid-side converter and the grid are described by Eq. (4.7)[67]

$$\begin{aligned} P &= \frac{3}{2}(V_{gd} i_d + V_{gq} i_q) \\ Q &= \frac{3}{2}(V_{gq} i_d - V_{gd} i_q) \end{aligned} \tag{4.7}$$

In vector-oriented control, the d-axis of the synchronous reference frame is aligned with the grid voltage vector [38]. Therefore, the grid voltage vector only has the d-axis component V_{gd}, while the q-axis component V_{gq} is set to zero. That is, $V_{gd}=V$ and $V_{gq}=0$. Therefore, Eq. (4.7) becomes Eq. (4.8)

$$P = \frac{3}{2} V_{gd} i_d$$
$$Q = -\frac{3}{2} V_{gd} i_q \tag{4.8}$$

4.1.2 DC-side dynamics for a 3-L NPC Converter

Considering the DC-link capacitor node, the DC-side dynamics of the NPC converter can be modelled as follows:

From fundamental principles, $I_C = C \frac{dV_{dc}}{dt}$

Therefore, the equation relating the voltage V_{c1} across upper capacitor C_1 and V_{c2} across the lower capacitor C_2 and the currents i_{c1} and i_{c2} flowing through the two DC-link capacitors is given by Eq. (4.9)[86]

$$\begin{bmatrix} \frac{dv_{c1}}{dt} \\ \frac{dv_{c2}}{dt} \end{bmatrix} = \frac{1}{C} \begin{bmatrix} 1 & 0 \\ 0 & 1 \end{bmatrix} \begin{bmatrix} i_{c1} \\ i_{c2} \end{bmatrix} \tag{4.9}$$

From the neutral point and DC-link loop, the neutral point current and DC-link voltage are given by Eq. (4.10) and Eq. (4.11), respectively, assuming the upper and lower capacitors have equal capacitances[86]

$$i_{c1} - i_{c2} = i_n \tag{4.10}$$

$$v_{c1} + v_{c2} = V_{dc} \tag{4.11}$$

Differentiating Eq. (4.11) and rearranging Eq. (4.10) and Eq. (4.11) in matrix form, Eq. (4.12) is obtained

$$\begin{bmatrix} i_{c1} \\ i_{c2} \end{bmatrix} = \frac{1}{2} \begin{bmatrix} 1 & 1 \\ -1 & 1 \end{bmatrix} \begin{bmatrix} i_n \\ 0 \end{bmatrix} \tag{4.12}$$

Substituting Eq. (4.12) into Eq. (4.9) gives Eq. (4.13) relating the neutral point current to the NPC DC-link capacitor voltages as follow

$$\begin{bmatrix} \frac{dv_{c1}}{dt} \\ \frac{dv_{c2}}{dt} \end{bmatrix} = \frac{1}{2} \frac{1}{C} \begin{bmatrix} 1 & 1 \\ -1 & 1 \end{bmatrix} \begin{bmatrix} i_n \\ 0 \end{bmatrix} \tag{4.13}$$

Equation (4.13) is used to provide information regarding the magnitude of the oscillations that the neutral-point may experience for a given load on the AC-side. Over a full fundamental period, the neutral-point current is usually zero. Therefore, the average of Eq. (4.13) over this period leads to $\frac{dv_{c1}}{dt}$ and $\frac{dv_{c2}}{dt}$ to equate to zero and hence the voltages across the capacitors remain balanced. As a result, the connection between the neutral point and the clamping diodes can be considered as an open circuit. As a result, the DC-side dynamics are described by Eq. (4.14)[19, 86]

$$\frac{dV_{dc}}{dt} = \frac{I_{dc} - I_L}{C_{equiv}} \tag{4.14}$$

Where C_{equiv} is the equivalent DC-link capacitance.

4.2 Control of the Generator-side and Grid-side NPC Converters

In this study, the new control approach is implemented to control the generator-side and grid-side converters. This is mainly because the new control approach is considered to beneficial from a fault-ride-through capability point of view. The vector-oriented control (VOC) is implemented in this study.

4.2.1 Generator-side Converter Controller Objective

The aim of the controller applied to the generator-side converter is to stabilize the DC-link voltage to its rated value. This ensures a continuous flow of active power from the WT generator to the grid. Moreover, the controller is required to keep the generator's stator voltage constant at its rated value which ensures that there is no risk of over-voltages.

4.2.2 Grid-side Converter Controller Objective

The objective of the controller applied to the grid-side converter is to extract maximum power from the wind resource when the wind speed is lower than the WT's rated wind speed. This is done by controlling the rotor speed. Moreover, the controller is used to adjust the reactive power fed into the grid to achieve unity power factor.

Figure 4.2 shows the detailed control block diagram of the generator-side and grid-side converters.

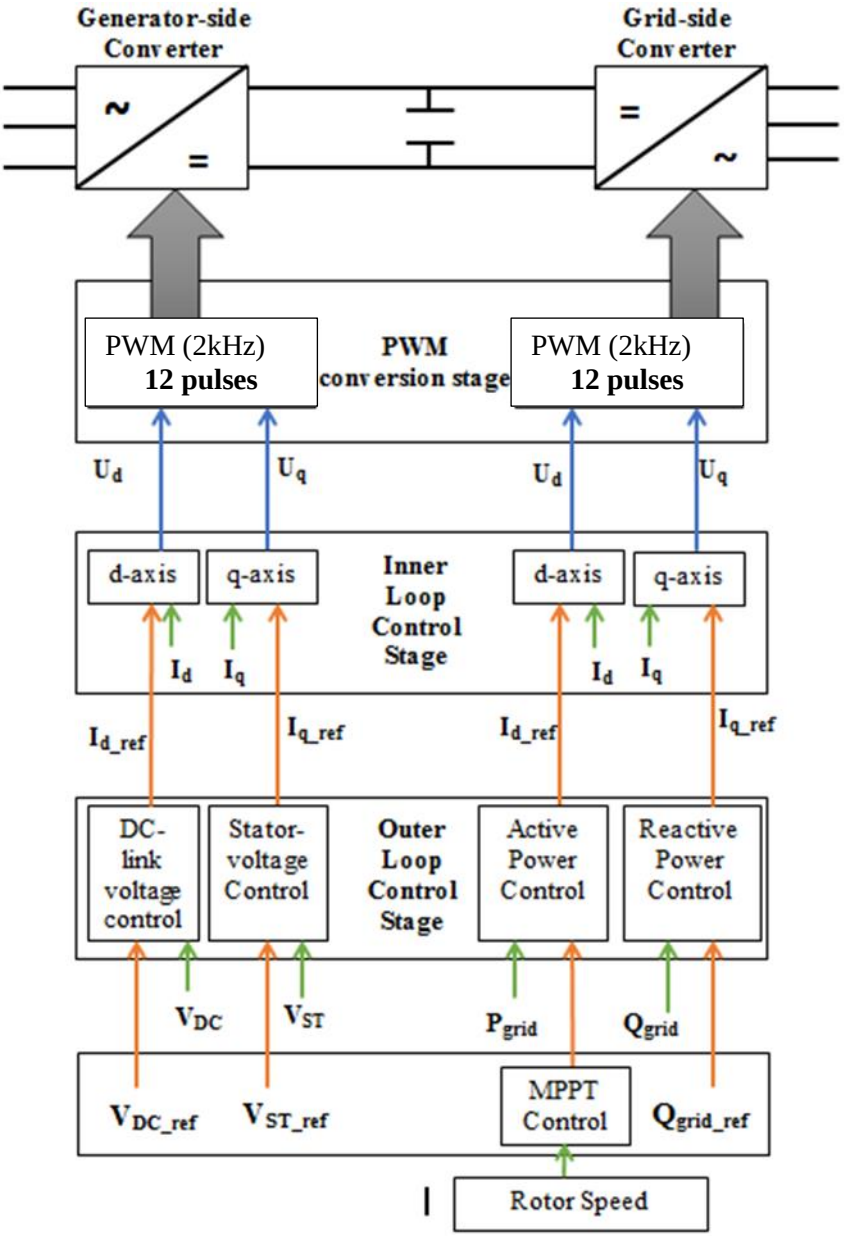

Figure 4. 2: Detailed generator-side and grid-side converter control block

4.2.3 Generator-side Converter Control

Figure 4.2 shows a typical overall control block of a converter station. The control loop is made up of a fast inner current control loop and a slower outer control loop. The outer control loops generate the current reference signals that serve as inputs into the inner control loops.

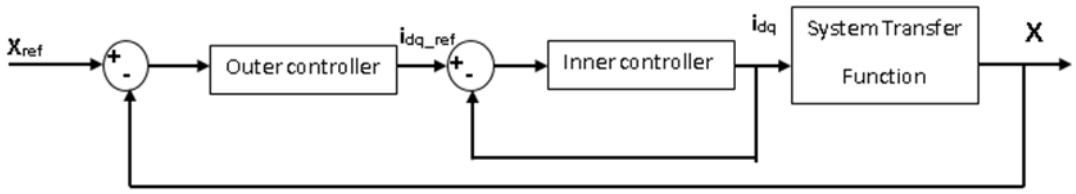

Figure 4. 3: Overall Control block

4.2.3.1 Inner Current Control Loop

The inner current control loop operates as follow:

The stator reference current from the outer controller loop(s) is compared to the output stator current. The controller forces the reference current to track the output current to obtain a good and desirable system performance. Figure 4.4 shows the inner current controller loop for the generator-side converter controller.

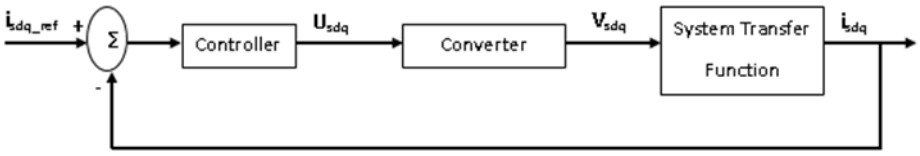

Figure 4. 4: Inner current control loop for the generator-side converter

a) Controller block

The error from the comparator is fed into the controller block,

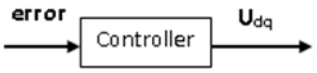

The output of the controller block is given by

U_{dq}=error*controller's transfer function

Where;

$$\text{error} = i_{\text{sdq\_ref}} - i_{sdq} \tag{4.15}$$

Therefore, the output of the controller block is given by Eq. (4.16);

$$U_{sdq} = (i_{sdq\_ref} - i_{sdq}) \times G_{c,i}(s) \tag{4.16}$$

Where $G_{c,i}(s)$ is the current controller's transfer function.

b) Converter block

A converter is usually considered as an ideal transformer with a time delay caused by the switching of the converter switches. The delay time is equal to half of the PWM converter's switching time. The transfer function of the converter is therefore given by Eq. (4.17) [38];

$$Y(s) = \frac{1}{T_a s + 1} \tag{4.17}$$

Where $T_a = \frac{T_{switch}}{2} = \frac{1}{2 f_{switch}}$ is the time delay in seconds.

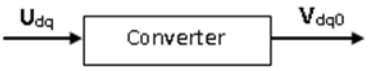

The output of the converter block, which serves as the input into the system transfer function block is given by Eq. (4.18)

$$\begin{aligned} v_{sdq0} &= U_{sdq} \times \frac{1}{T_a s + 1} \\ V_{sdq0} &= (i_{sdq\_ref} - i_{sdq}) \times G_{c,i}(s) \times \frac{1}{T_a s + 1} \end{aligned} \tag{4.18}$$

c) System Transfer Function

The system's behaviour is governed by the equations that represent the PMSG's stator currents in dq-synchronous reference frame given by Eq. (2.13). Rearranging Eq. (2.13) gives Eq. (4.19) that represents the input to the system transfer function block.

$$\begin{aligned} V_{sd} &= R_s i_{sd} + L_{sd} \frac{di_{sd}}{dt} - \omega_{se} L_{sq} i_{sq} \\ V_{sq} &= R_s i_{sq} + L_{sq} \frac{di_{sq}}{dt} + \omega_{se} (L_{sd} i_{sd} + \psi_f) \end{aligned} \tag{4.19}$$

From Eq. (4.19), the d-axis voltage equation has a speed or frequency induced term $\omega_{se} L_{sq} i_{sq}$ and the q-axis voltage equation has a speed or frequency and a flux induced term $\omega_{se} (L_{sd} i_{sd} + \psi_f)$ which ensures cross-coupling between the two axes. To obtain a good control performance, it is required to de-couple the d- and q- axis. This is normally done by employing a dual-closed-loop direct current controller comprising of decoupled current compensation and voltage feed-forward compensation [33, 38]. The cross-coupling terms are removed by changing Eq. (4.16) as follows;

$$\begin{aligned} U_{sd} &= (i_{sd\_ref} - i_{sd}) \times G_{c,i} - \omega_{se} L_{sq} i_q \\ U_{sq} &= (i_{sq\_ref} - i_{sq}) \times G_{c,i} + \omega_{se} (L_{sd} i_d + \psi_f) \end{aligned} \tag{4.20}$$

Substituting Eq. (4.20) into Eq. (4.18) gives Eq. (4.21)

$$V_{sd} = (i_{sd\_ref} - i_{sd}) \times G_{c,i} - \omega_{se} L_{sq} i_q \times \frac{1}{T_a s + 1}$$
$$V_{sq} = (i_{sq\_ref} - i_{sq}) \times G_{c,i} + \omega_{se} (L_{sd} i_d + \psi_f) \times \frac{1}{T_a s + 1} \quad (4.21)$$

Equating Eq. (4.21) to Eq. (4.19) cancels out the cross-coupling terms and hence giving the system's transfer function for both d and q axis as shown in Eq. (4.22)

$$V_{sd} = R_s i_{sd} + L_{sd} \frac{di_{sd}}{dt}$$
$$V_{sq} = R_s i_{sq} + L_{sq} \frac{di_{sq}}{dt} \quad (4.22)$$

Taking the Laplace transformation of Eq. (4.22) gives

$$V_{sd}(s) = R_s i_{sd}(s) + sL_{sd} i_{sd}(s)$$
$$V_{sq}(s) = R_s i_{sq}(s) + sL_{sq} i_{sq}(s) \quad (4.23)$$

Therefore, the system's transfer function is given by Eq. (4.24), relating the output stator current to the stator voltage

$$\frac{i_{sd}(s)}{V_{sd}(s)} = \frac{1}{sL_{sd} + R_s}$$
$$\frac{i_{sq}(s)}{V_{sq}(s)} = \frac{1}{sL_{sq} + R_s} \quad (4.24)$$

The complete controller block for the inner current control is as shown in Fig. 4.5

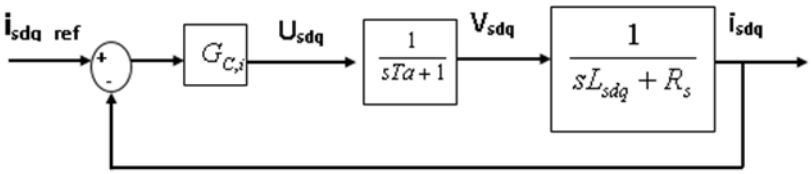

Figure 4. 5: Complete inner current control loop for the generator-side converter

Therefore, the open-loop transfer function of the inner current controller is given by Eq. (4.25)

$$G_{C,ol}(s) = \frac{G_{C,i}(s)}{(sTa + 1)(sL_{sdq} + R_s)} \quad (4.25)$$

While the closed-loop transfer function is given by Eq. (4.26)

$$G_{C,cl}(s)=\frac{\dfrac{G_{C,i}(s)}{(sTa+1)(sL_{sdq}+R_s)}}{1+\dfrac{G_{C,i}(s)}{(sTa+1)(sL_{sdq}+R_s)}}=\frac{G_{C,i}(s)}{(sTa+1)(sL_{sdq}+R_s)+G_{C,i}(s)} \quad (4.26)$$

Figure 4.6 represents the detailed block diagram of the inner current control loops.

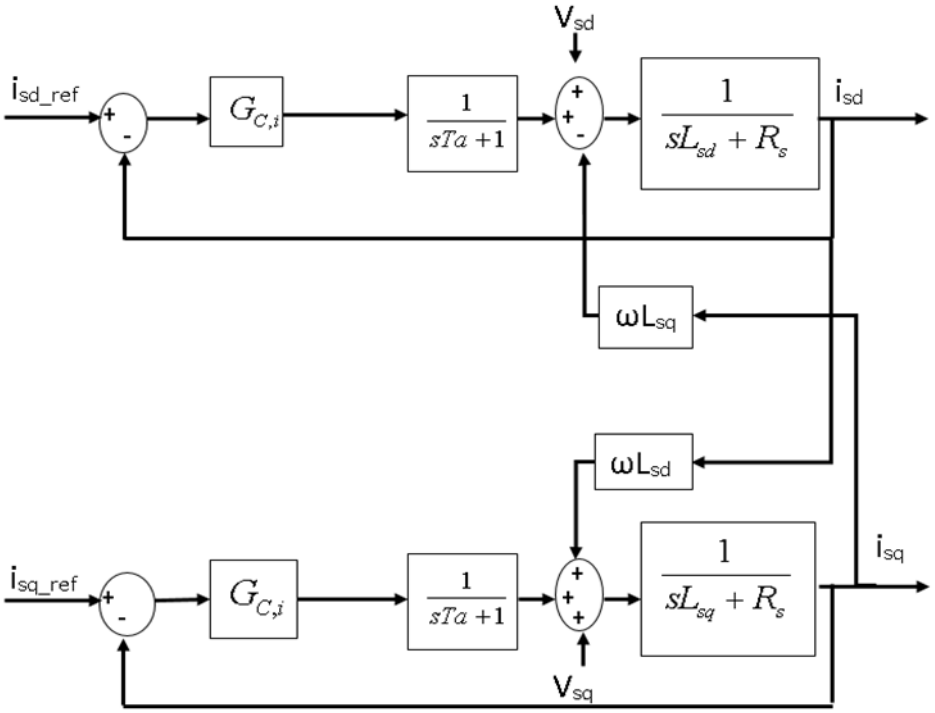

Figure 4. 6: Detailed block diagram of the generator-side converter's inner current control loops

4.2.3.2 Outer Control Loop(s)

4.2.3.2(a) DC-link Voltage Control Loop

The DC-link voltage controller provides the d-component of the stator's reference current for the inner current controller as shown in Fig. 4.7.

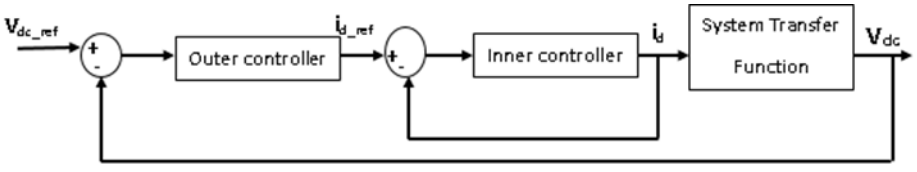

Figure 4. 7: DC-link voltage controller loop

a) Outer controller block

The DC-link voltage outer control loop operates as follow:

The reference DC-link voltage is compared to the output DC-link voltage. The error then serves as an input into the controller block. The output signal from the controller block is the reference current fed into the inner current control loop.

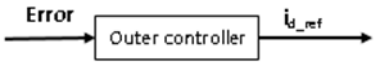

Therefore, the output signal of the outer control block is given by Eq. (4.27)

$$i_{sd\_ref} = (V_{dc\_ref} - V_{dc}) \times G_{c,v}(s) \tag{4.27}$$

Where $G_{c,v}(s)$ is the DC-link voltage controller's transfer function.

b) Inner Current Controller block

The Inner current controller block is simply represented by the closed-loop transfer function by Eq. (4.26). The output signal of the inner current controller is the d-axis current component which is then fed into the system transfer function's block.

c) System Transfer Function

Considering the DC-link capacitor node, the DC-side dynamics can be described by Eq. (4.28)

$$I_C = I_{dc} - I_L \tag{4.28}$$

Where, I_C, I_{dc}, and I_L, are the capacitor, DC-link and load current, respectively. The power on the DC side is given by Eq. (4.29)

$$P_{dc} = V_{dc} I_{dc} \tag{4.29}$$

Using the d-q axis theory, the instantaneous real and reactive power of the synchronous generator are described by Eq. (4.30) [38]

$$\begin{aligned} P_{gen} &= \frac{3}{2}(V_{sd} i_{sd} + V_{sq} i_{sq}) \\ Q_{gen} &= \frac{3}{2}(V_{sq} i_{sd} - V_{sd} i_{sq}) \end{aligned} \tag{4.30}$$

Considering the vector-oriented control, That is, $V_{sd}=V_s$ and $V_{sq}=0$. The instantaneous real and reactive power of the synchronous generator are described Eq. (4.31)

$$\begin{aligned} P_{gen} &= \frac{3}{2} V_{sd} i_{sd} \\ Q_{gen} &= -\frac{3}{2} V_{sd} i_{sq} \end{aligned} \tag{4.31}$$

Assuming a lossless converter and considering that the DC-link voltage controller ensures the power on the AC-side is equal to the power on the DC-side, the DC-link current is derived by equating Eq. (4.31) to Eq. (4.29) as follows

$$P_{gen} = P_{dc}$$
$$\frac{3}{2} V_{sd} i_{sd} = V_{dc} I_{dc}$$

Therefore,

$$I_{dc} = \frac{3}{2} \frac{V_{sd}}{V_{dc}} i_{sd} \tag{4.32}$$

Equation (4.29) becomes;

$$C \frac{dV_{dc}}{dt} = \frac{3}{2} \frac{V_{sd}}{V_{dc}} i_{sd} - I_L \tag{4.33}$$

The system's transfer function is derived from the DC-side dynamics described by Eq. (4.33). The DC-link current equation is non-linear. To carry out linear stability analysis of the system, the non-linear equation needs to be linearized around steady state reference points. The linearization of non-linear systems is carried out using the Taylor series expansion given by Eq. (4.34)[38]

$$\frac{dx}{dt} = f(x, y, z) = \frac{\partial f}{\partial x}\Big|_{\substack{y=y_0 \\ z=z_0}} \Delta x + \frac{\partial f}{\partial y}\Big|_{\substack{x=x_0 \\ z=z_0}} \Delta y + \frac{\partial f}{\partial z}\Big|_{\substack{x=x_0 \\ y=y_0}} \Delta z \tag{4.34}$$

Where; x_0, y_0, and z_0 are the initial conditions.

Therefore, the linearization of the DC-link voltage equation is given by Eq. (4.35)

$$\begin{aligned} C \frac{d\Delta V_{dc}}{dt} &= \frac{3}{2} \left(\frac{\partial}{\partial i_{sd}}\Big|_{\substack{V_{sd}=V_{sd0} \\ V_{dc}=V_{dc\_ref}}} \Delta i_{sd} + \frac{\partial}{\partial V_{sd}}\Big|_{\substack{i_{sd}=i_{sd0} \\ V_{dc}=V_{dc\_ref}}} \Delta V_{sd} + \frac{\partial}{\partial V_{dc}}\Big|_{\substack{i_{sd}=i_{sd0} \\ V_{sd}=V_{sd0}}} \Delta V_{dc} \right) - \Delta I_L \\ C \frac{d\Delta V_{dc}}{dt} &= \frac{3}{2} \left(\frac{V_{sd0}}{V_{dc\_ref}} \Delta i_{sd} + \frac{i_{sd0}}{V_{dc\_ref}} \Delta V_{sd0} - \frac{V_{sd0} \times i_{sd0}}{V_{dc\_ref}^2} \Delta V_{dc} \right) - \Delta I_L \end{aligned} \tag{4.35}$$

The only input of interest into the system transfer function is i_{sd}. I_L acts as a disturbance. Therefore, the simplified equation representing the system's transfer function is given by Eq. (4.36)

$$C \frac{d\Delta V_{dc}}{dt} = \frac{3}{2} \frac{V_{sd0}}{V_{dc\_ref}} \Delta i_{sd} \tag{4.36}$$

Taking the Laplace transform of Eq. (4.36) gives Eq. (4.37) that relates the d-component of the stator current to the DC-link voltage.

$$\begin{aligned} Cs\Delta V_{dc}(s) &= \frac{3}{2}\frac{V_{sd0}}{V_{dc\_ref}}\Delta i_{sd}(s) \\ \frac{\Delta V_{dc}}{\Delta i_{sd}(s)} &= \frac{3}{2}\frac{V_{sd0}}{V_{dc\_ref}}\times\frac{1}{Cs} \end{aligned} \tag{4.37}$$

The main aim of the DC-link voltage controller is to maintain a balanced active power transfer from the DC-side to the AC-side and vice versa. To do so, the capacitor current must be kept equal to zero. Therefore, from Eq. (4.29), $I_{dc}=I_L$. Thus, the reference value of i_{sd} is given by Eq. (4.38)

$$i_{sd} = \frac{2}{3}\frac{V_{dc}}{V_{sd}}I_L \tag{4.38}$$

Equation (4.38) represents the feed-forward term used to minimize the impacts of the slow dynamic response of cascaded control. The complete control block of the DC-link voltage controller is as shown in Fig.4.8

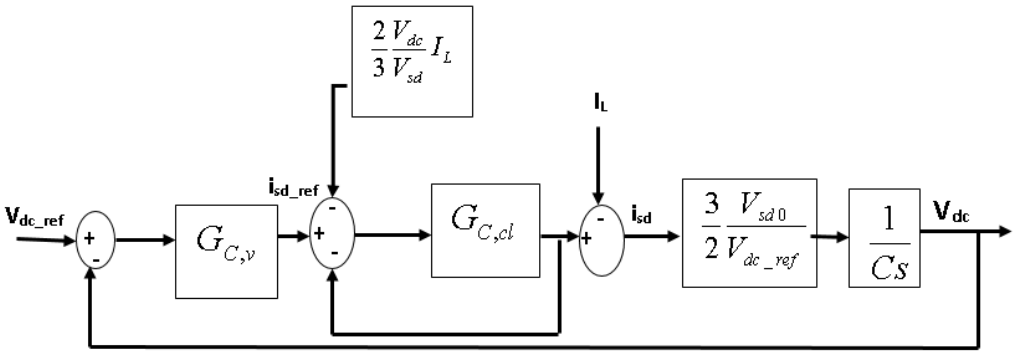

Figure 4. 8: Final DC-link voltage control loop

Therefore, the open-loop transfer function of the DC-link voltage controller is given by Eq.

$$\begin{aligned} G_{v,ol}(s) &= G_{C,v}(s)\times G_{C,cl}(s)\times\frac{3}{2}\frac{V_{sd0}}{V_{dc\_ref}}\times\frac{1}{Cs} \\ G_{v,ol}(s) &= \frac{3V_{sd0}G_{C,v}(s)G_{C,c}(s)}{2V_{dc\_ref}Cs[(sTa+1)(sL_{sd}+R_s)+G_{C,c}(s)]} \end{aligned} \tag{4.39}$$

The closed loop transfer function of the DC-link voltage controller is given by Eq. (4.40)

$$G_{v,cl}(s) = \frac{3V_{sd0}G_{C,v}(s)G_{C,c}(s)}{2V_{dc\_ref}Cs[(sTa+1)(sL_{sd}+R_s)+G_{C,c}(s)]+3V_{sd0}G_{C,v}(s)G_{C,c}(s)} \tag{4.40}$$

4.2.3.2(b) Stator voltage Control Loop

The stator voltage is regulated by the q-component of the stator current. Therefore, the outer controller block in Fig 4.9 is used to generate the reference q-component of the stator current which serves as the input into the inner current control loop.

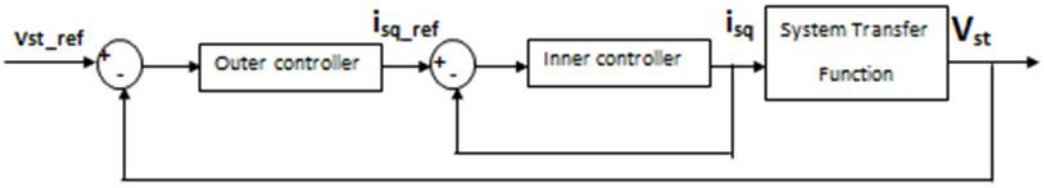

Figure 4. 9: Stator Voltage Control Loop

a) Outer controller block

In the stator voltage outer control loop, the reference stator voltage is compared to the output stator voltage. The error then serves as an input into the outer controller block. The output from the controller block is the reference current fed into the inner current control loop.

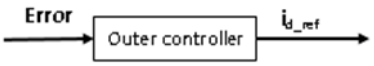

Therefore, the output of the outer control block is given by Eq. (4.41)

$$i_{sq\_ref} = (V_{st\_ref} - V_{st}) \times G_{c,st}(s) \tag{4.41}$$

Where $G_{c\_st}(s)$ is the stator voltage controller's transfer function.

b) Inner Current Controller block

The inner current controller block is simply represented by the closed-loop transfer function given by Eq. (4.26). The output of the inner current controller is the q-component of the stator current which is then fed into the system transfer function's block.

c) System Transfer Function

The voltage drop across the stator reactance can be described by Eq. (4.42) [38, 57]

$$\Delta V = V_s - V_{con} = \frac{R_s P_{gen} + X_s Q_{gen}}{V_s} \tag{4.42}$$

Where, V_s is the stator voltage, V_{con} is the converter voltage, R_s is the stator winding resistance and X_s is the synchronous reactance which is equal to $\omega_e (L_{sd}+L_{sq})$.

Assuming that $X_s >> R_s$ for the stator reactance, the voltage drop across the stator reactance depends only on the reactive power flow. From Eq. (4.31) and Eq. (4.42), the system's transfer function is given by Eq. (4.43)

$$\begin{aligned} \Delta V &= V_s - V_{con} = \frac{X_s Q_{gen}}{V_s} = \frac{-3X_s V_{sd}}{2V_{sd}} i_{sq} \\ \frac{V_{sd}}{i_{sq}} &= -\frac{3X_s}{2} + V_{con} = \frac{3\omega_e (L_{sd} + L_{sq})}{2} + V_{con} \end{aligned} \tag{4.43}$$

Figure 4.10 shows the stator voltage controller's block diagram.

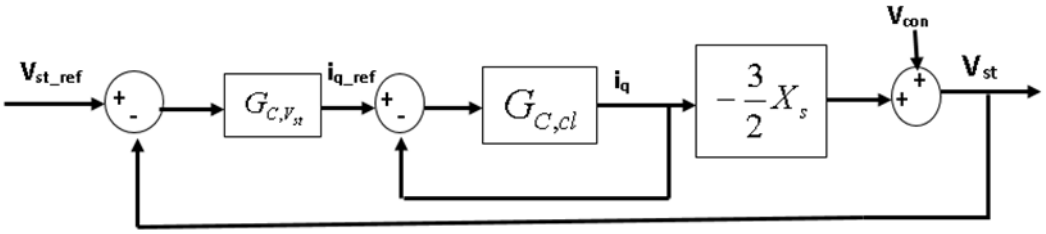

Figure 4. 10: Final stator voltage control loop

Therefore, the open-loop transfer function of the stator voltage controller is given by Eq. (4.44)

$$\begin{aligned} G_{v_{st},ol}(s) &= G_{C,v_{st}}(s) \times G_{C,cl}(s) \times \left(-\frac{3}{2} X_s + V_{con} \right) \\ G_{v_{st},ol}(s) &= -\frac{(3X_s + V_{con}) \times G_{C,v_{st}}(s) G_{C,c}(s)}{2[(sTa+1)(sL_{sq} + R_s) + G_{C,c}(s)]} \end{aligned} \tag{4.44}$$

The closed loop transfer function of the stator voltage controller is given by Eq. (4.45)

$$G_{v_{st},cl}(s) = \frac{(-3X_s + V_{con}) \times G_{C,v_{st}}(s) G_{C,c}(s)}{2[(sTa+1)(sL_{sq} + R_s) + G_{C,c}(s)] - (3X_s + V_{con}) \times G_{C,v_{st}}(s) G_{C,c}(s)} \tag{4.45}$$

4.2.4 Grid-side Converter Control

4.2.4.1 Inner Current Control Loop

The inner current control loop operates as follow:

The grid reference current from the outer controller loop(s) is compared to the output grid current. The current controllers force the reference current to track the output current to ensure a good and desirable system performance.

Figure 4.11 illustrates the block diagram of the inner current control loop.

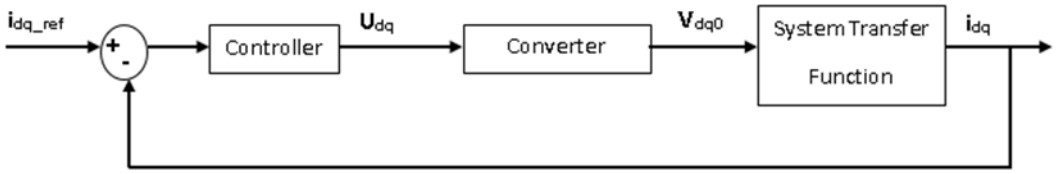

Figure 4. 11: Inner Current Control Loop for the grid-side converter

a) Controller block

The error from the comparator is fed into the controller block,

The output U_{dq} from the controller is equal to,

U_{dq}=error*controller's transfer function

Where;

$$\text{error} = i_{dq\_ref} - i_{dq} \tag{4.46}$$

Therefore, the output of the controller block is given by Eq. (4.47);

$$U_{dq} = (i_{dq\_ref} - i_{dq}) \times G_{c,i}(s) \tag{4.47}$$

Where $G_{c,i}(s)$ is the current controller's transfer function.

b) Converter block

A converter is usually considered as an ideal transformer with a time delay caused by the switching of the converter switches. The delay time is equal to half of the PWM converter's switching time. Therefore, the transfer function of the converter is given by Eq. (4.48) [38];

$$Y(s) = \frac{1}{T_a s + 1} \tag{4.48}$$

Where; $T_a = \frac{T_{switch}}{2} = \frac{1}{2 f_{switch}}$ is the time delay in seconds.

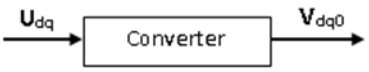

The output of the converter block, which serves as the input into the system transfer function block is given by Eq. (4.49)

$$v_{dq0} = U_{dq} \times \frac{1}{T_a s + 1}$$
$$V_{dq0} = (i_{dq\_ref} - i_{dq}) \times G_{c,i}(s) \times \frac{1}{T_a s + 1} \tag{4.49}$$

c) System transfer Function

The system's behaviour is governed by the fundamental frequency equations given in Eq. (4.6) that describes the AC-side dynamics of the converter [19, 86]. Rearranging Eq. (4.6) gives Eq. (4.50) representing the input to the system transfer function block.

$$V_{d0} = R_t i_d + L_t \frac{di_d}{dt} - \omega L_t i_q + V_{gd}$$
$$V_{q0} = R_t i_q + L_t \frac{di_q}{dt} + \omega L_t i_d + V_{gq} \tag{4.50}$$

In the *dq*-frame, the VSC acts as a nonlinear multiple-input-multiple-output system. The transformed equations of each axis have a speed or frequency induced term $\omega L_f i_q$ and $\omega L_f i_d$ for cross-coupling of the d-axis and the q-axis. To obtain a good control performance, it is required to de-couple the d- and q-axis. This is normally done by employing a dual-closed-loop direct current controller comprising of decoupled current compensation and voltage feed-forward compensation [33, 38]. The cross-coupling terms are removed as by changing Eq. (4.51) as follow,

$$U_d = (i_{d\_ref} - i_d) \times G_{c,i} - \omega L_t i_q + V_{gd}$$
$$U_q = (i_{q\_ref} - i_q) \times G_{c,i} + \omega L_t i_d + V_{gq} \tag{4.51}$$

Substituting Eq. (4.41) into Eq. (4.49) gives Eq. (4.52)

$$V_{d0} = (i_{d\_ref} - i_d) \times G_{c,i} - \omega L_t i_q + V_{gd} \times \frac{1}{T_a s + 1}$$
$$V_{q0} = (i_{q\_ref} - i_q) \times G_{c,i} + \omega L_t i_d + V_{gq} \times \frac{1}{T_a s + 1} \tag{4.52}$$

Equating Eq. (4.52) to Eq. (4.50) leads to the cancellation of the cross-coupling terms and hence giving the system's transfer function for both d- and q-axis as shown by Eq. (4.53)

$$V_{d0} = R_t i_d + L_t \frac{di_d}{dt}$$
$$V_{q0} = R_t i_q + L_t \frac{di_q}{dt} \tag{4.53}$$

Taking the Laplace transformation of Eq. (4.54) gives

$$V_{d0}(s) = R_t i_d(s) + sL_t i_d(s)$$
$$V_{q0}(s) = R_t i_q(s) + sL_t i_q(s) \tag{4.54}$$

Therefore, the system's transfer function is given by Eq. (4.55), relating the output current to the converter's output voltage.

$$\frac{i_d(s)}{V_{d0}(s)} = \frac{1}{sL_t + R_t}; \frac{i_q(s)}{V_{q0}(s)} = \frac{1}{sL_t + R_t} \tag{4.55}$$

It can be observed that the transfer functions for the d- and q-axis are the same. Figure 4.12 shows the complete block diagram of the inner current control loop.

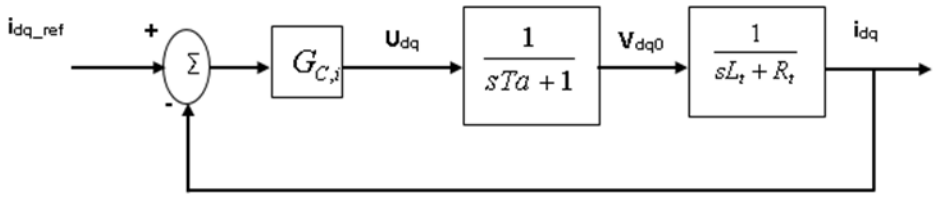

Figure 4. 12: Final Inner current controller loop

Therefore, the open-loop transfer function of the inner current controller is given by Eq. (4.56)

$$G_{C,ol}(s) = \frac{G_{C,i}(s)}{(sTa+1)(sL_t + R_t)} \tag{4.56}$$

The closed-loop transfer function is given by Eq. (4.57)

$$G_{C,cl}(s) = \frac{G_{C,i}(s)}{(sTa+1)(sL_t + R_t) + G_{C,i}(s)} \tag{4.57}$$

Figure 4.13 shows the detailed block diagram of the grid-side inner current control loops.

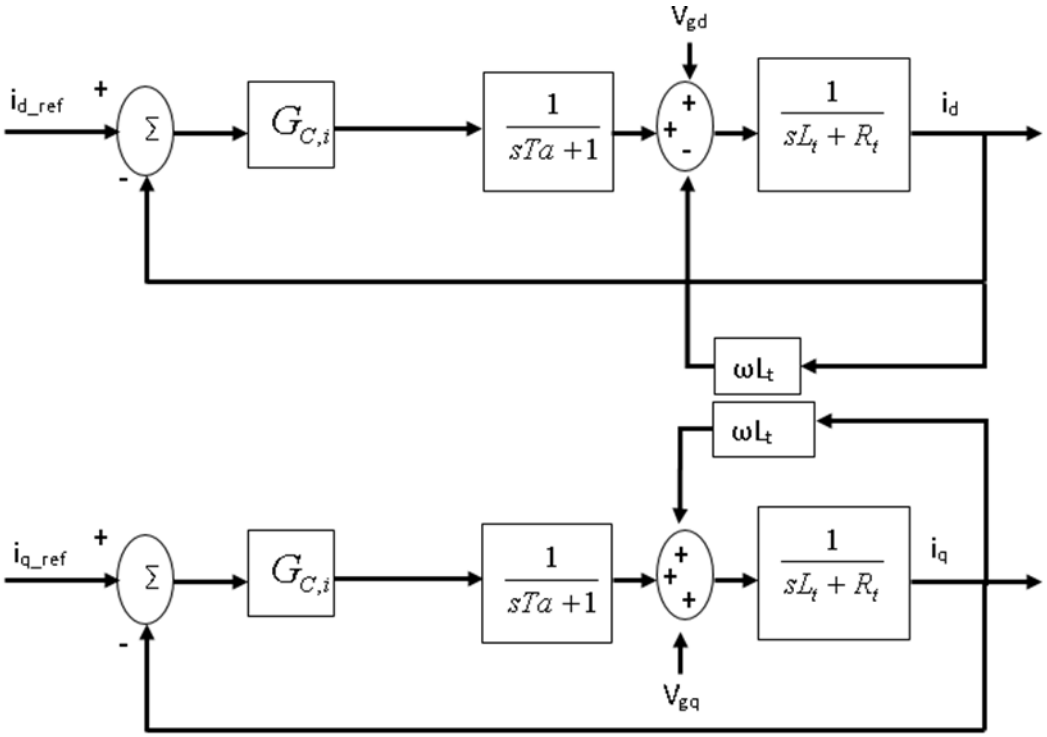

Figure 4. 13: Detailed Block diagram of the inner current control loops

4.2.4.2 Outer Control Loop(s): MPPT and Reactive Power Control

4.2.4.2(a) Active Power Control Loop/ MPPT control loop

A number of maximum power point tracking (MPPT) methods have been developed in the past decades as discussed in Chapter 2. In this study, the MPPT operation is achieved through the optimal relationship-based (ORB) control, whereby the measured rotor speed is used to track the optimal power from the wind turbine's maximum power curve relative to the change in wind speed [16, 57, 73].

a) MPPT Control stage

The maximum power extraction from the wind resource is achieved if the controller can properly track the optimal curve with variations in wind speed. The equation relating the optimal power to the optimal rotor speed can be recalled from Chapter 2 as given by Eq. (4.58) [16, 69, 70]:

$$P_{opt} = \frac{1}{2}\rho A C_{P_{opy}} \left(\frac{\omega_{r_{opy}} \times r}{\lambda_{opt}}\right)^3$$
$$P_{opt} = K_{opt}\omega_{r_{opt}}{}^3 \quad (4.58)$$

Where, K_{opt} is optimal power constant given by Eq. (4.59)

$$K_{opt} = \frac{1}{2}\rho A C_{P_{opt}} (\frac{r}{\lambda_{opt}})^3 \quad (4.59)$$

The output power from the MPPT stage serves as an input into the outer active power control loop. The active power control loop provides the d-axis current component to the inner current controller. Figure 4.14 shows the active power control loop.

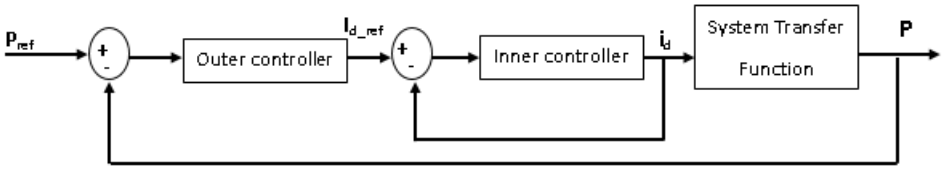

Figure 4. 14: Active Power Control Loop

b) Outer Controller block

The active power control loop operates as follow:

The reference active power is compared to the output active power. The error then serves as an input into the outer controller block. The output from the controller block is the reference current fed into the inner current control loop.

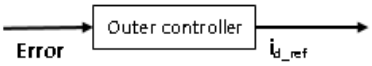

Therefore, the output of the outer control block is given by Eq. (4.60)

$$i_{d\_ref} = (P_{ref} - P) \times G_{c,p}(s) \quad (4.60)$$

Where $G_{c,p}(s)$ is the active power controller's transfer function.

c) Inner Current Controller block

The inner current controller block is simply represented by the closed-loop transfer function given by Eq. (4.57). The output of the inner current controller is the d-axis current component which is then fed into the system transfer function's block.

d) System Transfer Function

The system transfer function is derived from Eq. (4.8). Therefore, it is given by Eq. (4.61)

$$\frac{P}{i_d} = \frac{3}{2} V_{gd} \quad (4.61)$$

The complete control block for the active power control loop is as shown in Fig.4.15

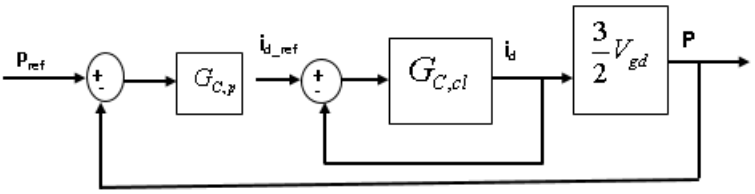

Figure 4. 15: Final active power control loop

The open-loop transfer function of the active power control loop is given by Eq. (4.62)

$$G_{P,ol}(s) = G_{C,p}(s) \times G_{C,cl}(s) \times \frac{3}{2} V_{gd} \tag{4.62}$$

The closed-loop transfer function of the active power control loop is given by Eq. (4.63)

$$G_{P,cl}(s) = \frac{G_{C,p}(s) \times G_{C,cl}(s) \times \frac{3}{2} V_{gd}}{1 + G_{C,p}(s) \times G_{C,cl}(s) \times \frac{3}{2} V_{gd}} = \frac{3V_{gd} G_{C,p}(s) G_{C,cl}(s)}{3V_{gd} G_{C,p}(s) G_{C,cl}(s) + 2} \tag{4.63}$$

4.2.4.2(b) Reactive Power Control Loop

The reactive power control loop provides the q-component of the grid reference current to the inner current control loop. The reference for the reactive power is usually set to zero to ensure unity power factor. Figure 4.16 shows the reactive power control loop.

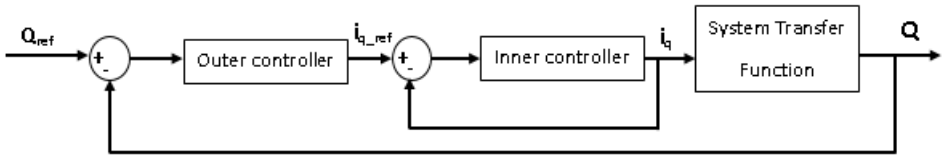

Figure 4. 16: Reactive Power Control Loop

a) Outer controller block

The reactive power control loop operates as follow: the reference reactive power is compared to the measured reactive power. The error then serves as an input into the outer controller block. The output from the controller block is the reference current fed into the inner current control loop.

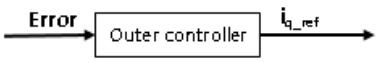

Therefore, the output of the outer controller block is given by Eq. (4.64)

$$i_{q\_ref} = (Q_{ref} - Q) \times G_{c,q}(s) \tag{4.64}$$

Where $G_{c,q}(s)$ is the reactive power controller's transfer function.

b) Inner controller block

The inner current controller block is simply represented by the closed-loop transfer function given by Eq. (4.57). The output of the inner current controller is the q-axis current component which is then fed into the system transfer function's block.

c) System Transfer Function

The system transfer function is derived from Eq. (4.8). Therefore, it is given by Eq. (4.65)

$$\frac{Q}{i_q} = -\frac{3}{2}V_{gd} \tag{4.65}$$

The complete control block for the active power controller is as shown in Fig.4.17

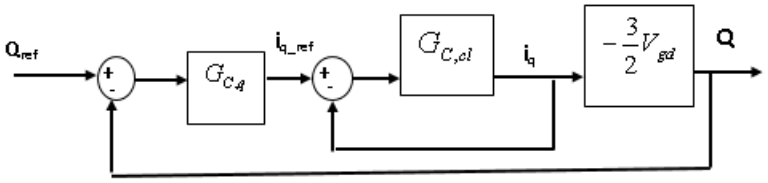

Figure 4. 17: Final Reactive Power Control Loop

The open-loop transfer function for the reactive power control loop is given by Eq. (4.66)

$$G_{Q,ol}(s) = -G_{C,q}(s) \times G_{C,cl}(s) \times \frac{3}{2}V_{gd} \tag{4.66}$$

The closed-loop transfer function of the reactive power control loop is given by Eq. (4.67)

$$G_{Q,cl}(s) = \frac{-G_{C,q}(s) \times G_{C,cl}(s) \times \frac{3}{2}V_{gd}}{1 + (-G_{C,q}(s) \times G_{C,cl}(s) \times \frac{3}{2}V_{gd})} = -\frac{3V_{gd}G_{C,q}G_{C,cl}}{3V_{gd}G_{C,q}G_{C,cl} + 2} \tag{4.67}$$

4.3 Pitch-Angle Controller

The pitch-angle controller is employed to prevent over-speeding of the wind turbine during high wind speeds [16, 101]. Figure 4.18 illustrates the block diagram of the pitch-angle controller.

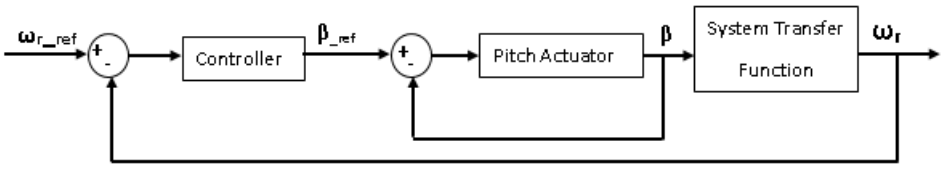

Figure 4. 18: Pitch Angle Control Loop

a) Controller block

The pitch-angle controller operates as follow: the reference rotor angular speed is compared to the measured rotor speed. The error is then sent to the controller block to generate the reference pitch-angle. The reference-pitch angle is then compared to the desired pitch angle and the error serves as an input into the pitch actuator block. The output from the controller block is given by Eq. (4.68);

$$\beta_{ref} = (\omega_{r\_ref} - \omega_r) \times G_{pitch} \tag{4.68}$$

Where G_{pitch} is the pitch angle controller's transfer function.

b) Pitch Actuator block

The pitch actuator is the mechanical/hydraulic system that turns the blades out of the wind. Figure 4.19 shows the pitch actuator block diagram.

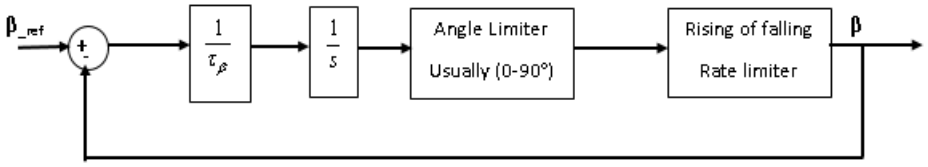

Figure 4. 19: Pitch Actuator model

From Fig. 4.19, $1/\tau_\beta$ represents the ―softness coefficient‖ that is responsible for smoothing the control process when the pitch angle limit is approaching [77].

$$G_{actuator,ol}(s) = \frac{1}{\tau_\beta s} \tag{4.69}$$

The closed-loop transfer function of the actuator system is given by Eq. (4.70)

$$G_{actuator,cl}(s) = \frac{\frac{1}{\tau_\beta s}}{1 + \frac{1}{\tau_\beta s}} = \frac{1}{\tau_\beta s + 1} \tag{4.70}$$

Where: τ_β is the time constant of the actuator system.

c) System Transfer Function

The system transfer function block represents the aerodynamic and mechanical system of the wind turbine system. Therefore, is it governed by the swing equation given by Eq. (2.11), which can be rearranged to make the rotor speed as a subject as shown by Eq. (4. 71)

$$J_{eq}\frac{d\omega_r}{dt}+B_{eq}\omega_r=T_m-T_e \tag{4.71}$$

Taking the Laplace transform of Eq. (4.71) gives Eq. (4.72) representing the system transfer function.

$$\begin{aligned}\omega_r(J_{eq}s+B_{eq})&=T_m-T_e\\ \omega_r&=\frac{T_m-T_e}{J_{eq}s+B_{eq}}\end{aligned} \tag{4.72}$$

Figure 4.20 shows the complete block diagram of the pitch-angle controller.

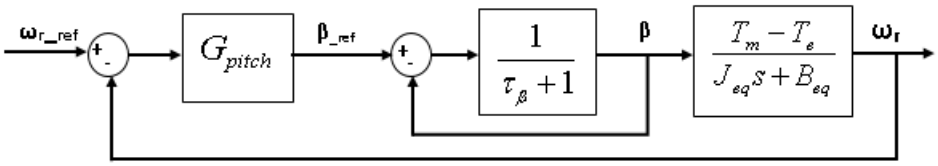

Figure 4. 20: Complete block diagram of the pitch-angle controller

Therefore, the open-loop transfer function of the pitch-angle controller is given by Eq. (4.73)

$$G_{pitch\_cont,ol}(s)=G_{pitch}(s)\times\frac{1}{\tau_\beta s+1}\times\frac{T_m-T_e}{J_{eq}s+B_{eq}}=\frac{G_{pitch}(s)(T_m-T_e)}{(\tau_\beta s+1)(J_{eq}s+B_{eq})} \tag{4.73}$$

The closed-loop transfer function is given by Eq. (4.74)

$$G_{pitch\_cont,cl}(s)=\frac{\dfrac{G_{pitch}(s)(T_m-T_e)}{(\tau_\beta s+1)(J_{eq}s+B_{eq})}}{1+\dfrac{G_{pitch}(s)(T_m-T_e)}{(\tau_\beta s+1)(J_{eq}s+B_{eq})}}=\frac{G_{pitch}(s)(T_m-T_e)}{(\tau_\beta s+1)(J_{eq}s+B_{eq})+G_{pitch}(T_m-T_e)} \tag{4.74}$$

4.4 Chapter Summary

This chapter dealt with the derivation of the open-loop and closed-transfer functions for the pitch-angle controller as well as the grid-side and generator-side converter's controllers. The derived transfer functions are summarized in Table 4.1

Table 4. 1: Derived open-loop and closed-loop transfer functions of the pitch-angle, generator-side converter and grid-side converter controllers

Type of Control Loop	Generator-side Converter Controller's Transfer Functions	Grid-side Converter Controller's Transfer Functions
Inner Current Loop	***Open Loop*** $$G_{C,ol}(s)=\frac{G_{C,i}(s)}{(sTa+1)(sL_{sdq}+R_s)}$$	***Open Loop*** $$G_{C,ol}(s)=\frac{G_{C,i}(s)}{(sTa+1)(sL_t+R_t)}$$
	Closed Loop $$G_{C,cl}(s)=\frac{G_{C,i}(s)}{(sTa+1)(sL_{sdq}+R_s)+G_{C,i}(s)}$$	***Closed Loop*** $$G_{C,cl}(s)=\frac{G_{C,i}(s)}{(sTa+1)(sL_t+R_t)+G_{C,i}(s)}$$
Outer Loop	***DC-link Voltage controller***	***MPPT controller***
	Open Loop $$G_{v,ol}(s)=\frac{3V_{sd0}G_{C,v}(s)G_{C,c}(s)}{2V_{dc\_ref}Cs[(sTa+1)(sL_{sd}+R_s)+G_{C,c}(s)]}$$	***Open Loop*** $$G_{P,ol}(s)=G_{C,p}(s)\times G_{C,cl}(s)\times\frac{3}{2}V_{gd}$$
	Closed Loop $$G_{v,cl}(s)=\frac{3V_{sd0}G_{C,v}(s)G_{C,c}(s)}{2V_{dc\_ref}Cs[(sTa+1)(sL_{sd}+R_s)+G_{C,c}(s)]+3V_{sd0}G_{C,v}(s)G_{C,c}(s)}$$	***Closed Loop*** $$G_{P,cl}(s)=\frac{3V_{gd}G_{C,p}(s)G_{C,cl}(s)}{3V_{gd}G_{C,p}(s)G_{C,cl}(s)+2}$$
	Stator Voltage Controller	***Reactive Power Controller***
	Open Loop $$G_{v_{st},ol}(s)=-\frac{(3X_s+V_{con})\times G_{C,v_{st}}(s)G_{C,c}(s)}{2[(sTa+1)(sL_{sq}+R_s)+G_{C,c}(s)]}$$	***Open Loop*** $$G_{Q,ol}(s)=-G_{C,q}(s)\times G_{C,cl}(s)\times\frac{3}{2}V_{gd}$$

	Closed Loop $G_{v_{st},cl}(s) = \frac{(-3X_s + V_{con}) \times G_{C,v_{st}}(s) G_{C,c}(s)}{2[(sTa+1)(sL_{sq} + R_s) + G_{C,c}(s)] - (3X_s + V_{con}) \times G_{C,v_{st}}(s) G_{C,c}(s)}$	***Closed Loop*** $G_{Q,cl}(s) = -\frac{3V_{gd} G_{C,q} G_{C,cl}}{3V_{gd} G_{C,q} G_{C,cl} + 2}$
Pitch Angle Controller		
Open Loop TF	$G_{pitch\_cont,ol}(s) = G_{pitch}(s) \times \frac{1}{\tau_\beta s + 1} \times \frac{T_m - T_e}{J_{eq} s + B_{eq}} = \frac{G_{pitch}(s)(T_m - T_e)}{(\tau_\beta s + 1)(J_{eq} s + B_{eq})}$	
Closed Loop TF	$G_{pitch\_cont,cl}(s) = \frac{G_{pitch}(s)(T_m - T_e)}{(\tau_\beta s + 1)(J_{eq} s + B_{eq}) + G_{pitch}(T_m - T_e)}$	
3-level NPC VSC AC-side and DC-side Dynamics		
AC-side	$\frac{di_d}{dt} = \frac{V_{d0} - V_{dg} - R_t i_d + \omega L_t i_q}{L_t}$ $\frac{di_q}{dt} = \frac{V_{q0} - V_{qg} - R_t i_q - \omega L_t i_d}{L_t}$	
DC-side	$\frac{dV_{dc}}{dt} = \frac{I_{dc} - I_L}{C_{equiv}}$	

The derived open-loop and closed-loop transfer functions will be employed in the subsequent chapters (5 and 6) to analyze the initial performance of the proposed wind energy conversion system. The respective controllers will then be modeled to be incorporated into the system to improve its initial performance in order to achieve the desired specifications thereby improving the performance of the proposed system.

CHAPTER 5: GENERATOR-SIDE CONVERTER CONTROL SYSTEM MODELING AND STABILITY ANALYSIS

This chapter outlines the design specifications that are to be achieved in this study, namely: bandwidth, phase margin, percentage overshoot, settling time and rise time. Furthermore, the chapter covers the design and stability analysis of the pitch-angle controller and generator-side converter controller using bode plots and step response curves in MATLAB software package.

5.1 Design Specifications

In large transient situations, the non-linear systems can reduce the system's loop gain and lead to system instability. Having additional phase- and gain- margin increases the stability-margin of the system. To prevent the ripple associated with the PWM from affecting the controller's performance, it is recommended that the controller's bandwidth should be less than or equal to one-fourth of PWM converter's switching frequency. The inner current control loop is required to have a shorter response time compared to the outer control loop to have a fast control system for the complete system.

In this study, the PWM converter is rated at 3MVA, equal to the rating of the wind turbine, and the terminal line-to-line output voltage is 620.62V as calculated in Chapter 3. The choice of the PWM converter's switching frequency mainly depends on the switches' blocking voltage (collector-emitter voltage) and current carrying capacity. According to [102, 103], the IGBTs are preferred over MOSFETs for blocking voltages above 250V. Furthermore, IGBTs have been the preferred devices under the following conditions:

- Low duty cycle
- Low frequencies (less than 20kHz for motor drive/control)
- High-voltage applications (>1000V)
- Operating at high output powers (>5kW)

The typical switching frequency for multi-megawatt VSCs ranges from 1kHz to 2kHz [15, 36, 104]. Therefore, in this study, the switching frequency is taken to be 2kHz. Therefore, the bandwidth of the inner current control loop is taken to be one-fourth of the PWM converter's switching frequency.

$$f_{inner\_Loop} = \frac{1}{4} \times 2000Hz = 500Hz$$

$$\omega_{BW\_inner\_loop} = 2\pi f_{inner\_Loop} = 2 \times \pi \times 500 = 3141.59 rad/s$$

The natural frequency of a system refers to the frequency of the oscillations of an undamped system. The bandwidth is related to the natural frequency by Eq. (5.1)[88, 89].

$$\omega_{BW} = \omega_n \sqrt{(1-2\zeta^2) + \sqrt{\zeta^4 - 4\zeta^2 + 2}} \tag{5.1}$$

Where; ζ is the damping ratio which is the ratio of the exponential decay frequency of the system to the natural frequency ω_n. The damping ratio remains constant regardless of the time scale of the response.

Settling time refers to the time required for the transient's damped oscillations to reach and stay within ±2% of its final/steady-state value. It is related to the natural frequency ω_n and damping ratio ζ by Eq. (5.2)[88, 89]

$$\omega_n = \frac{4}{T_s \zeta} \tag{5.2}$$

Peak time refers to the time required for the damped oscillation to reach the maximum peak. It is related to the natural frequency and damping ratio by Eq. (5.3) [88, 89]

$$T_p = \frac{\pi}{\omega_n \sqrt{1-\zeta^2}} \tag{5.3}$$

Rise time refers to the time required for the waveform to rise from 0.1 to 0.9 of the final value. It is related to the natural frequency and damping ratio by Eq. (5.4) [88, 89]

$$T_r = \frac{1.76\zeta^3 - 0.417\zeta^2 + 1.039\zeta + 1}{\omega_n} \tag{5.4}$$

Percentage overshoot refers to the amount that the waveform overshoots the steady-state value at peak time. It is related to the damping ratio ζ by Eq. (5.5)[89]

$$os = e^{-\pi\zeta / \sqrt{1-\zeta^2}} \tag{5.5}$$

The phase margin is related to the damping ratio by Eq. (5.6)

$$PM = \tan^{-1}\left(\frac{2\zeta}{\sqrt{\sqrt{1+4\zeta^2} - 2\zeta^2}} \right) \tag{5.6}$$

The phase margin is linearly related to the damping ratio. That is, the higher the phase margin, the greater the damping ratio.

5.1.1 Inner Current Control Loop

- Overshoot of 5%; since the inner loop is fast, the systems can recover from the overshoot faster. Moreover, IGBTs have no overload capacity, hence, the percentage overshoot needs to be as small as possible.

Therefore the damping ratio is calculated as follow

$$0.05 = e^{-\pi\zeta/\sqrt{1-\zeta^2}}$$

$$\zeta_{inner\_Loop} = \sqrt{\frac{\ln(0.05)^2}{\pi^2 + \ln(0.05)^2}} = 0.69$$

The phase margin corresponding to damping ratio is equal to,

$$PM_{inner\_Loop} = \tan^{-1}\left(\frac{2(0.69)}{\sqrt{\sqrt{1+4(0.69)^2} - 2(0.69)^2}}\right) = 57.85^o$$

Therefore, the natural frequency of the system corresponding to the specified bandwidth and damping ratio is calculated as follow,

$$\omega_{n\_inner\_Loop} = \frac{\omega_{BW_{inner\_Loop}}}{\sqrt{(1-2\zeta_{inner\_Loop}{}^2) + \sqrt{\zeta_{inner\_Loop}{}^4 - 4\zeta_{inner\_Loop}{}^2 + 2}}}$$

$$\omega_{n\_inner\_Loop} = \frac{3141.59}{\sqrt{(1-2(0.69)^2) + \sqrt{(0.69)^4 - 4(0.69)^2 + 2}}} = 4004.42 rad/s$$

The settling time corresponding to the system's natural frequency and damping ratio is calculated as follow,

$$T_{s\_inner\_Loop} = \frac{4}{\omega_{n\_inner\_Loop} \times \zeta_{inner\_Loop}} = \frac{4}{0.69 \times 4004.42} = 1.45ms$$

The peak time corresponding to the system's natural frequency and damping ratio is calculated as follow

$$T_{p\_inner\_Loop} = \frac{\pi}{4004.42\sqrt{1-0.69^2}} = 1.08ms$$

The rise time corresponding to the peak time is calculated as follow,

$$T_{r\_inner\_Loop} = \frac{1.76(0.69)^3 - 0.417(0.69)^2 + 1.039(0.69) + 1}{4004.42} = 0.52ms$$

5.1.2 Outer Control Loop

The outer control loops are expected to be slower than the inner current control loops. The bandwidth of the outer control loops is taken to be one-fourth of the inner current control loops' switching frequency. Therefore,

$$f_{outer\_L} = \frac{1}{4} \times 500Hz = 125Hz$$
$$\omega_{BW\_outer} = 2\pi f_{outer\_L} = 2 \times \pi \times 125 = 785.40 rad/s$$

- Overshoot of 5%; the slower outer loop needs to have a smaller overshoot as compared to the fast inner current controllers loop to get rid of as many oscillations in the controller as possible to enhance the stability of the entire system.

Therefore the damping ratio is calculated as follow

$$0.05 = e^{-\pi\zeta/\sqrt{1-\zeta^2}}$$
$$\zeta_{outer\_Loop} = \sqrt{\frac{\ln(0.05)^2}{\pi^2 + \ln(0.05)^2}} = 0.69$$

The phase margin corresponding to damping ratio is calculated as follow

$$PM_{outer\_Loop} = \tan^{-1}\left(\frac{2(0.69)}{\sqrt{\sqrt{1+4(0.69)^2} - 2(0.69)^2}}\right) = 57.85^o$$

Therefore, the natural frequency of the system corresponding to the specified bandwidth and damping ratio is equal to,

$$\omega_{n\_outer\_Loop} = \frac{\omega_{BW_{outer\_Loop}}}{\sqrt{(1-2\zeta_{outer\_Loop}{}^2) + \sqrt{\zeta_{outer\_Loop}{}^4 - 4\zeta_{outer\_Loop}{}^2 + 2}}}$$
$$\omega_{n\_outer\_Loop} = \frac{785.40}{\sqrt{(1-2(0.69)^2) + \sqrt{(0.69)^4 - 4(0.69)^2 + 2}}} = 1001.11 rad/s$$

The settling time corresponding to the system's natural frequency and damping ratio is equal to,

$$T_{s\_outer\_Loop} = \frac{4}{\omega_{n\_outer\_Loop} \times \zeta_{outer\_Loop}} = \frac{4}{0.69 \times 1001.11} = 5.79ms$$

The peak time corresponding to the system's natural frequency and damping ratio is equal to,

$$T_{p\_outer\_Loop} = \frac{\pi}{1001.11\sqrt{1-0.69^2}} = 4.34ms$$

The rise time corresponding to the peak time is equal to,

$$T_{r\_outer\_Loop} = \frac{1.76(0.69)^3 - 0.417(0.69)^2 + 1.039(0.69) + 1}{1001.11} = 2.09ms$$

To satisfy these design specifications, the performance of the systems' open-loop transfer functions will be analyzed using bode plots and step response curves. This will be done before and after the compensators have been applied to the uncompensated systems.

5.2 Generator-side Converter Controller's Stability Analysis

5.2.1 Inner Current Control Loop

The design specifications to be met by the compensators in the inner current controller are:

- A bandwidth of 3141.59 rad/s (500Hz)
- Overshoot of 5% resulting in a damping ratio of 0.69
- A phase margin of 57.85˚
- A gain margin of 0dB at the desired bandwidth
- A settling time of 1.45ms
- A rise time of 0.52ms

5.2.1.1 The uncompensated system

The open-loop transfer function of the uncompensated system is represented by Eq. (4.25). The bode plot used for the system's stability analyses is plotted using Eq. (5.7) by substituting the delay time, the synchronous inductance and stator winding resistance given in Table 3.2. As indicated in Chapter 4, the delay time is equal to half of the PWM converter's switching time. In this study, the switching frequency is 2 kHz, and hence the delay time is calculated as follow:

$$T_a = \frac{T_{switch}}{2} = \frac{1}{2f_{switch}} = \frac{1}{2 \times 2000} = 0.25ms$$

Therefore, the open-loop transfer function is given by Eq. (5.7) with T_a=0.25ms, L_{sd}=L_{sq}=1.5731mH, and R_s=0.821mΩ

$$G_{I_{,OL}\_uncompen}(s) = \frac{G_{C,i}(s)}{(T_a s + 1)(sL_{sdq} + R_s)} = \frac{G_{C,i}(s)}{(0.25 \times 10^{-3} s + 1)(1.573 \times 10^{-3} s + 0.821 \times 10^{-3})} \quad (5.7)$$

$$G_{I_{,OL}\_uncompen}(s) = \frac{G_{C,i}(s)}{3.93 \times 10^{-7} s^2 + 1.573 \times 10^{-3} s + 0.821 \times 10^{-3}}$$

Figure 5.1 shows the bode plot of the inner current control loop without a compensator, that is $G_{C,i}(s)$=1.

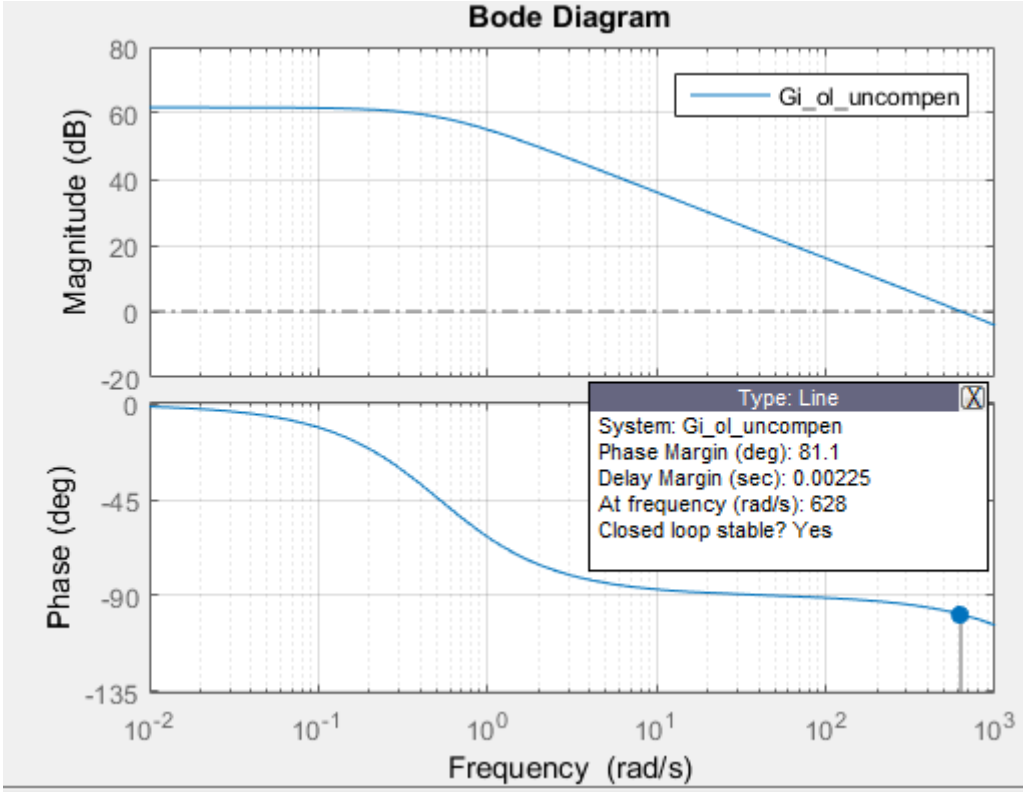

Figure 5. 1: Bode plot of the uncompensated inner current controller open-loop transfer function

Figure 5. 1 indicates that the phase margin and bandwidth frequency of the uncompensated system are 81.1˚ and 628 rad/s, respectively. The bandwidth frequency is too low as compared to the desired value of 3141.59 rad/s (500Hz) and hence the system response will be too slow. Furthermore, the phase margin is too high and much closer to 90˚. A phase margin equal to or greater than 90˚ reduces the system's response time.

To obtain the desired bandwidth, the system's open-loop transfer function needs to be multiplied by a gain *K* to raise the magnitude curve up. The gain is determined in such a way that the magnitude curve crosses the 0dB line at the desired bandwidth. The gain is computed as follow

$$\left|G_{I_{OL}\_uncompen}(j)\right| = \frac{K}{3.93\times10^{-7}\,j^2 + 1.573\times10^{-3}\,j + 0.821\times10^{-3}}$$

$$3141.59 = \frac{K}{(3.93\times10^{-7}\,j^2 + 1.573\times10^{-3}\,j + 0.821\times10^{-3})}$$

$$K = 3141.59(-3.93\times10^{-7} + 1.573\times10^{-3}\,j + 0.821\times10^{-3})$$

$$K = 3141.59(\sqrt{(8.2\times10^{-4})^2 + (1.573\times10^{-3})^2}$$

$$K = 6.27$$

Multiplying Eq. (5.7) with the gain *K* gives Eq. (5.8) which is used for plotting the bode plot of the gain-compensated transfer function.

$$G_{I_{,OL}\_compen\_gain}(s) = \frac{6.27}{3.93\times10^{-7}s^2 + 1.573\times10^{-3}s + 0.821\times10^{-3}} \tag{5.8}$$

Figure 5.2 illustrates the magnitude and phase of the gain-compensated open-loop transfer function of the inner current control loop. It can be seen that the magnitude curve crosses the 0dB line at the desired bandwidth.

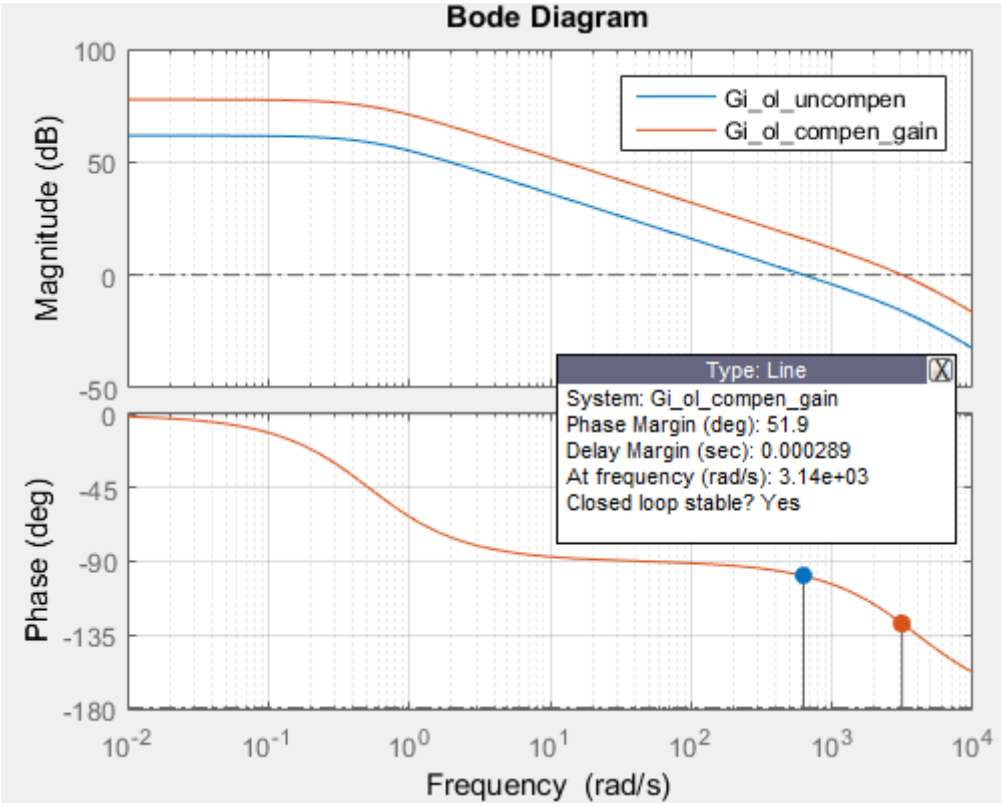

Figure 5. 2: Bode plot of the gain-compensated open-loop transfer function of the inner current controller

The phase margin at the desired bandwidth frequency is 51.9˚. To obtain the desired phase margin of 57.85˚, a phase-lead compensator is needed to shift the phase curve up.

5.2.1.2 Phase-lead compensator design

The phase-lead compensator is used to shift the phase curve up. This alternatively boosts the current phase margin to the desired value at the specified bandwidth. Therefore, the first step is to compute the phase-boost needed to obtain the desired phase margin. This is done by subtracting the phase margin of the current system from the desired phase margin as follow [92],

Phase-boost=$PM_{desired}$-$PM_{current}$

Phase-boost= 57.85°-51.9°=5.95°

The phase-boost needed is used to locate the pole p_c and zero z_c of the phase-lead compensator by calculating the frequency [Hz] where the pole and zero will be located using Eq. (5.9) [92]

$$f_z = f_{BW}\sqrt{\frac{1-\sin(phase-boost)}{1+\sin(phase-boost)}}$$
$$f_p = f_{BW}\sqrt{\frac{1+\sin(phase-boost)}{1-\sin(phase-boost)}} \quad (5.9)$$

Where f_{BW} is the bandwidth frequency, which in this study is equal to 500Hz. Therefore, f_p and f_z are calculated as follow

$$f_z = 500\sqrt{\frac{1-\sin(5.95^o)}{1+\sin(5.95^o)}} = 450.60Hz$$
$$f_p = 500\sqrt{\frac{1+\sin(5.95^o)}{1-\sin(5.95^o)}} = 554.82Hz$$

The angular frequencies where the pole and zero of the phase-lead compensator are located are calculated as follow

$$\omega_z = 2\pi \times 450.60Hz = 2831.20rad/s$$
$$\omega_p = 2\pi \times 554.82Hz = 3486.04rad/s$$

Therefore, the transfer function of the phase-lead compensator is given by Eq. (5.10)

$$G_{lead}(s) = G_{co}\left(\frac{\tau_{lead}s+1}{\alpha\tau_{lead}s+1}\right) = \frac{31.83\times10^{-5}s+0.901}{28.69\times10^{-5}s+1}$$
$$where;$$
$$\alpha = \omega_z/\omega_p = 2831.20/3486.04 = 0.812 \quad (5.10)$$
$$G_{co} = \sqrt{\alpha} = \sqrt{0.812} = 0.901$$
$$\tau_{lead} = 1/\omega_z = 1/2831.20 = 0.035\times10^{-3}$$

The phase-lead compensator is applied to the gain-compensated system, and hence, multiplying Eq. (5.8) by Eq. (5.10) gives Eq. (5.11) which represents the transfer function of the phase-lead compensated system for the inner current control loop.

$$G_{I_{,OL}\_compen\_lead}(s) = G_{I_{,OL}\_compen\_gain}(s)\times G_{lead}(s)$$
$$G_{I_{,OL}\_compen\_lead}(s) = \frac{1.99\times10^{-3}s+5.65}{1.13\times10^{-10}s^3+8.45\times10^{-7}s^2+1.57\times10^{-3}s+0.821\times10^{-3}} \quad (5.11)$$

Figure 5.3 illustrates the magnitude and phase curves of the phase-lead compensated open-loop transfer function of the inner current control loop.

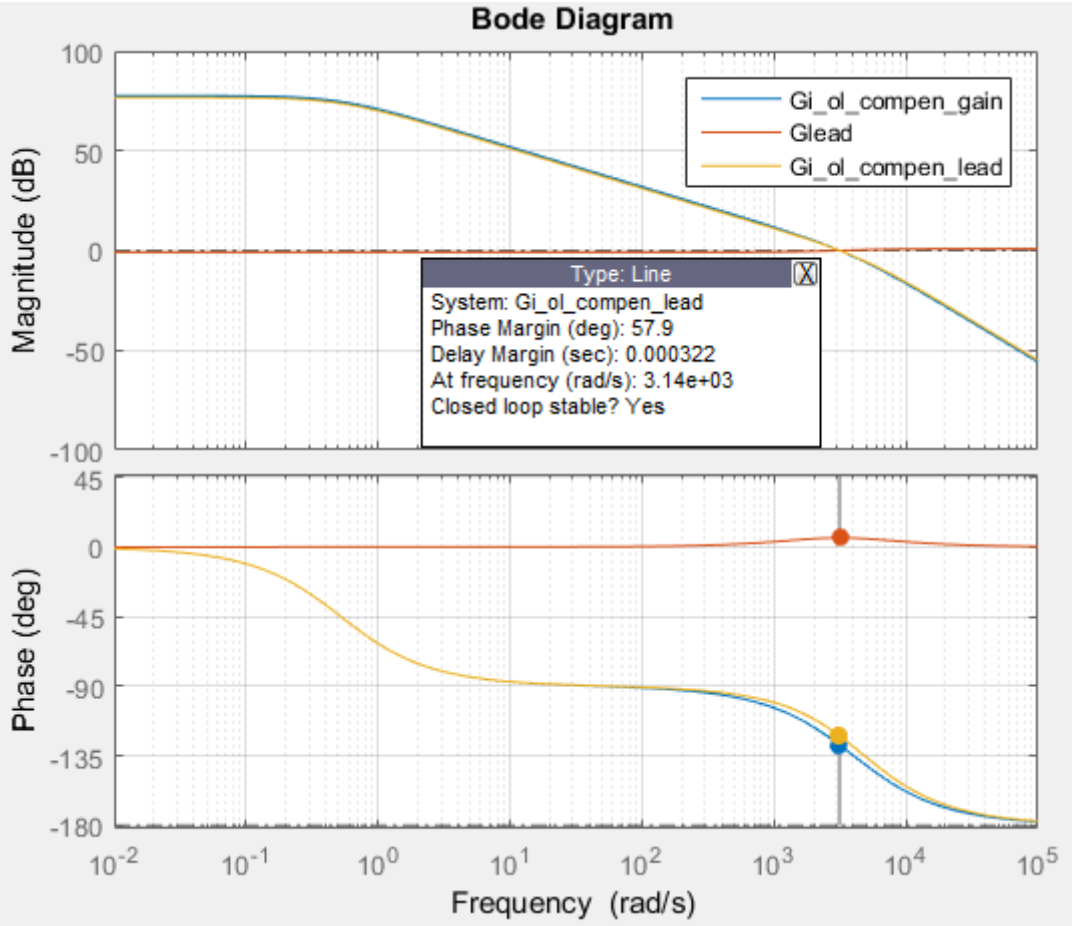

Figure 5. 3: Bode plot of the phase-lead compensated inner stator current controller's open-loop transfer function

It is observed that the phase-lead compensator shifted the phase curve up to yield the phase-margin of 57.9°. The bandwidth is maintained at 3141.59 rad/s (500Hz). Therefore, the phase-margin and bandwidth design specifications have been met.

Figure 5.4 shows the step response curve indicating the peak response of the uncompensated, gain-compensated and phase-lead compensated closed-loop transfer function of the inner stator current control loop.

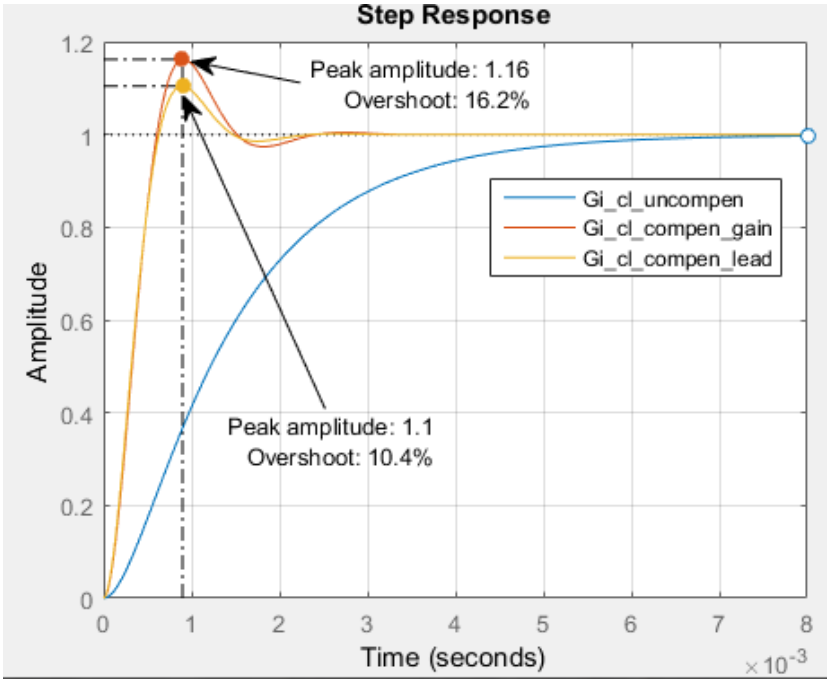

Figure 5. 4: Peak-response of the uncompensated, gain-compensated and phase-lead compensated transfer functions

It can be observed that the overshoot of the gain-compensated system is 16.2%, while the phase-lead compensator reduces it further to 10.4%. Figure 5.5 shows the step response curve indicating the settling time of the uncompensated, gain-compensated and phase-lead compensated closed-loop transfer functions of the inner stator current control loop.

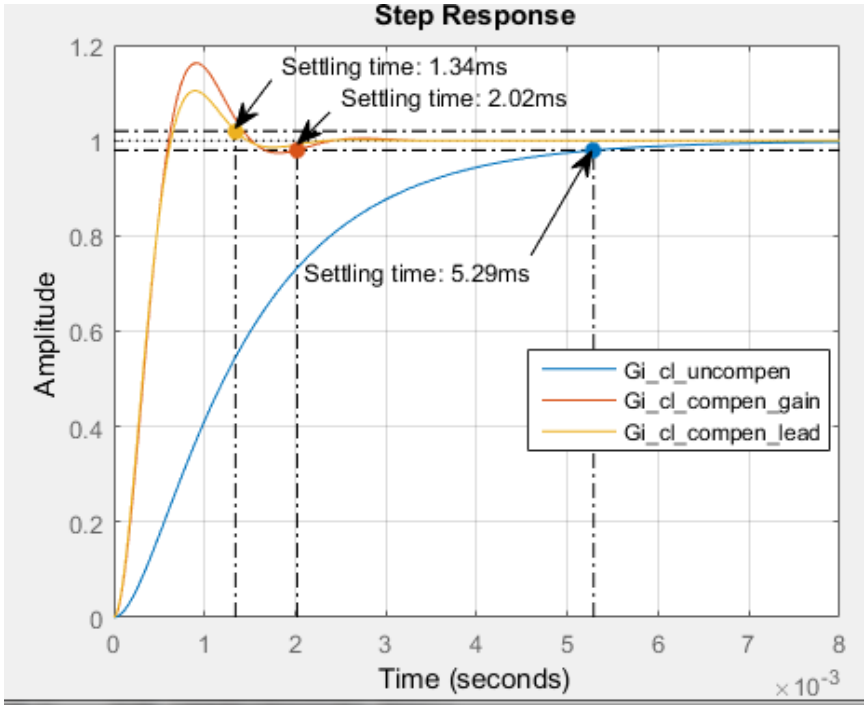

Figure 5. 5: Settling time of the uncompensated, gain-compensated and phase-lead compensated transfer functions

It can be observed that gain *K* reduced the settling time of the uncompensated system from 5.29ms to 2.02ms. The phase-lead compensator further reduced the settling time of the gain-compensated system to 1.34ms which is still within the desired settling time of 1.45ms. This illustrates that the settling time design specification has been met.

Figure 5.6 shows the step response curve indicating the rise time of the uncompensated, gain-compensated and phase-lead compensated closed-loop transfer functions of the inner stator current control loop.

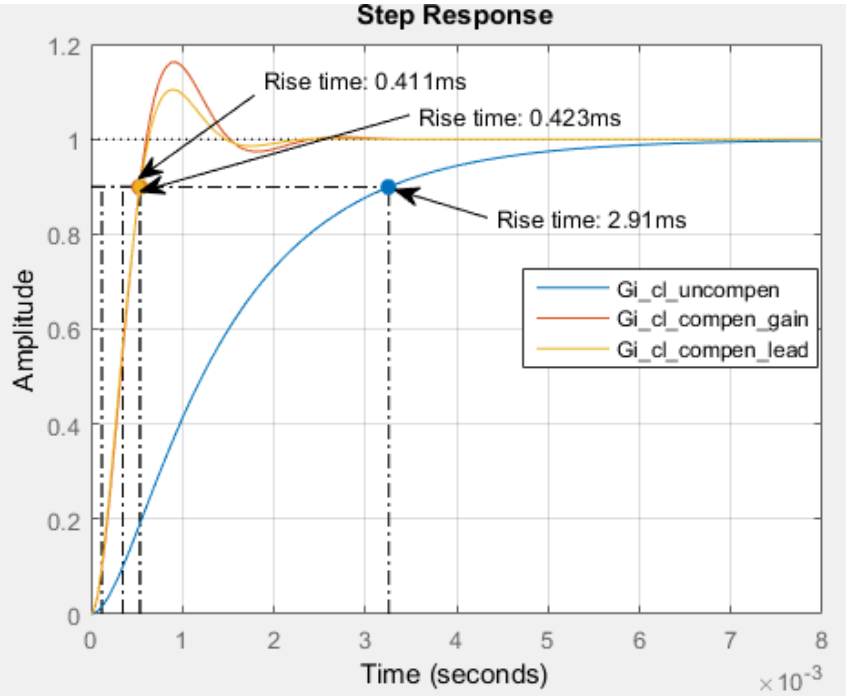

Figure 5. 6: Rise time of the uncompensated, gain- compensated and phase-lead compensated transfer functions

It can be observed that gain *K* reduced the rise-time of the uncompensated system from 2.91ms to 0.411ms and hence speeding up the system response. However, the phase-lag compensator increased the gain-compensated system's rise time to 0.423ms which is within the desired rise time of 0.52ms. This illustrates that the rise time design specification has been met.

5.2.2 Outer Control Loops

The design specifications to be met by the compensators in the outer loop controller are:

- A bandwidth of 785.40 rad/s (125Hz)
- Overshoot of 5% resulting in a damping ratio of 0.69
- A phase margin of 57.85˚
- A gain margin of 0dB at the desired bandwidth/crossover frequency
- A settling time of 5.79ms
- A rise time of 2.09ms

5.2.2.1 DC-link Voltage Controller

5.2.2.1(a) The uncompensated system

The DC-link voltage controller loop's open-loop transfer function is given by Eq. (4.39). Substituting in the given values: the d-component of the stator voltage of 690V (equal to the rated stator line-to-line voltage), the reference DC-link voltage of 1126.77V, and the rated DC-link capacitance of 23.63mF, gives Eq. (5.12)

$$G_{V_{dc,OL}\_uncompen}(s) = \frac{3 \times V_{sd0} \times G_{C,v}(s) \times G_{I_{,CL}\_compen\_lead}(s)}{2V_{dc\_ref} Cs} = \frac{2070 G_{C,v}(s) G_{C,cl}(s)}{53.25s} \quad (5.12)$$

Where, $G_{I,cl\_compen\_lead}(s)$ is the closed-loop transfer function of the phase-lead compensated inner stator current loop given by Eq. (5.13).

$$G_{I_{,CL}\_compen\_lead}(s) = \frac{1.97 \times 10^{-3} s + 5.65}{1.13 \times 10^{-10} s^3 + 8.45 \times 10^{-7} s^2 + 3.57 \times 10^{-3} s + 5.65} \quad (5.13)$$

Therefore, substituting Eq. (5.13) into Eq. (5.12) gives Eq. (5.14) which is used to plot the bode plot of the uncompensated outer DC-link voltage loop.

$$G_{Vdc_{,OL}\_uncompen}(s) = \frac{(4.13s + 1.17 \times 10^4) \times G_{C,v}(s)}{6.01 \times 10^{-9} s^4 + 4.49 \times 10^{-5} s^3 + 0.19 s^2 + 300.9s} \quad (5.14)$$

Figure 5.7 illustrates the bode plot of the uncompensated outer DC-link voltage control loop. That is, $G_{C,v}(s)$ is equal to one.

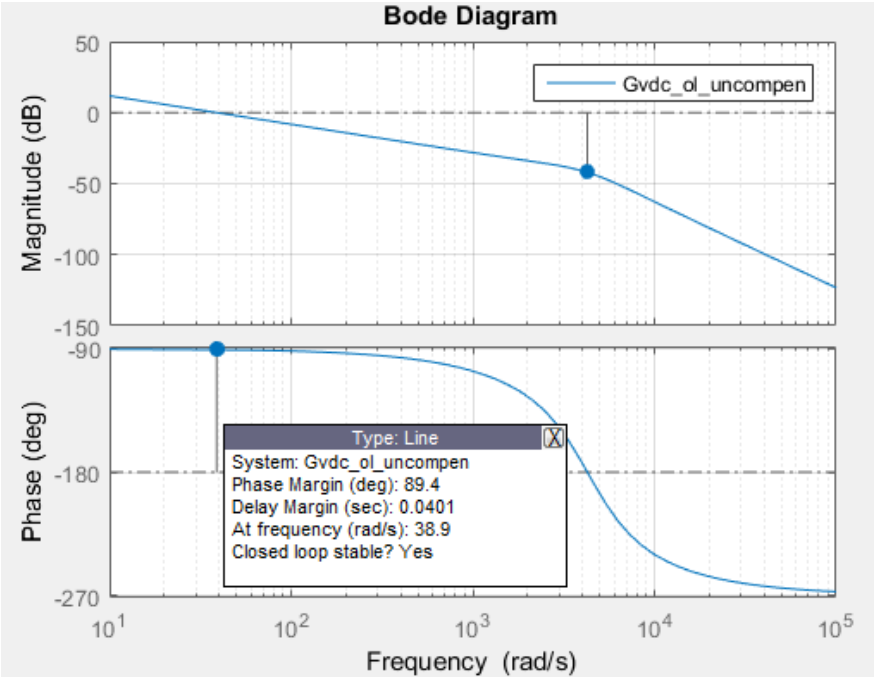

Figure 5. 7: Bode plot of the uncompensated outer DC-link voltage controller's open-loop transfer function

It is observed that the phase-margin and bandwidth of the uncompensated system are 89.4˚ and 38.9 rad/s, respectively. The bandwidth is too low as compared to the desired bandwidth of 785.40rad/s (125Hz) and hence the system response will be slow. Furthermore, the phase-margin is too high and equal to 90˚. A phase-margin equal to or greater than 90˚ reduces the system's response time. To obtain the desired bandwidth frequency, the system's open-loop transfer function needs to be multiplied with a gain K to raise the magnitude curve up. The gain is computed as follow

$$\left|G_{Vdc_{,OL}\_uncompen}(j)\right| = \frac{(4.13j + 1.14\times10^{4})K}{6.01\times10^{-9}\,j^{4} + 4.498\times10^{-5}\,j^{3} + 0.190\,j^{2} + 300.9\,j}$$

$$785.40 = \frac{(4.13j + 1.14\times10^{4})K}{6.01\times10^{-9}(-1)^{2} + 4.498\times10^{-5}(-1)\,j + 0.190(-1) + 300.9\,j}$$

$$785.40(6.01\times10^{-9} - 4.498\times10^{-5}\,j - 0.190 + 300.9\,j) = (4.13j + 1.14\times10^{4})K$$

$$K = \frac{785.40(\sqrt{296.40^{2} + (-0.189)^{2}})}{\sqrt{4.13^{2} + (1.14\times10^{4})^{2}}} = 20.05$$

Multiplying Eq. (5.14) by the gain K gives Eq. (5.15) which is used to plot the bode plot of the gain-compensated system.

$$G_{Vdc_{,OL}\_compen\_gain}(s) = \frac{(82.83s + 2.35\times10^{5})}{6.01\times10^{-9}\,s^{4} + 4.498\times10^{-5}\,s^{3} + 0.190s^{2} + 300.9s} \qquad (5.15)$$

Figure 5.8 illustrates the bode plot of the gain-compensated open-loop transfer function of the DC-link voltage control loop. The magnitude curve crosses the 0dB line at the desired crossover frequency.

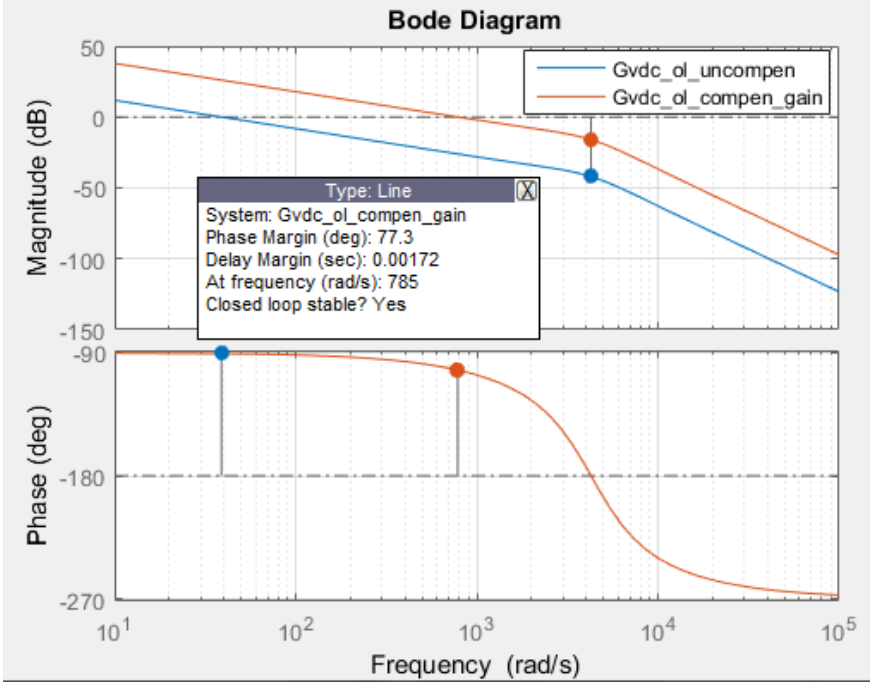

Figure 5. 8: Bode plot of the gain-compensated open-loop transfer function of the DC-link voltage

The phase-margin at the desired crossover frequency is 77.3˚. To obtain the desired phase-margin of 57.85˚, a phase-lag compensator is needed to shift the phase curve down.

5.2.2.1(b) Phase-lag compensator design

The phase-lag compensator is used to shift the phase curve down. This alternatively attenuates the current phase margin to the desired value at the specified bandwidth. Therefore, the first step is to compute the phase-attenuation needed to obtain the desired phase margin. This is done by subtracting the phase margin of the current system from the desired phase margin as follow,

Phase-attenuation=$PM_{desired}$-$PM_{current}$

Phase-attenuation= 57.85°-77.3°= -19.45°

The phase-attenuation needed is used to locate the pole p_c and the zero z_c of the phase-lag compensator by calculating the frequency [Hz] where the pole and zero will be located using Eq. (5.9)[90]

$$f_z = 125\sqrt{\frac{1-\sin(-19.45^o)}{1+\sin(-19.45^o)}} = 176.71Hz$$

$$f_p = 125\sqrt{\frac{1+\sin(-19.45^o)}{1-\sin(-19.45^o)}} = 88.42Hz$$

The angular frequencies where the pole and zero of the phase-lag compensator are calculated as follow

$$\omega_z = 2\pi \times 176.71Hz = 1110.30rad/s$$
$$\omega_p = 2\pi \times 88.42Hz = 555.56rad/s$$

Therefore, the transfer function of the phase-lag compensator is given by Eq. (5.16)

$$\mathrm{G_{lag}(s)} = \mathrm{G_{co}}\left(\frac{\tau_{lag}\mathrm{s}+1}{\alpha\tau_{lag}\mathrm{s}+1}\right) = \frac{1.27\times10^{-3}s+1.41}{1.8\times10^{-3}s+1}$$

where;

$$\alpha = \omega_z/\omega_p = 1110.30/555.56 = 1.99 \qquad (5.16)$$
$$\mathrm{G_{co}} = \sqrt{\alpha} = \sqrt{1.99} = 1.41$$
$$\tau_{lag} = 1/\omega_z = 1/1110.30 = 0.90\times10^{-3}$$

The phase-lag compensator is applied to the gain-compensated system, and hence, multiplying Eq. (5.15) by Eq. (5.16) gives the transfer function of the phase-lag compensated system as follow

$$G_{Vdc_{,OL}\_compen\_lag}(s) = G_{Vdc_{,OL}\_compen\_gain}(s) \times G_{lag}(s)$$

$$G_{Vdc_{,OL}\_compen\_lag}(s) = \frac{0.106s^2 + 415.7s + 3.32\times10^5}{1.08\times10^{-11}s^5 + 8.69\times10^{-8}s^4 + 38.71\times10^{-5}s^3 + 0.732s^2 + 300.9s} \quad (5.17)$$

Figure 5.9 illustrates the bode plot of the phase-lag compensated open-loop transfer function of the outer DC-link voltage control loop.

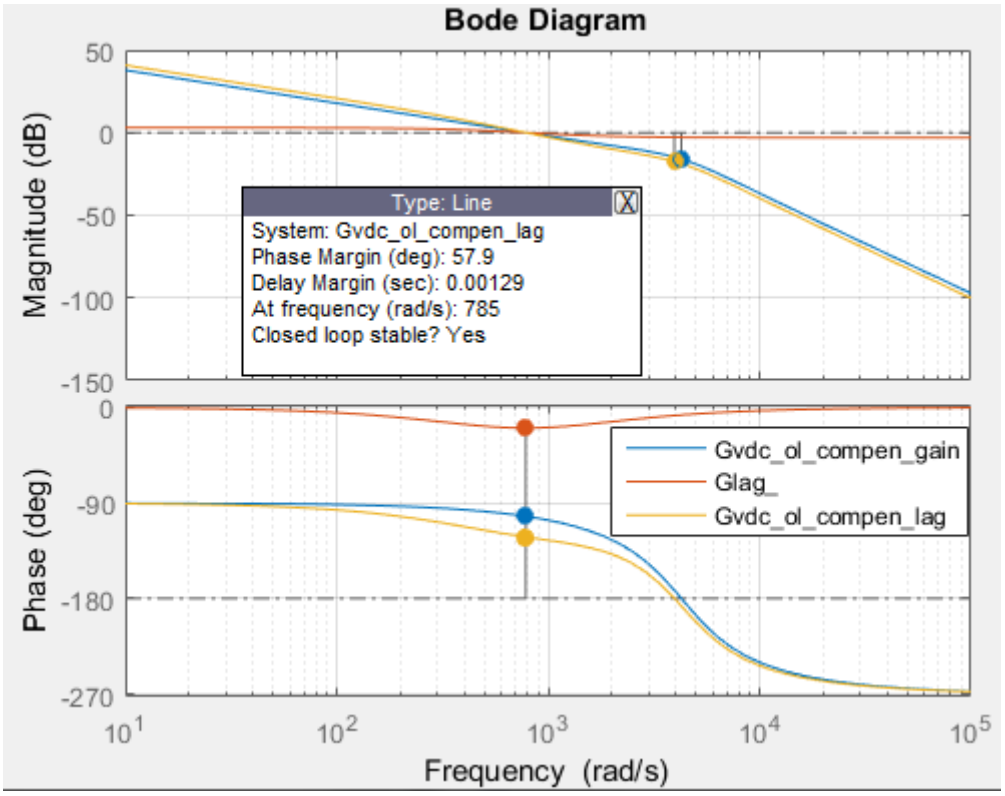

Figure 5. 9: Bode plot of the phase -lag compensated DC-link voltage control loop

It is observed that the phase-lag compensator shifted the phase curve down to yield the phase margin of 57.9°. The bandwidth is maintained at 785 rad/s (125Hz). Therefore, the phase margin and bandwidth design specifications have been met.

Figure 5.10 shows the step response curve indicating the peak response of the uncompensated, gain-compensated and phase-lag compensated closed-loop transfer function of the DC-link voltage control loop.

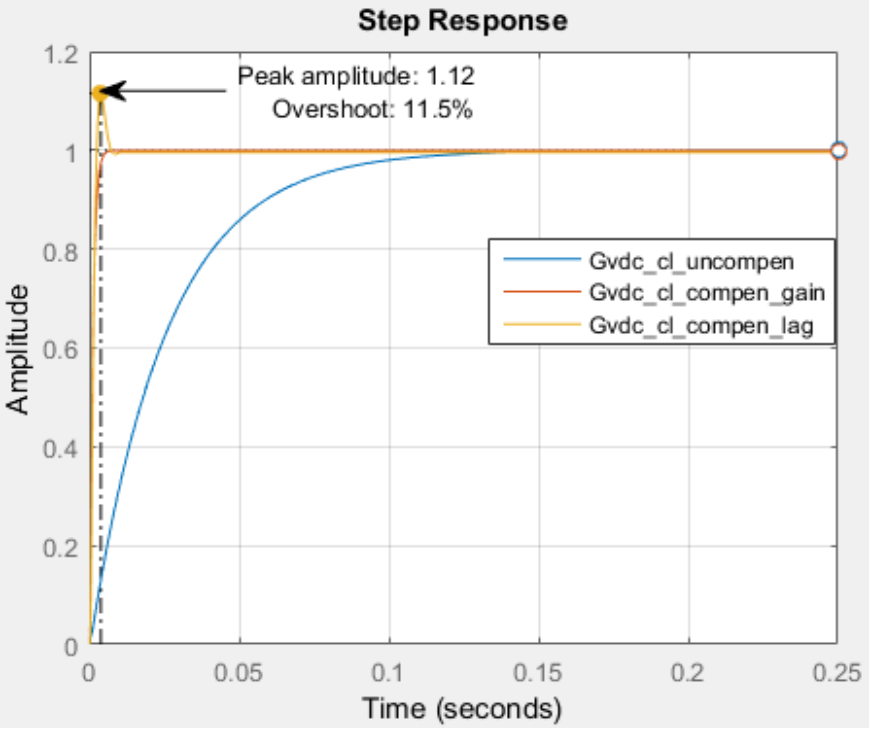

Figure 5. 10: Peak-response of the phase-lag compensated transfer function

It is observed that the overshoot of the phase-lag compensated system is 11.5%. Figure 5.11 shows the step response indicating the settling time of the uncompensated, gain-compensated and phase-lag compensated closed-loop transfer functions of the DC-link voltage control loop.

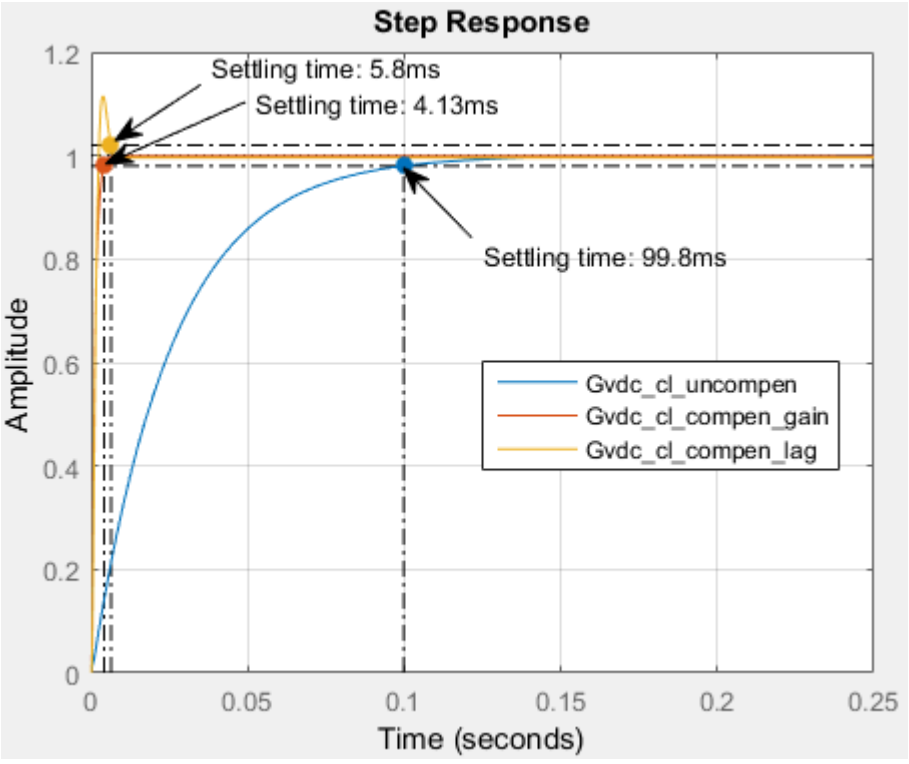

Figure 5. 11: Settling time of the uncompensated, gain-compensated and phase-lag compensated transfer functions

It is observed that gain *K* reduced the settling time of the uncompensated system from 99.8ms to 4.13ms. However, the phase-lag compensator increased the settling-time to 5.8ms which is equal to the desired settling time. This illustrates that the settling-time design specification has been met.

Figure 5.12 shows the step response indicating the rise time of the uncompensated, gain-compensated and phase-lag compensated closed-loop transfer functions of the DC-link voltage control loop.

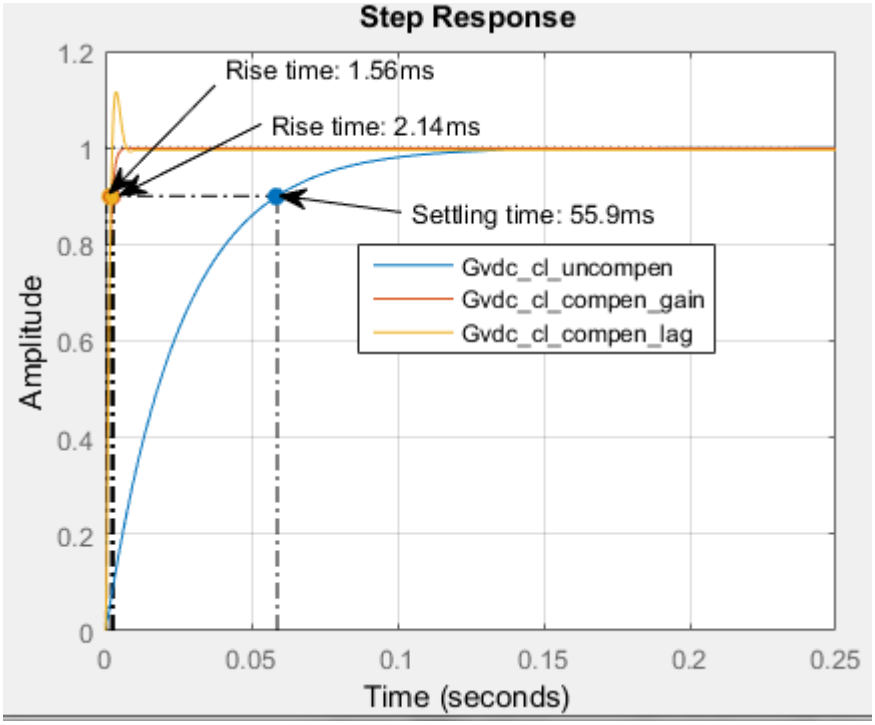

Figure 5. 12: Rise time of the uncompensated, gain- compensated and phase-lag compensated transfer functions

It can be observed that gain *K* reduced the rise time of the uncompensated system from 55.9ms to 2.14ms and hence speeding up the system response. The phase-lag compensator then further reduced the system's rise time to 1.56ms which is within the desired rise time of 2.09ms. This illustrates that the rise time design specification has been met.

5.2.2.2 Stator Voltage Outer Control Loop

5.2.2.2(a) The uncompensated system

The open-loop transfer function of the uncompensated outer stator voltage control loop is represented by Eq. (4.44). The bode plot used for the system's stability analysis is plotted using Eq. (5.18) by substituting in the compensated closed-loop transfer function of the q-component of the stator current given by Eq. (5.13) as well as the converter's terminal voltage of 620.62V calculated in Eq. (3.5).

$$G_{V_{st,OL\_uncompen}}(s) = \frac{(2.48s + 7010) \times G_{C,V_{st}}(s)}{2.256 \times 10^{-10} s^3 + 1.689 \times 10^{-6} s^2 + 7.14 \times 10^{-3} s + 11.3} \quad (5.18)$$

Figure 5.13 illustrates the magnitude and phase curves of the uncompensated open-loop transfer function of the outer stator voltage control loop. That is, $G_{C,Vst}(s)$ is equal to one.

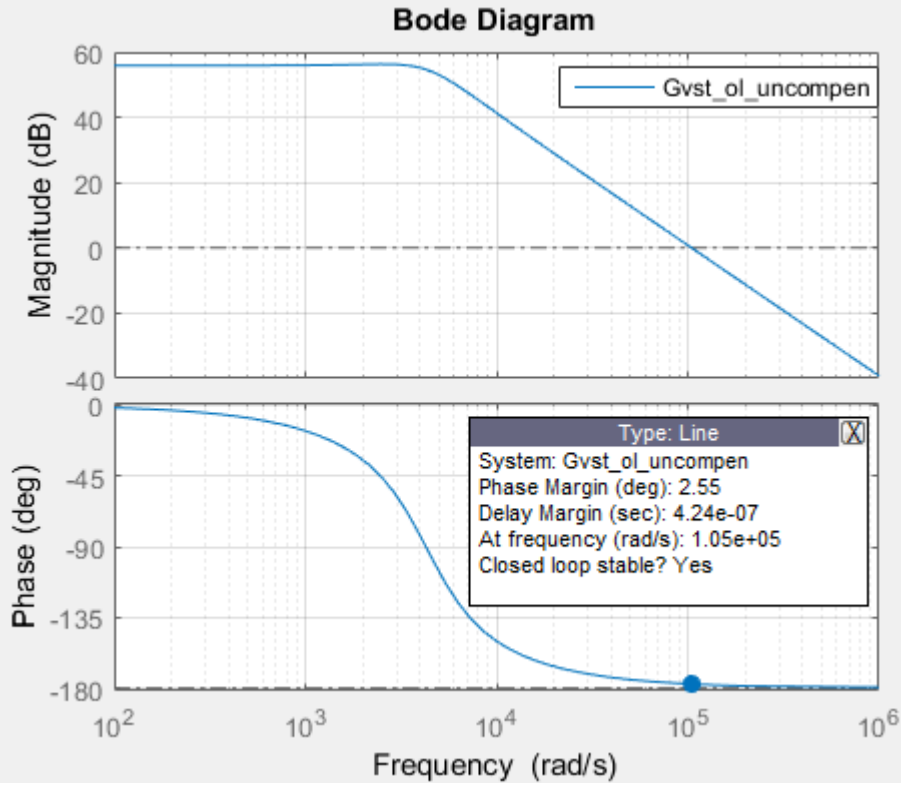

Figure 5. 13: Bode plot of the uncompensated outer stator voltage controller's open-loop transfer function

It is observed that the phase-margin and bandwidth of the uncompensated system are 2.55˚ and 1.05×10^5 rad/s, respectively. The bandwidth is much higher than the desired value. Furthermore, the phase margin is very small. To reduce the bandwidth, a phase-lag compensator is needed to drop the magnitude curve down so that it crosses the 0dB line at the desired bandwidth of 785.40rad/s (125Hz).

5.2.2.2(b) Phase-lag compensator design

The phase-lag compensator is used to shift the magnitude curve down in order to reduce the bandwidth to the desired value. Therefore, the first step is to identify the gain magnitude corresponding to the desired bandwidth on the magnitude curve. The gain magnitude at the desired bandwidth is 55.9dB as shown in Figure 5.14.

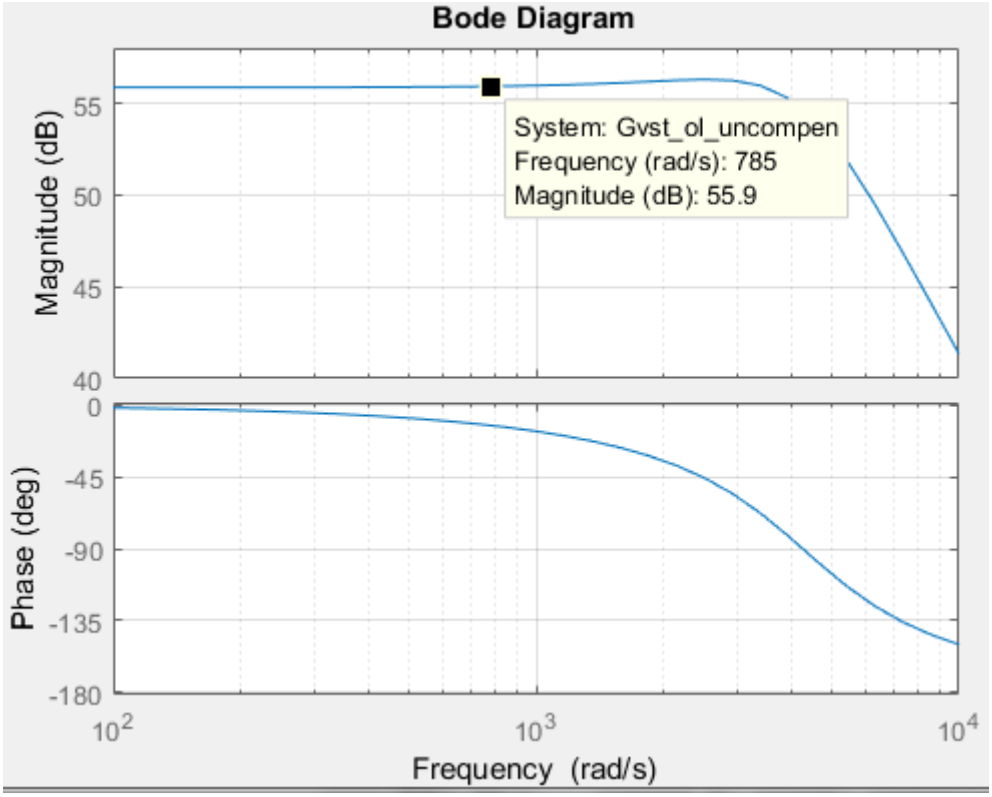

Figure 5. 14: Gain magnitude at the desired bandwidth

The magnitude at the desired bandwidth is then used to calculate the attenuation α needed to shift the magnitude curve down. The attenuation is also used to locate the pole and zero of the phase-lag compensator. The attenuation α is calculated using Eq. (5.19)

$$\alpha = 10^{\frac{gain}{10}} = 10^{\frac{55.9}{10}} = 389045.15 \tag{5.19}$$

The frequencies where the pole and zero will be located are calculated using Eq. (5.20). Therefore the pole and zero of the phase-lag compensator with a bandwidth of 785.40 rad/s

$$\begin{aligned} z_c &= \omega_{bandwidth} \times \sqrt{\alpha} = 785.40 \times \sqrt{389045.15} = 0.490 \times 10^6 \, rad/s \\ p_c &= \frac{z_c}{\alpha} = \frac{0.490 \times 10^6}{389045.15} = 1.259 rad/s \end{aligned} \tag{5.20}$$

Therefore, the transfer function of the phase-lag compensator is given by Eq. (5.21)

$$G_{lag}(s) = \frac{(s/z_c + 1)}{(s/p_c + 1)} = \frac{2.042 \times 10^{-6} s + 1}{0.795s + 1} \tag{5.21}$$

Substituting Eq. (5.21) into Eq. (5.18) gives Eq. (5.22) representing the open-loop transfer function of the phase-lag compensated system.

$$G_{Vst_{,OL}\_compen\_lag}(s) = \frac{5.056 \times 10^{-6} s^2 + 2.49s + 7010}{1.79 \times 10^{-10} s^4 + 1.34 \times 10^{-6} s^3 + 5.67 \times 10^{-3} s^2 + 8.98s + 11.3} \tag{5.22}$$

Figure 5.15 shows the magnitude and phase curves of the phase-lag compensated system.

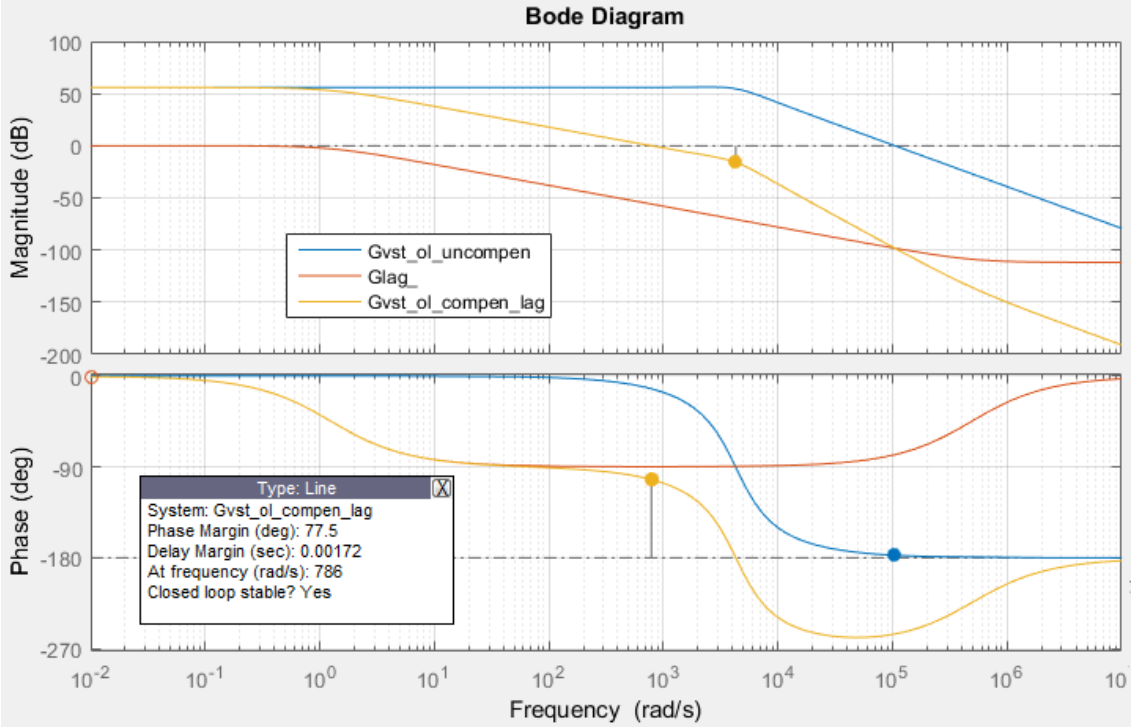

Figure 5. 15: Bode plot of the phase-lag compensated stator voltage controller

It can be seen that phase-lag compensator shifted the magnitude curve down by 55.9dB at the bandwidth of 786 rad/s, which is close to the desired bandwidth and hence, the bandwidth design specification has been met. The phase-margin at the desired bandwidth is 77.5°. Therefore, a second phase-lag compensator is needed to shift the phase curve down to obtain the desired phase-margin of 57.85°.

5.2.2.2(c) Second Phase-lag compensator design

The phase-lag compensator is used to shift the phase curve down. This alternatively attenuates the current phase margin to the desired value at the specified bandwidth. Therefore, the first step is to compute the phase-attenuation needed to obtain the desired phase margin. This is done by subtracting the phase margin of the current system from the desired phase margin as follow,

Phase-attenuation=$PM_{desired}$-$PM_{current}$

Phase-attenuation= 57.85°-77.5°= -19.65°

The phase-attenuation is used to locate the pole p_c and zero z_c of the phase-lag compensator by calculating the frequency [Hz] where the pole and zero will be located using Eq. (5.9)[90]

$$f_z = f_{BW}\sqrt{\frac{1-\sin(phase-attenuation)}{1+\sin(phase-attenuation)}} = 125\sqrt{\frac{1-\sin(-19.65^o)}{1+\sin(-19.65^o)}} = 177.36Hz$$

$$f_p = f_{BW}\sqrt{\frac{1+\sin(phase-attenuation)}{1-\sin(phase-attenuation)}} = 125\sqrt{\frac{1+\sin(-19.65^o)}{1-\sin(-19.65^o)}} = 88.09Hz$$

The angular frequencies where the pole and zero of the phase-lag compensator will be located are calculated as follow

$$\omega_z = 2\pi \times 177.36Hz = 1114.39rad/s$$
$$\omega_p = 2\pi \times 88.09Hz = 553.49rad/s$$

Therefore, the transfer function of the phase-lag compensator is given by Eq. (5.23)

$$G_{lag_2}(s) = G_{co}\left(\frac{\tau_{lag}s+1}{\alpha\tau_{lag}s+1}\right) = \frac{1.27\times10^{-3}s+1.42}{1.81\times10^{-3}s+1}$$

where;

$$\alpha = \omega_z/\omega_p = 1114.39/553.49 = 2.01 \quad (5.23)$$
$$G_{co} = \sqrt{\alpha} = \sqrt{2.01} = 1.42$$
$$\tau_{lag} = 1/\omega_z = 1/1114.39 = 0.89\times10^{-3}$$

The second phase-lag compensator is applied to the phase-lag compensated system, and hence, multiplying Eq. (5.22) by Eq. (5.23) gives the transfer function of the phase-lag-lag compensated system as follow

$$G_{Vst_{OL}\_compen\_lag\_lag}(s) = G_{Vst_{OL}\_compen\_lag}(s)\times G_{lag_2}(s)$$
$$= \frac{6.44\times10^{-9}s^3+31.78\times10^{-3}s^2+12.46s+9947}{3.24\times10^{-13}s^5+2.61\times10^{-9}s^4+1.16\times10^{-5}s^3+21.9\times10^{-3}s^2+9.01s+11.3} \quad (5.24)$$

Figure 5.16 illustrates the bode plot of the phase-lag compensated open-loop transfer function of the outer stator voltage controller.

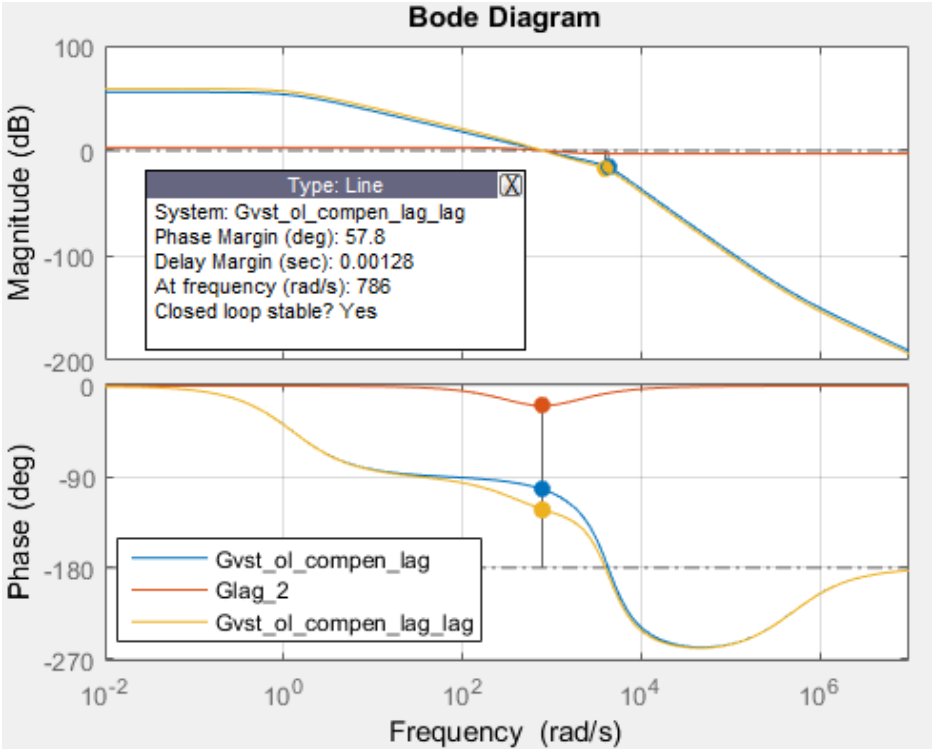

Figure 5. 16: Bode plot of the phase-lag-lag compensated stator voltage control loop

It is observed that the second lag compensator shifted the phase curve down to the phase margin of 57.8° which is equal to the desired phase margin. The bandwidth is maintained at 786 rad/s (125Hz). Therefore, the phase margin and bandwidth design specifications have been met.

Figure 5.17 shows the step response curve indicating the peak responses of the uncompensated, the phase-lag compensated and phase-lag-lag compensated closed-loop transfer function of the outer stator voltage control loop.

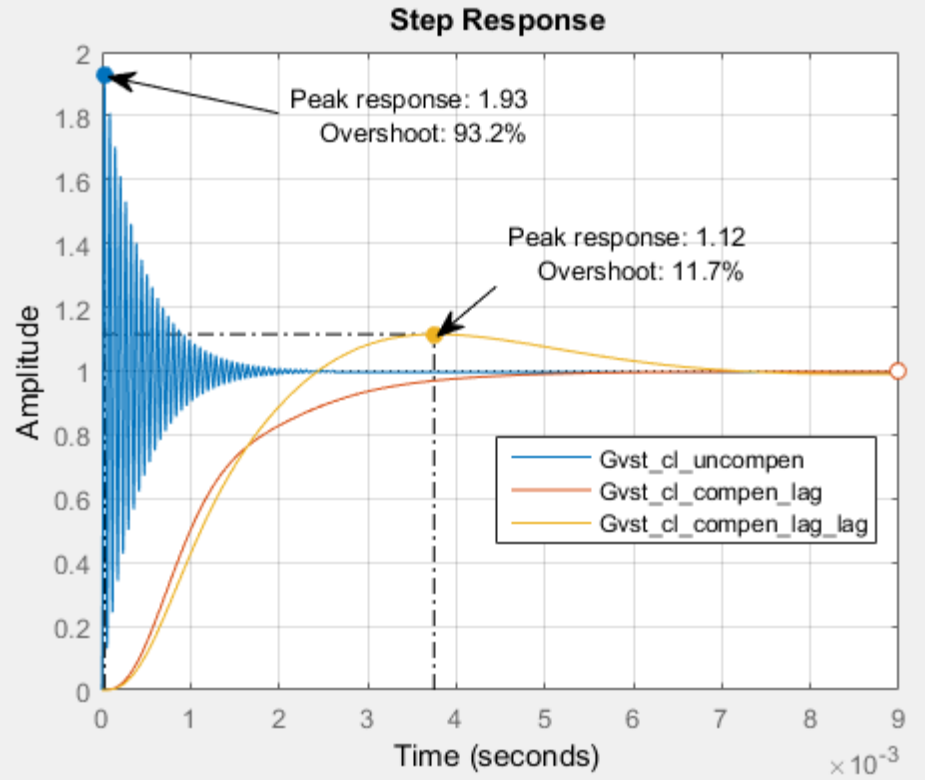

Figure 5. 17: Peak-response of the uncompensated and phase-lag compensated transfer functions

It can be observed that the phase-lag-lag compensated system reduced the percentage overshoot of the uncompensated system from 93.2% to 11.7%. Figure 5.18 shows the step response curve indicating the settling time of the uncompensated, phase-lag compensated and phase-lag-lag compensated closed-loop transfer functions of the outer stator voltage control loop.

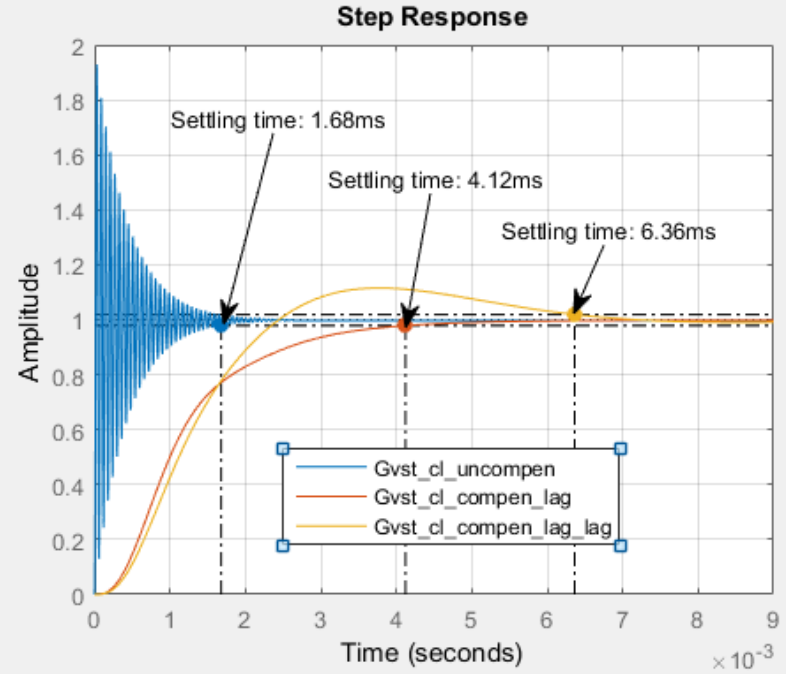

Figure 5. 18: Settling time of the uncompensated and phase-lag compensated transfer functions

It is observed that the first phase-lag compensator increased the settling time of the uncompensated system from 1.68ms to 4.12ms. The second phase-lag compensator further increased the settling time of the phase-lag compensated system to 6.36ms.

Figure 5.19 shows the step response curve indicating the rise time of the uncompensated, phase-lag compensated and phase-lag-lag compensated closed-loop transfer function of the outer stator voltage control loop.

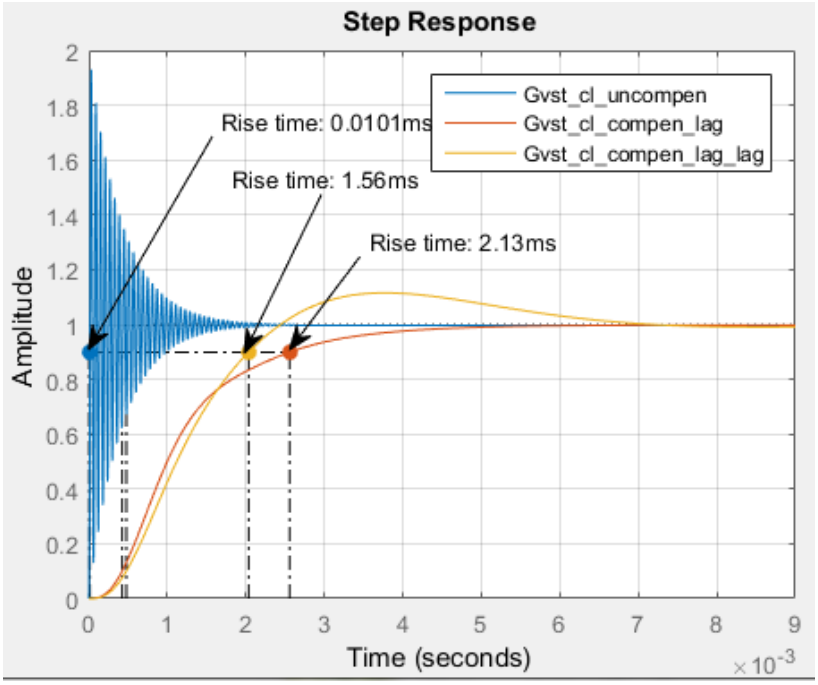

Figure 5. 19: Rise time of the uncompensated and phase-lag compensated transfer functions

It is observed that the rise-time of the uncompensated system is 10.1μs. The first phase-lag compensator increased the system's rise time to 2.13ms, while the second phase-lag compensator decreased the rise time of the phase-lag compensated system to 1.56ms which is within the desired rise time of 2.09ms. This illustrates that the rise time design specification has been met.

5.3 Pitch-Angle Controller Design and Stability Analysis

The pitch angle controller is responsible for increasing the angle of attack / pitch angle during high wind speeds to protect the wind turbine from sudden wind gusts. The pitch angle only changes at a finite rate. The maximum rate of change of the pitch angle is in the order of 3 /s to 10 /s, depending on the size of the wind turbine [65]. Considering a rate of change of 10 /s, the bandwidth of the pitch angle controller can be taken to be 10 rad/s (1.59Hz).

5.3.1 Design specifications of the pitch-angle controller

- Overshoot of 5%; the pitch-angle controller needs to have a smaller overshoot to get rid of as many oscillations in the controller as possible to enhance the stability of the entire system.

Therefore the damping ratio is calculated as follow

$$0.05 = e^{-\pi\zeta/\sqrt{1-\zeta^2}}$$

$$\zeta_{pitch} = \sqrt{\frac{\ln(0.05)^2}{\pi^2 + \ln(0.05)^2}} = 0.69$$

The phase margin corresponding to damping ratio is calculated as follow

$$PM_{pitch} = \tan^{-1}\left(\frac{2(0.69)}{\sqrt{\sqrt{1+4(0.69)^2} - 2(0.69)^2}}\right) = 57.85^o$$

Therefore, the natural frequency of the system corresponding to the specified bandwidth and damping ratio is equal to,

$$\omega_{n\_pitch} = \frac{\omega_{BW_{pitch}}}{\sqrt{(1-2\zeta_{outer\_Loop}{}^2) + \sqrt{\zeta_{outer\_Loop}{}^4 - 4\zeta_{outer\_Loop}{}^2 + 2}}}$$

$$\omega_{n\_pitch} = \frac{10}{\sqrt{(1-2(0.69)^2) + \sqrt{(0.69)^4 - 4(0.69)^2 + 2}}} = 12.76 rad/s$$

The settling time corresponding to the system's natural frequency and damping ratio is equal to,

$$T_{s\_pitch} = \frac{4}{\omega_{n\_pitch} \times \zeta_{pitch}} = \frac{4}{0.69 \times 12.76} = 0.45s$$

The peak time corresponding to the system's natural frequency and damping ratio is equal to,

$$T_{p\_pitch} = \frac{\pi}{12.76\sqrt{1-0.69^2}} = 0.34s$$

The rise time corresponding to the peak time is equal to,

$$T_{r\_pitch} = \frac{1.76(0.69)^3 - 0.417(0.69)^2 + 1.039(0.69) + 1}{12.76} = 0.164s$$

To satisfy these design specifications, the performance of the systems' open-loop transfer functions were analyzed using bode plots and step response curves. This was carried out before and after the compensators has been applied to the uncompensated systems.

5.3.1.1 The uncompensated system

The open-loop transfer function of the uncompensated system is represented by Eq. (4.73). The bode plot used for the system's stability analyses is plotted using Eq. (5.25) by substituting the equivalent inertia, equivalent damping coefficient, rated aerodynamic and electromagnetic torque into Eq. (4.73). Therefore, the open-loop transfer function is given by Eq. (5.25)

$$\begin{aligned} G_{pitch\_ol\_uncompen}(s) &= \frac{G_{pitch}(s)(T_m - T_e)}{(\tau_\beta s + 1)(J_{eq} s + B_{eq})} = \frac{G_{pitch}(s)[(848.83 \times 10^3) - (32.65 \times 10^3)]}{(0.1s + 1)(6.25 \times 10^6 s + 2000)} \\ G_{pitch\_ol\_uncompen}(s) &= G_{pitch}(s) \times \frac{8.162 \times 10^5}{6.25 \times 10^5 s^2 + 6.25 \times 10^6 s + 2000} \end{aligned} \quad (5.25)$$

Figure 5.20 illustrates the magnitude and phase curves of the uncompensated open-loop transfer function of the pitch-angle controller, that is $G_{pitch}(s)$=1.

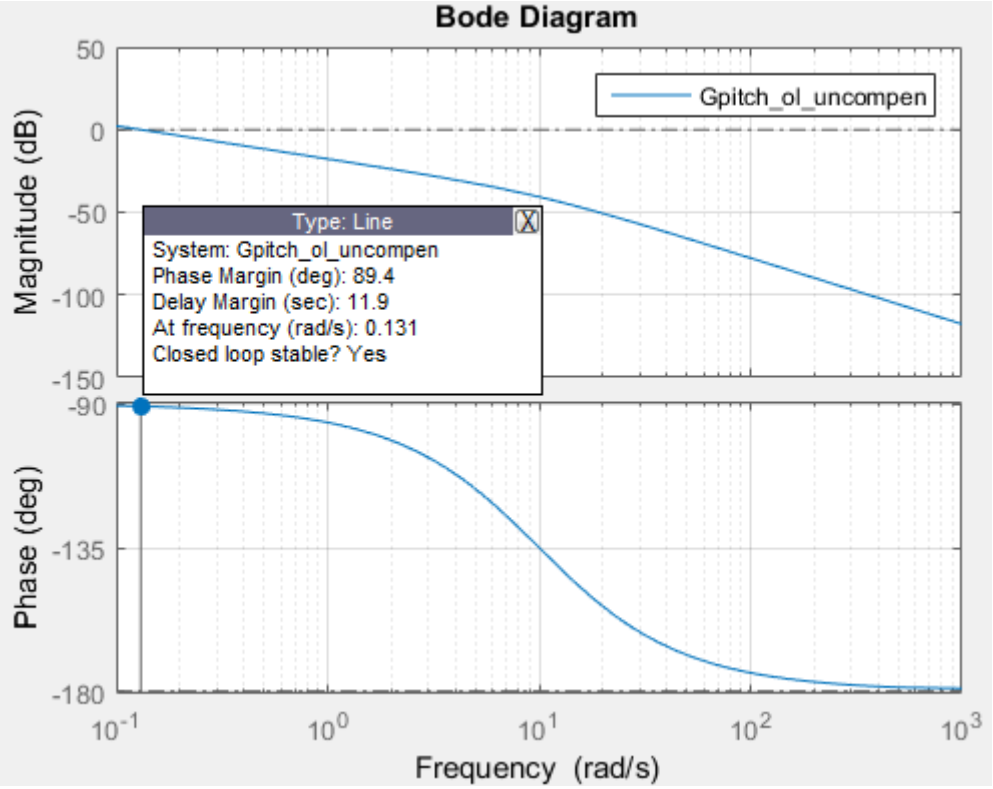

Figure 5. 20: Bode plot of the uncompensated pitch-angle controller's open-loop transfer function

Figure 5.20 indicates that the phase margin and bandwidth frequency of the uncompensated system are 89.4˚ and 0.131 rad/s, respectively. The bandwidth frequency is too low as compared to the desired value of 10 rad/s (1.59Hz) and hence the system response will be too slow. Furthermore, the phase-margin is too high and close to 90˚. A phase-margin equal to or close to 90˚ reduces the system's response time.

To obtain the desired bandwidth, the system's open-loop transfer function needs to be multiplied by a gain K to raise the magnitude curve up. The gain is determined in such a way that the magnitude curve crosses the 0dB line at the desired bandwidth. The gain is computed using Eq. (5.7) as follow

$$\left|G_{pitch_{OL}\_uncompen}(j)\right| = \frac{8.162\times10^5 \times K}{6.25\times10^5\, j^2 + 6.25\times10^6\, j + 2000}$$

$$10 = \frac{8.162\times10^5 \times K}{(-6.25\times10^5 + 6.25\times10^6\, j + 2000)}$$

$$K = \frac{10(-6.25\times10^5 + 6.25\times10^6\, j + 2000)}{8.162\times10^5}$$

$$K = \frac{10(\sqrt{(6.23\times10^5)^2 + (6.25\times10^6)^2}}{8.162\times10^5}$$

$$K = 109.1$$

Multiplying Eq. (5.25) with the gain *K* gives Eq. (5.26) which is used for plotting the bode plot of the gain-compensated transfer function.

$$G_{pitch_{OL}\_compen\_gain}(s) = \frac{8.896\times10^{7}}{6.25\times10^{5}s^{2} + 6.25\times10^{6}s + 2000} \tag{5.26}$$

Figure 5.21 illustrates the magnitude and phase curves of the gain-compensated open-loop transfer function of the pitch-angle controller. It can be seen that the magnitude curve crosses the 0dB line at the desired bandwidth.

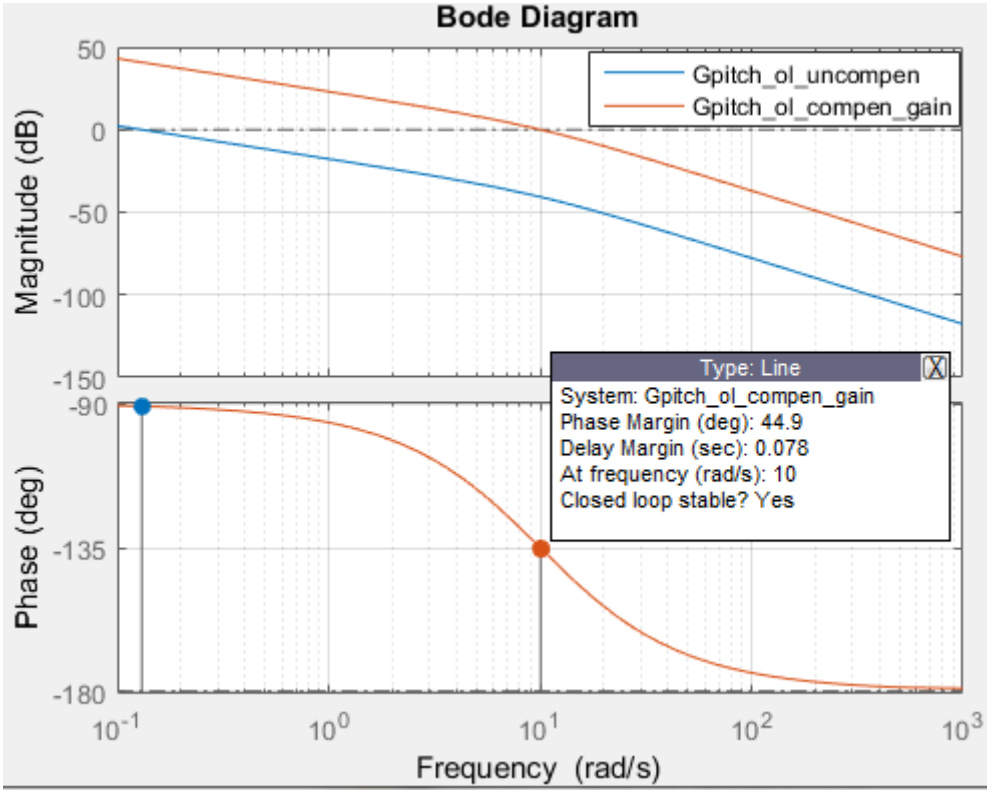

Figure 5. 21: Bode plot of the gain-compensated open-loop transfer function of the pitch-angle controller

The phase margin at the desired bandwidth frequency is 44.9˚. To obtain the desired phase margin of 57.85 ˚, a phase-lead compensator is needed to boost the phase margin by shifting the phase curve up.

5.3.1.2 Phase-lead compensator design

The phase-lead compensator is used to shift the phase curve up. This alternatively boosts the current phase margin to the desired value at the specified bandwidth. Therefore, the first step is to compute the phase-boost needed to obtain the desired phase margin. This is done by subtracting the phase margin of the current system from the desired phase margin as follow,

Phase-boost=$PM_{desired}$-$PM_{current}$

Phase-boost= 57.85°-44.9°=12.95°

The phase-boost needed is used to locate the pole p_c and zero z_c of the phase-lead compensator by calculating the frequency [Hz] where the pole and zero will be located using Eq. (5.27)[92]

$$\begin{aligned} f_z &= f_{BW}\sqrt{\frac{1-\sin(phase-boost)}{1+\sin(phase-boost)}} \\ f_p &= f_{BW}\sqrt{\frac{1+\sin(phase-boost)}{1-\sin(phase-boost)}} \end{aligned} \tag{5.27}$$

Where f_{BW} is the crossover frequency, which is equal to 1.59Hz (10rad/s/2π). Therefore, f_p and f_z are calculated as follow

$$f_z = 1.59\sqrt{\frac{1-\sin(12.95^o)}{1+\sin(12.95^o)}} = 1.266Hz$$
$$f_p = 1.59\sqrt{\frac{1+\sin(12.95^o)}{1-\sin(12.95^o)}} = 1.997Hz$$

The angular frequencies where the pole and zero of the phase-lag compensator are located are calculated as follow

$$\omega_z = 2\pi \times 1.266Hz = 7.955rad/s$$
$$\omega_p = 2\pi \times 1.997Hz = 12.548rad/s$$

Therefore, the transfer function of the phase-lead compensator is given by Eq. (5.28)

$$\begin{aligned} &G_{\text{lead}}(s) = G_{\text{co}}\left(\frac{\tau_{lead}s+1}{\alpha\tau_{lead}s+1}\right) = \frac{0.1001s+0.796}{0.0797s+1} \\ &where; \\ &\alpha = \omega_z/\omega_p = 7.955/12.548 = 0.634 \\ &G_{\text{co}} = \sqrt{\alpha} = \sqrt{0.634} = 0.796 \\ &\tau_{lead} = 1/\omega_z = 1/7.955 = 0.126 \end{aligned} \tag{5.28}$$

The phase-lead compensator is applied to the gain-compensated system, and hence, multiplying Eq. (5.26) by Eq. (5.28) gives Eq. (5.29) which represents the transfer function of the phase-lead compensated system for the pitch-angle control loop.

$$\begin{aligned} G_{pitch_{OL}\_compen\_lead}(s) &= G_{pitch_{OL}\_compen\_gain}(s) \times G_{lead}(s) \\ G_{pitch_{OL}\_compen\_lead}(s) &= \frac{8.905\times10^6 s + 7.083\times10^7}{4.981\times10^4 s^3 + 1.123\times10^6 s^2 + 6.25\times10^6 s + 2000} \end{aligned} \tag{5.29}$$

Figure 5.22 illustrates the magnitude and phase curves of the phase-lead compensated open-loop transfer function of the pitch-angle controller.

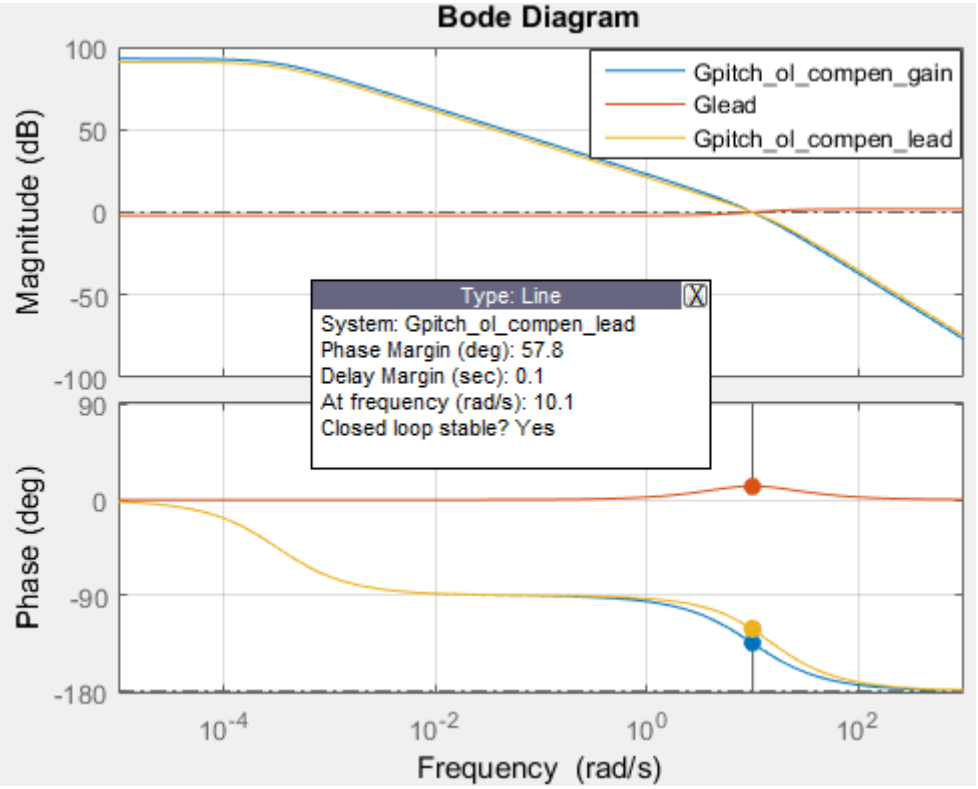

Figure 5. 22: Bode plot of the phase-lead compensated pitch-angle controller's open-loop transfer function

It is shown that the phase-lead compensator shifted the phase curve up to yield the phase-margin of 57.8°. The bandwidth is maintained at 10rad/s (1.59Hz). Therefore, the phase-margin and bandwidth design specifications have been met.

Figure 5.23 shows the step response curve indicating the peak response of the uncompensated, gain-compensated and phase-lead compensated closed-loop transfer function of pitch-angle control loop.

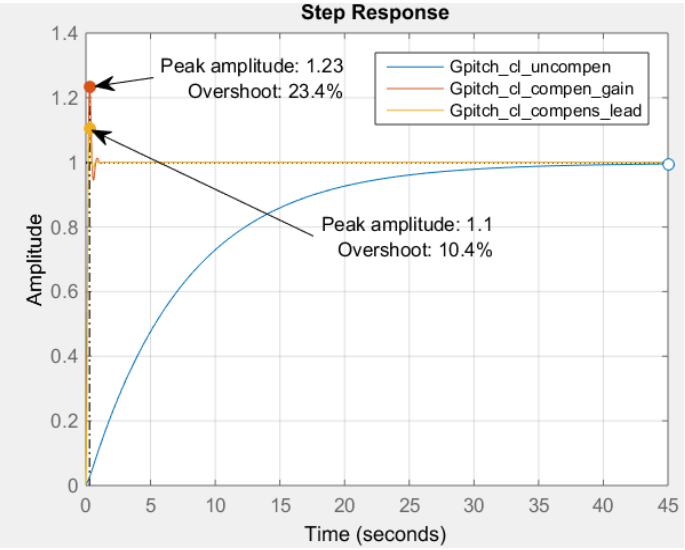

Figure 5. 23: Peak-response of the uncompensated, gain-compensated and phase-lead compensated transfer functions

It can be observed that the percentage overshoot of the gain-compensated system is 23.4%, while the overshoot of the phase-lead compensated system is 10.4%. Figure 5.24 shows the step response curve indicating the settling time of the uncompensated, gain-compensated and phase-lead compensated closed-loop transfer functions of the pitch-angle control loop.

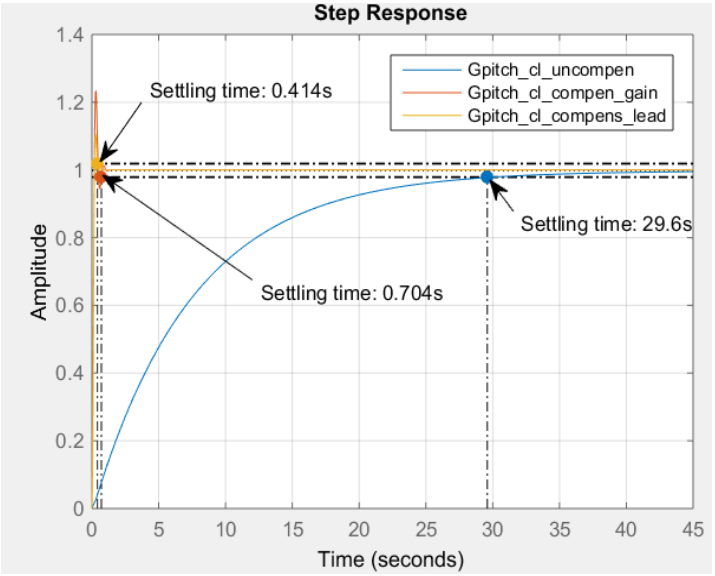

Figure 5. 24: Settling time of the uncompensated, gain-compensated and phase-lead compensated transfer functions

It can be observed that gain *K* reduced the settling time of the uncompensated system from 29.6s to 0.704s. The phase-lead compensator reduced the settling time of the gain-compensated system to 0.414s which is still within the desired settling time of 0.45s. This illustrates that the settling time design specification has been met.

Figure 5.25 shows the step response curve indicating the rise time of the uncompensated, gain-compensated and phase-lead compensated closed-loop transfer functions of the pitch-angle control loop.

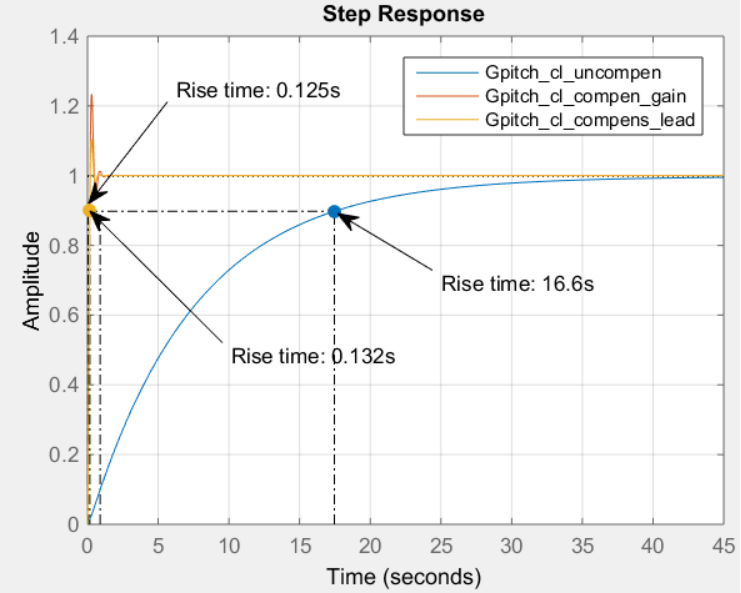

Figure 5. 25: Rise time of the uncompensated, gain- compensated and phase-lead compensated transfer functions

It is observed that gain *K* reduced the rise-time of the uncompensated system from 16.6s to 0.125s and hence speeding up the system response. However, the phase-lag compensator increased the gain-compensated system's rise time to 0.132s which is within the desired rise time of 0.164s. This illustrates that the rise time design specification has been met.

5.4 Chapter Summary

This chapter dealt with computing/determining the design specifications that are to be achieved in this study, namely: bandwidth, phase margin, percentage overshoot, settling time and rise time. A thorough design and stability analysis of the pitch-angle controller and generator-side converter controller has been carried out using bode plots and step response curves in MATLAB software package with the aim of achieving the aforementioned design specifications. The pitch-angle, inner current, DC-link voltage and stator voltage controllers' performance values of the uncompensated, gain-compensated, phase-lead compensated and phase-lag compensated systems are summarized in Table 5.1- Table 5.4.

Table 5. 1: Inner current controller's performance values of the uncompensated, gain-compensated and phase-lead compensated system

Design Specification	**Desired values**	**Measured values/outcome**		
		Uncompensated	***Gain-compensated***	***Phase-lead compensated***
Bandwidth (rad/s)	3141.59	628	$3.14x10^3$	$3.14x10^3$
Phase margin (˚)	57.85	81.1	51.9	57.9
Gain margin (dB)	0	-16	0	0
Overshoot (%)	5	undefined	16.2	10.4
Settling time (ms)	1.45	5.29	2.02	1.34
Rise time (ms)	0.52	2.91	0.411	0.423

Table 5. 2: DC-link voltage controller's performance values of the uncompensated, gain-compensated and phase-lag compensated system

Design Specification	**Desired values**	**Measured values/outcome**		
		Uncompensated	***Gain-compensated***	***Phase-lag compensated***
Bandwidth (rad/s)	785.40	38.9	785	785
Phase margin (˚)	57.85	89.4	77.3	57.9
Gain margin (dB)	0	-22.9	0	0
Overshoot (%)	5	undefined	0.99	11.5
Settling time (ms)	5.79	99.8	4.13	5.8
Rise time (ms)	2.09	55.9	2.14	1.56

Table 5. 3: Stator voltage controller's performance values of the uncompensated, gain-compensated and phase-lag compensated system

Design Specification	**Desired values**	**Measured values/outcome**		
		Uncompensated	***Gain-compensated***	***Phase-lag compensated***
Bandwidth (rad/s)	785.40	1.05×10^{5}	786	786
Phase margin (˚)	57.85	2.55	77.5	57.8
Gain margin (dB)	0		0	0
Overshoot (%)	5	93.2	0.99	11.7
Settling time (ms)	5.79	1.68	4.12	6.36
Rise time (ms)	2.09	1.01×10^{-5}	2.13	1.56

Table 5. 4: Pitch-angle controller's performance values of the uncompensated, gain-compensated and phase-lead compensated system

Design Specification	**Desired values**	**Measured values/outcome**		
		Uncompensated	***Gain-compensated***	***Phase-lead compensated***
Bandwidth (rad/s)	10	0.131	10	10.1
Phase margin (˚)	57.85	89.4	44.9	57.8
Gain margin (dB)	0	-48	0	0
Overshoot (%)	5	undefined	23.4	10.4
Settling time (s)	0.45	29.6	0.704	0.414
Rise time (s)	0.164	16.6	0.126	0.132

CHAPTER 6: GRID-SIDE CONVERTER CONTROL SYSTEM MODELING AND STABILITY ANALYSIS

This chapter covers the design and stability analysis of the grid-side converter controller using bode plots and step response curves in MATLAB software package to achieve the desired controller specifications.

6.1 Grid-side Converter Controller's Stability Analysis

6.1.1 Inner Grid Current Control Loop

6.1.1.1 Design Specifications

The design specifications to be met by the compensators in the inner current controller are:

- A bandwidth of 3141.59 rad/s (500Hz)
- Overshoot of 5% resulting in a damping ratio of 0.69
- A phase margin of 57.85˚
- A gain margin of 0dB at the desired bandwidth
- A settling time of 1.45ms
- A rise time of 0.52ms

6.1.1.2 The uncompensated system

The open-loop transfer function of the uncompensated system is represented by Eq. (4.57). The bode plot used for the system's stability analyses is plotted using Eq. (6.1) by substituting the delay time of 0.25ms calculated in chapter 5, and the interfacing reactor's inductance and resistance calculated in chapter 3. Therefore, the open-loop transfer function is given by Eq. (6.1) with T_a=0.25ms, L_t=66.5mH, and R_t=0.665mΩ

$$G_{I_{OL}\_uncompen}(s) = \frac{G_{C,i}(s)}{(T_a s+1)(sL_{sdq}+R_s)} = \frac{G_{C,i}(s)}{(0.25\times10^{-3}s+1)(66.5\times10^{-3}s+0.665\times10^{-3})}$$
$$G_{I_{OL}\_uncompen}(s) = \frac{G_{C,i}(s)}{1.66\times10^{-5}s^2+66.5\times10^{-3}s+6.65\times10^{-5}} \quad (6.1)$$

Figure 6.1 illustrates the magnitude and phase curves of the inner current controller's open-loop transfer function without a compensator, that is $G_{c,i}(s)$ =1.

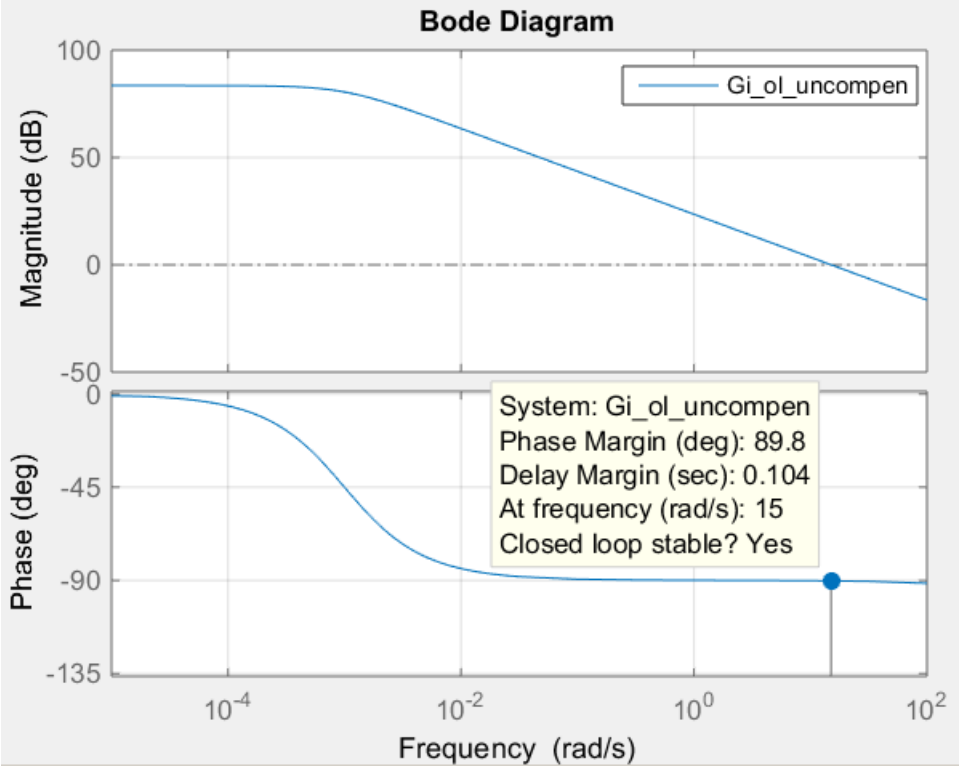

Figure 6. 1: Bode plot of the uncompensated inner controller open-loop transfer function

It is observed that the phase margin and bandwidth of the uncompensated system are 89.8˚ and 15 rad/s, respectively. The bandwidth frequency is too low as compared to the desired bandwidth of $3.14\text{x}10^3$ rad/s (500Hz) and hence the system response will be too slow. Furthermore, the phase-margin is too high and much closer to 90˚. A phase margin equal to or greater than 90˚ reduces the system's response time.

To obtain the desired bandwidth frequency, the system's open-loop transfer function needs to be multiplied by a gain *K* to raise the magnitude curve up. The gain is determined in such a way that the magnitude curve crosses the 0dB line at the desired crossover frequency. The gain is computed as follow

$$\left|G_{I_{OL}\_uncompen}(j)\right| = \frac{K}{1.66\times10^{-5}\,j^2 + 66.5\times10^{-3}\,j + 6.65\times10^{-5}}$$

$$3141.59 = \frac{K}{(1.66\times10^{-5}\,j^2 + 66.5\times10^{-3}\,j + 6.65\times10^{-5})}$$

$$K = 3141.59(-1.66\times10^{-5} + 66.5\times10^{-3}\,j + 6.65\times10^{-5})$$

$$K = 3141.59(\sqrt{(4.99\times10^{-5})^2 + (66.5\times10^{-3})^2}$$

$$K = 266.01$$

Multiplying Eq. (6.1) with gain *K* gives Eq. (6.2) which is used for plotting the bode plot of the gain-compensated transfer function.

$$G_{I_{OL}\_compen\_gain}(s) = \frac{266.01}{1.66\times10^{-5}s^2 + 66.5\times10^{-3}s + 6.65\times10^{-5}} \quad (6.2)$$

Figure 6.2 shows the bode plot of the gain-compensated open-loop transfer function of the inner current controller. It can be seen that the magnitude curve crosses the 0dB line at the desired crossover frequency.

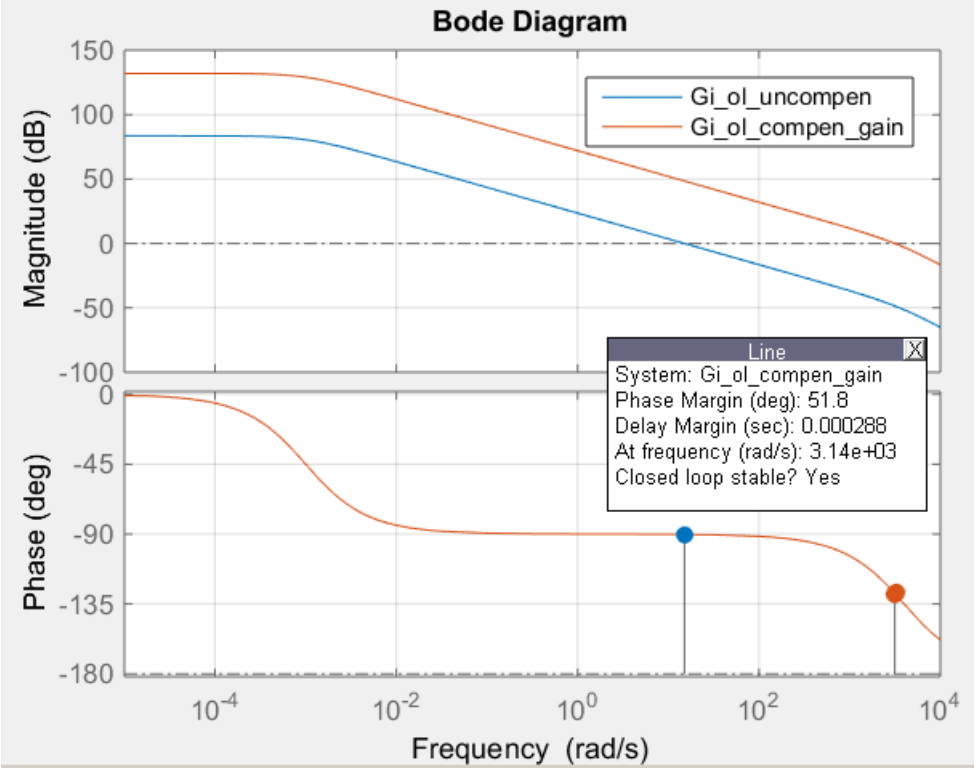

Figure 6. 2: Bode plot of the gain-compensated open-loop transfer function of the inner current controller

The phase-margin at the desired crossover frequency is 51.8˚. The desired phase-margin of 57.85˚ can be obtained by shifting the phase curve up. This is done by applying a phase-lead compensator to the gain-compensated system.

6.1.1.3 Phase-lead compensator design

The phase-lead compensator is used to shift the phase curve up. This alternatively boosts the current phase margin to the desired value at the specified bandwidth. Therefore, the first step is to compute the phase-boost needed to obtain the desired phase margin. This is done by subtracting the phase margin of the current system from the desired phase margin as follow,

Phase-boost=$PM_{desired}$-$PM_{current}$

Phase-boost= 57.85°-51.8°= 6.05°

The phase-boost is used to locate the pole p_c and zero Zc of the phase-lead compensator. This is done by calculating the frequency [Hz] where the pole and zero will be located using Eq. (6.3)[92]

$$\begin{aligned} f_z &= f_{BW}\sqrt{\frac{1-\sin(phase-boost)}{1+\sin(phase-boost)}} \\ f_p &= f_{BW}\sqrt{\frac{1+\sin(phase-boost)}{1-\sin(phase-boost)}} \end{aligned} \tag{6.3}$$

Where f_{BW} is the bandwidth frequency, which in this study is equal to 500Hz. Therefore, f_p and f_z are calculated as follow

$$f_z = 500\sqrt{\frac{1-\sin(6.05^o)}{1+\sin(6.05^o)}} = 449.81Hz$$
$$f_p = 500\sqrt{\frac{1+\sin(6.05^o)}{1-\sin(6.05^o)}} = 555.79Hz$$

The angular frequencies where the pole and zero of the phase-lead compensator are located are calculated as follow

$$\omega_z = 2\pi \times 449.81Hz = 2826.24rad/s$$
$$\omega_p = 2\pi \times 555.79Hz = 3492.13rad/s$$

Therefore, the transfer function of the phase-lead compensator is given by Eq. (6.4)

$$\begin{aligned} &\mathrm{G}_{\mathrm{lead}}(\mathrm{s}) = \mathrm{G}_{\mathrm{co}}\left(\frac{\tau_{lead}\mathrm{s}+1}{\alpha\tau_{lead}\mathrm{s}+1}\right) = \frac{31.8\times10^{-5}s+0.899}{28.6\times10^{-5}s+1} \\ &where; \\ &\alpha = \omega_{\mathrm{z}}/\omega_p = 2826.24/3492.13 = 0.809 \\ &\mathrm{G}_{\mathrm{co}} = \sqrt{\alpha} = \sqrt{0.809} = 0.899 \\ &\tau_{lag} = 1/\omega_z = 1/2826.24 = 0.354\times10^{-3} \end{aligned} \tag{6.4}$$

The phase-lead compensator is applied to the gain-compensated system, and hence, multiplying Eq. (6.2) by Eq. (6.4) gives Eq. (6.5) which represents the phase-lead compensated open-loop transfer function of the inner current control loop.

$$\begin{aligned} &G_{I_{,OL\_compen\_lead}}(s) = G_{I_{,OL\_compen\_gain}}(s)\times G_{lead}(s) \\ &G_{I_{,OL\_compen\_lead}}(s) = \frac{84.7\times10^{-3}s+239.3}{4.76\times10^{-9}s^3+3.57\times10^{-5}s^2+66.5\times10^{-3}s+6.65\times10^{-5}} \end{aligned} \tag{6.5}$$

Figure 6.3 illustrates the magnitude and phase curves of the phase-lead compensated open-loop transfer function of the inner current control loop.

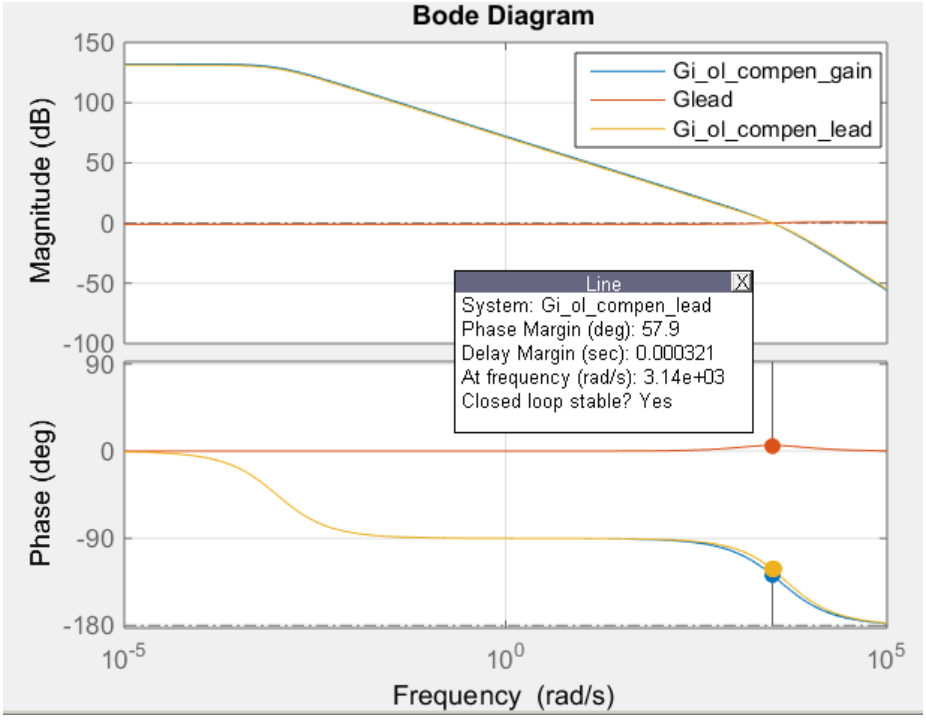

Figure 6. 3: Bode plot of the phase-lead compensated inner current controller's open-loop transfer function

It is observed that the phase-lead compensator shifted the phase curve down to yield the phase margin of 57.9°. The bandwidth is maintained at $3.14x10^3$rad/s (500Hz). Therefore, the phase-margin and bandwidth design specifications have been met. Figure 6.4 shows the step response curve indicating the peak response of the uncompensated, gain-compensated and phase-lead compensated closed-loop transfer function of the inner current control loop.

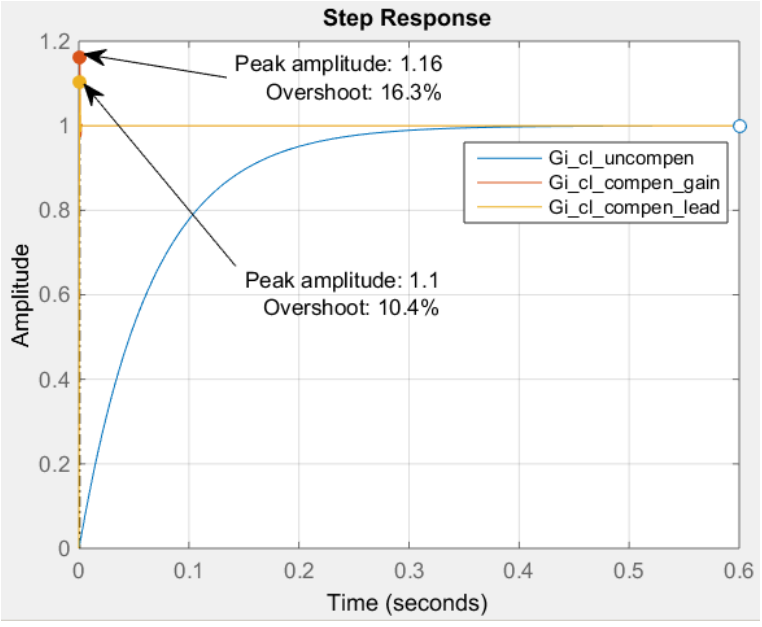

Figure 6. 4: Peak-response of the uncompensated, gain-compensated and phase-lead compensated transfer functions

It can be observed that the overshoot of the gain-compensated system is 16.2%, while the phase-lead compensator further reduced the overshoot to 10.4%. Figure 6.5 shows the step response curve indicating the settling time of the uncompensated, gain-compensated and phase-lead compensated closed-loop transfer functions of the inner current control loop.

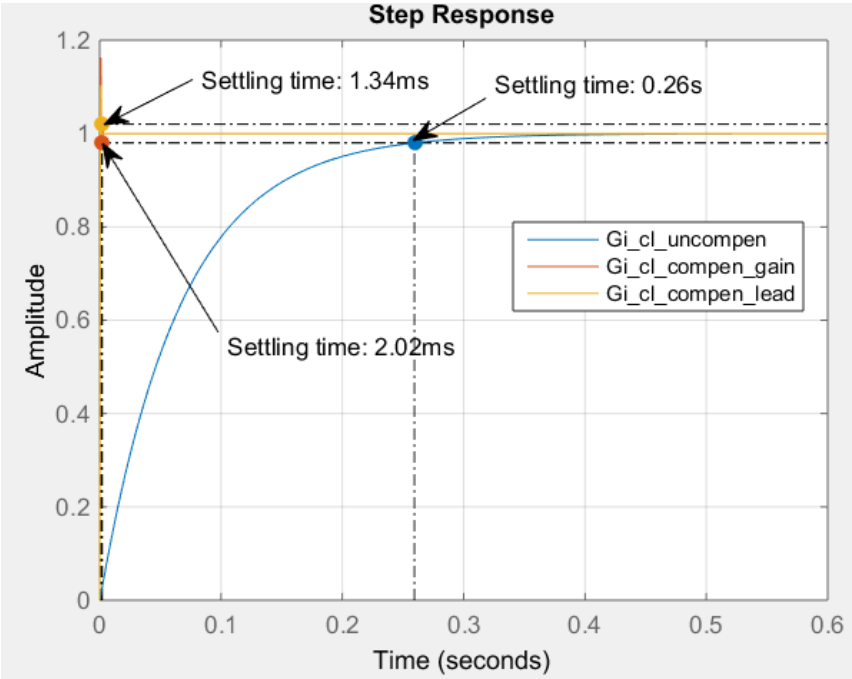

Figure 6. 5: Settling time of the uncompensated, gain-compensated and phase-lag compensated transfer functions

It can be observed that gain *K* reduced the settling time of the uncompensated system from 0.26s to 2.02ms. The phase-lead compensator further reduced the settling time of the gain-compensated system to 1.34ms which is still within the desired settling time of 1.45ms. This illustrates that the settling time design specification has been met.

Figure 6.6 shows the step response curve indicating the rise time of the uncompensated, gain-compensated and phase- lead compensated closed-loop transfer functions of the inner current control loop.

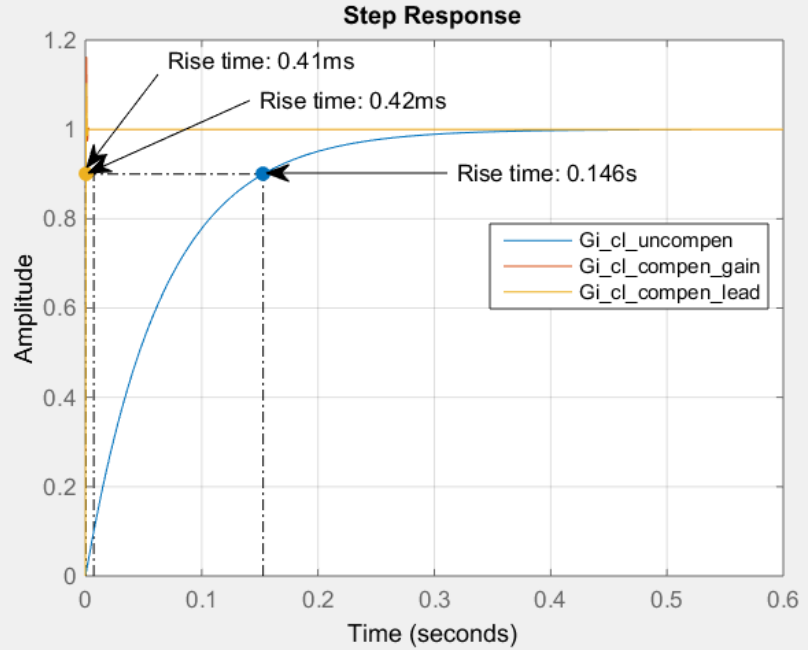

Figure 6. 6: Rise time of the uncompensated, gain- compensated and phase-lag compensated transfer functions

It can be observed that gain *K* reduced the rise time of the uncompensated system from 0.146s to 0.41ms and hence speeding up the system response. However, the phase-lead compensator increased the gain-compensated system's rise time to 0.42ms which is within the desired rise time of 0.52ms. This illustrates that the rise time design specification has been met.

6.1.2 Outer Control Loops: Active power (MPPT) and Reactive power control

The design specifications to be met by the compensators in the outer loop controller are:

- A bandwidth of 785.40 rad/s (125Hz)
- Overshoot of 5% resulting in a damping ratio of 0.69
- A phase margin of 57.85˚
- A gain margin of 0dB at the desired bandwidth/crossover frequency
- A settling time of 5.79ms
- A rise time of 2.09ms

To obtain these design specifications, the performance of the systems' open-loop transfer functions will be analyzed using Bode plots and step response curves. This will be done before and after the compensators have been applied to the uncompensated systems.

6.1.2.1 Active Power (MPPT) Outer Control Loop

6.1.2.1(a) The uncompensated System

The outer active power control loop generates the d-component of the grid's reference current. Recalling the open-loop transfer function of the outer MPPT control loop given by Eq. (4.62), and substituting in the grid-side converter's voltage of 620.62V gives Eq. (6.6)

$$G_{P_{OL}\_uncompen}(s) = 930.9 \times G_{C,P}(s) \times G_{I_{CL}\_compen\_lead}(s) \tag{6.6}$$

Where, $G_{I,cl\_compen\_lead}(s)$ is the closed-loop transfer function of the phase-lag compensated grid-side inner current loop given by Eq. (6.7).

$$G_{I_{CL}\_compen\_lead}(s) = \frac{84.67\times10^{-3}s + 239.3}{4.76\times10^{-9}s^3 + 3.57\times10^{-5}s^2 + 151.2\times10^{-3}s + 239.3} \tag{6.7}$$

The bode plot used for the system's stability analysis is plotted using Eq. (6.8) by substituting in the compensated closed loop transfer function of the d-component of the grid current.

$$G_{P_{OL}\_uncompen}(s) = \frac{(157.7s + 4.46\times10^{5}) \times G_{C,P}(s)}{9.52\times10^{-9}s^3 + 7.13\times10^{-5}s^2 + 302.3\times10^{-3}s + 478.6} \tag{6.8}$$

Figure 6.7 shows the bode plot of the uncompensated outer active power control loop. That is, $G_{C,P}(s)$ is equal to one.

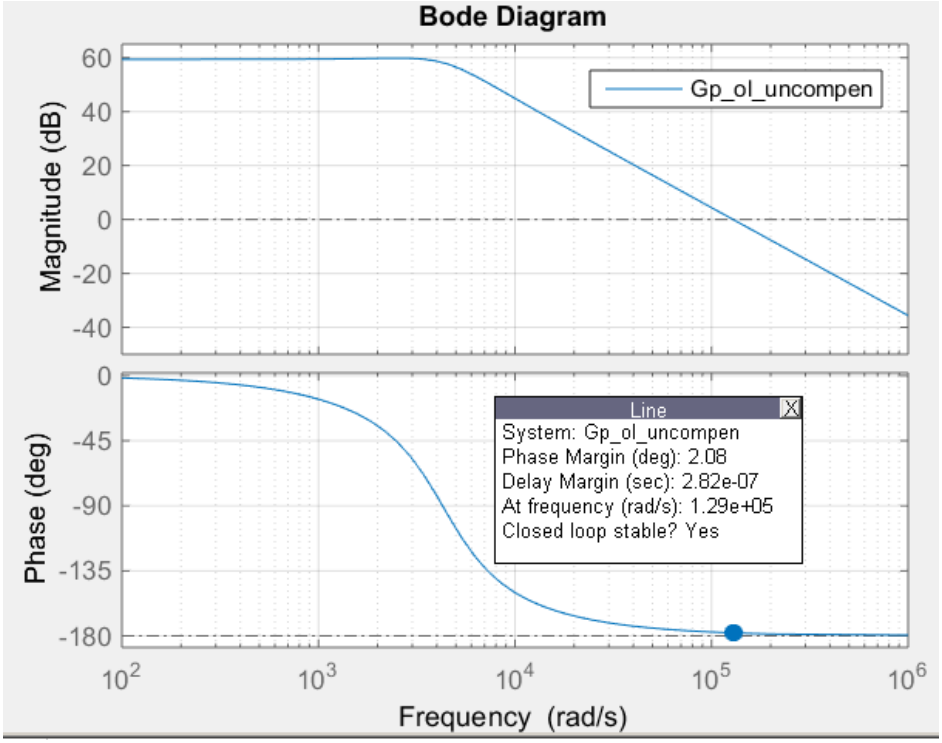

Figure 6. 7: Bode plot of the uncompensated outer active power controller's open-loop transfer function

It can be observed that the phase-margin and bandwidth of the uncompensated system are 2.08˚ and 1.29x10^5 rad/s, respectively. The bandwidth is much higher than the desired value. Furthermore, the phase-margin is very small. To reduce the bandwidth, a phase-lag compensator is needed to drop the magnitude curve down so that it crosses the 0dB line at the desired bandwidth of 785.40rad/s (125Hz). The compensator is designed using the procedures outlined in Chapter 2.

6.1.2.1(b) Phase-lag compensator design

In this context, the phase-lag compensator is used to shift the magnitude curve down in order to reduce the bandwidth to the desired value. Therefore, the first step is to identify the gain magnitude corresponding to the desired bandwidth on the magnitude curve. The gain magnitude at the desired bandwidth is 59.4dB as shown in Figure 6.8.

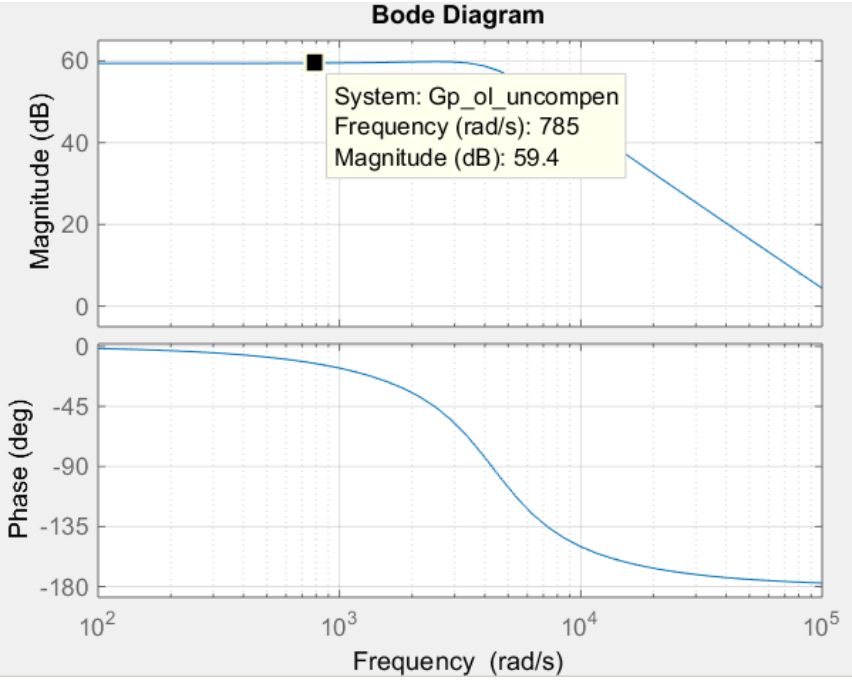

Figure 6. 8: Gain magnitude at the desired bandwidth

The magnitude at the desired crossover frequency is then used to calculate the attenuation α needed to shift the magnitude curve down. The attenuation is used to locate the pole and zero of the phase-lag compensator. The attenuation α is calculated using Eq. (6.9)

$$\alpha = 10^{\frac{gain}{10}} = 10^{\frac{59.4}{10}} = 870963.59 \tag{6.9}$$

The frequencies where the pole and zero will be located are calculated using Eq. (6.10). Therefore the pole and zero of the phase-lag compensator with a bandwidth of 785 rad/s and an attenuation of 870963.59 are calculated as follow

$$z_c = \omega_{bandwidth} \times \sqrt{\alpha} = 785 \times \sqrt{870963.59} = 0.733 \times 10^6 \, rad/s$$
$$p_c = \frac{z_c}{\alpha} = \frac{0.733 \times 10^6}{870963.59} = 0.841 rad/s \quad (6.10)$$

Therefore, the transfer function of the phase-lag compensator is given by Eq. (6.11)

$$G_{lag}(s) = \frac{(s/z_c + 1)}{(s/p_c + 1)} = \frac{1.36 \times 10^{-6} s + 1}{1.195 s + 1} \quad (6.11)$$

Multiplying Eq. (6.10) by Eq. (6.8) gives Eq. (6.12) which represents the open-loop transfer function of the phase-lag compensated system.

$$G_{P_{OL}\_compen\_lag}(s) = \frac{0.214 \times 10^{-3} s^2 + 158.3 s + 4.45 \times 10^5}{1.138 \times 10^{-8} s^4 + 8.53 \times 10^{-5} s^3 + 0.361 s^2 + 572.3 s + 478.6} \quad (6.12)$$

Figure 6.9 illustrates the magnitude and phase curves of the phase-lag compensated open-loop transfer function of the outer active power control loop.

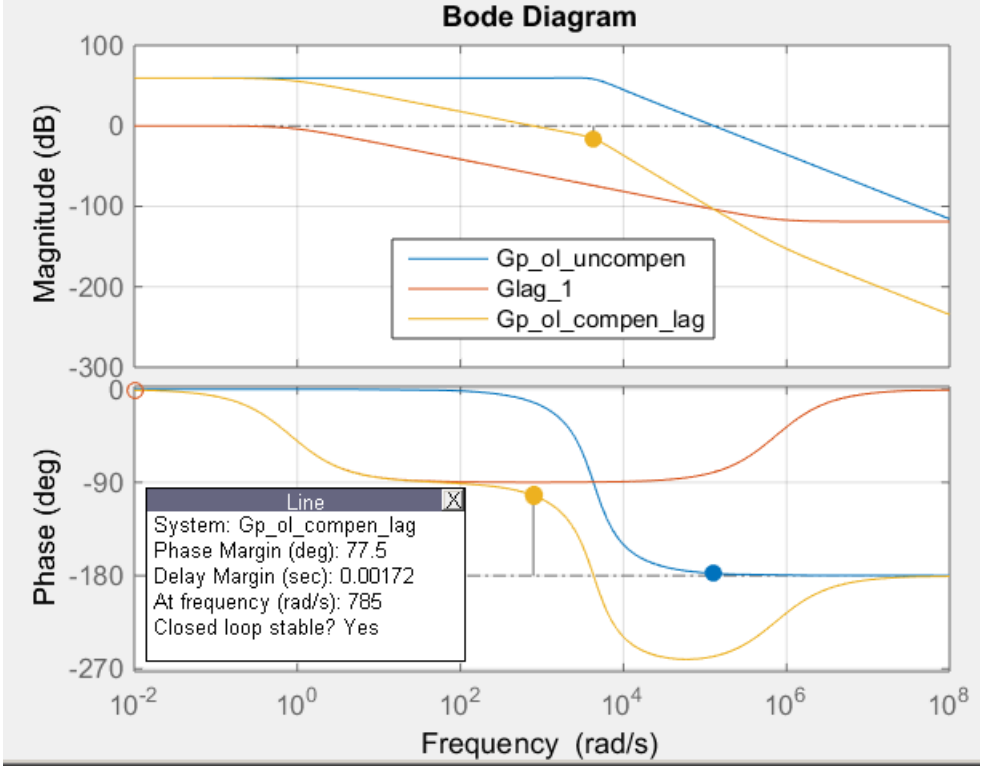

Figure 6. 9: Bode plot of the phase-lag compensated active power controller

It is observed that phase-lag compensator shifted the magnitude curve down by 59.4dB at the bandwidth of 785 rad/s, and hence, the bandwidth design specification has been met. The phase-margin at the desired bandwidth is 77.5°. Therefore, a second phase-lag compensator is needed to shift the phase curve down to obtain the desired phase margin of 57.85°.

6.1.2.1(c) Second Phase-lag compensator design

The phase-lag compensator is used to shift the phase curve down. This alternatively attenuates the current phase margin to the desired value at the specified bandwidth. Therefore, the first step is to compute the phase-attenuation needed to obtain the desired phase margin. This is done by subtracting the phase margin of the current system from the desired phase margin as follow,

Phase-attenuation=$PM_{desired}$-$PM_{current}$

Phase-attenuation= 57.85°-77.5°= -19.65°

The phase shift that needs to be eliminated is used to locate the pole p_c and zero *Zc* of the phase- lag compensator. This is done by calculating the frequency [Hz] where the pole and zero will be located using Eq. (6.3)

$$f_z = f_{BW}\sqrt{\frac{1-\sin(phase-attenuation)}{1+\sin(phase-attenuation)}} = 125.\sqrt{\frac{1-\sin(-19.65^o)}{1+\sin(-19.65^o)}} = 177.36Hz$$

$$f_p = f_{BW}\sqrt{\frac{1+\sin(phase-attenuation)}{1-\sin(phase-attenuation)}} = 125\sqrt{\frac{1+\sin(-19.65^o)}{1-\sin(-19.65^o)}} = 88.10Hz$$

The angular frequencies where the pole and zero of the phase-lag compensator will be located are calculated as follow

$$\omega_z = 2\pi \times 177.36Hz = 1114.39rad/s$$
$$\omega_p = 2\pi \times 88.10Hz = 553.55rad/s$$

Therefore, the transfer function of the phase-lag compensator is given by Eq. (6.13)

$$G_{lag_2}(s) = G_{co}\left(\frac{\tau_{lag}s+1}{\alpha\tau_{lag}s+1}\right) = \frac{1.27\times10^{-3}s+1.419}{1.81\times10^{-3}s+1}$$

where;

$$\alpha = \omega_z/\omega_p = 1114.39/553.55 = 2.01 \quad (6.13)$$
$$G_{co} = \sqrt{\alpha} = \sqrt{2.01} = 1.42$$
$$\tau_{lag} = 1/\omega_z = 1/1114.39 = 0.898\times10^{-3}$$

The second phase-lag compensator is applied to the phase-lag compensated system, and hence, multiplying Eq. (6.12) by Eq. (6.13) gives the transfer function of the phase-lag-lag compensated system as follow

$$G_{P_{,OL}\_compen\_lag\_lag}(s) = G_{P_{,OL}\_compen\_lag}(s)\times G_{lag_2}(s)$$
$$= \frac{2.723\times10^{-7}s^3+0.202s^2+791.8s+6.32\times10^5}{2.056\times10^{-11}s^5+1.654\times10^{-7}s^4+0.738\times10^{-3}s^3+1.395s^2+573.2s+478.6} \quad (6.14)$$

Figure 6.10 represents the bode plot of the active power controller's open-loop transfer function compensated with the two phase-lag compensators.

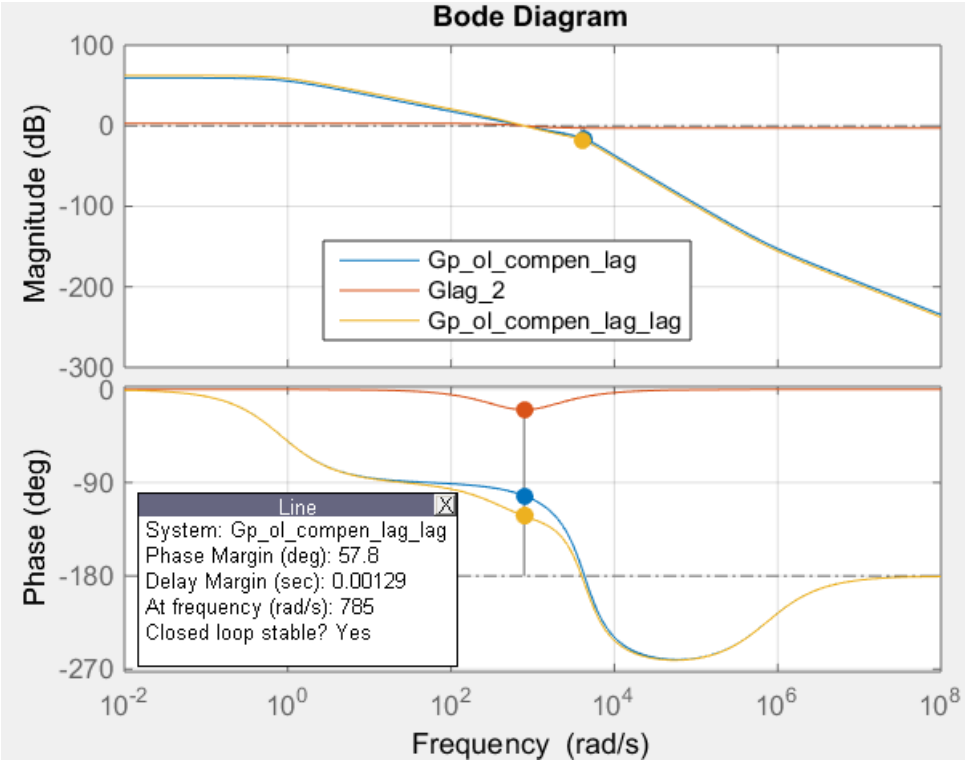

Figure 6. 10: Bode plot of the phase-lag-lag compensated active power control loop

It is observed that the second phase-lag compensator shifted the phase curve down to yield the phase-margin of 57.8°. The bandwidth is maintained at 785 rad/s (125Hz). Therefore, the phase-margin and bandwidth design specifications have been met.

Figure 6.11 shows the step response curve indicating the peak responses of the uncompensated, the phase-lag compensated and phase-lag-lag compensated closed-loop transfer function of the outer active power control loop.

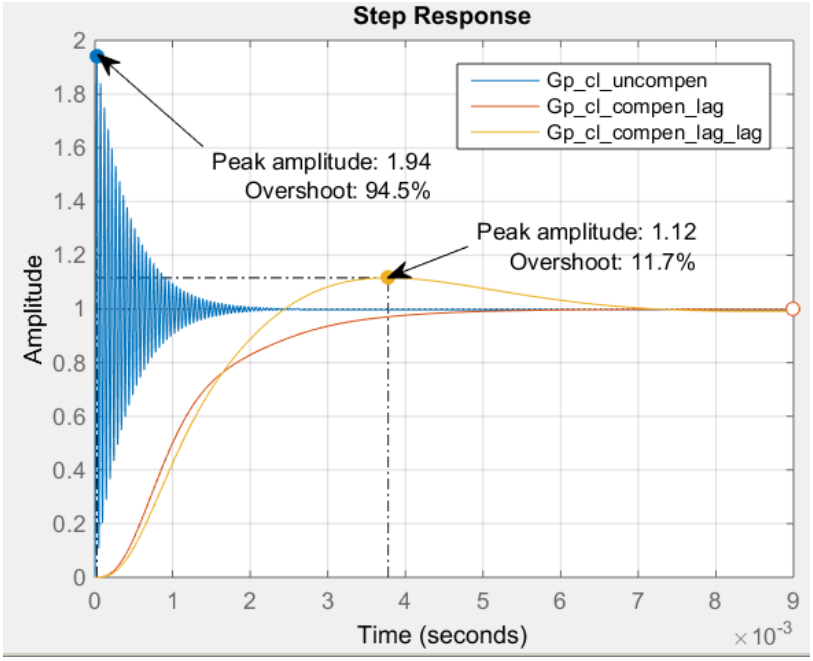

Figure 6. 11: Peak-response of the uncompensated and phase-lag compensated transfer functions

It is observed that the phase-lag compensated system reduced the percentage overshoot of the uncompensated system from 94.5% to 11.7%. Figure 6.12 shows the step response curve indicating the settling time of the uncompensated, phase-lag compensated and phase-lag-lag compensated closed-loop transfer functions of the outer active power control loop.

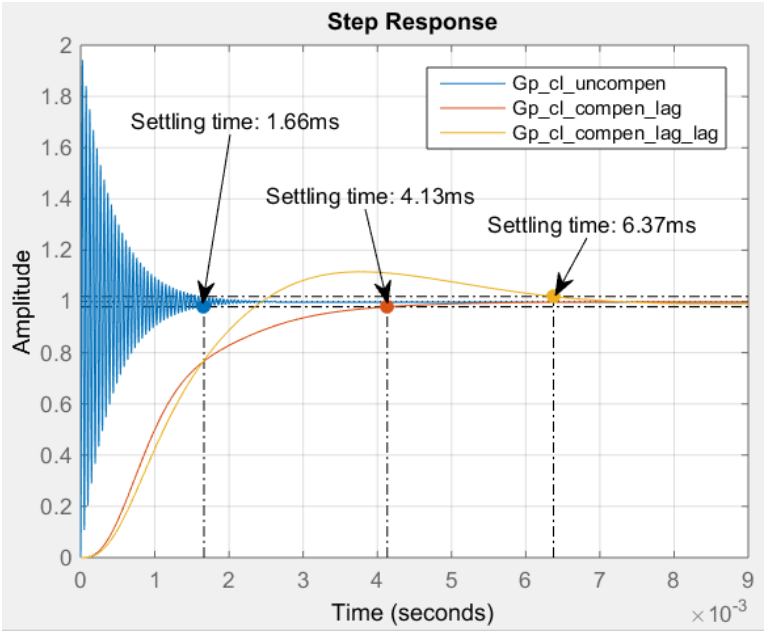

Figure 6. 12: Settling time of the uncompensated and phase-lag compensated transfer functions

It is observed that the first phase-lag compensator increased the settling time of the uncompensated system from 1.66ms to 4.13ms. The second phase-lag compensator further increased the settling time of the phase-lag compensated system 6.37ms.

Figure 6.13 shows the step response curve indicating the rise time of the uncompensated, phase-lag compensated and phase-lag-lag compensated closed-loop transfer function of the outer active power control loop.

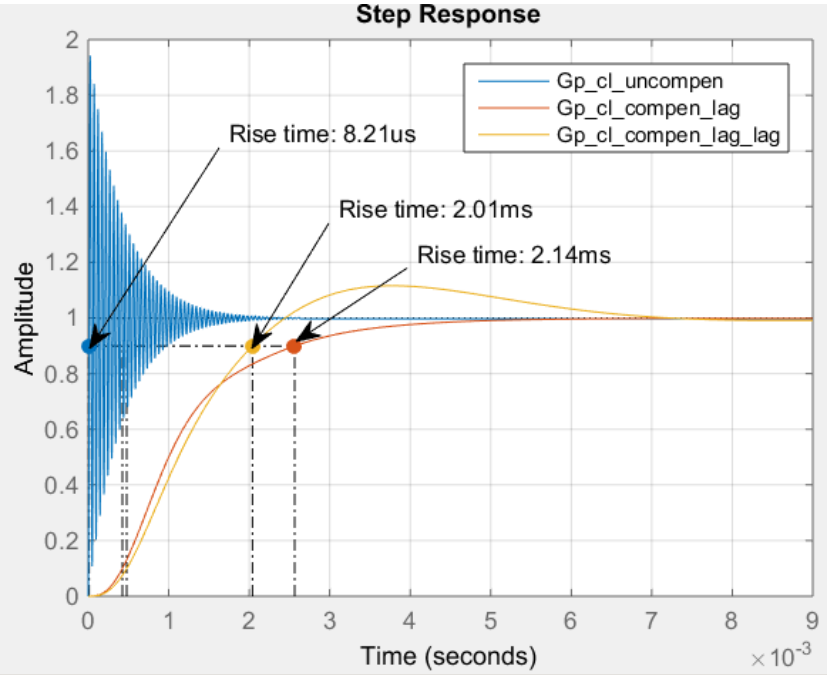

Figure 6. 13: Rise time of the uncompensated and phase-lag compensated transfer functions

It is observed that the first phase-lag compensator increased the rise time of the uncompensated system from 8.21μs to 2.14ms. The second phase-lag compensator decreased the rise time of the phase-lag compensated system to 2.01ms which is within the desired rise time of 2.09ms. This illustrates that the rise time design specification has been met.

6.1.2.2 Reactive Power Outer Control Loop

6.1.2.2(a) The uncompensated system

The outer reactive power control loop generates the q-component of the grid's reference current. Recalling the open-loop transfer function of the outer reactive power control loop given by Eq. (4.66), and substituting in the grid-side converter's voltage of 620.62V gives Eq. (6.15)

$$G_{Q_{,OL\_uncompen}}(s) = -930.9 \times G_{C,Q}(s) \times G_{I_{,CL\_compen\_lead}}(s) \tag{6.15}$$

Where, $G_{C,cl\_compen\_lead}(s)$ is the closed-loop transfer function of the phase-lead compensated inner current control loop which is given by Eq. (6.7).

The bode plot used for the system's stability analysis is plotted using Eq. (6.16) by substituting in the compensated closed-loop transfer function of the q-component of the grid current given by Eq. (6.7)

$$G_{Q_{OL}\_uncompen}(s) = \frac{(-157.7s - 4.46\times10^{5})\times G_{C,Q}(s)}{9.521\times10^{-9}s^{3} + 7.134\times10^{-5}s^{2} + 0.302s + 478.6} \qquad (6.16)$$

Figure 6.14 illustrates the magnitude and phase curves of the uncompensated open-loop transfer function of the outer reactive power control loop. That is, $G_{C,Q}(s)$ is equal to one.

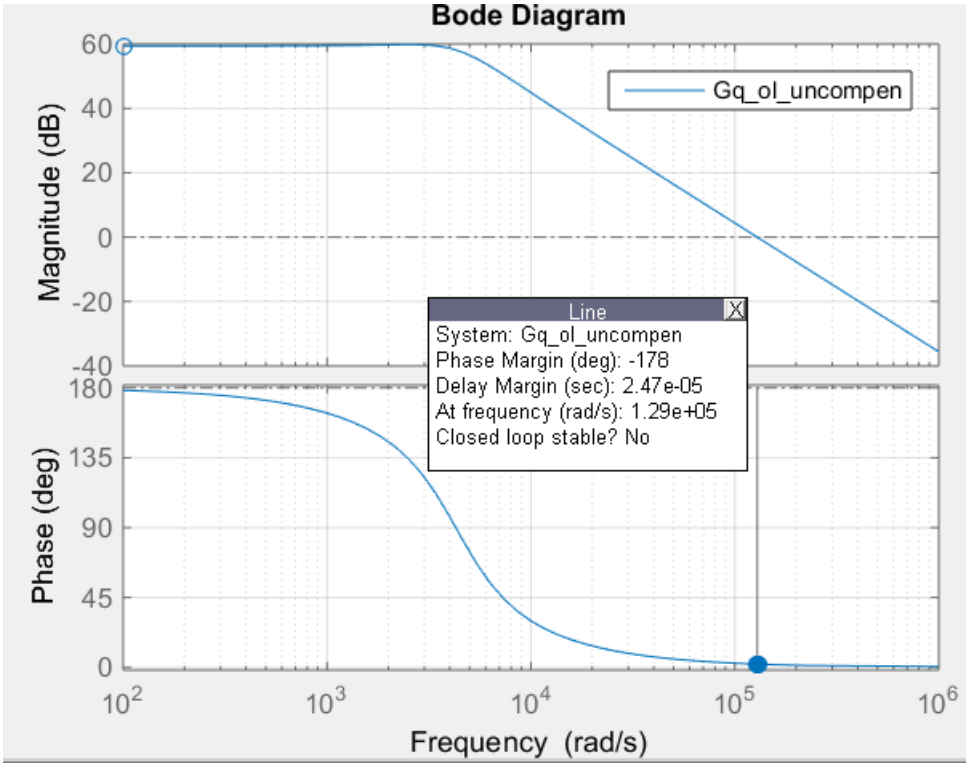

Figure 6. 14: Bode plot of the uncompensated outer reactive power controller's open-loop transfer function

It is observed that the phase-margin and bandwidth of the uncompensated system are -178˚ and 1.29x10^5 rad/s, respectively. The bandwidth is much higher than the desired value. Furthermore, the phase-margin is negative making the system unstable. To reduce the bandwidth, a phase-lag compensator is needed to drop the magnitude curve down so that it crosses the 0dB line at the desired bandwidth of 785rad/s (125Hz). The compensator is designed using the procedures outlined in Chapter 2.

6.1.2.2(b) Phase-lag compensator design

The phase-lag compensator is used to shift the magnitude curve down in order to reduce the bandwidth to the desired value. Therefore, the first step is to identify the gain magnitude corresponding to the desired bandwidth on the magnitude curve.

The gain magnitude at the desired bandwidth is 59.4dB as shown in Figure 6.15.

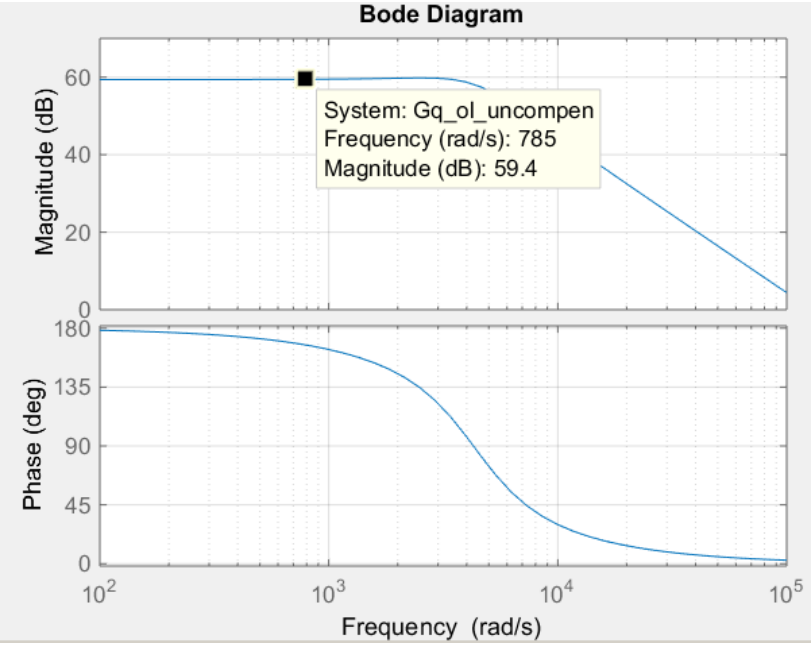

Figure 6. 15: Gain magnitude at the desired bandwidth

The magnitude at the desired crossover frequency is then used to calculate the attenuation α needed to shift the magnitude curve down. The attenuation is used to locate the pole and zero of the phase-lag compensator. The attenuation α is calculated using Eq. (6.9)

$$\alpha = 10^{\frac{gain}{10}} = 10^{\frac{59.4}{10}} = 870963.59$$

The frequencies where the pole p_c and zero z_c will be located are calculated using Eq. (6.10). Therefore the pole and zero of the phase-lag compensator with a bandwidth of 785 rad/s and an attenuation of 870963.59 are calculated as follow

$$z_c = \omega_{bandwidth} \times \sqrt{\alpha} = 785 \times \sqrt{870963.59} = 0.733 \times 10^6 \, rad/s$$

$$p_c = \frac{z_c}{\alpha} = \frac{0.733 \times 10^6}{870963.59} = 0.841 rad/s$$

Therefore, the transfer function of the phase-lag compensator is given by Eq. (6.17)

$$G_{lag}(s) = \frac{(s/z_c + 1)}{(s/p_c + 1)} = \frac{-1.356 \times 10^{-6} s - 1}{1.195s + 1} \quad (6.17)$$

Multiplying Eq. (6.16) by Eq. (6.17) gives Eq. (6.18) which represents the open-loop transfer function of the phase-lag compensated system.

$$G_{Q_{OL}\_compen\_lag}(s) = \frac{0.214 \times 10^{-3} s^2 + 158.3s + 4.46 \times 10^5}{1.14 \times 10^{-8} s^4 + 8.53 \times 10^{-5} s^3 + 0.361 s^2 + 572.3s + 478.6} \quad (6.18)$$

Figure 6.16 illustrates the magnitude and phase curves of the phase-lag compensated open-loop transfer function of the reactive power control loop.

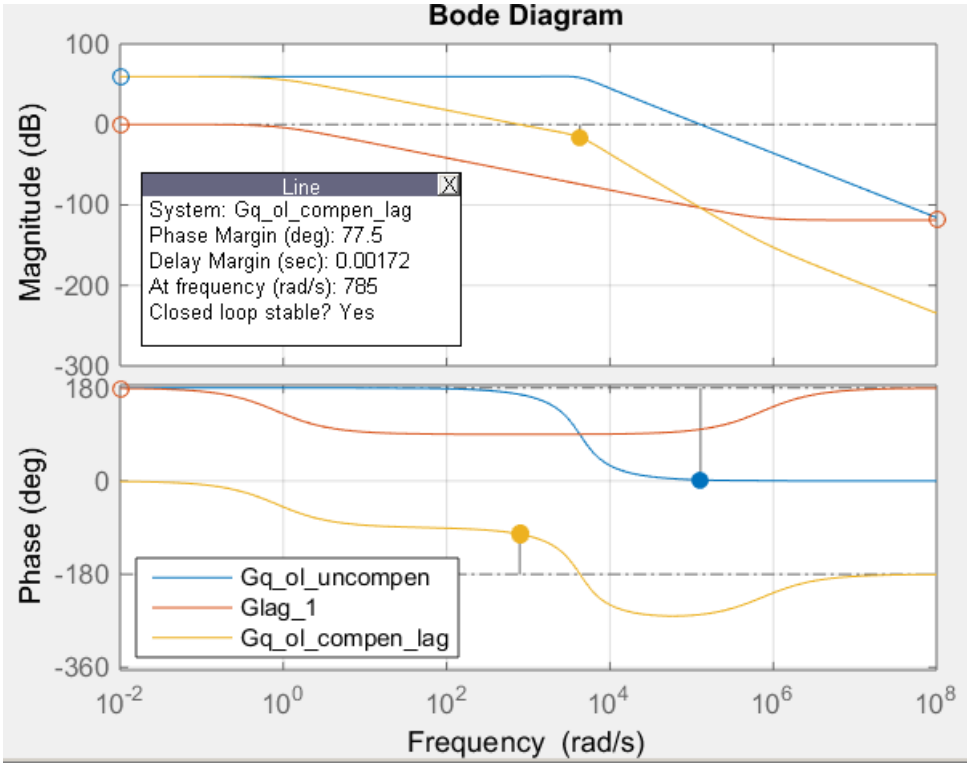

Figure 6. 16: Bode plot of the phase-lag compensated reactive power controller

It is observed that phase-lag compensator shifted the magnitude curve down by 59.4dB at the bandwidth of 785rad/s, and hence, the bandwidth design specification has been met. The phase-margin at the desired bandwidth is 77.5°. Therefore, a second phase-lag compensator is needed to shift the phase curve down to obtain the desired phase margin of 57.85°.

6.1.2.2(c) Second Phase-lag compensator design

The phase-lag compensator is used to shift the phase curve down. This alternatively attenuates the current phase-margin to the desired value at the specified bandwidth. Therefore, the first step is to compute the phase-attenuation needed to obtain the desired phase margin. This is done by subtracting the phase margin of the current system from the desired phase margin as follow,

$\text{Phase-attenuation}=PM_{desired}-PM_{current}$

$\text{Phase-attenuation}= 57.85°-77.5°= -19.65°$

The phase-attenuation is used to locate the pole p_c and zero z_c of the phase-lag compensator. This is done by calculating the frequency [Hz] where the pole and zero will be located using Eq. (6.3)

$$f_z = f_{BW}\sqrt{\frac{1-\sin(phase-attenuation)}{1+\sin(phase-attenuation)}} = 125\sqrt{\frac{1-\sin(-19.65^o)}{1+\sin(-19.65^o)}} = 177.36Hz$$

$$f_p = f_{BW}\sqrt{\frac{1+\sin(phase-attenuation)}{1-\sin(phase-attenuation)}} = 125\sqrt{\frac{1+\sin(-19.65^o)}{1-\sin(-19.65^o)}} = 88.10Hz$$

The angular frequencies where the pole and zero of the phase-lag compensator will be located are calculated as follow

$$\omega_z = 2\pi \times 177.36Hz = 1114.39rad/s$$
$$\omega_p = 2\pi \times 88.10Hz = 553.55rad/s$$

Therefore, the transfer function of the phase-lag compensator is given by Eq. (6.19)

$$\mathrm{G}_{\mathrm{lag}_2}(\mathrm{s}) = \mathrm{G}_{\mathrm{co}}\left(\frac{\tau_{lag}\mathrm{s}+1}{\alpha\tau_{lag}\mathrm{s}+1}\right) = \frac{1.27\times10^{-3}s+1.419}{1.81\times10^{-3}s+1}$$

where;

$$\alpha = \omega_z/\omega_p = 1114.39/553.55 = 2.013 \quad (6.19)$$

$$\mathrm{G}_{\mathrm{co}} = \sqrt{\alpha} = \sqrt{2.013} = 1.42$$

$$\tau_{lag} = 1/\omega_z = 1/1114.39 = 0.90\times10^{-3}$$

The second phase-lag compensator is applied to the phase-lag compensated system, and hence, multiplying Eq. (6.18) by Eq. (6.19) gives the transfer function of the phase-lag-lag compensated system as follow

$$G_{Q_{,OL}\_compen\_lag\_lag}(s) = G_{Q_{,OL}\_compen\_lag}(s)\times G_{lag_2}(s)$$
$$= \frac{2.723\times10^{-7}s^3+0.202s^2+791.8s+6.32\times10^5}{2.056\times10^{-11}s^5+1.65\times10^{-7}s^4+0.738\times10^{-3}s^3+1.395s^2+573.2s+478.6} \quad (6.20)$$

Figure 6.17 illustrates the magnitude and phase curves of the reactive power controller's open-loop transfer function compensated with two phase-lag compensators.

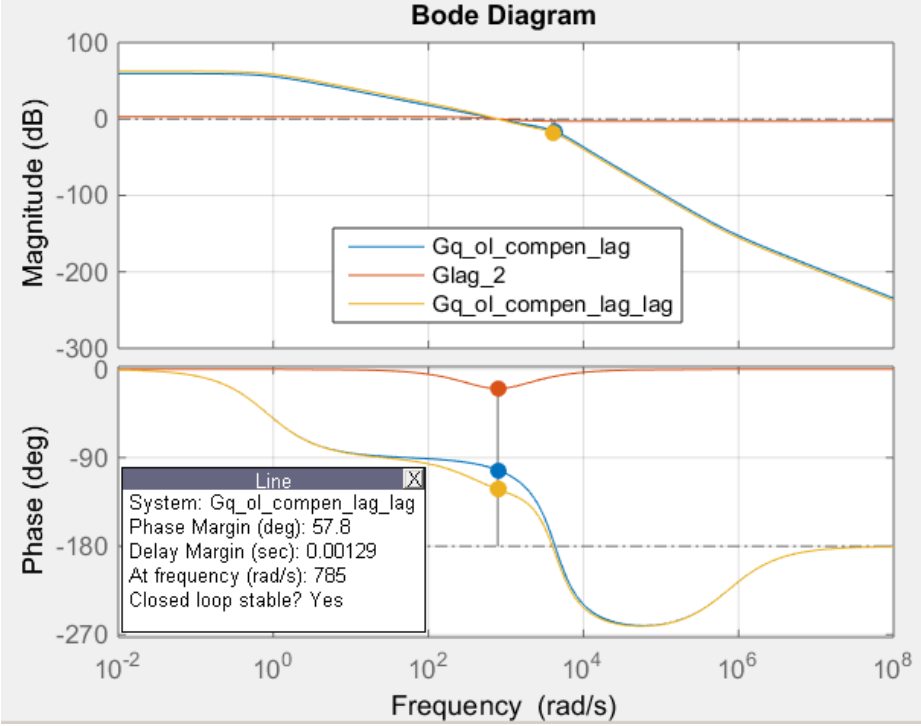

Figure 6. 17: Bode plot of the phase-lag-lag compensated reactive power control loop

It is observed that the second phase-lag compensator shifted the phase curve down to yield the phase-margin of 57.8°. The bandwidth is maintained at 785 rad/s (125Hz). Therefore, the phase-margin and bandwidth design specifications have been met.

Figure 6.18 shows the step response of the uncompensated closed-loop transfer function of the outer reactive power control loop.

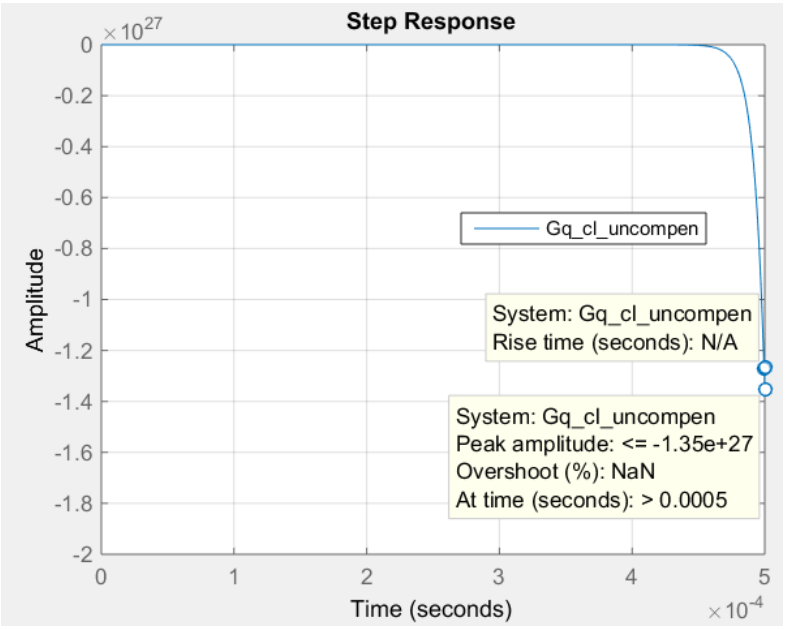

Figure 6. 18: Step response of the uncompensated closed-loop transfer function of the reactive power controller

It is observed that the uncompensated system has an undefined overshoot, settling time and rise time. Figure 6.19 shows the step response curve indicating the peak responses of the phase-lag compensated and phase-lag-lag compensated closed-loop transfer function of the outer reactive power control loop.

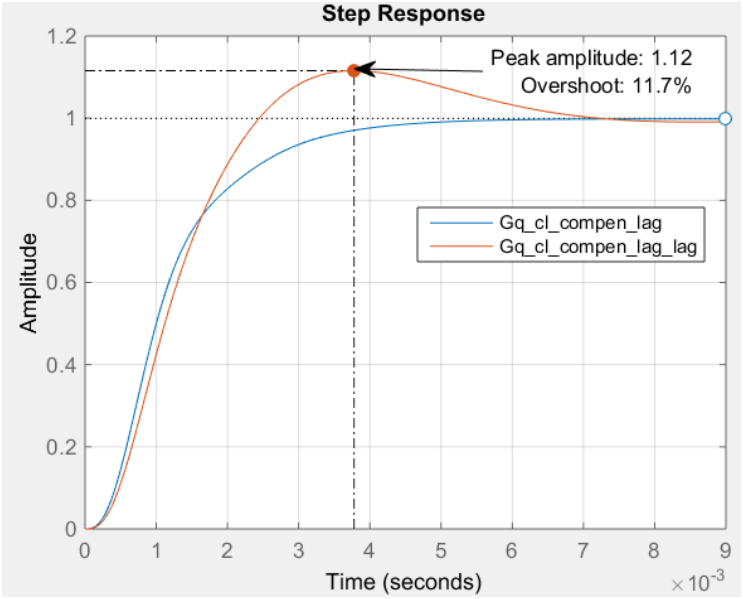

Figure 6. 19: Peak-response of the phase-lag compensated transfer functions

It is observed that the phase-lag compensated system reduced the percentage overshoot of the uncompensated system to 11.7%. Figure 6.20 shows the step response curve indicating the settling time of the phase-lag compensated and phase-lag-lag compensated closed-loop transfer functions of the outer reactive power control loop.

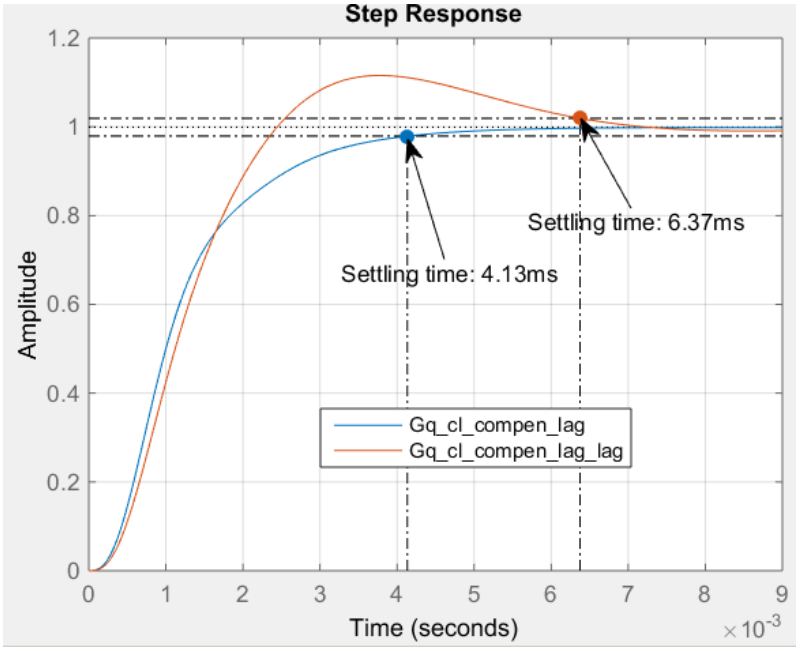

Figure 6. 20: Settling time of the phase-lag compensated transfer functions

It is observed that the first phase-lag compensator increased the settling time of the uncompensated system to 4.13ms. The second phase-lag compensator further increased the settling time of the phase-lag compensated system to 6.37ms. Figure 6.21 shows the step response curve indicating the rise time of the phase-lag compensated and phase-lag-lag compensated closed-loop transfer function of the outer reactive power control loop.

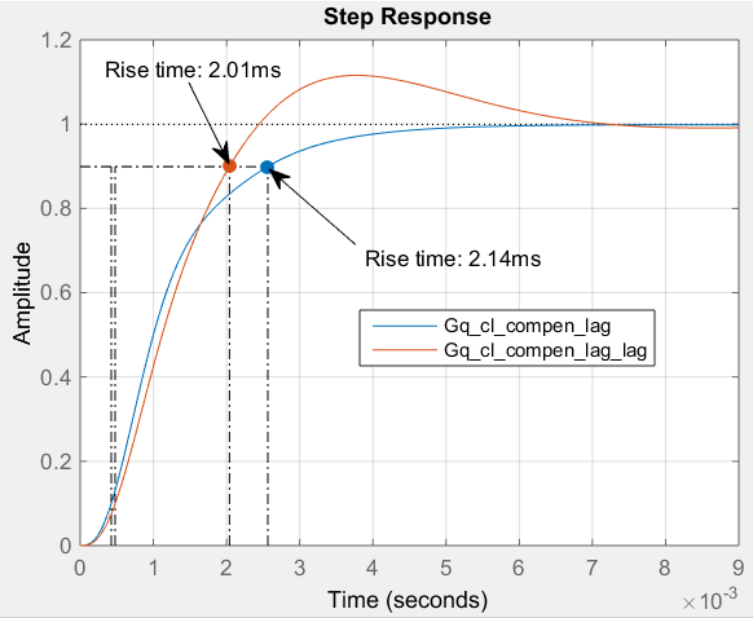

Figure 6. 21: Rise time of the phase-lag compensated transfer functions

It is seen that the rise time of the uncompensated system is undefined as illustrated in Figure 6.18. However, the first phase-lag compensator increased the uncompensated system's rise time to 2.14ms, while the second phase-lag compensator decreased the rise time of the phase-lag compensated system to 2.01ms which is within the desired rise time of 2.09ms. This illustrates that the rise time design specification has been met.

6.2 Chapter Summary

A thorough design and stability analysis of the grid-side converter controller has been carried out in this chapter using bode plots and step response curves in MATLAB software package in order to achieve the desired specifications computed in Chapter 5. The inner current, MPPT and reactive power controllers' performance values of the uncompensated, gain-compensated, and phase-lag compensated systems are summarized in Table 6.1 - Table 6.3

Table 6. 1: Inner current controller's performance values of the uncompensated, gain-compensated and phase-lead compensated system

Design Specification	**Desired values**	**Measured values/ outcome**		
		Uncompensated	***Gain-compensated***	***Phase-lead compensated***
Bandwidth (rad/s)	3141.59	15	$3.14x10^3$	$3.14x10^3$
Phase margin (˚)	57.85	89.8	51.8	57.9
Gain margin (dB)	0	-48.5	0	0
Overshoot (%)	5	undefined	16.3	10.4
Settling time (ms)	1.45	259	2.02	1.34
Rise time (ms)	0.52	146	0.41	0.42

Table 6. 2: MPPT controller's performance values of the uncompensated, gain-compensated and phase-lag compensated system

Design Specification	**Desired Values**	**Measured values/ outcome**		
		Uncompensated	***Gain-compensated***	***Phase-lag compensated***
Bandwidth (rad/s)	785.40	$1.29x10^5$	785	785
Phase margin (˚)	57.85	2.08	77.5	57.8
Gain margin (dB)	0	59.4	0	0
Overshoot (%)	5	94.5	0.99	11.7
Settling time (ms)	5.79	1.66	4.13	6.37
Rise time (ms)	2.09	0.00821	2.14	2.01

Table 6. 3: Reactive power controller's performance values of the uncompensated, gain-compensated and phase-lag compensated system

Design Specification	**Desired values**	**Measured values/ outcome**		
		Uncompensated	***Gain-compensated***	***Phase-lag compensated***
Bandwidth (rad/s)	785.40	$1.29x10^5$	785	785
Phase margin (˚)	57.85	-178	77.5	57.8
Gain margin (dB)	0	59.4	0	0
Overshoot (%)	5	undefined	0.99	11.7
Settling time (ms)	5.79	undefined	4.13	6.37
Rise time (ms)	2.09	undefined	2.14	2.01

CHAPTER 7: WTG SYSTEM MODELLING AND IMPLEMENTATION

This chapter focuses on the implementation of the proposed wind energy conversion system and the pitch-angle, generator-side and grid-side controllers in PSIM software package to further analyse the entire system's performance.

7.1 Proposed Subsystems

The proposed model is made up of a wind turbine equipped with a permanent magnet synchronous generator (PMSG). The WT is to be integrated into a power utility grid via a conversion stage made up of a generator-side converter and a grid-side converter which are interconnected by an intermediate DC-link capacitor. Figure 7.1 shows the proposed subsystems.

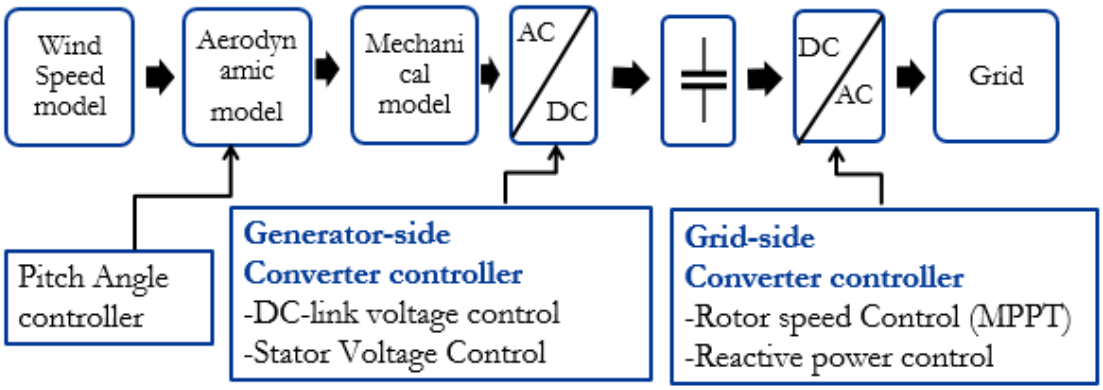

Figure 7. 1: Subsystems' block diagram

The three control schemes implemented on the proposed model are as shown in Fig.7.1, namely: pitch-angle controller, generator-side converter controller, and grid-side converter controller.

7.2 Wind Turbine and PMSG Model

Figure 7.2 illustrates the software implementation of the wind turbine, drive train and the PMSG.

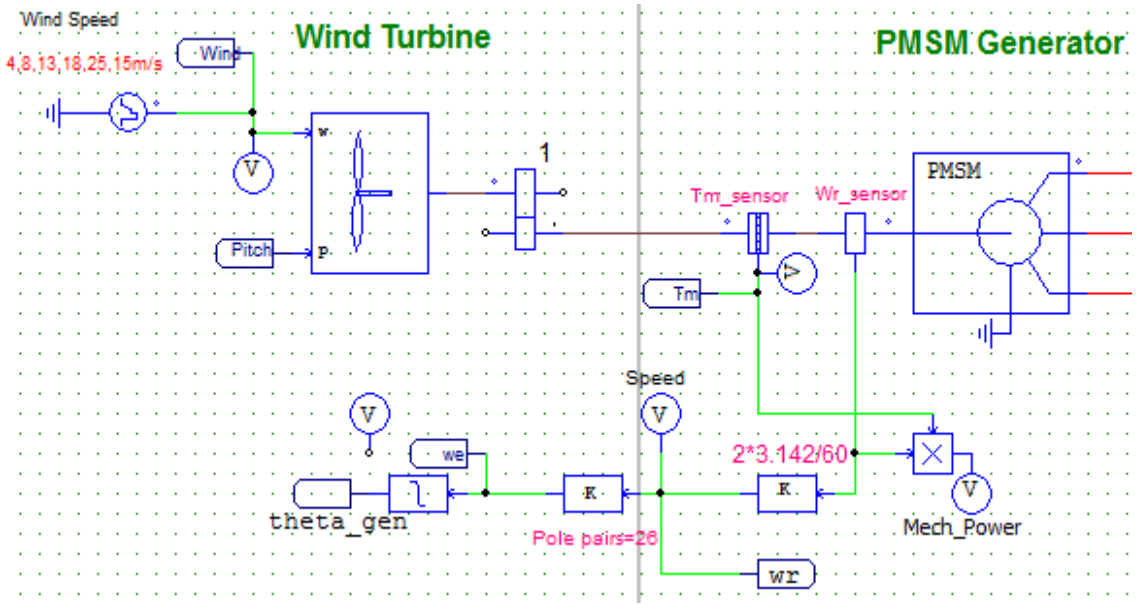

Figure 7. 2: Wind Turbine and PMSG Model

A signal generator is used to generate different wind speeds that serve as an input into the wind turbine block in addition to the pitch angle generated by the pitch angle controller. The wind turbine block is coupled to the PMSG via a one mass/ramped drive train. The torque and speed sensors are used to measure the mechanical torque in Nm and rotor speed in revolution per minute (rpm), respectively. The measured rotor speed is used to generate the angle *theta_gen* that is used to carry out Clarke and Park Transformation of the stator voltage and current.

7.3 Generator-side and Grid-side Converter Model

The generator-side and grid-side converter stations are of 3-level Neutral Point Clamped VSC topology. Each phase/leg is made up of four switches adding up to twelve switches per converter as shown in Figure 7.3. The two converters are interconnected via a DC-link that is made up of two equally-sized capacitors.

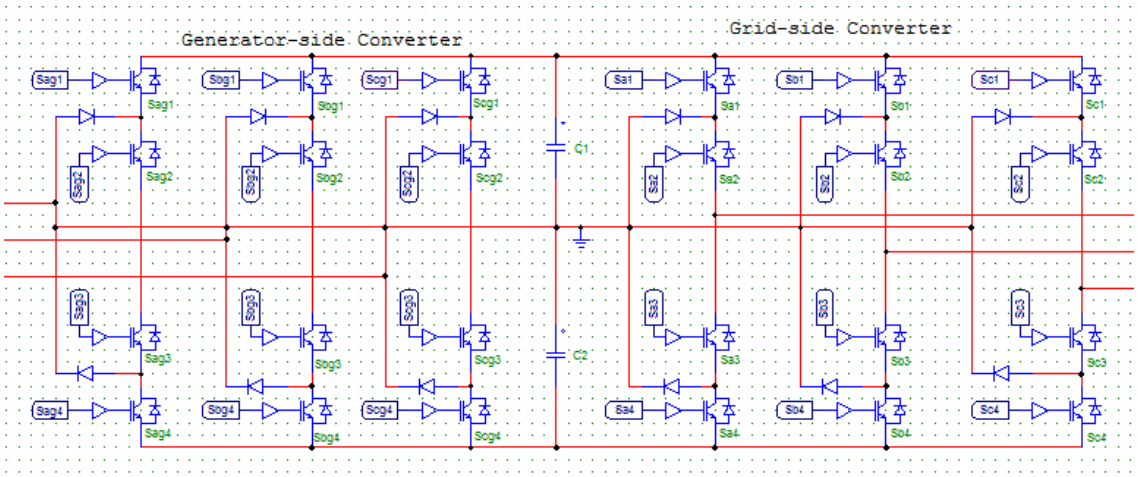

Figure 7. 3: Generator-side and Grid-side converter model

7.4 Power Utility Grid Implementation

The grid-side converter is connected to a 33kV power utility grid via a phase reactor and a power transformer as shown in Figure 7.4. The Power Utility grid is represented by an AC source.

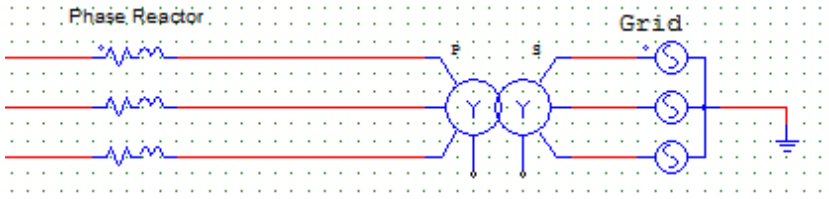

Figure 7. 4: Power Utility Grid Implementation

7.5 Control System Implementation

7.5.1 Pitch-Angle Controller

The pitch angle controller is used to generate the pitch angle that serves as a second input into the wind turbine block. Figure 7.5 shows the components making up a pitch-angle controller's block diagram. The phase-lead compensator is represented by the *Lead* block.

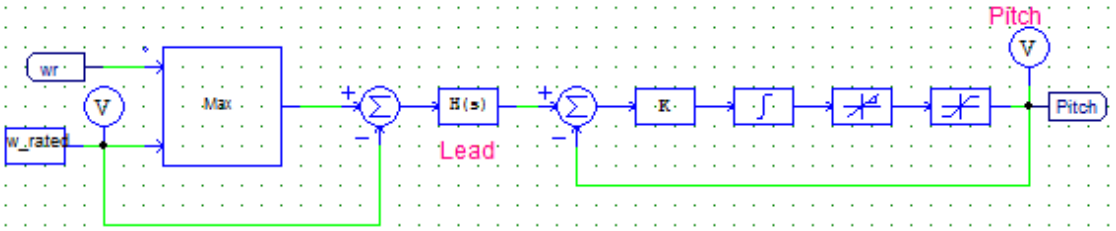

Figure 7. 5: Pitch-Angle Controller

7.5.2 Generator-side Converter Controller

7.5.2.1 ABC-DQ Transformation

The measured stator voltage and stator current are transformed from the *abc* reference frame to the *dq* synchronous reference frame using the *abc-to-dq* block as shown in Figure 7.6.

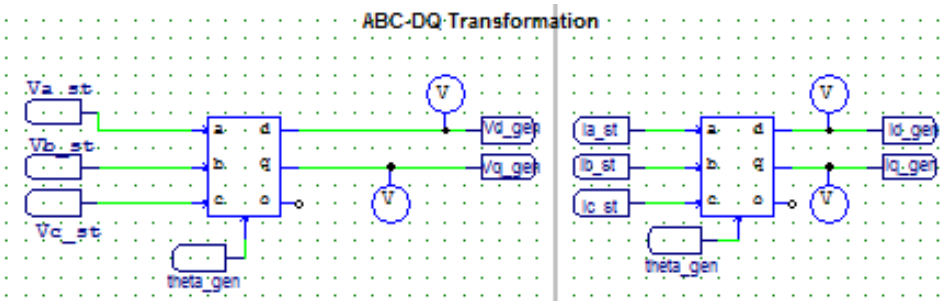

Figure 7. 6: ABC-dq Transformation of Stator Voltage and Stator Current

7.5.2.2 Outer-Control Loops

The generator-side converter controller's outer control loops are used to generate the d- and q-components of the stator's reference current. Figure 7.7 shows the DC-link voltage and stator voltage control loops.

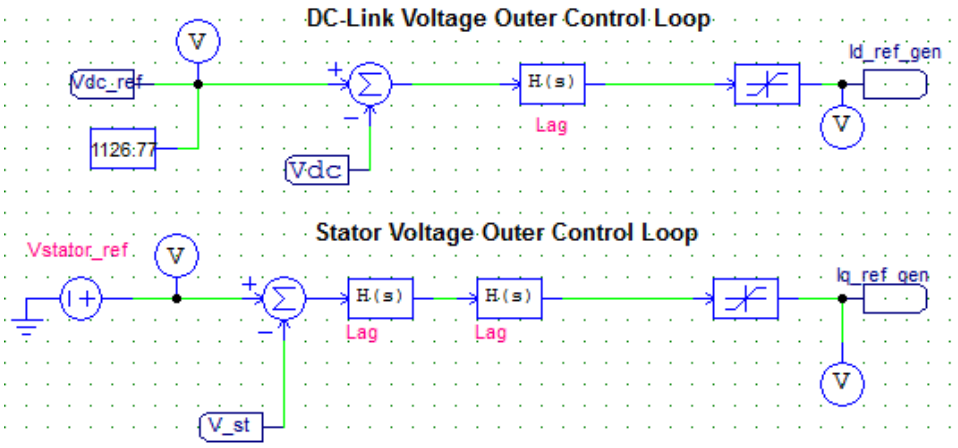

Figure 7. 7: Generator-side Converter Controller's Outer Control Loops

The phase-lag compensators are represented by the *Lag* blocks. DC-link voltage control loop generates the d-component of the stator's reference current while the stator voltage control loop generates the q-component of the stator's reference current.

7.5.2.3 Inner-current Control Loops

Figure 7.8 shows the generator-side converter's inner current control loops.

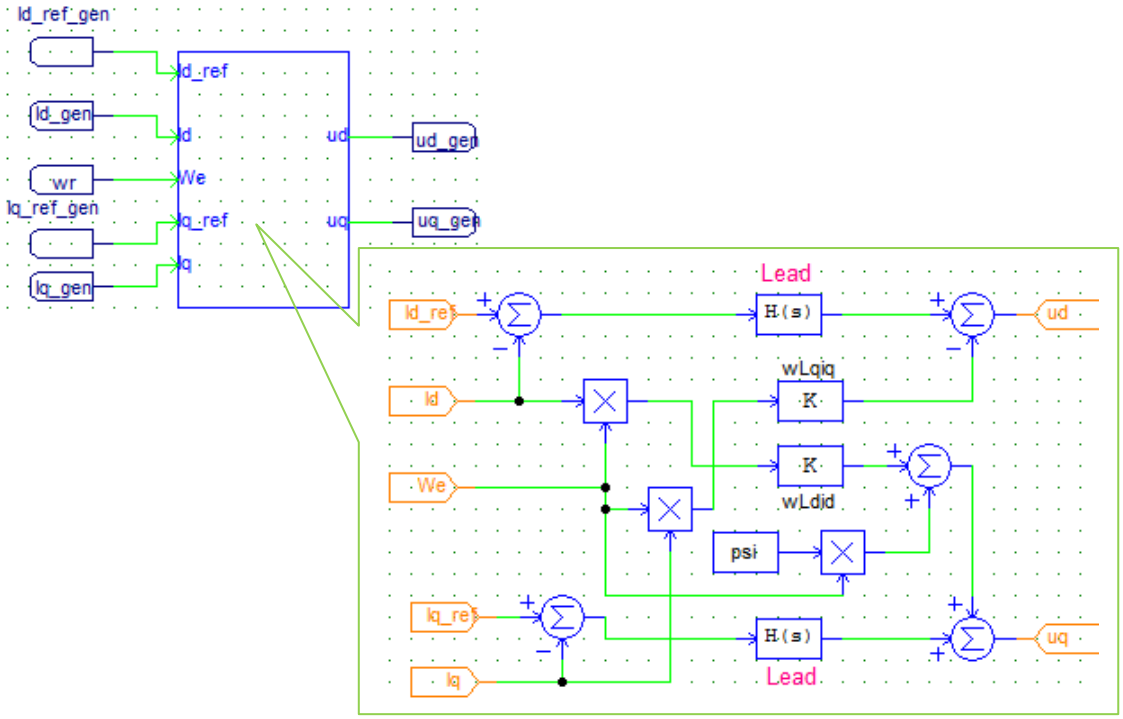

Figure 7. 8: Generator-side Converter Controller's Inner-current Control Loops

The phase-lead compensators are represented by the *Lead* blocks. The output signals u_d and u_q from the inner current control loops serve as inputs into the PWM block.

7.5.3 Grid-side Converter Controller

7.5.3.1 Phase Locked Loop (PLL)

A Phase Locked Loop (PLL) is a device that is commonly used to obtain the phase angle and frequency from the grid voltages. This is done to ensure unity power factor by synchronizing the inverter current angle with the grid voltage angle.

The angle obtained from the PLL is used to transform the measured grid voltages and currents from the *abc* 3-phase reference frame to *dq* synchronous reference frame using Clarke and Park Transformation. Figure 7.9 (a) and (b) shows the components making up a PLL and the angle *theta* generated by the PLL, respectively.

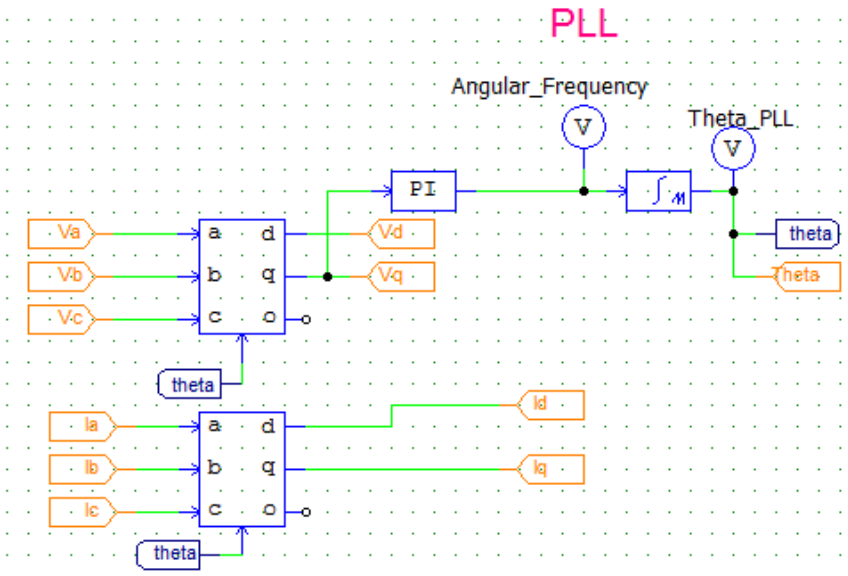

(a)

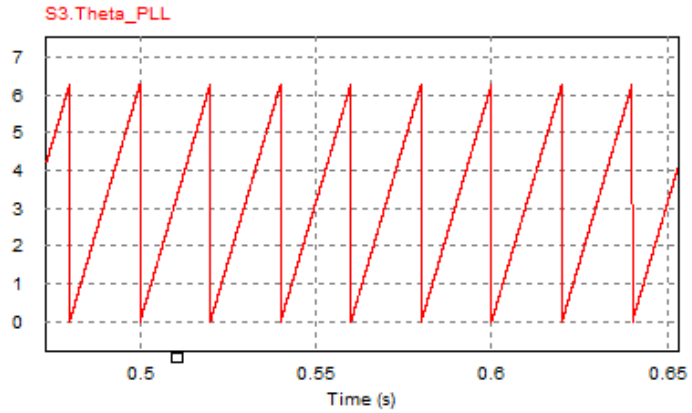

(b)

Figure 7. 9: (a) Components making up the PLL; (b) Angle theta generated by the PLL

7.5.3.2 Outer Control Loops

The grid-side converter controller's outer control loops are used to generate the d- and q-components of the grid's reference current. Figure 7.10 shows the MPPT and reactive power outer control loops. The phase-lag compensators are represented by the *Lag* blocks. The MPPT control loop generates the d-component of the grid's reference current while the reactive power control loop generates the q-component of the grid's reference current.

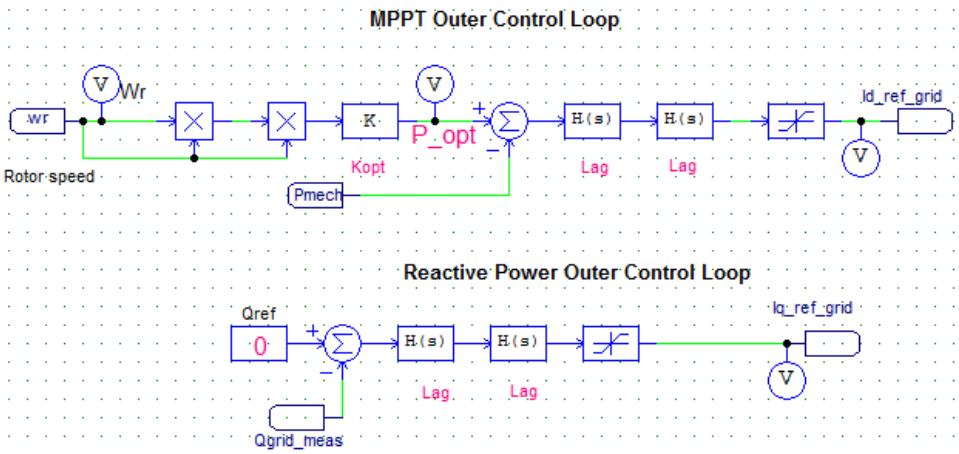

Figure 7. 10: Grid-side Converter Controller's Outer Control Loops

7.5.3.3 Inner-Current Control Loops

Figure 7.11 shows the grid-side converter's inner current control loops.

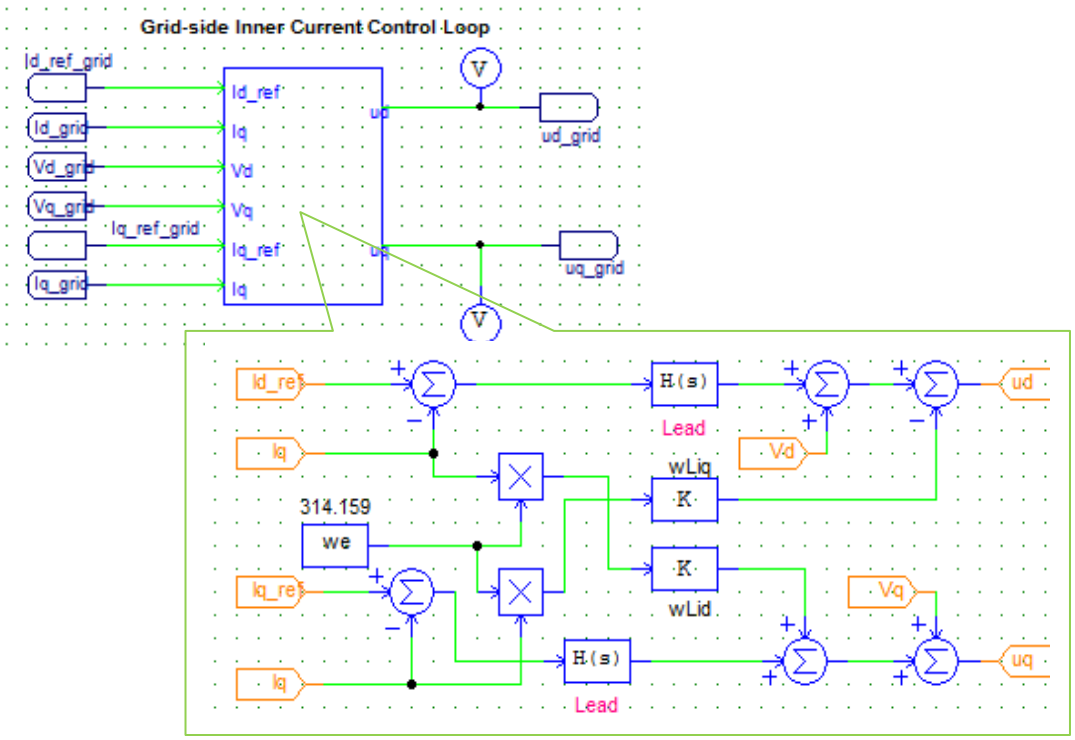

Figure 7. 11: Grid-side Converter Controller's Inner-current Control Loops

The phase-lead compensators are represented by the *Lead* blocks. The output signals u_d and u_q from the inner current control loops serve as inputs into the PWM block.

7.5.4 Pulse Width Modulation (PWM) Block

The PWM block is used to generate the gating pulses used to turn the converter switches on and off. According to literature studies [19, 86], for an N-level NPC multilevel converter, N-1 high-frequency triangular carriers with the same frequency and magnitude are arranged in such a way that they occupy the band between $V_{dc}/2$ to $-V_{dc}/2$. Considering a 3-level NPC topology, two (2) high-frequency triangular carriers with the same frequency of 2 kHz (switching frequency) are considered. According to [19], the Phase Disposition (PD) carrier arrangement removes the high carrier frequency harmonics in the line-to-line voltage and gets rid of the main contributors to the harmonic current generation process. As a result, the converter's output current waveforms improve significantly and hence reducing the size of the required AC filters. Therefore, in this study, the PD carrier arrangement is employed to synthesize the gating signals for the NPC converter switches. Figure 7.12 shows the PD carrier arrangement. The upper and lower carrier signals are arranged to be in-phase with one another. The upper carrier determines the switching process of the upper converter switches, while the lower carrier determines the switching process of the lower converter switches.

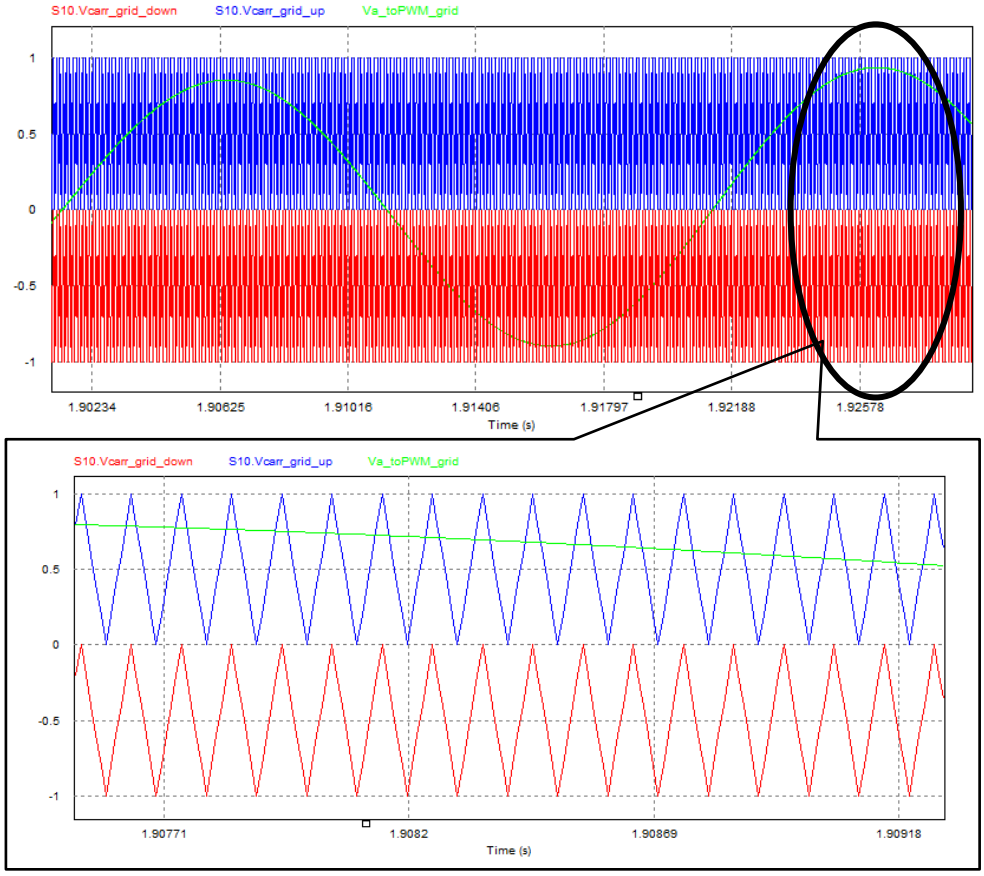

Figure 7. 12: Phase Disposition Carrier Arrangement

Figure 7.13 shows the generation process of the pulses used for commutating each converter switch. This is done for phase *A*, *B* and *C*. As mentioned earlier, in a 3-level NPC VSC topology, switches S_{a1}, and S_{a3} and S_{a2} and S_{a4} of phase *a* operate in a complementary manner. This means that turning S_{a1} on excludes S_{a3} from switching on, and switching S_{a2} on excludes Sa4 from switching on, and the same applies to the remaining phases *b* and *c*.

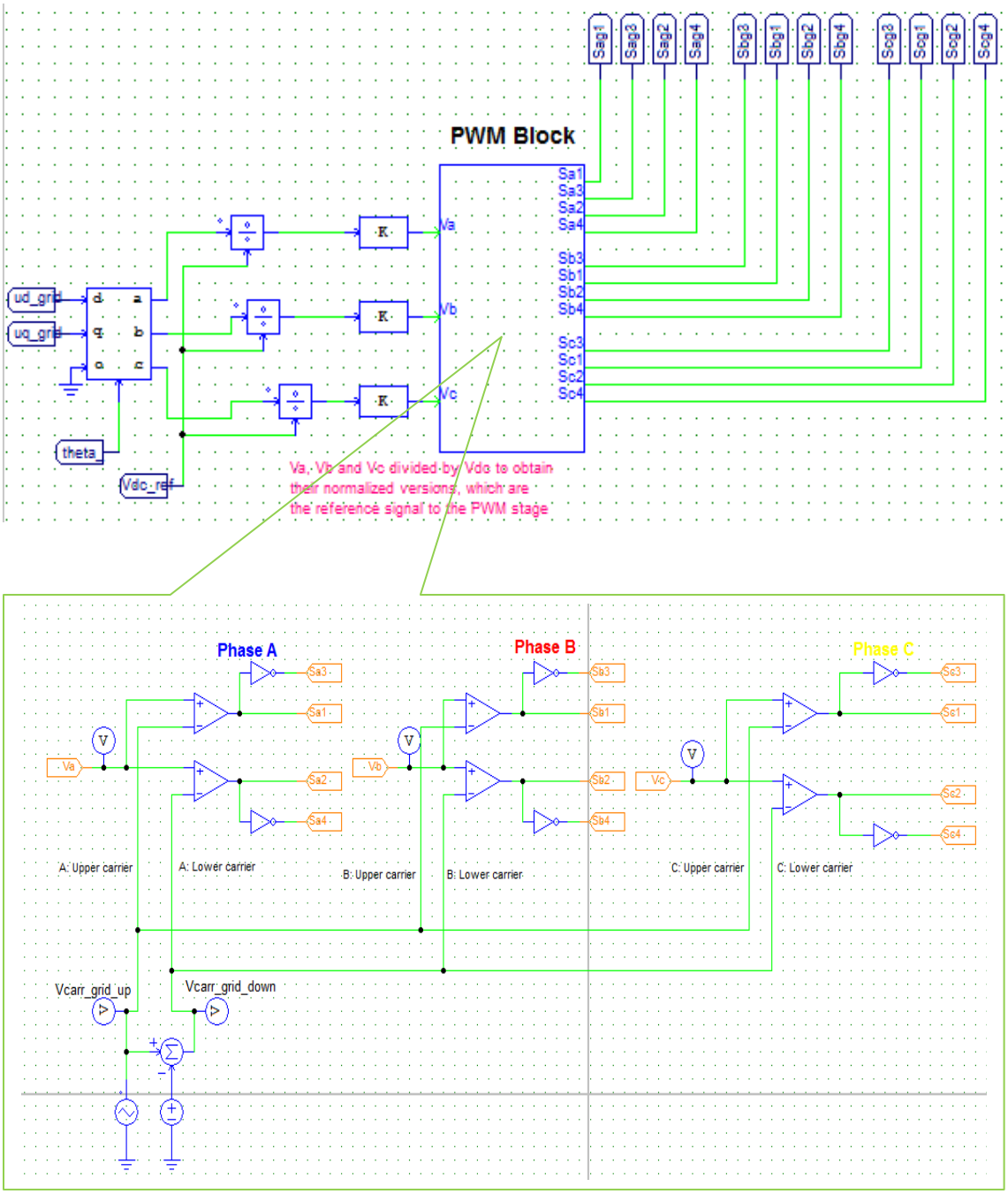

Figure 7. 13: PWM/ Pulse Generation

Figure 7.14 shows the gating signals of the converter switches for phase *a*.

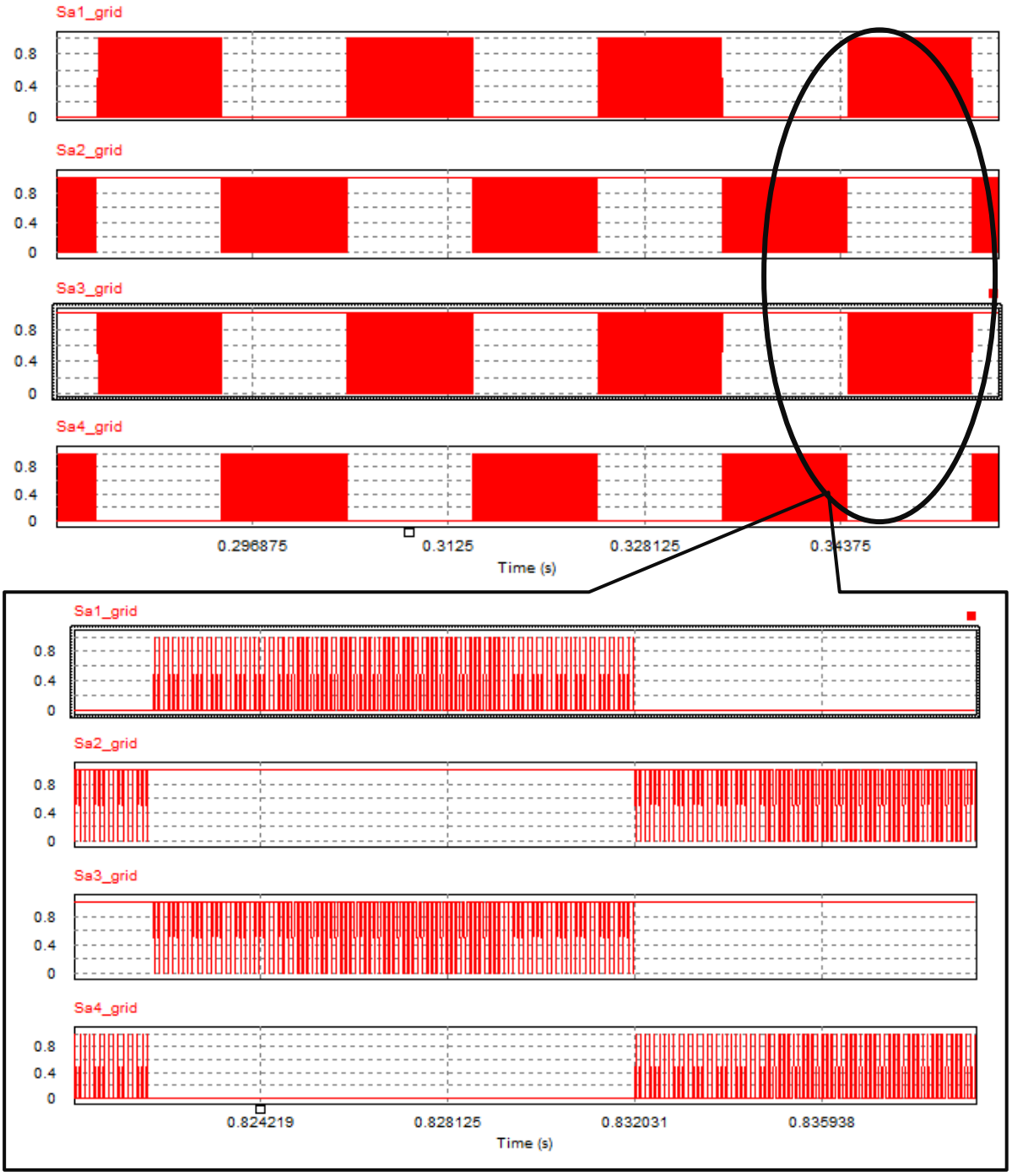

Figure 7. 14: Gating Signals for switching devices of phase *a*

7.6 Chapter Summary

This chapter dealt with the implementation of all the fundamental components making up the proposed wind energy conversion system (WECS) and the controller schemes; pitch-angle, generator-side and grid-side in PSIM software package. Figure 7.15 shows the complete diagram of the proposed WECS.

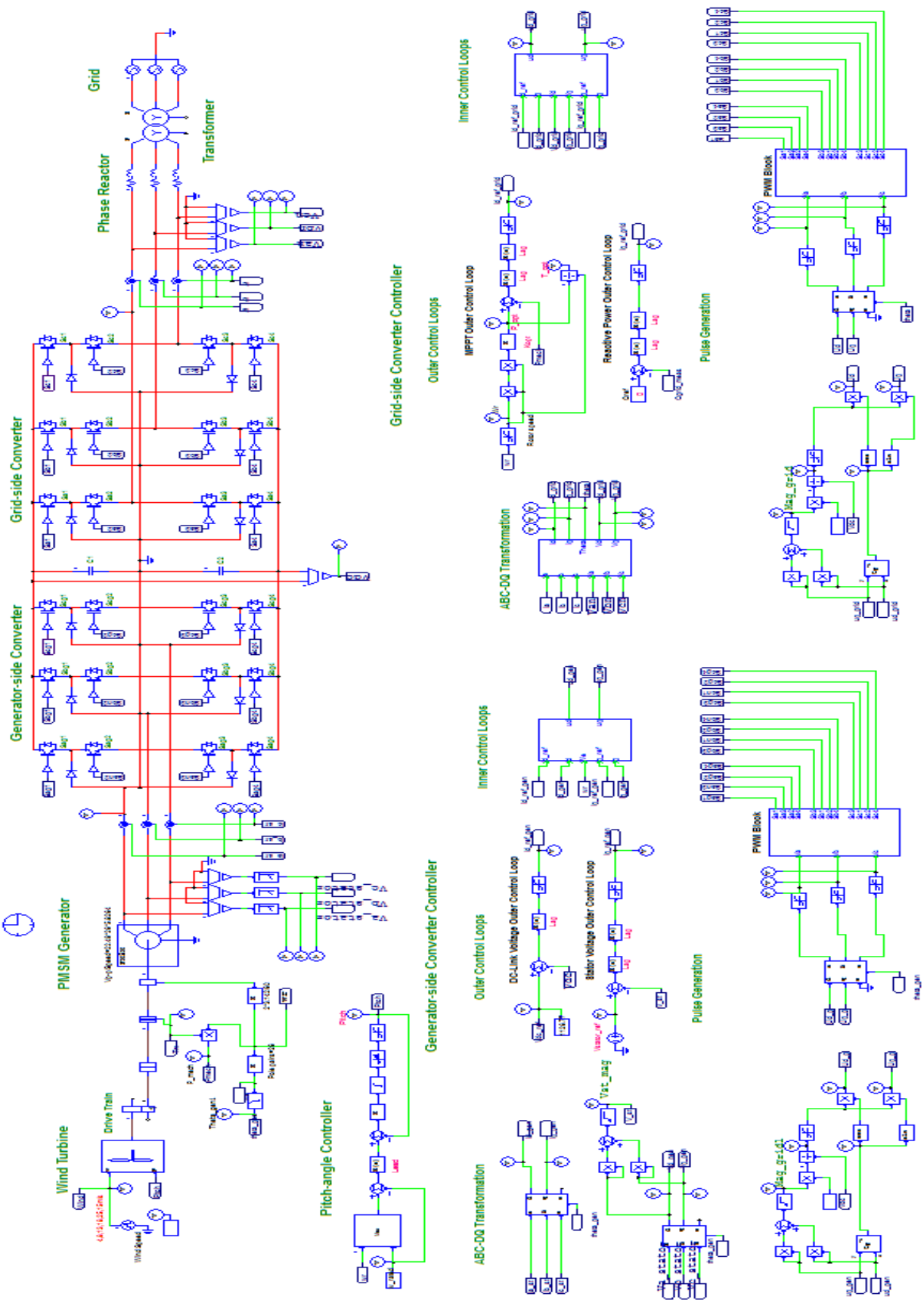

Figure 7. 15: Complete diagram of the proposed WECS

CHAPTER 8: RESULTS AND DISCUSSIONS

This chapter discusses the results obtained by running simulations on the proposed wind energy conversion system in Fig. 7.15 with the aim of validating whether the proposed control schemes meet the objectives of this study. Therefore, these discussions focus on the effectiveness of the pitch-angle controller to protect the wind turbine generator from over-speeding and mechanical stresses during high wind gusts. Furthermore, the discussion focuses on analyzing the effectiveness of the generator-side converter controller to stabilise the DC-link voltage to ensure a continuous active power flow from the wind turbine generator to the utility grid, as well as to control the stator voltage to avoid the risk of overvoltage. Moreover, the effectiveness of the grid-side converter controller to control the rotor speed for maximum power point tracking (MPPT) and reactive power control to ensure unity power factor has been analyzed. The chapter ends with a comparison of the new control approach to the conventional approach with the aim of investigating the effectiveness of the new control approach in the area of enhancing the fault-ride-through capability of the proposed WT connected to the grid via a three-level NPC VSC

8.1 Wind Speed Model

The wind speed is made to vary to analyze how the system reacts to the change in wind speed. Figure 8.1 shows the variation in wind speed from the wind turbine's cut-in wind speed (4m/s) and increases to the rated wind speed (13m/s) at 0.6s up until 18m/s, approaching the wind turbine's cut-out wind speed.

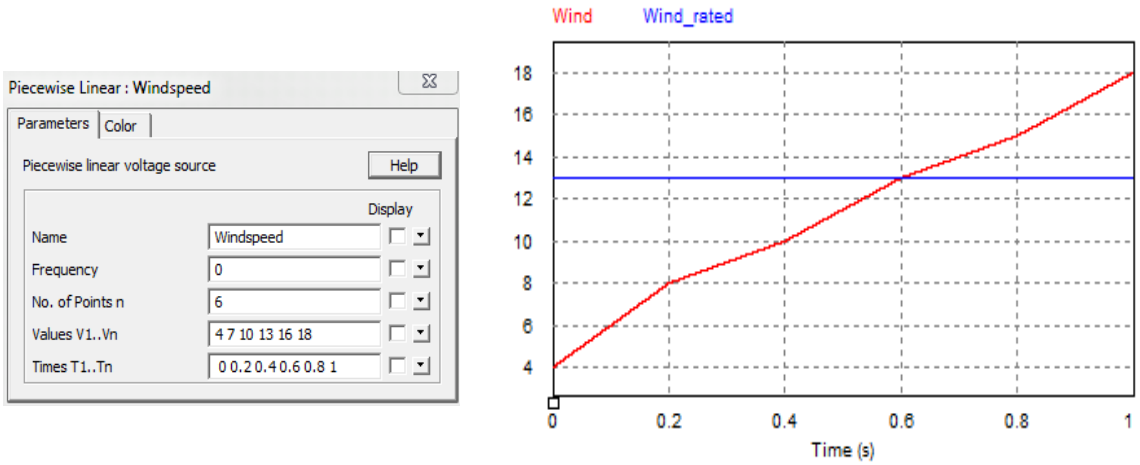

Figure 8. 1: Wind Speed Curve

8.2 Pitch-angle Control Scheme

Figure 8.2(a) shows the variation in pitch angle relative to the change in wind speed. Figure 8.2(b) shows the power coefficient curve.

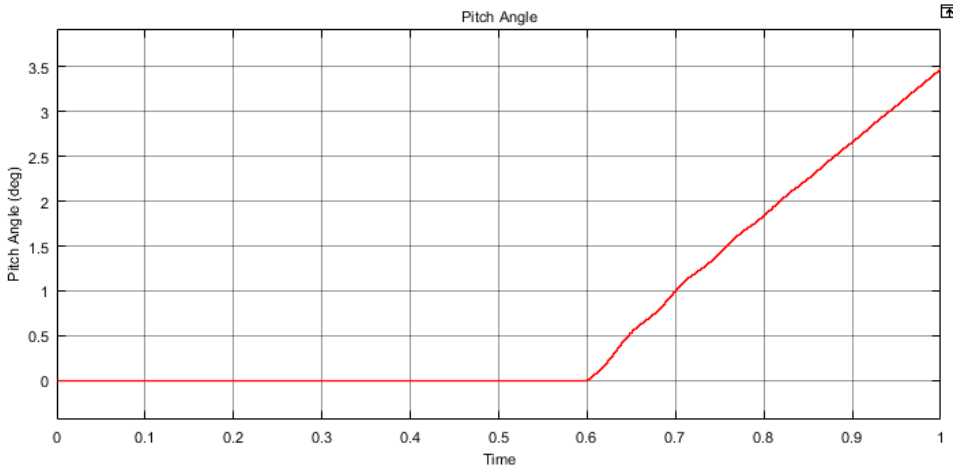

(a)

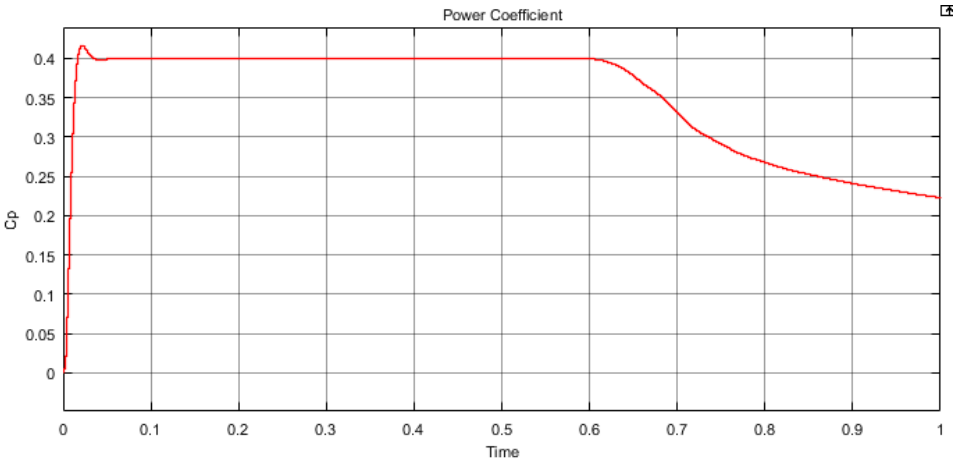

(b)

Figure 8. 2: (a) Pitch Angle; (b) Power Coefficient

From Figure 8.2(a), it is shown that the pitch angle controller remains inactive when the wind speed is lower than the WT's rated wind speed and only gets activated when the wind speed exceeds the WT's rated wind speed. Figure 8.2(b) shows that the power coefficient C_p increases and remains constant at the rated value and it only starts decreasing when the wind speed exceeds the WT's rated wind speed. This occurs due to the activation of the pitch angle controller, and hence, the amount of power extracted from the wind resource by the wind turbine decreases.

8.3 Generator-side Converter's Control Scheme

8.3.1 DC-Link Voltage Control

Figure 8.3 (a) and (b) illustrates the converter's terminal/ output voltage waveform and the DC-link voltage waveform, respectively.

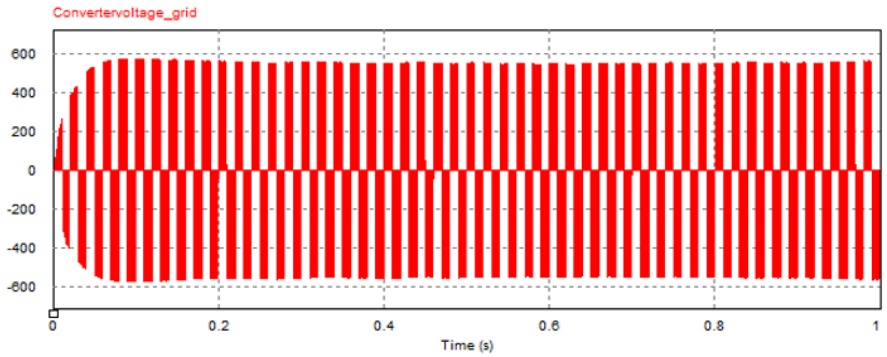

(a)

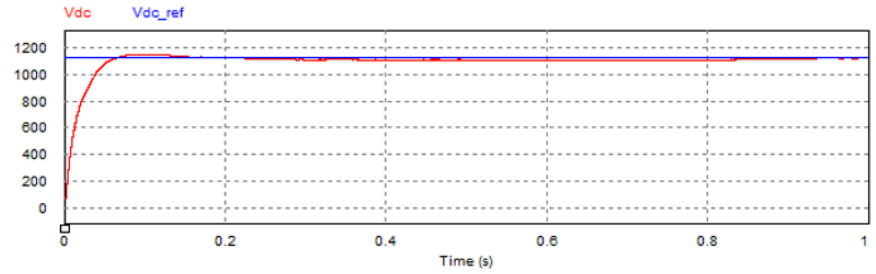

(b)

Figure 8. 3: (a) The converter's terminal/ output voltage; (b) the corresponding DC-link voltage waveform

It is seen that the DC link voltage is maintained within the allowable ranges close to 1126.77V as expected. The Equivalent DC-link voltage is a sum of the voltages across the two series-connected DC-link capacitors. Figure 8.4 shows the DC voltages across the upper DC-link capacitor and the lower DC-link capacitor, V_{c1}, and V_{c2}, respectively. It is shown that the DC-link voltage is equally distributed across the two DC-link capacitors.

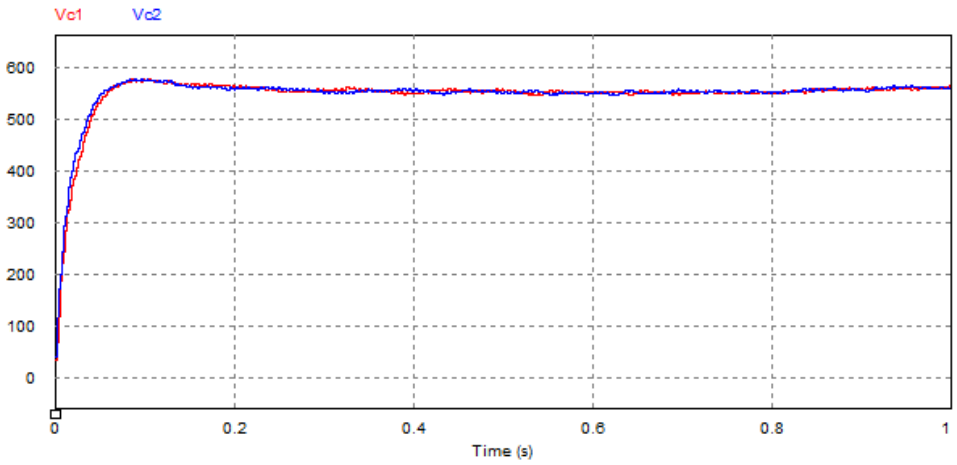

Figure 8. 4: DC Voltage distribution across the two series-connected DC-link capacitors

From fundamental principles, the inner control loops are required to ensure that the measured stator currents track the reference stator currents which are obtained from the outer control loops. To ensure that the amount of the current flowing through the converter switches remains within the desired converter limits, the reference current should be limited to a certain value. The DC-link voltage control loop provides the d-component of the stator current. Considering the DC-link voltage limits stipulated in Chapter 3, that is, 1183.11V to 1070.43V, and the fact that the active power on the AC-side must be equal to the active power on the DC-side, that is, 2MW, the d-component's reference current are calculated as follow

$$P_{dc} = V_{dc} I_{dc}$$

$$I_{dc} = \frac{P_{dc}}{V_{dc}} = \frac{2 \times 10^6 W}{1126.77V} = 1774.99A$$

Therefore, the d-component's reference current must remain within the following limits,

$$I_{dc\_\max} = \frac{P_{dc}}{V_{dc\min}} = \frac{2 \times 10^6 W}{1070.43V} = 1868.41A$$

$$I_{dc\_\min} = \frac{P_{dc}}{V_{dc\max}} = \frac{2 \times 10^6 W}{1183.11V} = 1690.46A$$

Figure 8.5 (a) and (b) shows the measured d-component and q-component of the stator currents tracking the reference stator currents which are obtained from the DC-link voltage control loop, respectively.

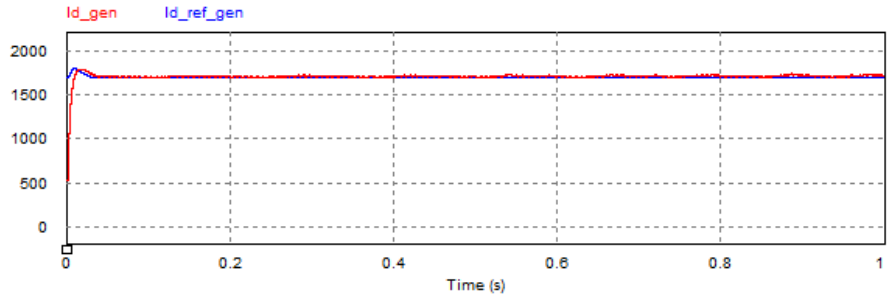

(a)

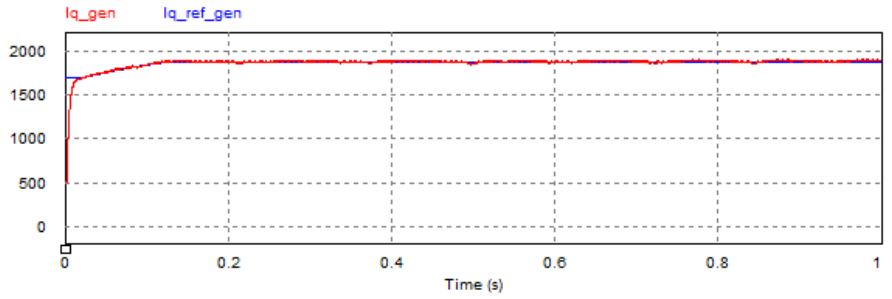

(b)

Figure 8. 5: Reference and measured stator currents (a) d-component (b) q-component

The ability of the measured current values to track the reference currents obtained from the outer control loops and to maintain these currents within the desired limits prove the effectiveness of the inner current controllers.

8.3.2 Stator Voltage Control

The stator voltage is controlled to ensure that it is maintained within ±5% of its rated value to avoid the risk of over voltages. The rated stator phase voltage (rms) is calculated from the rated line-line voltage of 690V as follow,

$$V_{phase(rms)} = \frac{690V}{\sqrt{3}} = 398.37V$$

Therefore, the stator voltage should be maintained within the range of 378.45V to 418.29V. Figure 8.6 (a) and (b) shows the stator voltage and stator current waveforms, respectively.

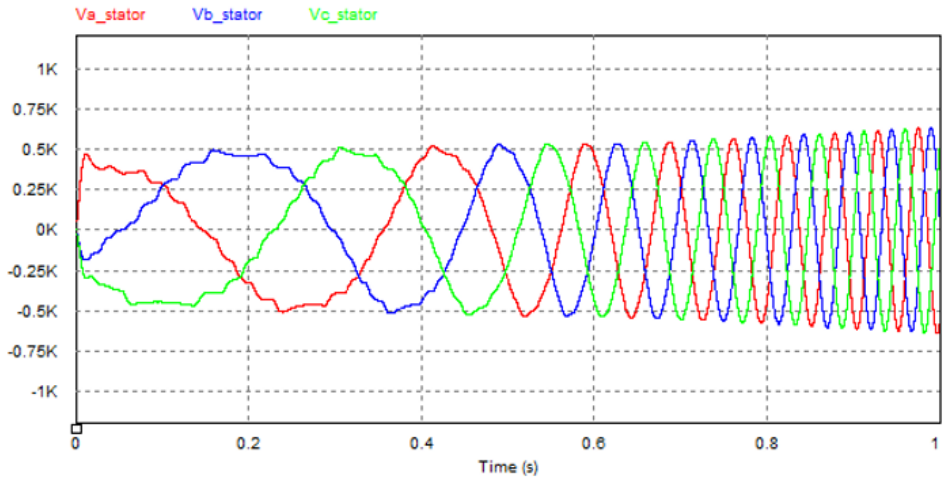

(a)

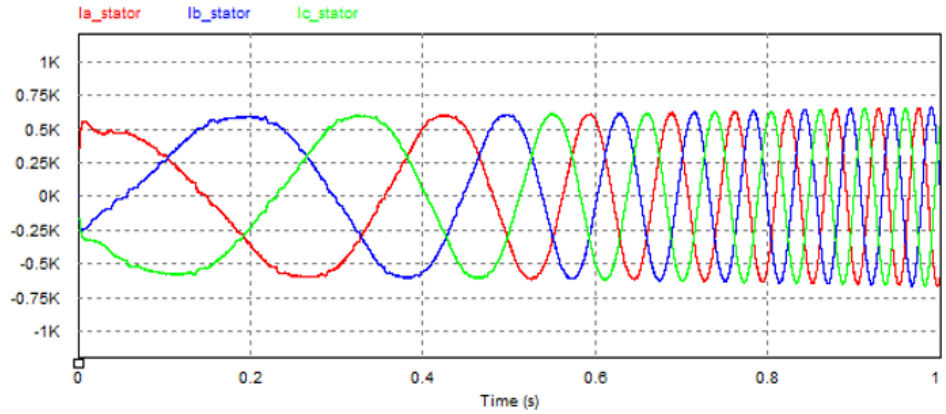

(b)

Figure 8. 6: (a) Stator Voltage waveform; (b) Stator Current waveform

It is observed that the stator voltage and stator current increases as the wind speed increases. Furthermore, as the wind speed increases, the rotor angular speed also increases, and hence, as it can be observed in the stator voltage and current waveforms, the frequency increases. This is mainly due to the relationship between the rotor angle speed and frequency, that is, $\omega_r=2\pi f$.

8.4 Grid-side Converter's Control Scheme

8.4.1 Maximum Power Point Tracking

The optimal relation-based (ORB) MPPT technique has been implemented in this study. The ORB technique ensures that optimal power is extracted from the wind resource by varying the rotor speed ω_r with respect to the change in wind speed v_w. Therefore, optimal aerodynamic efficiency at a given wind speed can be achieved if the MPPT controller allows the generated power to properly track the pre-defined optimal power curve with variations in wind speed.

Figure 8.7 (a), (b) and (c) shows the rotor angular speed, the aerodynamic power, and aerodynamic torque, respectively.

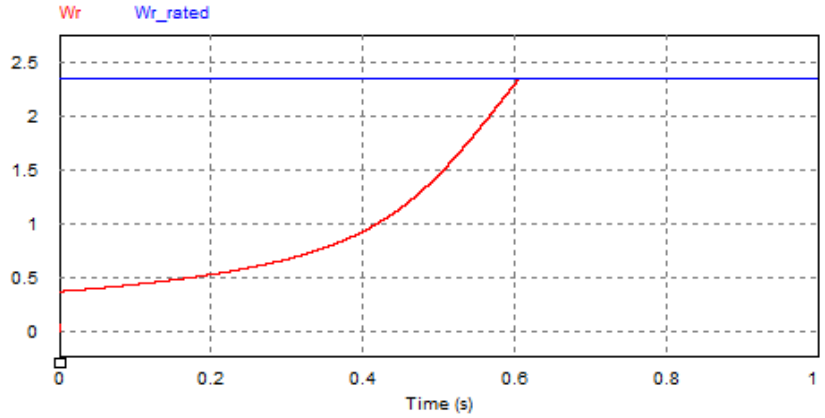

(a)

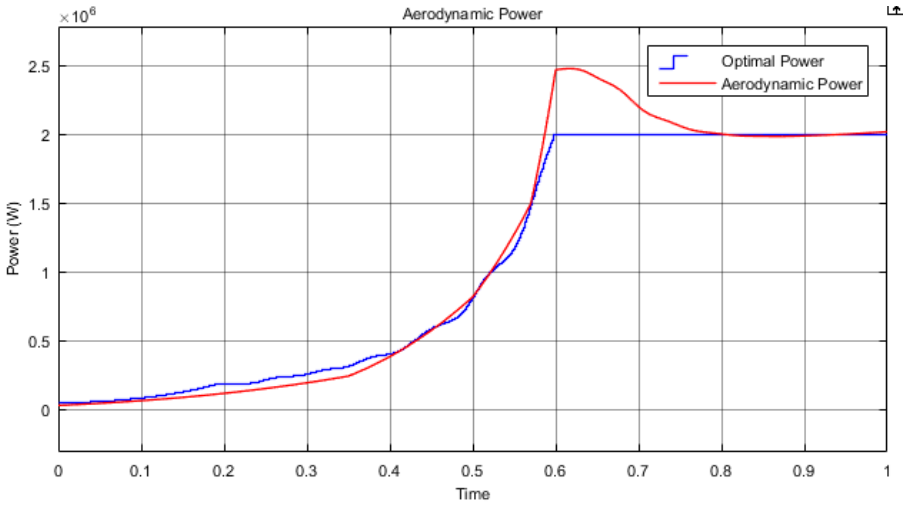

(b)

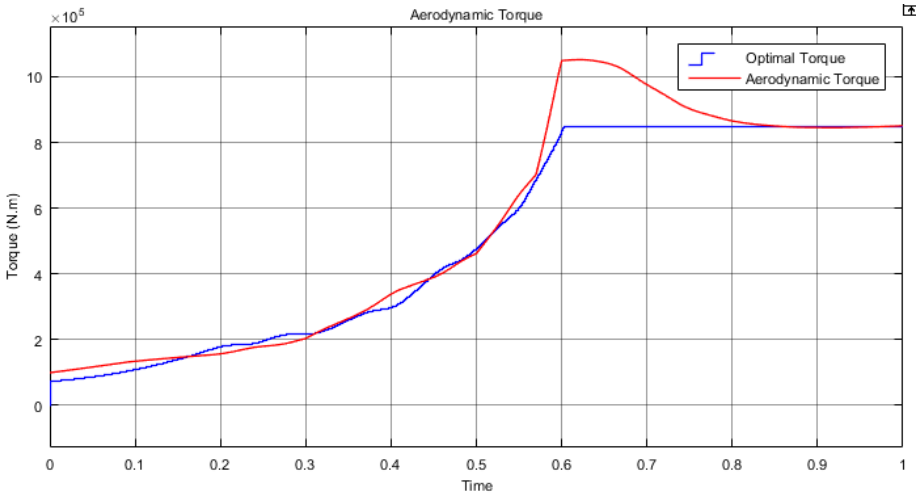

(c)

Figure 8. 7: MPPT (a) Rotor Angular Speed; (b) Aerodynamic power; (c) Aerodynamic Torque

It can be observed from Figure 8.9 (a) that the rotor angular speed increases as the wind speed increases. Moreover, at the rated wind speed (13m/s), the measured rotor speed is equal to the rated rotor speed, which is 2.356rad/s. Figure 8.9(b) shown that, when the wind speed is below the WT's rated wind speed (13m/s), the power generated from the WT tracks the optimal power curve to ensure MPPT. When the wind speed is equal to the WT's rated wind speed, the power generated is equal to 2MW which is the WT's rated power. Moreover, as the wind speed increases further above the WT's rated wind speed, the generated power remains equal to the rated power. This is possible because of the pitch-angle control technique explained earlier. Figure 8.4 (c) shown that, during the MPPT stage, the generated torque closely tracks the optimal torque curve until the rated WT's rated torque. At the rated power (2MW), the torque is almost equal to the WT generator's rated torque of 849kNm, which can also be verified mathematically as follow,

$$T_{opt} = \frac{P_{opt}}{\omega_{r\_opt}} = \frac{2\times10^{6}}{2.356} = 848kNm$$

Figure 8.8 shows the measured d-component of the grid current tracking the reference d-component of the grid current which is obtained from the MPPT control loop. The d-component's reference current is ensured to remain within the limits computed earlier, that is ±1868.41A.

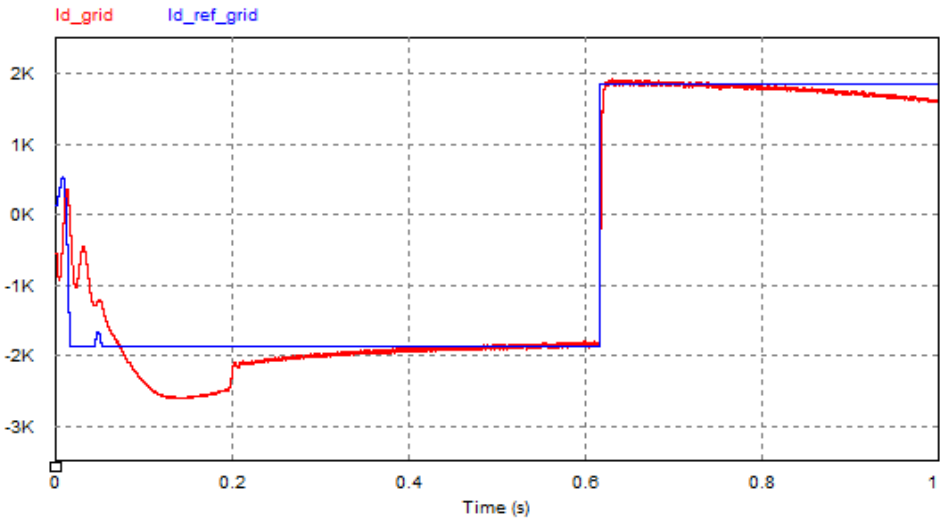

Figure 8. 8: Measured and reference d-components of the grid current

8.4.2 Reactive Power Control

The reactive power fed into the grid is controlled for power factor correction purposes. From control theory, unity power factor is ensured by setting the reference reactive power Q_{ref} equal to zero. As a result, the q-component of the grid current's reference will also be equal to zero. Figure 8.9 shows the measured q-component of the grid current tracking the reference q-component of the grid current which is obtained from the reactive power control loop.

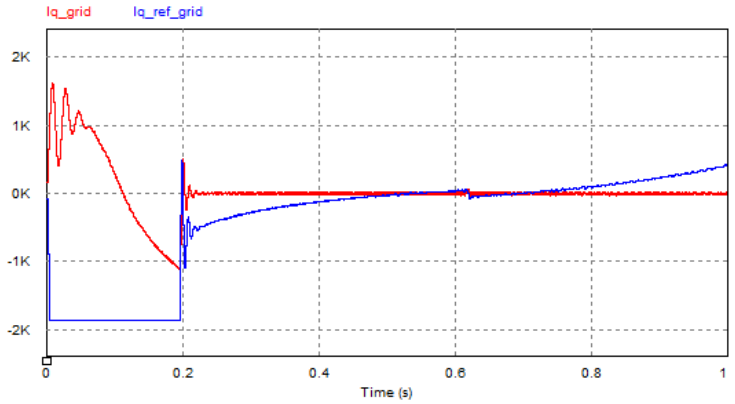

Figure 8. 9: Measured and reference q-components of the grid current

It is observed that the q-component of the grid current is kept to a minimum and close to zero to ensure that the reactive power absorbed or generated by the converter is also kept to a minimum to ensure unity power factor. Figure 8.10 shows the active and reactive power exchanged between the grid-side converter and the grid.

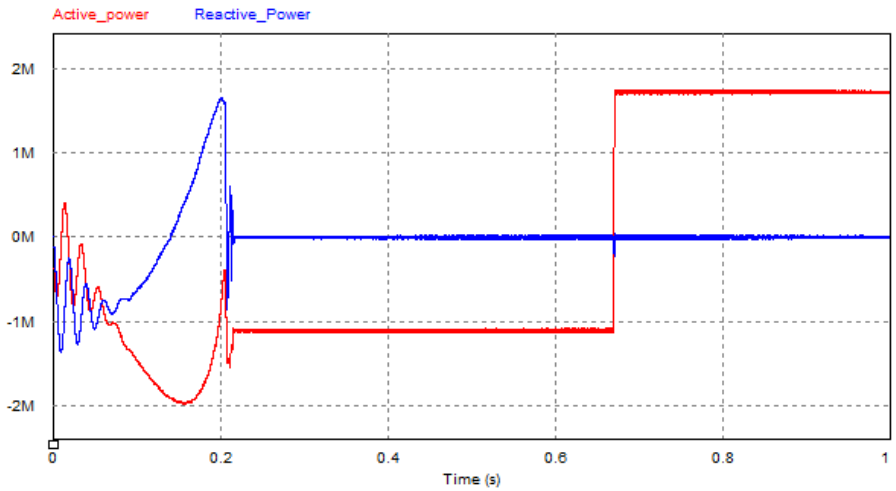

Figure 8. 10: Active and reactive power flow between the grid-side converter and the grid

From Figure 8.10, it is observed that after the system stabilizes at 0.2s, the reactive power is maintained equal to zero to ensure unity power factor. Figure 8.11 shows the grid-side converter's terminal voltage and current waveforms with power factor close to unity.

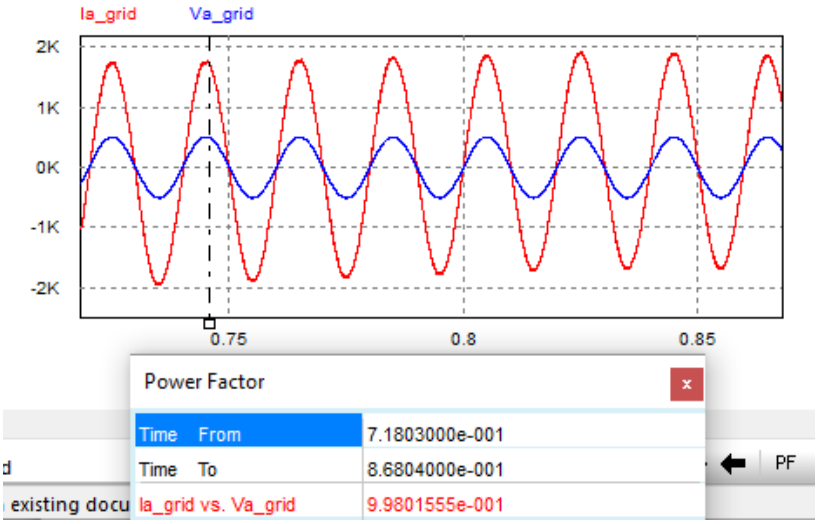

Figure 8. 11: Grid-side Converter's terminal voltage and current waveforms with power factor close to unity

Figure 8.17 (a) and (b) shows the filtered grid-side converter's output voltage waveform and the current flowing through the phase reactor, respectively.

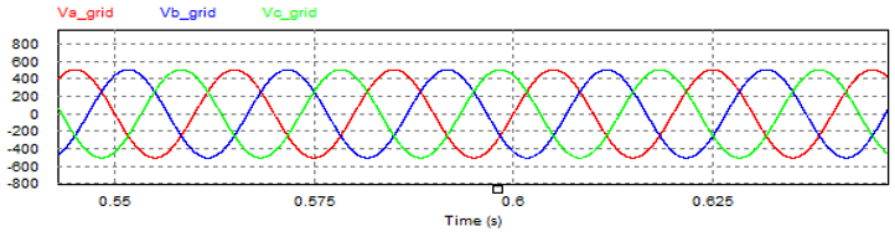

(a)

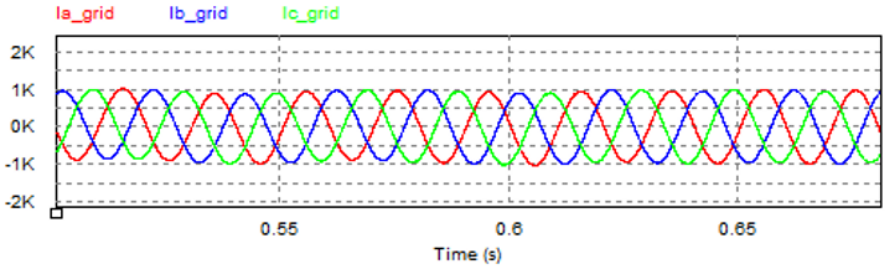

(b)

Figure 8. 12: (a) Grid-side converter's filtered output voltage; (b) Current flowing through the phase reactor

From Figure 8.12(a), the grid-side converter's output phase voltage is 358.31V, and hence, the line-to-line voltage is equal to 620.62(*rms*). Considering the active power fed into the grid from a 2MW WT generator, the line current is calculated as follow:

$$P = 3V_L I_L \cos\theta$$

$$I_{L(rms)} = \frac{2\times10^6}{3\times620.62\times0.99} = 1085.05\angle 8.11^o$$

$$I_{phase(rms)} = \frac{1085.05A}{\sqrt{3}} = 626.45A$$

In this study, the vector-oriented control (VOC) approach was implemented. From literature, in VOC, the d-axis of the synchronous reference frame is to be aligned with the grid voltage vector. Therefore, the grid voltage vector only has the d-axis component V_{gd}, while the q-axis component V_{gq} is set to zero. Figure 8.16 shows the d- and q- component of the grid-side converter's terminal voltage.

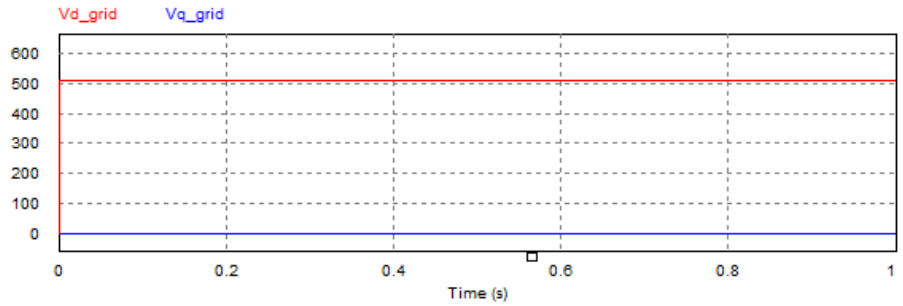

Figure 8. 13: d- and q-component of the grid-side converter's terminal voltage

8.5 Comparison of the New and Conventional Control Approaches: Fault-ride-through Capability Analysis

During fault conditions, it is required that the wind turbine remains connected to the grid to offer grid support, this is referred to as fault ride-through capability. The control of the converters interconnecting the wind turbine to the electrical grid plays a major role in the behaviour of the entire system during normal and fault conditions. Considering the vector-oriented control approach, there are two generic control strategies used to control both the grid-side and generator-side converter stations. Namely: the traditional/ conventional and the new control approach.

In this study, the new control approach has been implemented to integrate the proposed WT into the grid. This section will briefly compare the new control approach to the conventional approach with the main aim of investigating how effective the new control approach is in the area of enhancing the fault-ride-through capability of the proposed WT connected to the grid via a three-level NPC VSC.

In this context, the comparison is done in terms of the ability of the DC-link voltage to remain constant during fault conditions to ensure that the power generated by the wind turbine continues flowing to the grid. The comparison is done in MATLAB software package whereby a fault was applied on the grid-side at 0.3 seconds and cleared after 0.2 seconds. That is, at 0.5s.

Figure 8.17 (a) shows the DC-Link voltage before the fault has been applied. Figure 8.17 (b) shows the DC-link voltage controlled using the new control approach when the fault has been applied. Figure 8.17(c) the DC-link voltage controlled using the traditional control approach when the fault has been applied.

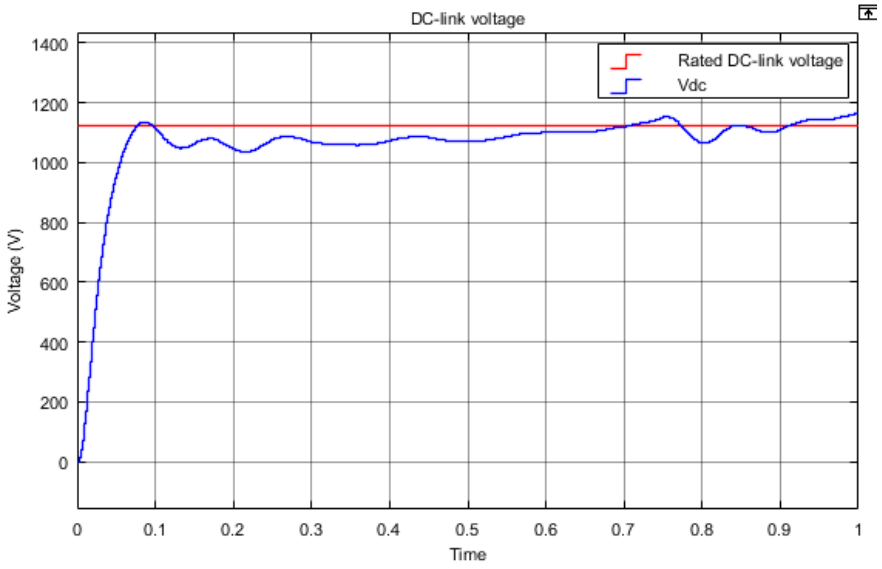

(a)

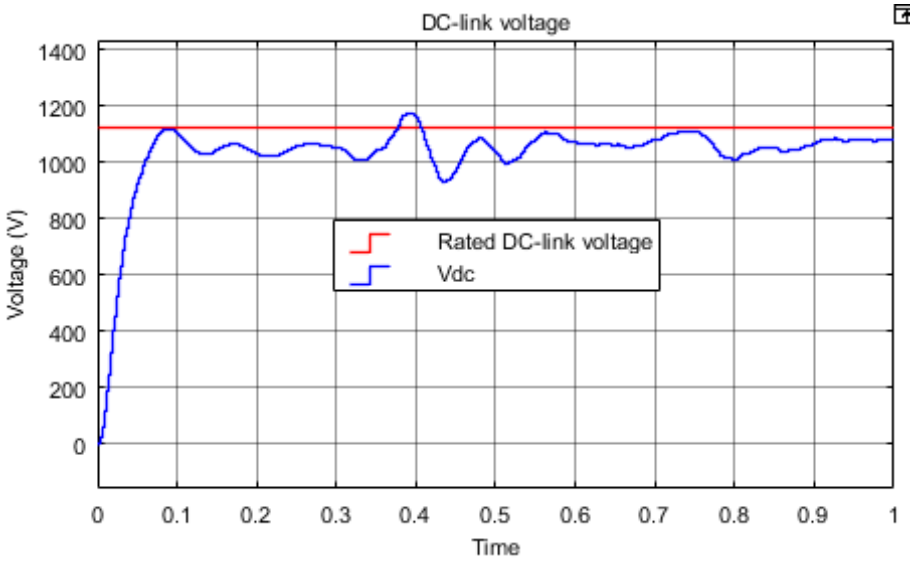

(b)

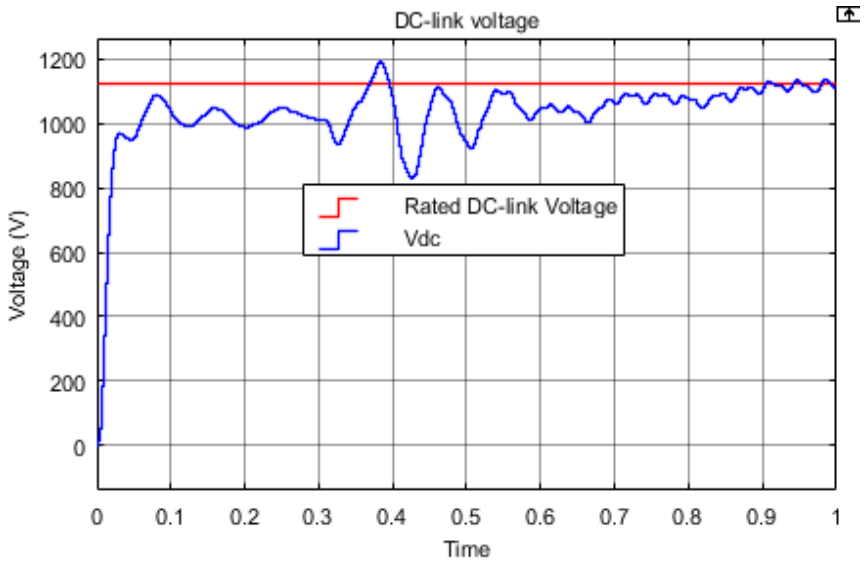

(c)

Figure 8. 14: DC-link voltage (a) Before the fault; (b) During the fault; new control technique; (c) During the fault: traditional control approach

From Figure 8.17(b), it is observed that despite the minimal disturbances in the DC-link voltage during the fault condition, the DC-link voltage remains within the allowable range, that is, ±5% of 1126.77V, and hence, it does not overcharge the DC-link capacitors. This is mainly because, in the new control approach, the DC-link voltage controller is applied to the generator-side converter and not on the grid-side converter. Therefore, the DC-link voltage controller does not get impaired during fault conditions and hence there is power flowing from the WT generator to the grid. Therefore, the wind turbine remains connected to the grid to offer grid support.

On the other hand, this is not the case with the conventional control approach. From Figure 8.17 (c), it is observed that during the fault, the grid-side converter controller's ability to stabilize the DC-link voltage gets impaired and therefore it can no longer effectively transfer as much active power from the WT generator to the grid. The surplus power leads to the charging of the DC-link capacitor(s) causing over-voltages in the DC-link. Consequently, this may lead to a significant damage to the converter stations and the DC-link capacitor(s) which will consequently disconnect the wind turbine from the grid.

8.6 Chapter Summary

This chapter discussed the results obtained by running simulations on the proposed wind energy conversion system in Fig. 7.15 with the aim of validating whether the proposed control schemes meet the objectives of this study. Table 8.1 summarizes the effectiveness of the pitch-angle controller, the generator-side converter controller to stabilize the DC-link and stator voltage, and the grid-side converter controller to carry out MPPT and reactive power control.

Table 8.2 summarizes the comparison of the new control approach to the conventional approach in the area of enhancing the fault-ride-through capability of the proposed WT connected to the grid via a three-level NPC VSC.

Table 8. 1: Consolidated effectiveness of the pitch-angle, generator-side converter and grid-side converter controllers in achieving the objectives of the study

Controller		**Controller Objective**	**Result/ Outcome**
Pitch- Angle controller		To limit the amount of power extracted from the wind resource when the wind speed exceeds the WT's rated wind speed (13m/s).	-The pitch-angle controller remained inactive when the wind speed was lower than the WT's rated wind speed and only got activated when the wind speed exceeded the WT's rated wind speed (13m/s). - The power coefficient C_p remained constant at its rated value and only started dropping when the wind speed exceeded the WT's rated wind speed. - As a result, the amount of power extracted from the wind resource by the wind turbine decreased to protect the WT from sudden wind gusts.
Generator-side converter controller	DC-link voltage controller	To stabilise the DC-link voltage at rated value (1126.77V) to ensure a continuous active power flow from the wind turbine generator to the utility grid.	The DC-link voltage controller managed to keep the DC-link voltage fixed at the desired value of 1126.77V.
	Stator voltage controller	To stabilize the stator voltage at its rated value to avoid the risk of over-voltages	The stator voltage controller maintained the stator voltage within the desired limits to avoid the risk of over-voltages.
Grid-side converter controller	MPPT controller	To control the rotor speed for MPPT when the wind speed is lower than the wind turbine's rated speed (13m/s).	-The MPPT controller enabled the power generated from the WT to closely track the pre-defined optimal power curve to ensure maximum wind power extraction when the wind

			speed is less than the WT's rated wind speed (13m/s). -The MPPT controller also enabled the generated torque to closely track the optimal torque curve when the wind speed is lower than the WT's rated wind speed.
	Reactive power controller	To control the reactive power so as to ensure unity power factor by keeping it as close to 0Var as possible	The reactive power controller ensured that the reactive power absorbed or generated by the converter is kept to a minimum to achieve unity power factor. After the system stabilizes, the reactive power was maintained equal to zero to ensure unity power factor.

Table 8. 2: Comparison of the conventional and new control approach in terms of analysing the effect of a fault on the performance of a DC-link voltage controller

	Conventional control approach	**New control approach**
Effect of a fault on the effectiveness of the DC-link voltage controller	-During the fault, the ability of the DC-link voltage controller to stabilize the DC-link voltage gets impaired and hence, the transfer of active power from the WT generator to the grid reduces. - The surplus power leads to the charging of the DC-link capacitor(s) causing over- voltages in the DC-link. Consequently, this may lead to a significant damage to the converter stations and the DC-link capacitor(s) which will eventually disconnect the wind turbine from the grid.	- The DC-link voltage controller does not get impaired during fault conditions. -Therefore, despite the minimal disturbances in the DC-link voltage during the fault condition, the DC-link voltage remained within the allowable range, that is, ±5% of 1126.77V and hence, it does not overcharge the DC-link capacitors. - Hence, there is power flowing from the WT generator to the grid. Therefore, the wind turbine remains connected to the grid to offer grid support.

CHAPTER 9: CONCLUSIONS AND RECOMMENDATIONS

9.1 Conclusions

The following conclusions can be drawn from the investigation:

- The detailed mathematical modelling and sizing of the proposed wind energy conversion system's components has been carried out.
- The mathematical modelling of a three-level neutral-point-clamped VSC topology emphasizing on its AC-side and DC-side dynamics has been discussed.
- The detailed derivation of the open-loop and closed-loop transfer functions of the outer and inner current control loops for the generator-side and grid-side converter controllers was carried out.
- The design specifications that were to be achieved or met in this study were clearly defined.
- The design and stability analysis of the generator-side converter controller using bode plots and step response curves was carried out in MATLAB software package.
- The design and stability analysis of the pitch-angle controller was also carried out in MATLAB software package using bode plots and step response curves.
- The design and stability analysis of the grid-side converter controller using bode plots and step response curves was carried out in MATLAB software package.
- The modelling and implementation of the system components and controllers was successfully implemented in PSIM software package to further analyze the overall system's performance.

Simulations were carried out on the modelled system with the main aim of validating whether the proposed model and the control schemes met the objectives and whether the research questions have been answered. The following conclusions were drawn:

- The wind speed was made to vary to analyze how the system reacts to the change in wind speed.
- As mentioned earlier, the pitch-angle controller is responsible for protecting the wind turbine (WT) from sudden wind gusts. Therefore, as expected, it was shown that the pitch-angle controller remained inactive when the wind speed was lower than the WT’s rated wind speed and only gets activated when the wind speed exceeds the WT’s rated wind speed.

- It was shown that the power coefficient C_p remained constant at its rated value and only started dropping when the wind speed exceeded the WT's rated wind speed. This occurs due to the activation of the pitch-angle controller, and hence, the amount of power extracted from the wind resource by the wind turbine decreases to protect the WT from sudden wind gusts.
- As mentioned previously, the DC-link voltage is required to be stabilized at its desired value to ensure a continuous flow of active power from the WT to the grid. It was observed that the DC-link voltage controller managed to keep the DC-link voltage fixed at the desired value of 1126.77V.
- It was shown that the DC-link voltage was also equally distributed across the two DC- link capacitors. This is a requirement for 3-level NPC VSC topologies.
- It was observed that the stator voltage controller maintained the stator voltage within the desired limits to avoid the risk of over-voltages.
- The effectiveness of the inner current controller was proven by the ability of the measured currents to track the reference currents obtained from the outer control loops and to maintain these currents within the desired limits.
- It was shown that as the wind speed increases, the rotor angular speed increases as well and at the rated wind speed (13m/s), the measured rotor speed is equal to the rated rotor speed, which is 2.356rad/s.
- It was observed that the MPPT controller enabled the power generated from the WT to closely track the optimal power curve to ensure maximum power generation when the wind speed is less than the WT's rated wind speed (13m/s).
- It was also observed that when the wind speed is equal to the WT's rated wind speed, the aerodynamic power generated is equal to 2MW which is the WT's rated power. As the wind speed increased further above the WT's rated wind speed, the generated power initially overshoots and dropped thereafter and remained equal to the rated power. This is possible because of the pitch-angle control technique.
- The MPPT controller also enabled the generated torque to closely track the optimal torque curve when the wind speed is lower than the WT's rated wind speed. As the wind speed increased further above the WT's rated wind speed, the aerodynamic torque remained equal to the WT torque.
- The reactive power controller ensured that the q-component of the grid current is kept to a minimum and close to zero to ensure that the reactive power absorbed or generated by the converter is also kept to a minimum to achieve unity power factor. It was observed that after the system stabilizes, the reactive power was maintained equal to zero to ensure unity power factor.

- It was also observed that the grid-side converter's terminal voltage and current waveforms gave a power factor close to unity. That is 0.99.
- It was observed that the grid voltage vector only had the d-axis component V_{gd}, while the q-axis component V_{gq} was equal to zero. This is a requirement for the vector- oriented control approach which was implemented in this study.

Therefore, to address the research questions, a wind turbine coupled to a PMSG was controlled using the optimal relation-based (ORB) MPPT technique in order to extract maximum power from the wind resource at a wide range of wind speeds thereby enhancing its aerodynamic efficiency. Moreover, the WT's generator and other parts in the nacelle were protected from over-speeding and mechanical stresses by using a rotor-speed-based pitch-angle control technique. Furthermore, the continuous flow of active power from the WT generator to the grid was ensured by keeping the DC-link voltage constant at its desired value of 1126.77V by using a DC-link voltage controller.

The new control approach was compared to the traditional control approach with the aim of assessing how effective the new control approach is in the area of enhancing the fault-ride-through capability of the proposed WT connected to the grid via a three-level NPC VSC. The comparison was carried out-in terms of the ability of the DC-link voltage controller to stabilize the DC-link voltage during fault conditions as this ensures that the power generated by the wind turbine continues flowing effectively to the grid. The comparison was done in MATLAB software package whereby a fault was applied on the grid-side at 0.3 seconds and cleared after 0.2 seconds. That is, at 0.5s. The following conclusions can be drawn:

- It was observed that, for the new controller approach, despite the minimal disturbances in the DC-link voltage during the fault condition, the DC-link voltage remained within the allowable range, that is, ±5% of 1126.77V and hence, it does not overcharge the DC-link capacitors.
- This means that the DC-link voltage controller does not get impaired during fault conditions and hence there is power flowing from the WT generator to the grid. Therefore, the wind turbine remains connected to the grid to offer grid support.
- Conversely, it was observed that during the fault, the ability of the DC-link voltage controller in the traditional control approach to stabilize the DC-link voltage gets impaired and therefore it can no longer effectively transfer as much active power from the WT generator to the grid.

- The surplus power leads to the charging of the DC-link capacitor(s) causing over-voltages in the DC-link. Consequently, this may lead to a significant damage to the converter stations and the DC-link capacitor(s) which will eventually disconnect the wind turbine from the grid.

9.2 Recommendations

Currently, the focus is shifting towards the implementation of renewable energy sources as an alternative to the conventional energy sources such as fossil fuels, and hence more emphasis must be put on the integration of large wind farms into the utility grid. Therefore, from this study, it is recommended that, the same analysis carried out for one wind turbine should be applied to a model with multiple wind turbines making up a large wind farm.

A three-level NPC VSC topology has been implemented in this study. Although this topology performs better than the two-level VSC topology, the modular multilevel converter (MMC) topology certainly performs better than the three-level NPC topology. Therefore, the recommendation for future work is to implement the MMC topology on the same model that is covered in this study and carry out analysis accordingly.

Power-angle (direct) control and vector-oriented control (VOC) are the well-developed control techniques used for independent control of the active and reactive power in grid-connected WECS. Although the VOC method has been proven to be advantages compared to the power-angle control and therefore it is predominantly used in today's industrial practices, several researchers have experienced that for a very weak ac-network, the performance of VOC diminishes due to the presence of the low-frequency resonances. Further, the dynamics of the Phase-Locked Loop (PLL) associated with the VOC control has negative impacts on the performance of the VSC-HVDC systems [21, 105].

Recently, a novel control technique called the power synchronization control has been proposed and it is still undergoing development. In the power synchronization control technique, instead of using a PLL, the VSC synchronizes with the grid directly through the active power control (power synchronization loop (PSL)) like a synchronous machine. Furthermore, a PLL and an inner current control loop are not necessary during normal operations. However, during severe system faults, the control system eventually switches to the current-control mode in order to limit the current flowing through the converter valves and a backup PLL is then applied to provide synchronism [21]. Therefore, for future studies, it is recommended that the current study and analysis should be carried out using the power- synchronization control instead of the vector-oriented control and analyze its effectiveness on the performance of the current model.

This study only focused on a minimal fault analysis on the grid-side. It is recommended that, a thorough fault analysis study should be carried out on the same model considering two conditions. That is, when the fault has occurred on the wind turbine side and when the fault has occurred on the DC-link. Further studies may also be carried out by using the current model to create a multi-terminal DC network and carry out basic analysis accordingly.

REFERENCES

[1] M. Bello, C. Carter-Brown, S. Salvoldi, K. Leask, C. Mushwana, B. Magoro, *et al.*, "Eskom's initiatives to support renewable energy grid integration," in *Energize Journal*, South Africa, 2010.

[2] S. J. T. Mwale and I. E. Davidson, "Power deficits and outage planning in South Africa," in *2nd International Symposium Energy Challenges and Mechanics*, Scotland, United Kingdom, 2014, pp. 1-4.

[3] G. J. Herbert, S. Iniyan, E. Sreevalsan, and S. Rajapandian, "A review of wind energy technologies," *Renewable and sustainable energy Reviews*, vol. 11, pp. 1117-1145, 2007.

[4] T. Ackermann and L. Söder, "Wind energy technology and current status: a review," *Renewable and sustainable energy reviews*, vol. 4, pp. 315-374, 2000.

[5] EWEA, "Wind Energy-the facts," ed, 2009.

[6] S. Szewczuk and E. Prinsloo, "Wind Atlas for South Africa (WASA): Project overview and current status," in *Science real and relevant conference*, CSIR International Convention Centre, Pretoria, 2010.

[7] I. E. Davidson, H. Muashekele, and N. Mukapuli, "Benguela Community/UNAM Wind Power Demonstration Project—Experiences in Implementation," *Journal of Energy and Power Engineering*, vol. 8, pp. 1067-1072, 30 June 2014.

[8] G. Carrara, S. Gardella, M. Marchesoni, R. Salutari, and G. Sciutto, "A new multilevel PWM method: a theoretical analysis," *IEEE Transactions on Power Electronics*, vol. 7, pp. 497-505, 1992.

[9] M. Davies, M. Dommaschk, J. Dorn, J. Lang, D. Retzmann, and D. Soerangr, "HVDC PLUS- Basics and Principles of Operation," ed. Freyeslebenstrasse 1, 91058 Erlangen, Germany: Siemens AG, Energy Sector, 2008.

[10] T. Magg, M. Manchen, E. Krige, J. Wasborg, and J. Sundin, "Connecting networks with VSC HVDC in Africa: Caprivi Link Interconnector," in *IEEE PES PowerAfrica 2012 Conference and Exposition*, Johannesburg, South Africa, 2012, pp. 25-31.

[11] V. K. Sood, *HVDC and FACTS Controllers: Applications of Static Converters in Power Systems*. New York, USA: Springer Science + Business Media, 2004.

[12] ABB, "HVDC Light: It's time to connect," G. S.-H. ABB AB, Ed., ed. SE-771 80 Ludvika, Sweden, 2012.

[13] J. S. Bakhda, T. V. Patel, and A. Deshpande, "Simulation and Modelling of VSC Based HVDC Transmission Line," *International Journal of Research in Electronics and Communication Technology*, vol. 1, pp. 41-45, 2014.

[14] F. Schettler, H. Huang, and N. Christl, "HVDC transmission systems using voltage sourced converters design and applications," in *Power Engineering Society Summer Meeting,*, Seattle, WA, 2000, pp. 715 - 720

[15] N. Flourentzou, V. G. Agelidis, and G. D. Demetriades, "VSC-based HVDC power transmission systems: An overview," *IEEE Transactions on Power Electronics*, vol. 2, March 2009.

[16] S. M. Tripathi, A. N. Tiwari, and S. Deependra, "Grid-integrated permanent magnet synchronous generator based wind energy conversion systems: A technology review," *Renewable and Sustainable Energy Reviews*, vol. 51, pp. 1288-1305, 2015.

[17] Z. Chen and J. M. Guerrero, "A review of the state of the art of power electronics for wind turbines," *IEEE Transaction on Power Electronics*, vol. 24, pp. 1859-1875, August 2009.

[18] M. R. Islam, Y. G. Guo, and J. G. Zhu, "Power converters for wind turbines: current and future development," *Materials and processes for energy: communicating current research and technological developments*, vol. 1, pp. 559-571, 2013.

[19] G. P. Adam, *Voltage Source Converter: modulation, modelling, control and applications in power systems*, 1 ed. Charleston, SC, USA: CreateSpace Independent Publishing Platform, 2014.

[20] N. Freire, J. Estima, and A. Cardoso, "A Comparative Analysis of PMSG Drives Based on Vector Control and Direct Control Techniques for Wind Turbine Applications," *Electrical Review*, vol. 88, pp. 184-187, 2012.

[21] L. Zhang, L. Harnefors, and H. P. Nee, "Power-synchronization control of grid-connected voltage-source converters," *Power Systems*, vol. 25, pp. 809-820, 2010.

[22] S. Li, T. A. Haskew, and L. Xu, "Conventional and novel control designs for direct driven PMSG wind turbines," *Electric Power Systems Research*, vol. 80, pp. 328-338, 2010.

[23] S. Mishra, S. Chatterji, S. L. Shimi, and S. Shukla, "Modelling and Control of Standalone PMSG WECS for Grid Compatibility at Varying Wind Speeds," *International Journal of Engineering Trends and Technology*, vol. 17, pp. 495-501, 2014.

[24] H. Q. Minh, N. Frédéric, E. Najib, and H. Abdelaziz, "Control of permanent magnet synchronous generator wind turbine for stand-alone system using fuzzy logic," in *7th Conference of the European Society for Fuzzy Logic and Technology*, Aix-les-Bains, France, 2011, pp. 720-725.

[25] J. Chen, H. Wu, M. Sun, W. Jiang, L. Cai, and C. Guo, "Modeling and simulation of directly driven wind turbine with permanent magnet synchronous generator," in *Innovative Smart Grid Technologies- Asia*, Tianjin, 2012, pp. 1-5.

[26] A. D. Hansen and G. Michalke, "Modelling and Control of variable speed Multi-pole Permanent Magnet Synchronous generator Wind Turbine," *Wind Energy*, vol. 11, pp. 537-554, 2008.

[27] A. D. Hansen and G. Michalke, "Multi-pole permanent magnet synchronous generator wind turbines' grid support capability in uninterrupted operation during grid faults," *IET Renewable Power Generation*, vol. 3, pp. 333-348, 2009.

[28] R. Radervall, J. P. Charpentier, and R. Sharma, "High Voltage Direct Current (HVDC) Transmission Systems: Technology Review Paper," in *Energy Week*, Washington DC, USA, 2000.

[29] M. Aberg, K. Eriksson, M. Byggeth, U. Axelsson, A. Holm, and C. Liljegren, "The Gotland HVDC Light project- experiences from trial and commercial operation," in *16th Internation Conference and Exhibition on Electricity Distribution*, Amsterdam, 2001.

[30] U. Axelsson, A. Holm, C. Liljegren, K. Eriksson, and L. Weimer, "Gotland HVDC Light Transmission- The World's First Commercial Small Scale DC Transmission," in *Cigre Conference*, Nice, France, 1999, pp. 1-5.

[31] B. Snyder and M. J. Kaiser, "Ecological and economic cost-benefit analysis of offshore wind energy," *Renewable Energy*, vol. 34, pp. 1567-1578, 2009.

[32] V. Gevorgian, M. Singh, and E. Muljadi, "Variable Frequency Operations of an Offshore Wind Power Plant with HVDC-VSC," in *IEEE Power and Energy Society General Meeting*, San Diego, California, 2012, pp. 1-8.

[33] O. Gomis-Bellmunt, A. Junyent-Ferre, A. Sumper, and J. Begas-Jane, "Control of a Wind Farm Based on Synchronous Generators With a. Central HVDC-VSC Converter," *IEEE Transactions on Power Systems*, vol. 26, pp. 1632-1640, 2011.

[34] M. B. Uría, "Operation and control of Multi-Terminal DC (MTDC) Grids," Masters, Electrical Engineering, Aalborg University, 2013.

[35] P. Bresesti, W. L. Kling, and R. L. Hendriks, "HVDC Connection of Offshore Wind Farms to the Transmission System," *IEEE Transaction on Energy Conversion*, vol. 22, pp. 37-43, March 2007.

[36] M. P. Bahrman, J. G. Johansson, and B. A. Nilsson, "Voltage Source Converter Transmission Technologies: The Right Fit for the Application," *IEEE Power Engineering Society General Meeting*, pp. 1840-1847, July 2003.

[37] H. Patel, "Model of Voltage Source Converter Based HVDC Transmission System in EMTP-RV," Masters, Electrical and Computer Engineering, University of Ontario Institute of technology, 2010.

[38] T. W. Shire, "VSC-HVDC based Network Reinforcement," Masters, Department of High-Voltage Components and Power Systems, Delft University of Technology, 2009.

[39] J. A. Baroudi, V. Dinavahi, and A. M. Knight, "A review of power converter topologies for wind generators," *Renewable Energy*, vol. 32, pp. 2369–2385, 2007.

[40] J.-S. Lai and F. Z. Peng, "Multilevel converters-a new breed of power converters," *IEEE Transactions on industrial Applications*, vol. 32, May/June 2002.

[41] C. C. Bonilla and S. M. Tigga, "Design and Performance Comparison of Two-level and Multilevel Converters for HVDC Applications," Masters, Department of Energy and Environment, Chalmers University of Technology, Goteborg, Sweden, 2011.

[42] M. Islam, Y. Guo, J. Zhu, and D. Dorrell, "Design and comparison of 11 kV multilevel voltage source converters for local grid based renewable energy systems," in *37th Annual Conference on IEEE Industrial Electronic Socety*, 2011, pp. 3596-3601.

[43] A. Antonopoulos, L. Angquist, and H.-P. Nee, "On dynamics and voltage control of the modular multilevel converter," in *Power Electronics and Applications, 2009. EPE'09. 13th European Conference on*, 2009, pp. 1-10.

[44] W. Li, L.-A. Gregoire, and J. Bélanger, "Control and performance of a modular multilevel converter system," in *CIGRÉ Canada, Conference on Power Systems, Halifax*, 2011, pp. 1-8.

[45] S. S. Fazel, S. Bernet, D. Krug, and J. K, "Design and comparison of 4-kV neutral-point-clamped, flying-capacitor, and series-connected H-bridge multilevel converters," *IEEE Transaction on Industry Applications*, vol. 43, pp. 1032-1040, July/August 2007.

[46] S. Allebrod, R. Hamerski, and R. Marquardt, "New transformerless, scalable modular multilevel converters for HVDC-transmission," in *Power Electronics Specialists Conference, 2008. PESC 2008. IEEE*, 2008, pp. 174-179.

[47] A. Lesnicar and R. Marquardt, "An innovative modular multilevel converter topology suitable for a wide power range," in *Power Tech Conference Proceedings, 2003 IEEE Bologna*, 2003, p. 6 pp. Vol. 3.

[48] J. M. Carrasco and L. G. Franquelo, "Power-electronic systems for the grid integration of renewable energy sources: A survey," *IEEE Transactions on Industrial Electronics*, vol. 53, pp. 1002-1016, August 2006.

[49] A. L. Soriano, W. Yu, and J. J. Rubio, "Modeling and control of wind turbine," *Mathematical Problems in Engineering*, vol. 2013, pp. 1-13, 26 June 2013.

[50] B.Wu, Y. Lang, N. Zargari, and S.Kouro, *Power Conversion and Control of Wind Energy Systems*. New York, USA: John Wiley & Sons, 2011.

[51] G. E. Saady, E. A. Ibrahim, H. Ziedan, and M. M. Soliman, "Analysis of Wind Turbine Driven Permanent Magnet Synchronous Generator under Different Loading Conditions," *Innovative Systems Design and Engineering*, vol. 4, pp. 97-111, 2013.

[52] M. Yin, G. Li, M. Zhou, and C. Zhao, "Modeling of the wind turbine with a permanent magnet synchronous generator for integration," in *Power Engineering Society General Meeting*, Tampa, FL, 2007, pp. 1 - 6.

[53] J. Aho, A. Buckspan, J. Laks, P. Fleming, Y. Jeong, F. Dunne, *et al.*, "A tutorial of wind turbine control for supporting grid frequency through active power control," in *2012 American Control Conference*, Fairmont Queen Elizabeth, Montréal, Canada, 2012.

[54] D. C. Aliprantis and S. A. Papathanassiou, "Modeling and control of a variable-speed wind turbine equipped with permanent magnet synchronous generator," in *14th International Conference on Electrical Machines*, Espoo, Finland, 2000, pp. 558-562.

[55] S. K. Bisoyi, R. K. Jarial, and R. A. Gupta, "Modeling and Control of Variable Speed Wind Turbine Equipped with PMSG," *International Journal of Emerging Technologies in Computational and Applied Sciences*, vol. 6, pp. 56-62, September - November 2013.

[56] M. Chinchilla and S. Arnaltes, "Control of permanent-magnet generators applied to variable-speed wind-energy systems connected to the grid," *Energy Conversion*, vol. 21, pp. 130-135, 2006.

[57] Y. Errami, M. Ouassaid, and M. Maaroufi, "Control of a PMSG based wind energy generation system for power maximization and grid fault conditions," *Energy Procedia*, vol. 42, pp. 220-229, 2013.

[58] K. Bunjongjit and Y. Kumsuwan, "Performance Enhancement of PMSG Systems with Control of Generator-side Converter Using d-axis Stator Current Controller," *ECTI Transactions on Electrical Engineering, Electronics and Communications*, vol. 11, pp. 51-57, 2013.

[59] M. Islam, Y. Guo, and J. Zhu, "A review of offshore wind turbine nacelle: technical challenges, and research and developmental trends," *Renewable and Sustainable Energy Reviews*, vol. 33, pp. 161-176, 2014.

[60] H. W. Kim, S. S. Kim, and H. S. Ko, "Modeling and control of PMSG-based variable-speed wind turbine," *Electric Power Systems Research*, vol. 80, pp. 40-52, 2010.

[61] B. Malinga and J. E. Sneckenberger, "Modeling and control of a wind turbine as a distributed resource," in *Proceedings of the 35th Southeastern Symposium on System Theory*, Marriott Huntsville Huntsville, USA, 2003, pp. 108-112.

[62] G. Vazquez, D. Aguilar, and G. Azevedo, "Modeling of a variable speed wind turbine with a permanent magnet synchronous generator," in *IEEE International Symposium on Industrial Electronics (ISlE 2009)*, Seoul Olympic Parktel, Seoul, Korea, 2009, pp. 734-739.

[63] O. Wasynczuk, D. T. Man, and S. J. P., "Dynamic behavior of a class of wind turbine generators during randon wind fluctuations," *IEEE Transactions on Power Apparatus and Systems*, vol. PAS-100, pp. 2837-2845, June 1981.

[64] O. Yüksel, G. İrfan, and Ç. Hüseyin, "Power Quality Control and Design of Power Converter for Variable-Speed Wind Energy Conversion System with Permanent-Magnet Synchronous Generator," *The Scientific World Journal*, vol. 2013, pp. 1-14, 9 September 2013.

[65] J. G. Slootweg, S. W. H. Haan, H. Polinder, and W. L. Kling, "General model for representing variable speed wind turbines in power system dynamics simulations," *IEEE Transactions on Power Systems*, vol. 18, pp. 144-151, 2003.

[66] P. Kundur, *Power System Stability and Control*, 1 ed. New York: McGraw-Hill Education, 1994.

[67] M. Nasiri, J. Milimonfared, and S. H. Fathi, "Robust Control of PMS-based Wind Turbine under Grid Fault Conditions," *Indian Journal of Science and Technology*, vol. 8, pp. 1-13, July 2015.

[68] N. A. Orlando, M. Liserre, and R. Mastromauro, "A survey of control issues in PMSG-based small wind-turbine systems," *Industrial Informatics*, vol. 9, pp. 1211-1221, 2013.

[69] Y. Yang, K. T. Mok, S. C. Tan, and S. Y. Hui, "Nonlinear Dynamic Power Tracking of Low-Power Wind Energy Conversion System," *IEEE Transactions on Power Electronics*, vol. 30, pp. 5223-5236, 2015, 2015.

[70] A. Giallanza, M. Porretto, L. Cannizzaro, and G. Marannano, "Analysis of the maximization of wind turbine energy yield using a continuously variable transmission system," *Renewable Energy*, vol. 2016, pp. 1-6, 2016.

[71] Y. Errami, M. Ouassaid, and M. Maaroufi, "Optimal Power Control Strategy of Maximizing Wind Energy Tracking and Different Operating Conditions for Permanent Magnet Synchronous Generator Wind Farm," *Energy Procedia*, vol. 74, pp. 477-490, 2015.

[72] M. Nasiri, J. Milimonfared, and S. H. Fathi, "Modeling, analysis and comparison of TSR and OTC methods for MPPT and power smoothing in permanent magnet synchronous generator-based wind turbines," *Energy Conversion and Management*, vol. 86, pp. 892-900, 2014.

[73] S. R. Bowes and S. Grewal, "A novel harmonic elimination PWM strategy," in *Seventh International Conference on Power Electronics and Variable Speed Drives*, London, 1998, pp. 426-432.

[74] J. S. Thongam and M. Ouhrouche, *MPPT control methods in wind energy conversion systems*: INTECH Open Access Publisher, 2011.

[75] R. D. Shukla and R. Tripathi, "Maximum power extraction schemes & power control in wind energy conversion system," *International Journal of Scientific & Engineering Research*, vol. 3, pp. 1-7, 2012.

[76] K. Chatterjee and D. Kumar, "A review of conventional and advanced MPPT algorithms for wind energy systems," *Renewable and Sustainable Energy Reviews,* vol. 55, pp. 957-970, 2016.

[77] M. B. Smida and A. Sakly, "Pitch Angle Control for Variable Speed Wind Turbines," *Journal of Renewable Energy and Sustainable Development,* vol. 2015, pp. 81-88, June 2015.

[78] J. Zhang, M. Cheng, Z. Chen, and X. Fu, "Pitch angle control for variable speed wind turbines," in *Third International Conference on Electric Utility Deregulation and Restructuring and Power Technologies*, Nanjing Shi, China, 2008, pp. 2691-2696.

[79] A. Hwas and R. Katebi, "Wind Turbine Control Using Pitch Angle Controller," in *IFAC Conference on Advances in PID Control*, Brescia, Italy, 2012.

[80] M. B. Smida and A. Sakly, "Different conventional strategies of pitch angle control for variable speed wind turbines," in *15th International Conference on Sciences and Techniques of Automatic Control and Computer Engineering (STA)*, Sousse, Tunisia, 2014, pp. 803-808.

[81] I. Hamzaoui, F. Bouchafaa, and A. Talha, "Pitch Angle Control for Variable Speed Wind Turbines with Doubly Fed Induction Generators," *Journal of Electrical Engineering,* pp. 1-8, 2011.

[82] S. R. Bowes and D. Holliday, "Comparison of Pulse-width-modulation control strategies for three-phase inverter systems," *IEE Electrical Power Applications,* vol. 153, pp. 575-584, 2006.

[83] E. R. C. d. Silva, E. C. d. Santos, and C. B. Jacobina. (2011) Pulsewidth Modulation Strategies. *Industrial Electronics Magazine*. 37-45.

[84] M. S. A. Dahidah and V. G. Agelidis, "Selective harmonic elimination multilevel control with variant DC sources," in *4th IEEE Conference on Industrial Electronics and Applications*, Xi'an, China, 2009, pp. 3351-3356.

[85] F. A. B. Batista and I. Barbi, "Space Vector Modulation Applied to Three-phase Three-Switch Two-level Unidirectional PWM Rectifier," *IEEE Transaction on Power Electronics,* vol. 22, pp. 2245-2252, 2007.

[86] G. P. Adam, "Quasi Two-Level Operation of a Five-Level Diode Clmaped Inverter," PhD Thesis, Electrical and Electronic Engineering Department, University of Strathclyde, Glasgow, UK, 2007.

[87] D. G. Holmes and T. A. Lipo, *Pulse Width Modulation for Power Converters: Principles and Practice*. New York: John Wiley & Sons Inc, 2003.

[88] N. S. Nise, *Control Systems Engineering*, 3 ed. New York: John Wiley & Sons, 2000.

[89] A. Kumar, *Control System*. New Delhi: McGraw Hill Publishing Company Limited, 2006.

[90] G. Beale, "Phase Lag Compensator Design Using Bode Plots," George Mason University, Fairfax, Virginia2003.

[91] G. Beale, "Lag-Lead Compensator Design Using Bode Plots," George Mason University, Fairfax, Virginia2003.

[92] G. Beale, "Phase Lead Compensator Design Using Bode Plots," George Mason University, Fairfax, Virginia2003.

[93] J. D. Irwin, *The Industrial Electronics Hand Book*. USA: CRC Press & IEEE Press, 1997.

[94] P. V. Sreeraj, "Design and Implementation of PID Controller with Lead Compensator for Thermal Process," *International Journal of Computer Applications,* vol. 67, pp. 26-31, 2013.

[95] M. Islam, S. Mekhilef, and R. Saidur, "Progress and recent trends of wind energy technology," *Renewable and Sustainable Energy Reviews,* vol. 21, pp. 456-468, 2013.

[96] C. Yeroglu and N. Tan, "Note on fractional-order proportional-integral-differential controller design," *IET control theory & applications,* vol. 5, pp. 1978-1989, 2011.

[97] Z. Civelek, E. Çam, M. Lüy, and H. Mamur, "Proportional–integral–derivative parameter optimisation of blade pitch controller in wind turbines by a new intelligent genetic algorithm," *IET Renewable Power Generation,* vol. 10, pp. 1220-1228, 2016.

[98] Z. Zang, Y. Zhao, W. Qiao, and L. Qu, "A Discrete-Time Direct Torque Control for Direct-Drive PMSG-Based Wind Energy Conversion Systems," *IEEE Transactions on Industry Applications,* vol. 51, pp. 3504-3514, 2015.

[99] K. Ogata, *Modern Control Engineering*, 4 ed. Prentice Hall, NJ: Upper Saddle River, 2002.

[100] R. Pollaren, "Converter-flux-based current control of voltage source PWM rectifier analysis and implementation," PhD Thesis, Department of Electrical Engineering, Lappeenranta University of Technology, Finland, 2003.

[101] B. Bahraminejad and M. R. Iranpour, "Comparison of Interval Type-2 Fuzzy Logic Controller with PI Controller in Pitch Control of Wind Turbines," *International Journal of Renewable Energy Research (IJRER),* vol. 5, pp. 836-846, 2015.

[102] C. B. Carl Blake, "IGBT or MOSFET: Choose Wisely," ed: International Rectifier, 2010.

[103] S. Keshavarz, "Design and Evaluation of an Active Rectifier for a 4.1MW Off-Shore Wind Turbine," MSc, Department of Energy and Environment, Chambers University of Tecghnology, Goteborg, Sweden, 2011.

[104] O. A. Giddani, A. Y. M. Abbas, G. P. Adam, O. Anaya-Lara, and K. L. Lo, "Multi-task control for VSC–HVDC power and frequency control," *Electrical Power and Energy Systems* vol. 53, pp. 684–690, 2013.

[105] P. Mitra, L. Zhang, and L. Harnefors, "Offshore wind integration to a weak grid by VSC-HVDC links using power-synchronization control: A case study," *IEEE Transactions on Power Delivery*, vol. 29, pp. 453-461, February 2014.

[106] NERSA, "Grid Code Requirements for Wind Turbines Connected to Distribution or Transmission Systems in South Africa," ed, 2008.

[107] NERSA, "Grid Connection Code for Renewable Power Plants (RPPs) Connected to the Electricity Transmission System (TS) of the Distribution System (DS) in South Africa," 2014.

[108] B. D. Railin, J. J. Miller, G. Moreau, J. Wasborg, Y. Jiang-Häfner, and D. Stanley, "The DirectLink VSC-based HVDC Project and its Commissioning," in *Cigre Conference*, Paris, France, 2002, pp. 1-9.

[109] I. Mattsson, A. Ericsson, B. D. Railing, J. J. Miller, B. Williams, G. Moreau, *et al.*, "Murray link—the longest underground HVDC cable in the world," in *Cigré conference*, Paris, France, 2004, pp. 1-8.

[110] L. Tang, "HVDC Technologies & ABB Experience," ABB, Ed., ed, 2013.

[111] F. Wang, L. Bertling, T. Le, A. Mannicoff, and A. Bergman, "An Overview Introduction of VSC-HVDC: State-of-art and Potential Applications in Electric Power Systems," in *Cigre Conference*, Paris, France, 2011, pp. 1-10.

APPENDICES

The appendix section is made up of the M-files with the MATLAB codes of the proposed controllers, the Clarke and Park transformations, and a brief review the South African grid code requirements for integrating wind energy systems into the main power utility grid, and the current VSC-based HVDC projects in operation worldwide,

Appendix A: M-File Codes for the Proposed Controllers

A.1 Generator-side converter's inner current controller design

****

%System Parameters

R_t=0.821e-3; L_t=1.5731e-3; C=23.63e-3; t=L_t/R_t;

F_{switch}=2000; $T_{switch}=1/F_{switch}$; Ta=$T_{switch}/2$

%Stator Current Controller

num_ol= [1]; %Numerator of the uncompensated system

den_ol= [T_a*L_t (T_a*R_t) +L_t R_t]; %Denominator of the uncompensated system

$G_{i\_ol\_uncompen}$=tf (num_ol, den_ol) %Transfer function: uncompensated system

bode ($G_{i\_ol\_uncompen}$) %Bode plot of the uncompensated system

hold on

%Gain compensation

Gain=6.27; %Gain K

Gi_ol_compen_gain=Gi_ol_uncompen*Gain %Transfer function: gain-compensated system

bode ($G_{i\_ol\_compen\_gain}$) %Bode plot of the gain-compensated system

hold on

$w_{\_BW}$=3141.59; %Bandwidth of the inner current control loop

%Phase-Lead Compensator Design

Q=57.85-51.9; %Phase boost needed

$F_c=w_{\_BW}/(2*pi)$; %Cross-over frequency in Hz

$F_z=F_c$*sqrt ((1-sin (Q))/ (1+sin (Q))); %Frequency where the zero will be located

$F_p=F_c$*sqrt ((1+sin (Q))/ (1-sin (Q))); %Frequency where the pole will be located

$w_c=2*pi*F_c$;

w_z=2*pi*450.60; %Angular frequency where the zero will be located

w_p=2*pi*554.82; %Angular frequency where the pole will be located

tau=1/w_z; alpha_lead=w_z/w_p; G_{co}=sqrt (alpha_lead);

```
num_lead= [Gco*tau Gco];                    %Numerator of the lead compensator
den_lead= [alpha_lead*tau 1];               %Denominator of the phase-lead compensator
Glead=tf (num_lead, den_lead)               %Phase-lead compensator's transfer function
bode (Glead)                                %Bode plot of the phase-lead compensator
hold on
Gi_ol_compen_lead=Gi_ol_compen_gain*Glead   %Transfer function: phase-lead compensated
bode (Gi_ol_compen_lead)
%*************************************************************************
                    Closed Loop Transfer Functions
%*************************************************************************
Gi_cl_uncompen=feedback (Gi_ol_uncompen, 1)
Gi_cl_compen_gain=feedback (Gi_ol_compen_gain, 1)
Gi_cl_compen_lead=feedback (Gi_ol_compen_lead, 1)
%*************************************************************************
                    Step Response Curves
%*************************************************************************
step (Gi_cl_uncompen)                       %Step response of the uncompensated system
hold on
step(Gi_cl_compen_gain)                     %Step response of the gain-compensated system
hold on
step (Gi_cl_compen_lead)                    %Step response of the phase-lead compensated system
%*************************************************************************
```

A.2 DC-Link voltage controller design

```
%*************************************************************************
%Uncompensated System
Gisd_compens_=Gi_cl_compen_lead             %Closed loop transfer function: d-component
Vsd=690; Vdc_ref=1126.77;
num_v= [3*Vsd];                             %Numerator of the uncompensated system
den_v= [2*Vdc_ref*C 0];                     %Denominator of the uncompensated system
Gvdc=tf (num_v, den_v);                     %Transfer function: Uncompensated system
bode (Gvdc)
hold on
Gvdc_ol_uncompen=Gisd_compens_*Gvdc         %Transfer function: Uncompensated system
bode (Gvdc_ol_uncompen)                     %Bode plot of the uncompensated system
%Gain compensation
```

```
Gain_v=20.05                                  %Gain K
G_vdc_ol_compen_gain=G_vdc_ol_uncompen*Gain_v  %Gain-compensated system
bode (G_vdc_ol_compen_gain)                   %Bode plot of the gain-compensated system
w_BW_v=785.40;                                %Bandwidth of the outer control loop

%Phase-Lag Compensator Design
Q_v=57.85-77.3;                               %Phase attenuation needed
F_c_v=w_BW_v/ (2*pi);                         %Cross-over frequency in Hz
F_z_v=F_c_v*sqrt ((1-sin (Q_v))/ (1+sin (Q_v)));   %Frequency where the zero will be located
F_p_v=F_c_v*sqrt ((1+sin (Q_v))/ (1-sin (Q_v)));   %Frequency where the pole will be located
w_c_v=2*pi*F_c_v;
w_z_v=2*pi*176.71;                            %Angular frequency where the zero will be located
w_p_v=2*pi*88.42;                             %Angular frequency where the pole will be located
tau_v=1/w_z_v; alpha_lag_v=w_z_v/w_p_v; G_co_v=sqrt (alpha_lag_v);
num_lag_v= [G_co_v*tau_v G_co_v];             %Numerator of the phase-lag compensator
den_lag_v= [alpha_lag_v*tau_v 1];             %Denominator of the phase-lag compensator
G_lag_=tf (num_lag_v, den_lag_v)              %Transfer function of the phase-lag compensator
bode (G_lag_)                                 %Bode plot of the phase-lag compensator
G_vdc_ol_compen_lag=G_vdc_ol_compen_gain*G_lag_   % Phase-lag compensated
bode (G_vdc_ol_compen_lag)                    %Bode plot of the phase-lag compensated system
%*************************************************************************

Closed Loop Transfer Functions

%*************************************************************************
G_vdc_cl_uncompen=feedback (G_vdc_ol_uncompen, 1);
G_vdc_cl_compen_gain=feedback (G_vdc_ol_compen_gain, 1);
G_vdc_cl_compen_lag=feedback (G_vdc_ol_compen_lag, 1);
%*************************************************************************

Step Response Curves

%*************************************************************************
step (G_vdc_cl_uncompen)                      %Step response of the uncompensated system
hold on
step (G_vdc_cl_compen_gain)                   %Step response of the gain-compensated system
hold on
step (G_vdc_cl_compen_lag)                    %Step response of the phase-lag compensated system
%*************************************************************************
```

A.3 Stator Voltage Controller Design

```
%*************************************************************************
Gisq_compens_cl=Gi_cl_compen_lead                    %Closed-loop transfer function: q-component
Lst=1.5731e-3; Vcon=620.62;
rpm=22.9; np=26; we=2*pi*((np*rpm)/60); Xs=we*(Lst*2);
num_v= [-3*Xs+2*Vcon];                               %Numerator of the uncompensated system
den_v= [2];                                          %Denominator of the uncompensated system
Gvst=tf (num_v, den_v);                              %Transfer function: uncompensated system
bode (Gvst)
Gvst_ol_uncompen=Gisq_compens_cl*Gvst                %Transfer function: uncompensated system
bode (Gvst_ol_uncompen)                              %Bode plot of the uncompensated system
w_BW_v=785.40;                                       %Bandwidth of the outer control loop

%Phase-Lag Compensator Design
alpha_v=389045.15;                                   % Phase attenuation alpha
zc_v=w_BW_v*sqrt (alpha_v);                          %Zero location
pc_v=zc_v/alpha_v;                                   %Pole location
num_l= [1/zc_v 1];                                   %Numerator of the phase-lag compensator
den_l= [1/pc_v 1];                                   %Denominator of the phase-lag compensator
Glag_1=tf (num_l, den_l)                             %Transfer function: phase-lag compensator
bode (Glag_1)                                        %Bode plot of the phase-lag compensator
hold on
Gvst_ol_compen_lag=Gvst_ol_uncompen*Glag_1           %Transfer function: phase-lag compensated
bode (Gvst_ol_compen_lag)                %Bode plot of the phase-lag compensated system

%Second Phase-Lag Compensator Design
Q_v=57.85-77.5;                                      %Phase attenuation needed
Fc_v=w_BW_v/ (2*pi);                                 %Crossover frequency in Hz
Fz_v=Fc_v*sqrt ((1-sin (Q_v))/ (1+sin (Q_v)));       %Frequency where the zero will be located
Fp_v=Fc_v*sqrt ((1+sin (Q_v))/ (1-sin (Q_v)));       %Frequency where the pole will be located
wc_v=2*pi*Fc_v;
wz_v=2*pi*177.36;                        %Angular frequency where the zero will be located
wp_v=2*pi*88.09;                         %Angular frequency where the pole will be located
tau_v=1/wz_v; alpha_lag_v=wz_v/wp_v; Gco_v=sqrt (alpha_lag_v);
num_lag_v= [Gco_v*tau_v Gco_v];          %Numerator of the second phase-lag compensator
```

```
den_lag_v= [alpha_lag_v*tau_v 1];        %Denominator of the second phase-lag compensator
G_lag_2=tf (num_lag_v, den_lag_v)        %Transfer function: second phase-lag compensator
bode (G_lag_2)                           %Bode plot of the second phase-lag compensator
G_vst_ol_compen_lag_lag=G_vst_ol_compen_lag*G_lag_2 % TF: Phase-lag compensated system
bode (G_vst_ol_compen_lag_lag)           %Bode plot of the phase-lag compensated system
%*************************************************************************
```

Closed Loop Transfer Functions

```
*************************************************************************
G_vst_cl_uncompen=feedback (G_vst_ol_uncompen, 1);
G_vst_cl_compen_lag=feedback (G_vst_ol_compen_lag, 1);
G_vst_cl_compen_lag_lag=feedback (G_vst_ol_compen_lag_lag, 1);
%*************************************************************************
```

Step Response Curves

```
*************************************************************************
step (G_vst_cl_uncompen)                 %Step response of the uncompensated system
hold on
step (G_vst_cl_compen_lag)               %Step response: first phase-lag compensated system
hold on
step (G_vst_cl_compen_lag_lag)           %Step response: second phase-lag compensated system
%*************************************************************************
```

A.4 Grid-side Converter's Inner Current Controller Design

```
%*************************************************************************
```

%System Parameters

```
R_t=0.665e-3; L_t=66.5e-3; C=23.63e-3; t=L_t/R_t;
F_switch=2000; T_switch=1/F_switch; Ta=T_switch/2
```

%Stator Current Controller

```
num_ol= [1];                             %Numerator of the uncompensated system
den_ol= [T_a*L_t (T_a*R_t) +L_t R_t];    %Denominator of the uncompensated system
G_i_ol_uncompen=tf (num_ol, den_ol)      %Transfer function: uncompensated system
bode (G_i_ol_uncompen)                   %Bode plot of the uncompensated system
hold on
```

%Gain compensation

```
Gain=266.01;                                    %Gain K
Gi_ol_compen_gain=Gi_ol_uncompen*Gain    %Transfer function: gain-compensated system
```

```
bode (G_i_ol_compen_gain)                    %Bode plot of the gain-compensated system
hold on
w_BW=3141.59;                                %Bandwidth of the inner current control loop

%Phase-Lead Compensator Design
Q=57.85-51.8;                                %Phase boost needed
F_c=w_BW/ (2*pi)       ;                     %Cross-over frequency in Hz
F_z=F_c*sqrt ((1-sin (Q))/ (1+sin (Q)));     %Frequency where the zero will be located
F_p=F_c*sqrt ((1+sin (Q))/ (1-sin (Q)));     %Frequency where the pole will be located
w_c=2*pi*F_c;
w_z=2*pi*449.81;                             %Angular frequency where the zero will be located
w_p=2*pi*555.79;                             %Angular frequency where the pole will be located
tau=1/w_z; alpha_lead=w_z/w_p; G_co=sqrt (alpha_lead);
num_lead= [G_co*tau G_co];                   %Numerator of the lead compensator
den_lead= [alpha_lead*tau 1];                %Denominator of the phase-lead compensator
G_lead=tf (num_lead, den_lead)               %Phase-lead compensator's transfer function
bode (G_lead)                                %Bode plot of the phase-lead compensator
hold on
G_i_ol_compen_lead=G_i_ol_compen_gain*G_lead %Transfer function: phase-lead compensated
bode (G_i_ol_compen_lead)
%*************************************************************************
                    Closed Loop Transfer Functions
%*************************************************************************
G_i_cl_uncompen=feedback (G_i_ol_uncompen, 1)
G_i_cl_compen_gain=feedback (G_i_ol_compen_gain, 1)
G_i_cl_compen_lead=feedback (G_i_ol_compen_lead, 1)
%*************************************************************************
                    Step Response Curves
%*************************************************************************
step (G_i_cl_uncompen)                       %Step response of the uncompensated system
hold on
step(G_i_cl_compen_gain)                     %Step response of the gain-compensated system
hold on
step (G_i_cl_compen_lead)                    %Step response of the phase-lead compensated system
%*************************************************************************
```

A.5 MPPT Controller Design

```
%*************************************************************************
Gigd_compens_cl=Gi_cl_compen_lead;                %Closed-loop transfer function: d-component
Vgd=620.62;
num_p= [3*Vgd];                                  %Numerator of the uncompensated system
den_p= [2];                                      %Denominator of the uncompensated system
Gmppt=tf (num_p, den_p)                          %Transfer function: Uncompensated system
bode (Gmppt)
Gp_ol_uncompen=Gigd_compens_cl*Gmppt              %Transfer function: uncompensated system
bode (Gp_ol_uncompen)                            %Bode plot of the uncompensated system

%Phase-Lag Compensator Design
w_BW_p=785.40;                                   %Bandwidth of the outer control loop
alpha_p=870963.59;                               %Attenuation alpha
zc_v=w_BW_p*sqrt (alpha_p);                      %Zero location
pc_v=zc_v/alpha_p;                               %Pole location
num_l= [1/zc_v 1];                               %Numerator of the phase-lag compensator
den_l= [1/pc_v 1];                               %Denominator of the phase-lag compensator
Glag_=tf (num_l, den_l)                  %Transfer function of the phase-lag compensator
bode (Glag_)
hold on                                  %Bode plot of the phase-lag compensator
Gp_ol_compen_lag=Gp_ol_uncompen*Glag_    %Transfer function: phase-lag compensated
bode (Gp_ol_compen_lag)                  %Bode plot of the phase-lag compensated system

%Second-Lag Compensator Design
Q_p_1=57.85-77.5;                                %Phase attenuation needed
Fc_p=w_BW_p/ (2*pi);                             %Crossover frequency in Hz
Fz_p_1=Fc_p*sqrt (1-sin (Q_p_1)/1+sin (Q_p_1)); %Frequency where the zero will be located
Fp_p_1=Fc_p*sqrt (1+sin (Q_p_1)/1-sin (Q_p_1)); %Frequency where the pole will be located
wc_p_1=2*pi*Fc_p;
wz_p_1=2*pi*177.36;                              %Angular frequency where the zero will be located
wp_p_1=2*pi*88.10;                               %Angular frequency where the pole will be located
tau_p_1=1/wz_p_1
alpha_lag_p_1=wz_p_1/wp_p_1
Gco_p_1=sqrt (alpha_lag_p_1)
num_lag_p_1= [Gco_p_1*tau_p_1 Gco_p_1];          %Numerator: second phase-lag compensator
```

```
den_lag_p_1= [alpha_lag_p_1*tau_p_1 1];        %Denominator: second phase-lag compensator
G_lag_2=tf (num_lag_p_1, den_lag_p_1)          %Transfer function: second phase-lag compensator
bode (G_lag_2)                                 %Bode plot of the second phase-lag compensator
G_p_ol_compen_lag_lag=G_p_ol_compen_lag*G_lag_2   %2nd Phase-lag compensated system
bode (G_p_ol_compen_lag_lag)                   %Bode plot: second phase-lag compensated system
%*************************************************************************
```

Closed Loop Transfer Functions

```
%*************************************************************************
G_p_cl_uncompen=feedback (G_p_ol_uncompen, 1);
G_p_cl_compen_lag=feedback (G_p_ol_compen_lag, 1);
G_p_cl_compen_lag_lag=feedback (G_p_ol_compen_lag_lag, 1);
%*************************************************************************
```

Step Response Curves

```
%*************************************************************************
step (G_p_cl_uncompen)                         %Step response of the uncompensated system
hold on
step (G_p_cl_compen_lag)                       %Step response: first phase-lag compensated system
hold on
step (G_p_cl_compen_lag_lag)                   %Step response: second phase-lag compensated system
%*************************************************************************
```

A.6 Reactive Power Controller Design

```
%*************************************************************************
G_igq_compens_cl=G_i_cl_compen_lead                %Closed-loop transfer function: q-component
V_gd=620.62;
num_q= [3*V_gd];                                   %Numerator of the uncompensated system
den_q= [2];                                        %Denominator of the uncompensated system
G_q=-tf (num_q, den_q)                         %Transfer function of the uncompensated system
bode (G_q)
hold on
G_q_ol_uncompen=G_igq_compens_cl*G_q           %Transfer function of the uncompensated system
bode (G_q_ol_uncompen)                         %Bode plot of the uncompensated system
```

%Phase-Lag Compensator Design

```
w_BW_q=785.40;                                     %Bandwidth of the outer control loop
alpha_q=870963.59;                                 %Attenuation alpha
```

```
z_c_q=w_BW_q*sqrt (alpha_q);                    %Zero location
p_c_q=z_c_q/alpha_q;                            %Pole location
num_l= [1/z_c_q 1];                             %Numerator of the phase-lag compensator
den_l= [1/p_c_q 1];                             %Denominator of the phase-lag compensator
G_lag_=-tf (num_l, den_l)                       %Transfer function of the phase-lag compensator
bode (G_lag_)                                   %Bode plot of the Phase-lag compensator
G_q_ol_compen_lag=G_q_ol_uncompen*G_lag_        %Transfer function: Phase-lag compensated
bode (G_q_ol_compen_lag)                        %Bode plot of the phase-lag compensated system
hold on
```

%Second Phase-Lag Compensator Design

```
Q_q_1=57.85-77.5;                               %Phase attenuation needed
F_c_q=w_BW_q/ (2*pi);                           %Crossover frequency in Hz
F_z_q_1=F_c_p*sqrt (1-sin (Q_p_1)/1+sin (Q_p_1));   %Frequency where the zero will be located
F_p_q_1=F_c_q*sqrt (1+sin (Q_p_1)/1-sin (Q_p_1));   %Frequency where the pole will be located
w_c_q_1=2*pi*F_c_q;
w_z_q_1=2*pi*177.36;                            %Angular frequency where the zero will be located
wp_q_1=2*pi*88.10;                              %Angular frequency where the pole will be located
tau_q_1=1/w_z_q_1; alpha_lag_q_1=w_z_q_1/w_p_q_1; G_co_q_1=sqrt (alpha_lag_q_1);
num_lag_q_1= [G_co_q_1*tau_q_1 G_co_q_1];       %Numerator of the 2nd phase-lag compensator
den_lag_q_1= [alpha_lag_q_1*tau_q_1 1];         %Denominator: 2nd phase-lag compensator
G_lag_2=tf (num_lag_q_1, den_lag_q_1)           %Transfer function: second phase-lag compensator
G_q_ol_compen_lag_lag=G_q_ol_compen_lag*G_lag_2 %TF: phase-lag compensated
bode (G_q_ol_compen_lag_lag)                    %Bode plot: second phase-lag compensated system
%*************************************************************************
```

Closed Loop Transfer Functions

```
%*************************************************************************
G_q_cl_uncompen=feedback (G_q_ol_uncompen, 1);
G_q_cl_compen_lag=feedback (G_q_ol_compen_lag, 1);
G_q_cl_compen_lag_lag=feedback (G_q_ol_compen_lag_lag, 1);
%*************************************************************************
```

Step Response Curves

```
%*************************************************************************
step (G_q_cl_uncompen)                          %Step response of the uncompensated system
hold on
step (G_q_cl_compen_lag)                        %Step response: first phase-lag compensated system
hold on
```

step ($G_{q\_cl\_compen\_lag\_lag}$) %Step response: second phase-lag compensated system

A.7 Pitch-Angle Controller

****

%System Parameters

J_{eq}=6.25e6; B_{eq}=2e3; T_m=848.826e3; P_m=2e6; w_r=2.356; n_p=26; T_e=P_m/ (n_p*w_r); tau_b=0.1;

num=[T_m-T_e]; %Numerator of the uncompensated system

den= [tau_b*Jeq (tau_b*Beq) +Jeq Beq]; %Denominator of the uncompensated system

$G_{pitch\_ol\_uncompen}$=tf (num, den) %Transfer function of the uncompensated system

bode ($G_{pitch\_ol\_uncompen}$) %Bode plot of the uncompensated system

%Gain compensation

Gain=109.1; %Gain K

$G_{pitch\_ol\_compen\_gain}$=$G_{pitch\_ol\_uncompen}$*Gain; %TF: Gain-compensated system

bode ($G_{pitch\_ol\_compen\_gain}$) %Bode plot of the gain-compensated system

hold on

%**Phase-Lead Compensator Design**

$w_{\_BW}$=10; %Bandwidth of the pitch-angle controller

$Q_{\_p}$=57.85-44.9; %Phase boost needed

F_{c_p}=$w_{\_BW}$/ (2*pi); %Crossover frequency in Hz

F_{z_p}=F_{c_p}*sqrt (1-sin ($Q_{\_p}$)/1+sin ($Q_{\_p}$)); %Frequency where the zero will be located

F_{p_p}=F_{c_v}*sqrt (1+sin ($Q_{\_p}$)/1-sin ($Q_{\_p}$)); %Frequency where the pole will be located

w_{c_p}=2*pi*F_{c_p};

w_{z_p}=2*pi*1.266; %Angular frequency where the zero will be located

w_{p_p}=2*pi*1.997; %Angular frequency where the pole will be located

$tau_{\_p}$=1/w_{z_p}; $alpha_{\_lead\_p}$=w_{z_p}/w_{p_p}; G_{co_p}=sqrt ($alpha_{\_lead\_p}$);

$num_{\_lead\_p}$= [G_{co_p}*$tau_{\_p}$ G_{co_p}]; %Numerator of the phase-lead compensator

$den_{\_lead\_p}$= [$alpha_{\_lead\_p}$*$tau_{\_p}$ 1]; %Denominator of the phase-lead compensator

G_{lead_p}=tf ($num_{\_lead\_p}$, $den_{\_lead\_p}$) %Transfer Function: phase-lead compensator

bode (G_{lead_p}) %Bode plot of the phase-lead compensator

$G_{pitch\_ol\_compen\_lead}$=$G_{pitch\_ol\_compen\_gain}$*G_{lead_p}; %TF: Phase-lead compensated system

bode ($G_{pitch\_ol\_compen\_lead}$) %Bode plot of the phase-lead compensated system

%**********

Closed Loop Transfer Functions

%**********

$G_{pitch\_cl\_uncompen}$=feedback ($G_{pitch\_ol\_uncompen}$, 1);

$G_{pitch\_cl\_compen\_gain}$=feedback ($G_{pitch\_ol\_compen\_gain}$, 1);

$G_{pitch\_cl\_compen\_lead}$=feedback ($G_{pitch\_ol\_compen\_lead}$, 1);

%**********

Step Response Curves

%**********

step ($G_{pitch\_cl\_uncompen}$) %Step response of the uncompensated system

hold on

step ($G_{pitch\_cl\_compen\_gain}$) %Step response of the gain-compensated system

hold on

step ($G_{pitch\_cl\_compen\_lead}$) %Step response of the phase-lead compensated system

****

Appendix B: Clarke and Park Transformations

B.1 Implementation of αβ and dq transformations (Clarke and Park transformation)

Current and Voltage are usually described as three sinusoidal waves representing the 3 AC phases. Calculations in *abc*-frame are complex due to the sinusoidal components and its variability in the time-frame. Therefore, in order to facilitate the control design of 3-phase inverters, the 3-phase variables need to be transformed to two-phase variables [38, 86]. The three-phase variables are recovered with the inverse transform. Clarke and Park's transforms are used for carrying out this transformation[82].

B.1.1 Clarke Transformation

The Clarke Transformation (CkT) converts a stationary circuit to a stationary reference frame. CkT converts the three-dimensional vectors into a two-dimensional vector (*abc*-frame to *αβ*-frame)[86]. The transformation can be understood as the projection of the three-axis onto a 2-axis reference frame as shown in Figure B1.

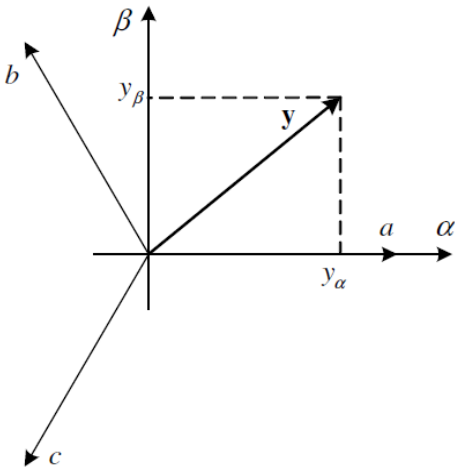

Figure B 1: Representation of the Clarke Transformation[82]

The variable change matrix is given by Eq. (B1) [82]

$$[y_{\alpha\beta}] = T_{\alpha\beta}[y_{abc}] \tag{B1}$$

Where, $T_{\alpha\beta}$ is the transformation matrix given by Eq. (B2)

$$T_{\alpha\beta} = \frac{2}{3}\begin{bmatrix} 1 & -\frac{1}{2} & -\frac{1}{2} \\ 0 & \frac{\sqrt{3}}{2} & -\frac{\sqrt{3}}{2} \end{bmatrix} \tag{B2}$$

In order for the transformation to be invertible, a third variable, known as the zero-sequence component (homo-polar component), which is orthogonal to (α, β) axis is added. The homopolar component is usually a constant value (zero if the system is balanced). The variable change matrix with the zero-component is given by Eq. (B3)

$$[y_{\alpha\beta 0}] = T_{\alpha\beta 0}[y_{abc}] \tag{B3}$$

Where, $T_{\alpha\beta 0}$ is the transformation matrix given by Eq. (B4)

$$T_{\alpha\beta 0} = \frac{2}{3}\begin{bmatrix} 1 & -\frac{1}{2} & -\frac{1}{2} \\ 0 & \frac{\sqrt{3}}{2} & -\frac{\sqrt{3}}{2} \\ \frac{1}{2} & \frac{1}{2} & \frac{1}{2} \end{bmatrix} \tag{B4}$$

The Inverse Clark Transformation (ICT) is given by Eq. (B5)

$$[y_{abc}] = T_{\alpha\beta 0}^{-1}[y_{\alpha\beta 0}] \tag{B5}$$

Where $T_{\alpha\beta0}^{-1}$ is the inverse transformation matrix given by Eq. (B6)

$$T_{\alpha\beta0}^{-1} = \frac{2}{3}\begin{bmatrix} 1 & 0 & 1 \\ -\frac{1}{2} & \frac{\sqrt{3}}{2} & 1 \\ -\frac{1}{2} & -\frac{\sqrt{3}}{2} & 1 \end{bmatrix} \tag{B6}$$

B.1.2 Park Transformation

The Park Transformation (PT) converts the two-phase vectors in the orthogonal stationary reference frame into orthogonal rotating reference frame (αβ to dq)[82]. Figure B2 shows the representation of the Park transformation. The dq frame rotates in the same direction as the αβ-vector with a speed that equals the angular frequency ω_1 of the AC system.

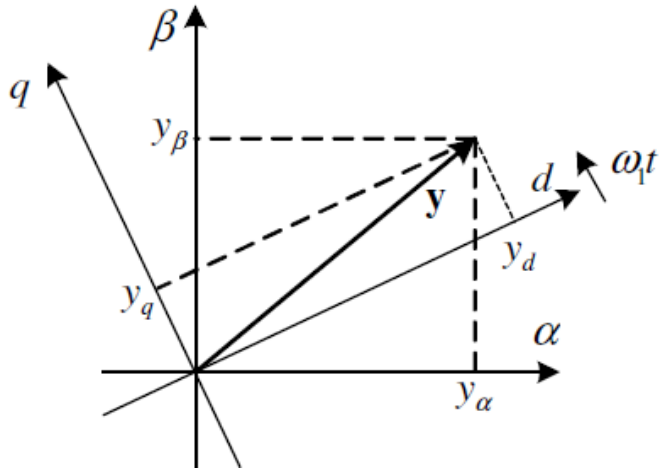

Figure B 2: Representation of Park Transformation [82]

The variable change matrix is given by Eq. (B7)[82]

$$\left[y_{dq}\right] = T_{dq}\left[y_{\alpha\beta}\right] \tag{B7}$$

Where T_{dq} is the transformation matrix given by Eq. (B8)

$$T_{dq} = \begin{bmatrix} \cos\omega t & \sin\omega t \\ -\sin\omega t & \cos\omega t \end{bmatrix} \tag{B8}$$

The inverse variable change matrix is given by Eq. (B9)

$$\left[y_{\alpha\beta}\right] = T_{dq}^{-1}\left[y_{dq}\right] \tag{B9}$$

Where T_{dq}^{-1} is the inverse transformation matrix given by Eq. (B10)

$$T_{dq}^{-1} = \begin{bmatrix} \cos\omega t & -\sin\omega t \\ \sin\omega t & \cos\omega t \end{bmatrix} \quad \text{(B10)}$$

Appendix C: South African Grid Code for Integration of Wind Energy Systems

The penetration level of wind power plants (WPPs) into the main power utility grid is increasing rapidly. To overcome the impacts of WPPs on the reliability and stability of the power systems, grid codes are put in place to serve as technical requirements for the connection and operation of WPPs in the transmission and distribution system. The following technical requirements are considered in this study[106, 107]

C.1 Frequency requirements

During normal the operation range, a WPP is required to be capable of operating continuously within a frequency range of 49 HZ to 51Hz. Figure C1 shows the graphical representation of the WPP's frequency operating range.

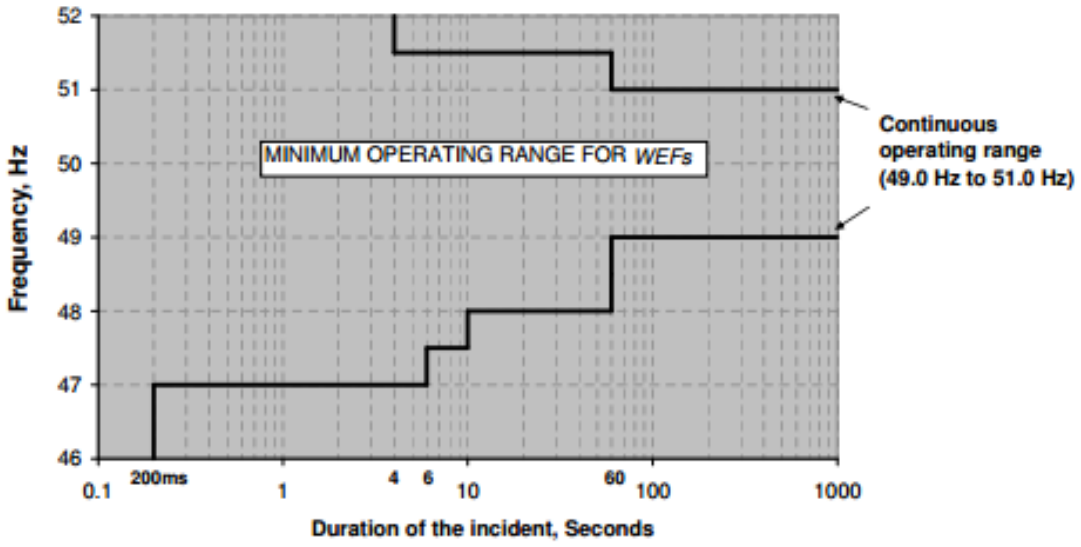

Figure C 1: Frequency operation range for WPP[106]

The WPP is required to remain connected to the network during the rate of change of frequencies up to and including 0.5Hz per second, provided the network frequency is still within the continuous frequency characteristics.

C.2 Voltage requirements

During normal operating range, the voltage level at the point of common coupling (PCC) is required to be within 90% to 110% of the nominal voltage. The maximum allowable voltage change at the PCC after switching operation shall not be greater than 2%.

C.3 Power Factor Control

A WPP with maximum export capacity (MEC) of less than 20MW is required to supply constant reactive power (MVar) of not less than 0.975 lagging and 0.975 leading power factor calculated at the rated active power output (MW) at the PCC under all operating conditions.

Figure C2 show the reactive power requirements for a WPP with MEC less than 20MW.

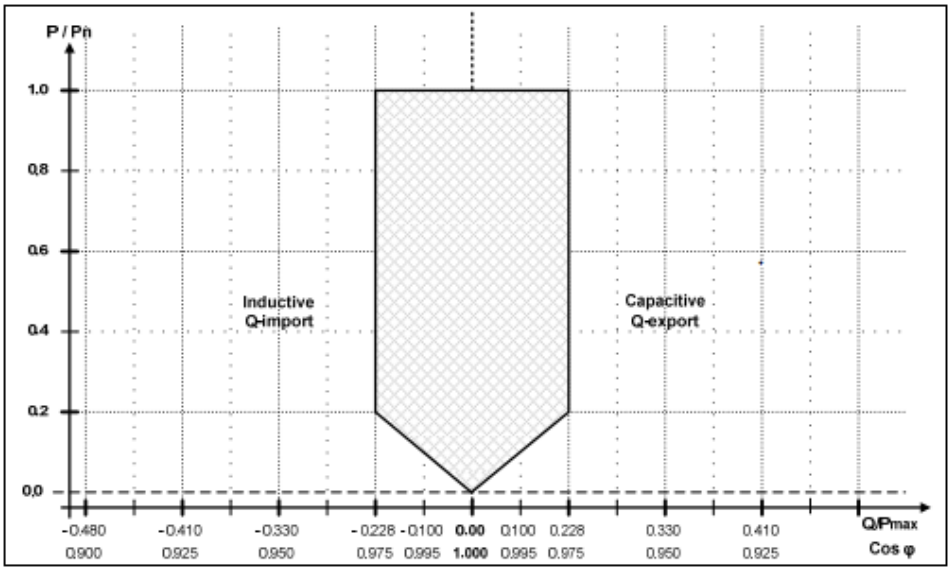

Figure C 2: Reactive power requirements for WPP with MEC less than 20MW[106]

A WPP with MEC equal to or greater than 20MW is required to supply a constant reactive power (MVar) of not less than 0.95 lagging and 0.95 leading power factor calculated at rated MW output at the PCC under all operating conditions. Figure C3 shows the reactive power requirements for a WPP with MEC equal to or greater than 20MW.

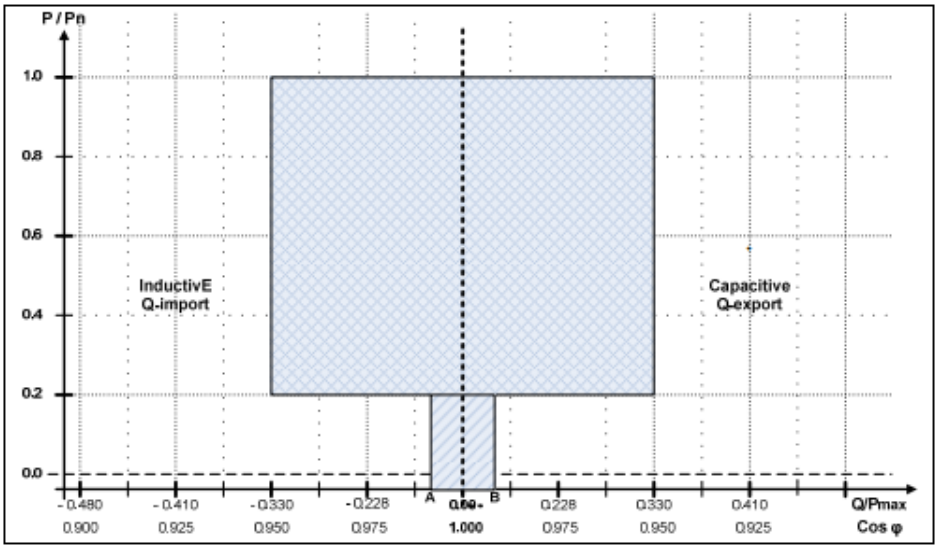

Figure C 3: Reactive power requirements for a WPP with MEC equal to or greater than 20MW[106]

C.4 Active Power Control

Active power control requirement is defined as the ability to adjust the active power output with respect to the change in frequency. Under normal operating conditions, the WPP is required to be capable of operating continuously at a power output level of 95% of the available active power and above. If the frequency rises to a level above 50.5Hz, the WPP is required to ramp down the active power output at a minimum rate of 1% of the rated capacity per second (MW/second). When the frequency is below the normal range and is recovering back towards the normal range, the Frequency Response System is required to ramp down the WPP's active power output in accordance with the frequency/ active power characteristic defined by line "A-B" on the Power-Frequency curve shown in Figure C4.

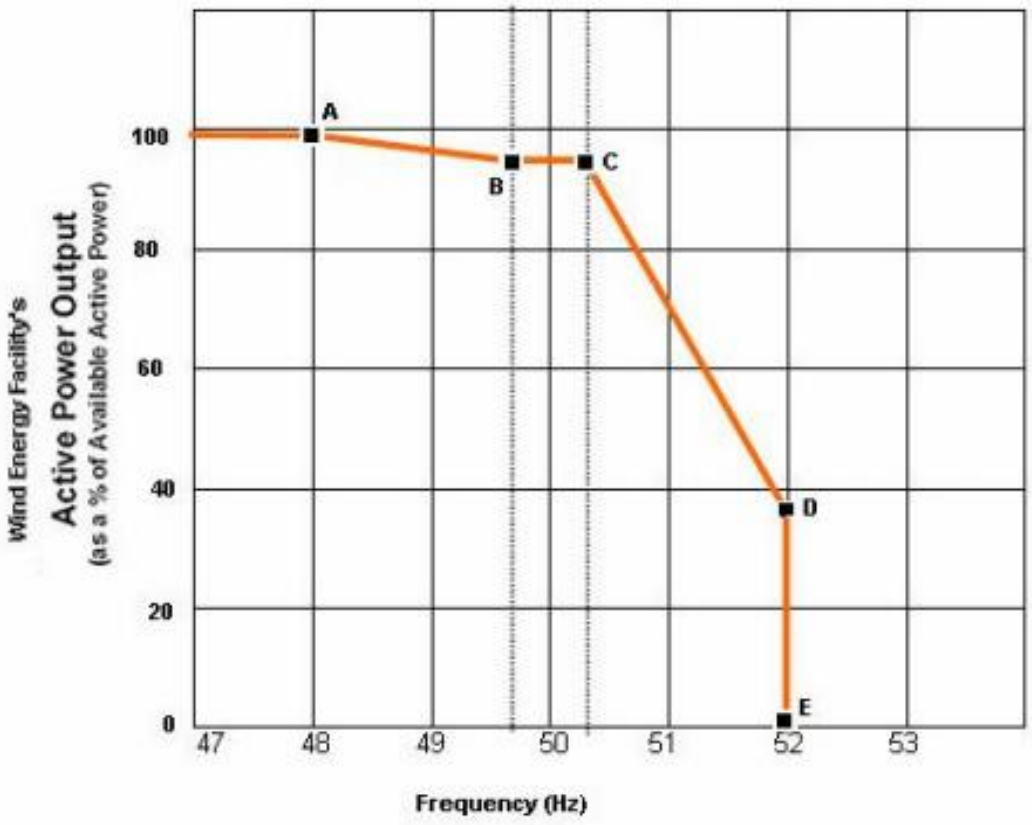

Figure C 4: Power-Frequency Control Curve[106]

Once the frequency rises to a level above point “C”, the Frequency Response System is required to ramp down the WPP’s active power output in accordance with the frequency/active power characteristic defined by the line “C-D-E”. The points on the Power-Frequency Control curve depend on a combination of the frequency, active power and MW curtailment set-point settings which are different for each WPP depending on the system conditions and the location of the WPP.

C.5 Low Voltage Ride-Through (LVRT) requirements

Grid disturbances in form of voltage sags or swells can lead to WPP getting disconnected from the network which may lead to grid instability and blackouts. The grid code requires that, regardless of the type of fault, the WPP must remain connected to the network for voltage levels within the range of 0.9p.u to 1.1p.u at the PCC, provided the power evacuation capability after the fault is maintained. For voltage levels below 0.9p.u at the PCC, the WPP will eventually be disconnected from the network. However, it is required that it gets reconnected to the network within 1 second after the voltage has been recovered to at least 0.9p.u of nominal voltage. Figure C5 shows the low voltage ride through capability requirement of a WPP.

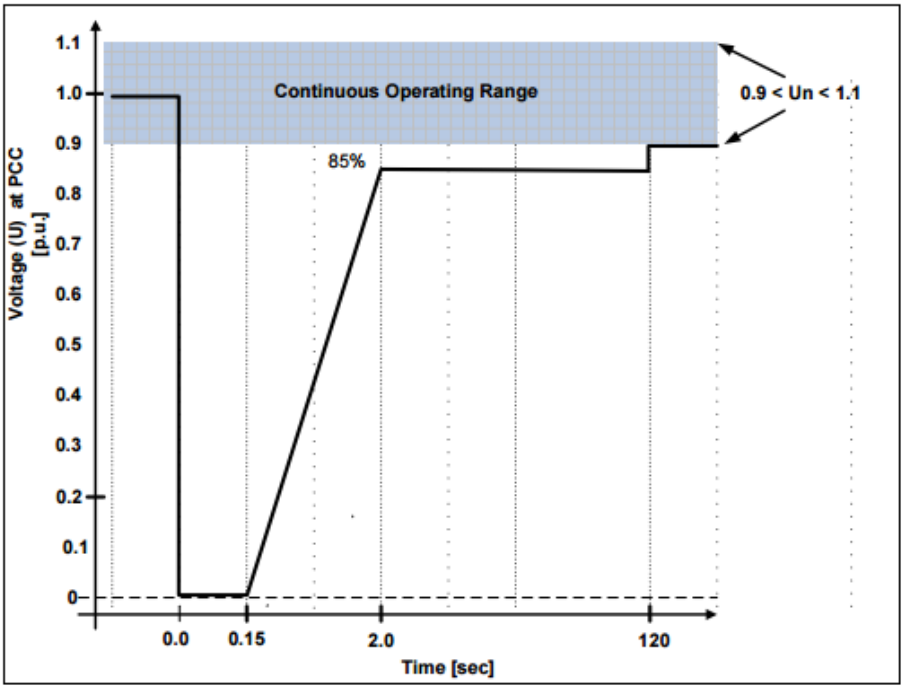

Figure C 5: Low Voltage Ride Through requirements for WPPs[106]

Appendix D: VSC-based HVDC projects in operation

Table D 1: VSC-based HVDC worldwide projects in operation[9, 12, 30, 108-111]

Project	**In service**	**Power (MW)**	**DC voltage (kV)**	**Station location**	**Transmission**	**Application**	**Customer**
HãllsjÖn Sweden	1997	3	±10	HãllsjÖn, 10kV Grãngesberg, 10kV	10km (overhead)	Pilot system	**VB Einãt**, Sweden

Gotland Sweden	1999	50	±80	Nãs, 77kV Bãcks, 77kV	70km	Wind, Undergrounding	**GEAB** Sweden
Directlink Australia	2000	3 x 60	±80	Terranora, 110kV Mullumbimby, 132kV	65km	Undergrounding	**TransEnergy**, USA **North Power**, Australia
Tjaereborg Denmark	2000	7,2	±9	Enge, 10.5V Tjaereborg, 10.5kV	4.4km	Wind, Undergrounding	**Eltra**, Denmark
Eagle Pass USA	2000	36	±15,9	Eagle Pass, 138km (both sides)	NA (back-to-back)	Grid reliability	**AEP**, USA
Cross Sound USA	2002	220	±150	New Haven, 345kV Shoreham, 138kV	40km	Grid reliability	**TransEnergy**, USA
Murraylink Australia	2002	220	±150	Berri, 132kV Red Cliffs, 220kV	180km	Undergrounding	**TransEnergie US**, USA
Troll Norway	2005	2 x 41	±60	Troll A, 56kV Kollsnes, 132kV	67km	Offshore	**Statoil**, Norway
Estlink Estonia-Finland	2006	350	±150	Espoo, 400kv Harku, 330kV	105km	Grid reliability, Undergrounding	**Nordic Energy Link AS**, Estonia
Valhall Norway	2010	78	±150	Lista, 300kV Valhall, 11kV	292km	Offshore	**BP**, Norway
BorWin1 Germany	2009	400	±150	Diele, 380kV BorWin Alpha, 170kV	200km	Offshore wind	Transpower, Germany

Caprivi Link Namibia	2009	300	±350	Zambezi, 330kV Gerus, 400kV	950km (overhead)	Grid reliability	**NamPower**, Namibia
East-West Interconnector Ireland-UK	2012	500	±200	Woodland, 400kV Deeside, 400kV	256km	Grid interconnection	**EirGrid** Ireland
DolWin Germany	2013	800	±320	DÖrpen/West, 380kV DolWin alpha, 155kV	165km	Offshore wind	**Transpower**, Germany